The MINERνA
Technical Design Report

Version 1.0

November 2006

The MINERνA Collaboration

University of Athens - University of California/Irvine - University of Dortmund - Fermilab - Hampton University - Illinois Institute of Technology - Institute for Nuclear Research, Moscow - James Madison University - Jefferson Lab - University of Minnesota-Duluth - Northern Illinois University - Northwestern University - Pontificia Universidad Catolica del Peru - University of Pittsburgh - University of Rochester - Rutgers University - Tufts University - Universidad Nacional de Ingenieria, Lima - College of William and Mary

Contents

List of Figures

List of Tables

Part I
Introduction

1 Introduction and Overview

1.1 Executive Summary

Current and upcoming neutrino oscillation experiments in the United States, Europe and Japan have driven the construction of new, very intense neutrino beamlines required to achieve reasonable event rates at detectors located hundreds of kilometers away. These new beamlines allow us to initiate a vigorous neutrino scattering research program at a detector, located close to the production target, where event rates are much higher than at the previous generation of neutrino beam facilities. Note, furthermore, that it is neutrino oscillation experiments, with their low-energy neutrinos and massive nuclear targets, which highlight the need for much improved knowledge of low-energy neutrino-Nucleus interactions.

At Fermilab, the NuMI beam, designed for the MINOS neutrino oscillation experiment, yields several orders of magnitude more events per kg of detector per year of exposure than the higher-energy Tevatron neutrino beam. With this much-increased intensity, one can now perform statistically-significant neutrino scattering experiments with much lighter targets than the massive iron, marble and other high-A detector materials used in the past. That these facilities are designed to study neutrino oscillations points out the second advantage of these neutrino scattering experiments: An excellent knowledge of the neutrino beam will be required to reduce the beam-associated systematic uncertainties of the oscillation result. This knowledge of the neutrino spectrum will also reduce the beam systematics in the measurement of neutrino-scattering phenomena.

The MINERνA experiment (Main INjector ExpeRiment: ν-A), a collaboration of elementary particle and nuclear physics groups and institutions, will run in the NuMI beamline, and be sited in the hall which currently houses the MINOS near detector. With considerable available space, the hall is an ideal environment for neutrino experiments. It provides a well-shielded area with sufficient infrastructure to support MINERνA as well as MINOS.

MINERνA will complete a physics program of high rate studies of exclusive final states in neutrino scattering including quasi-elastic scattering, and resonant and coherent pion production. MINERνA will also study the poorly understood transition region between non-perturbative and perturbative QCD in the higher mass resonance region and the application of duality with the weak current. MINERνA will contribute significantly to the study of parton distribution functions (PDFs) in the poorly known high-x_{Bj} region as well as quark-flavor dependent studies of generalized parton distributions (GPDs). Studies on several nuclear targets will explore nuclear effects, another topic that has not been studied with neutrinos up to now, and will bring important constraints to determining nuclear PDFs.

MINERνA results will also be very important for present and future neutrino oscillation experiments, where the details of neutrino cross-sections and final states as well as nuclear effects are essential in determining the energy of the incoming neutrino and in separating backgrounds to oscillation from signal.

MINERνA will address all these topics with a comparatively simple, high-precision detector composed of several sub-detectors with distinct functions in reconstructing neutrino inteactions. The target volume (approximately 6 tons) for most analyses is the inner "Totally Active Detector" where the only material is the sensitive scintillator strips themselves. The scintillator detector does not fully contain events due to its low density and lowZ, so the MINERνA design surrounds it with sampling detectors; electromagnetic and hadronic calorimeters. The nuclear targets of graphite, iron and lead will be located in the upstream end of the detector.

1.2 The NuMI Near Detector Hall

The NuMI Near Detector Hall[1] is a fully-outfitted experimental facility that can accomodate MINERνA with a limited number of additions to the infrastructure.

The hall is 45 m long, 9.5 m wide, 9.6 m high, with its upstream end just over 1 km from the NuMI target, at a depth of 106 m below grade. The MINOS near detector has been installed at the downstream end of the hall, and there is free space upstream amounting to, roughly, a cylinder 26 m in length and 3 m in radius. The neutrino beam centerline descends at a slope of $3.3°$ and enters the MINOS detector at a height of 3 m from the floor.

Ground water is pumped from the NuMI/MINOS complex at a rate of approximately 200 gallons (750 l) per minute. The hall floors and walls are occasionally damp in places, and a drip cover will be used to protect MINERνA from moisture. The air is held at a temperature between $60°$ F and $70°$ F ($15°$ C and $21°$ C), and 60% relative humidity.

1.2.1 Utilities

The MINOS Service Building on the surface houses the access shaft to the Near Detector Hall and is the entry point for electrical, cooling, and data services to the hall. A 15-ton capacity crane, with a hook height of 18.5 feet (5.66 m), was used to lower the 3.47 ton MINOS detector planes to the hall. MINOS planes were moved within the hall using an overhead 15-ton crane, with 22 foot (6.7 m) hook height and a coverage along the beam axis of approximately 40 m. The procedure for installing MINERνA will closely follow that used by MINOS.

Quiet power to the hall is provided by a 750 KVA transformer at the surface, which branches to a 45 KVA transformer for the muon monitoring alcoves, and two 75 KVA transformers for the Near Detector hall. The power needs of the MINOS detector account for the capacity of the 4 panelboards served by the two 75 KVA transformers. The estimated power consumption of MINERνA's electronics is around 5000 W. MINERνA will require an additional 75 KVA transformer as well as additional panelboards. Both the transformer and panelboards have already been installed by Fermilab.

The heat sink for the MINOS LCW cooling circuit is the flux of ground water collected in the MINOS sump. This cooling is adequate for MINOS, ¡with an output water temperature of $70°$ F. The relatively low heat load of the MINERνA electronics will be absorbed without problem by the MINOS hall air conditioning.

1.2.2 Detector placement

The downstream face of the last MINERνA plane will be placed 2.0 m upstream of the upstream face of the first MINOS plane as shown in Figure 2. This will leave sufficient work space between the two detectors and will avoid interfering with the MINOS coil, which extends approximately 1.7 m upstream of MINOS, to the lower right in the view of Figures 1 and 3. To have the beam axis intersect the detector axis close to the center of the active plastic target, the lowest corner of MINERνA will be placed 1.10 m above the hall floor. The beam centerline will enter the detector at an elevation of 3.4 m from the floor.

1.2.3 Impact on MINOS

The impact of MINERνA on the MINOS installation has been and will continue to be minor. The power supply for the MINOS coil had to be moved upstream and the stairway accessing the upper MINOS electronics racks had to be moved. The drip-ceiling covering the MINOS experiment will be extended to also cover MINERνA during an upcoming Fermilab shutdown.

The presence of the detector in the neutrino beam will cause an increase in the rate of activity in the MINOS detector, mainly in the first (upstream) 20 planes forming the MINOS veto region. Given MINERνA's total mass of $\approx$ 200 tons, for the majority running of the MINOS experiment that uses the lowest energy NuMI beam tune, the expected event rate in the detector is ≈ 1.2 charged-current interactions per 10^{13} protons on target (POT). For a spill of 2.5×10^{13} POT this corresponds to 3.0 charged-current events, plus an additional 1.0 neutral-current event per spill. Combining the excellent timing resolution of both MINERνA and MINOS with the fact that the vectors of all particles leaving MINERνA with a trajectory heading towards MINOS will be made available when MINERνA is taking data, this rate should be easily managable. Even when running the NuMI beam in the higher energy (ME) tune, the increase in rate should be $\approx$ 3.5, and that is still managable.

1.3 The NuMI Beam and MINERνA Event Sample

The NuMI neutrino beam is produced from π- and K-decay in a 675 m decay pipe beginning 50 m downstream of the graphite target that is followed by a double horn focusing system. At the end of the decay pipe a 10 m long hadron absorber stops the undecayed secondaries and non-interacting primary protons. Just downstream of the absorber, 240 m of Dolomite is used to range out muons before the ν beam enters the Near Detector Hall. Figure 4 shows the beamline and layout.

1.3.1 Energy options

The neutrino energy spectrum of the NuMI beam can be adjusted by changing the distances of the target and second horn with respect to the first (fixed) horn, as in a zoom lens. The three standard configurations result in three beam energy tunes for the low- (LE), medium- (ME), and high-energy (HE) ranges respectively. However, to switch from one beam mode to another requires down-time, to reconfigure the target hall, and a consequent loss of beam time. An alternative procedure, which also allows the peak energy to be varied, is to change the distance of target from the first horn and leave the second horn fixed in the LE position. Although the resulting event rates are lower in comparison with those involving the movement of the second horn (ME and HE), the movement of the LE target can be accomplished remotely and quickly with a maximum target excursion of -2.5 m upstream of the first horn from its nominal low-energy position. Moving the target -1.0 m results in a “semi-medium” energy beam tune (sME), and -2.5 m produces a “semi-high” energy beam (sHE). A considerably more efficient sHE beam is possible with three-day downtime to move the target to its normal HE

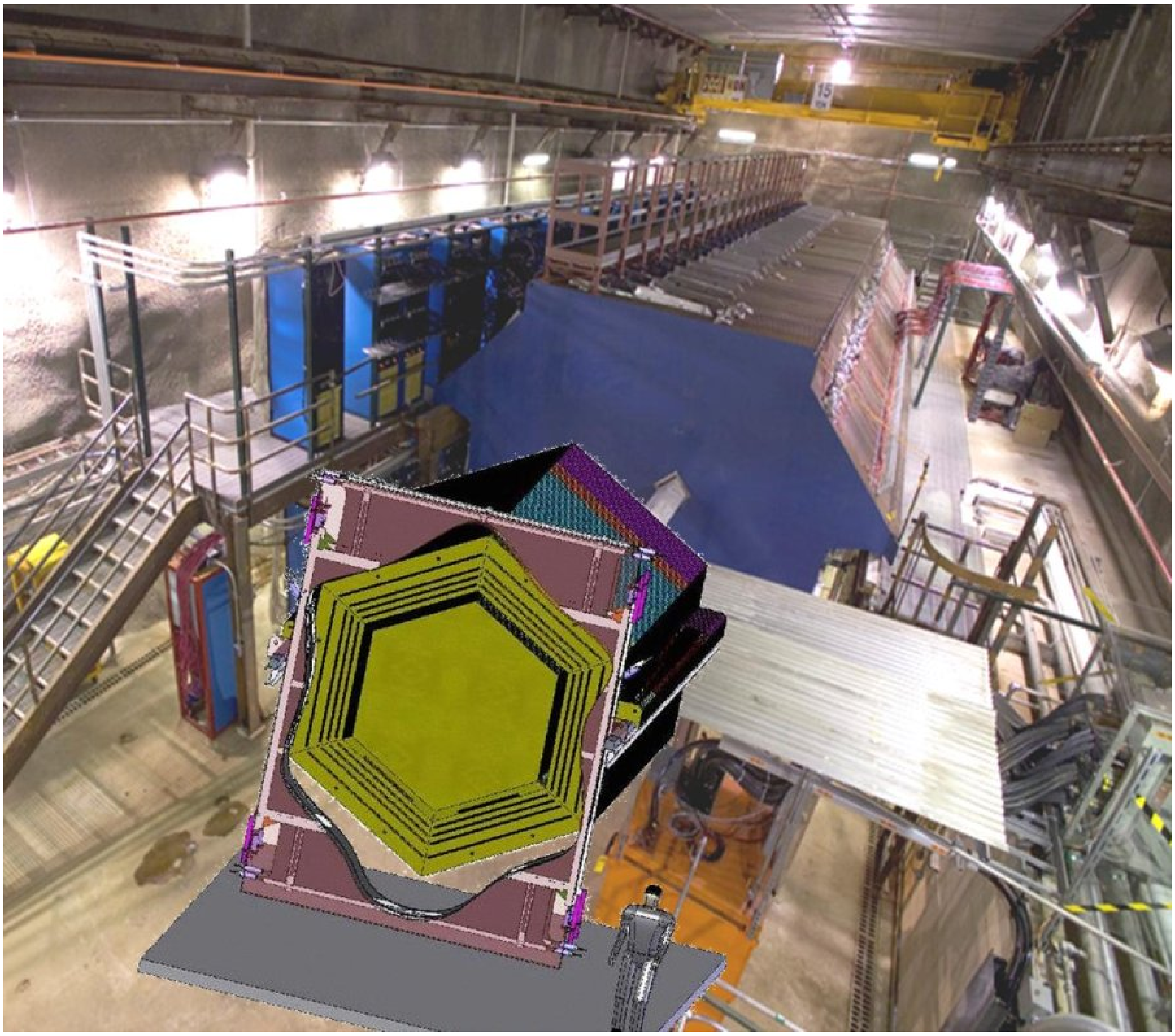

Figure 1: Isometric engineering concept of the proposed MINERνA detector in its home in the NuMI near hall. The photo looks downstream to the MINOS near detector.

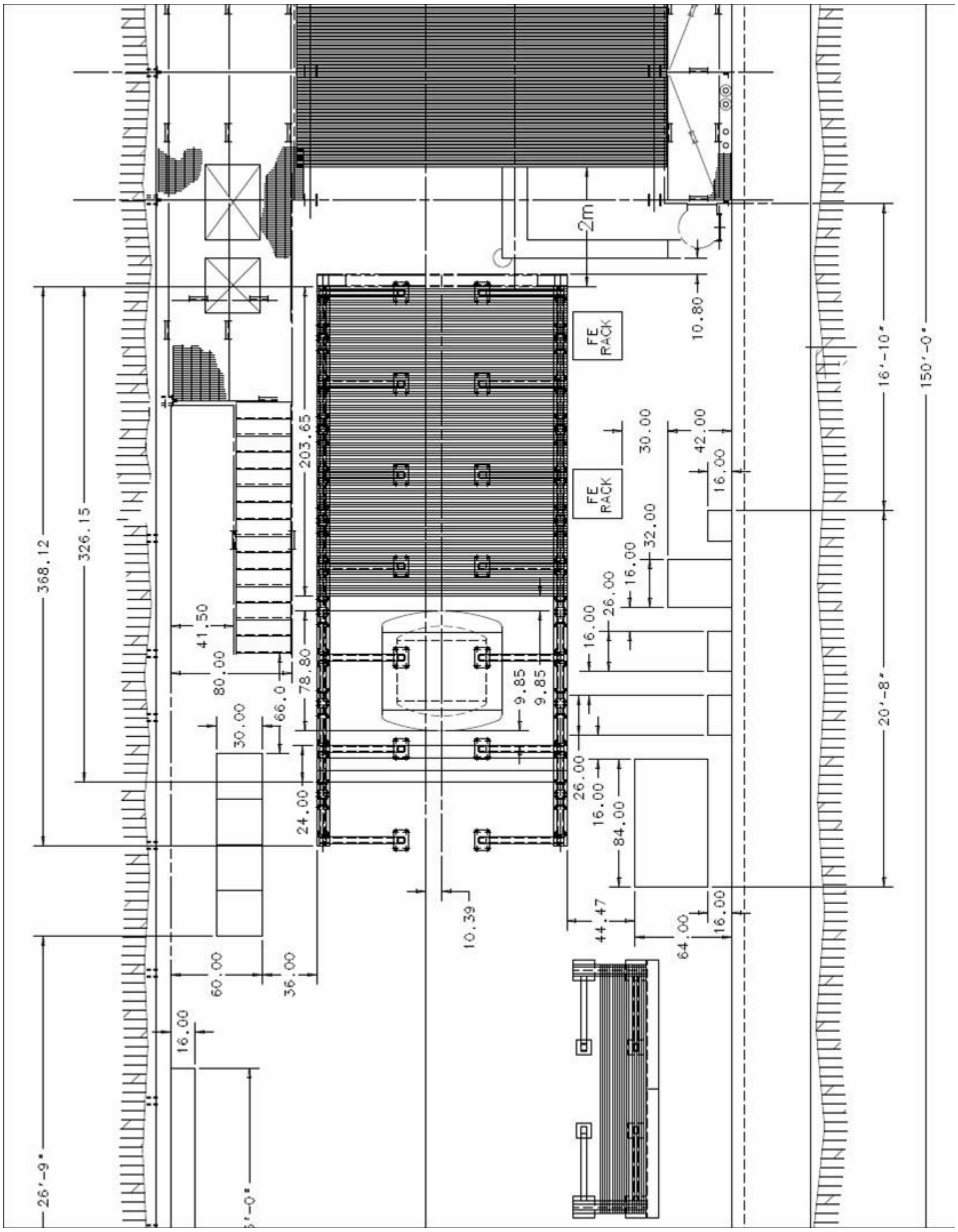

Figure 2: Plan view of MINERνA in the NuMI near hall

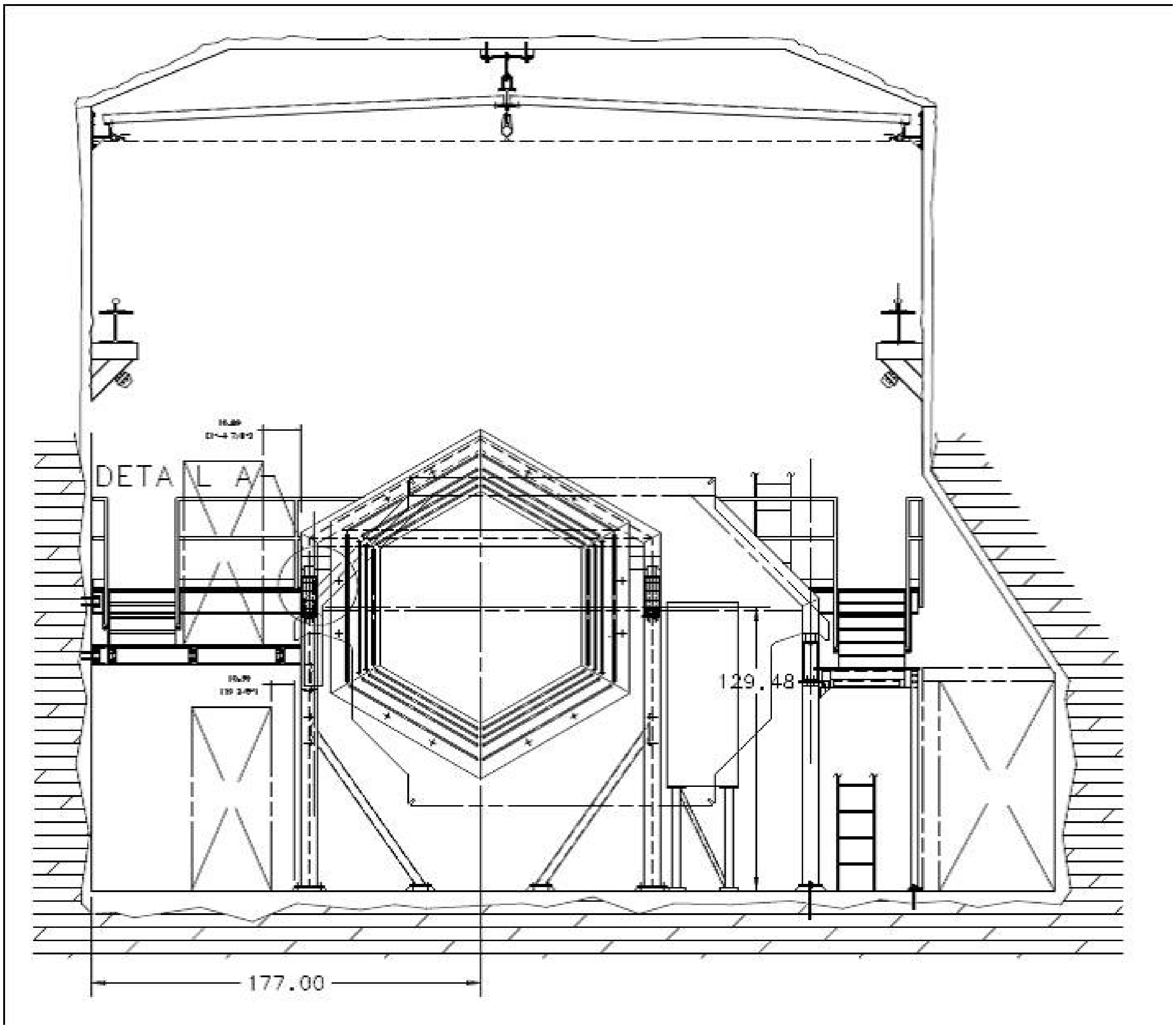

Figure 3: Front view of MINERνA in the NuMI near hall

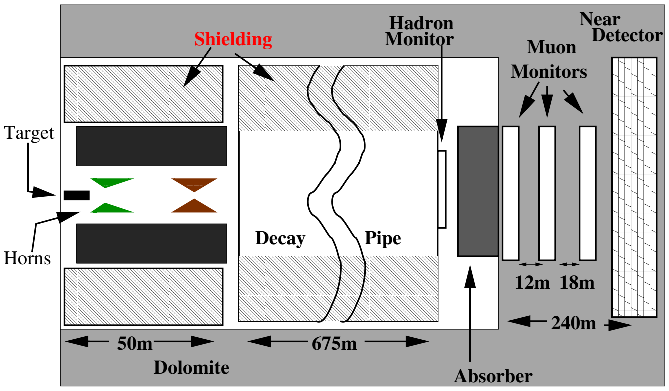

Figure 4: Layout of NuMI beamline components and near detector hall (not to scale).

position of -4.0 m. This more efficient sHE(-4.0) beam would yield over 50% more events than the sHE(-2.5) beam.

When MINERνA is running parasitically with MINOS, the beamline will be operating primarily at its lowest possible (LE) neutrino energy setting, to reach the lowest values of Δm^2. However, to minimize systematics, MINOS will also run in the sME and sHE configurations. The neutrino energy distributions for the LE, sME, and sHE running modes are shown in Figure 5.

When MINERνA is running parasitically with NOνA the beamline will be operating in the medium energy - ME- configuration.

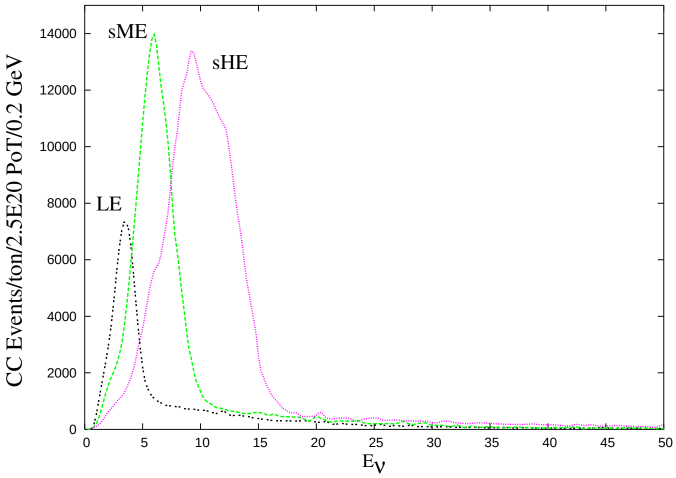

Figure 5: Neutrino energy distribution for charged-current interactions in three configurations of the NuMI beam corresponding to low-energy (LE), medium-energy (sME) and high-energy (sHE).

1.3.2 MINERνA event rates

Table 1 shows charged-current interaction rates per 10^{20} protons on target (PoT) per ton for different neutrino beam energy configurations.

Beam	CC ν_μ
LE	60 K
ME	235 K
sME	132 K
sHE	212 K

Table 1: MINERνA charged-current interactions per ton, per 10^{20} protons on target.

The same beam configurations with horn-currents reversed focus π^- to create anti-neutrino beams. The $\overline{\nu}_\mu$ charged-current interactions from anti-neutrino configurations (LErev, MErev, and HErev) are of great interest and would be highly desirable for MINERνA's physics program. Table 2 shows charged-current anti-neutrino interaction rates per 10^{20} protons on target (PoT) per ton for different neutrino beam energy configurations.

Beam	CC $\overline{\nu}_\mu$	CC ν_μ
LErev	26 K	34 K
MErev	56 K	10 K
HErev	75 K	13 K

Table 2: MINERνA charged-current $\overline{\nu}_\mu$ interactions per ton, per 10^{20} protons on target.

The baseline MINERνA four-year run plan assumes one year running parasitically with MINOS in the LE beam and 3 years running parasitically with NOνA in the ME beam. The assumed protons-on-target for each of the four years is 4×10^{20} PoT. With this 4-year run plan, the total expected charged current event rate is $\approx$ 2.9 million per ton of detector and the event rates per ton for each CC physics-channel is shown in Table 3. As will be described in detail in the MINERνA Project section of this report, the fiducial volume of the fully-active central detector will be 3 tons while the fiducial volume of the nuclear targets will be 0.14 ton, 0.69 ton and 0.86 ton for C, Fe and Pb respectively.

Process	CC/ton	NC/ton
Quasi-Elastic	270 K	90 K
Resonance	530 K	165 K
Transition	670 K	210 K
DIS	1370 K	400 K
Coherent	28 K	14 K
Total (ν)	2870 K	880 K

Table 3: MINERνA samples per ton for various processes assuming the 4-year run plan described in the text.

Required Statistics using the NuMI Low-energy (LE) Beam Configuration For the given distance between Fermilab and the MINOS or NOνA far detectors in northern Minnesota, the expected neutrino oscillation maximum is between 1 and 2 GeV. The neutrino energy region up to 3 GeV, that brackets oscillation maximum, is therefore crucial to both MINOS and NOνA. As shown in Figure 6, to maximize statistics in this region, the MINOS collaboration chose to run with the LE beam for the obvious benefit of extending the reach of the experiment to the lowest values of Δm^2. Although NOνA has chosen to run with the ME configuration, it is running with the far detector in an off-axis position so that the energy of neutrinos reaching their far detector is considerably lower than the on-axis spectrum and falls in the crucial $\leq$ 3 GeV region. It is then in this $\leq$ 3 GeV neutrino energy region that MINERνA must have the statistical precision to precisely measure cross sections and nuclear effects to optimally help MINOS and NOνA minimize their systematic errors.

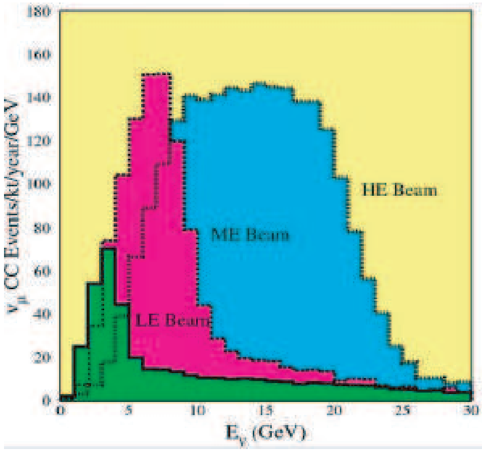

Figure 6: Neutrino energy distribution for charged-current interactions in three configurations of the NuMI beam corresponding to the on-axis low-energy (LE) , full medium-energy (ME) and full high-energy (HE) configurations.

The comparison between the LE and ME beams shown in Figure 6 clearly demonstrates that the LE beam delivers considerably more neutrino events per POT. Table 4 indicates quantitatively the superiority of the LE beam in delivering low-energy neutrino events.

Energy Bin	Ratio: LE to ME Events
0 - 1 GeV	8.0
1 - 2 GeV	3.25
2 - 3 GeV	1.5

Table 4: Expected ratio of events per POT using the NuMI LE compared to ME beam configurations in the energy bins between 0 and 3 GeV

If we change the baseline MINERνA four-year run plan to assume no running in the LE beam and 4 years running parasitically with NOνA in the ME beam (4×10^{20} PoT/year), the loss of statistics in the crucial neutrino energy bins is summarized in table 5.

Energy Bin	Fraction of Events Lost
0 - 1 GeV	0.65
1 - 2 GeV	0.4
2 - 3 GeV	0.15

Table 5: Expected loss of events with a 4-year ME beam run compared to a 1-year LE + 3-year ME beam run.

This loss of statistics on an absolute scale is sufficient to reduce the number of events, for example, in the study of the contentious low-energy behavior (0 - 2 GeV) of CC coherent pion production from 500 to just over 200 events. This will compromise the statistical weight of MINERνA's ability to compare with the recent surprising K2K result [10] and to distinguish between competing models in this energy region. The effect of this loss of statistics in the low-energy region is being studied quantitatively for other channels including quasi-elastic, resonant 1-π production, nuclear effects and the ν_e analysis.

1.3.3 Precision of neutrino flux prediction

In addition to huge event rates, one of MINERνA's significant advantages over previous wide-band neutrino scattering experiments will be better knowledge of the neutrino flux and energy spectrum. Since the NuMI beamline is designed for the MINOS oscillation experiment, considerable effort has been devoted to control of beam-related systematic uncertainties.

The largest source of uncertainty in the neutrino energy spectrum arises from the hadron ($\pi^{\pm}$ and K) prodution spectra. To reduce this uncertainty, a dedicated Fermilab experiment called MIPP (E-907)[7, 4] is directly measuring these hadron production spectra for various nuclear targets. One of the E-907 measurements has been to expose the actual NuMI LE target to the 120 GeV Main Injector proton beam. Using the NuMI target material and shape, E-907's data will include secondary and tertiary hadron production, which significantly modifies the spectra relevant for neutrino production. With input from E-907, the bin-to-bin energy spectrum should be known to $\approx 2\%$ and the absolute neutrino flux should be known to $\approx 5\%$.

For the absolute flux of neutrinos, a second uncertainty concerns the number of protons on target. With the current NuMI primary proton beamline instrumentation[8], the number of protons on target will be known to within (1 - 1.5)%, the range being determined by control of the drift in the proton beam toroid devices.

Flux uncertainty estimates Figure 7 shows the level of flux precision at present (without input from the MIPP experiment), for the LE and ME beam configurations (from MINOS) [11].

The impact that these flux uncertainties will have on MINERνA physics is illustrated in Figure 8 which shows the size of flux uncertainties on the quasi-elastic cross section measurement. Error bars on points show the contributions to the flux uncertainty which arise from beamline component modeling at the current level of precision (from MINOS). The Outer band shows the combined total error from current production (pre MIPP) and beamline component modeling in quadrature. At

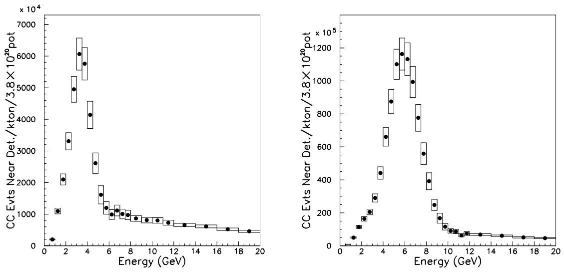

Figure 7: Uncertainties from modeling production and from beamline element optics (alignment, currents) in GNUMI from MINOS. The plots are LE beam (left) and sME beam (right). Note that the sME beam will not have the same uncertainties in the focusing peak as for the optimized ME beam.

the current level of precision flux uncertainty will dominate the QE cross section measurement in MINERνA and limit precision to $\sim$8-15% level.

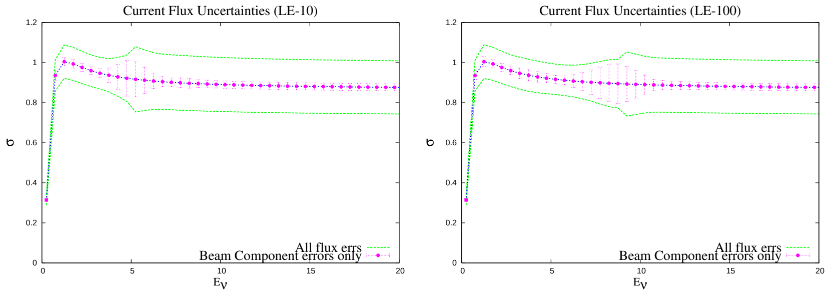

Figure 8: Uncertainties from knowledge of the flux. Error bars on points show the contributions to the flux uncertainty which arise from beamline component modeling at the current level of precision (from MINOS). Outer band shows the combined total error from current production (pre MIPP) and beamline component modeling in quadrature. The plots are LE beam (left) and sME beam (right).

Figure 9 shows the effect that MIPP projected uncertainties will have on the expected flux prediction. The plots assume that MIPP will reduce production uncertainties to the level of 4%. Beam component uncertainties will also change (the plots do not reflect this). After MIPP results are incorporated the flux prediction will be much improved and may be dominated by beamline component tolerances (alignment and current precision).

Figure 10 shows the effect of including flux errors on the measurement of the charged-current cross section in MINERνA$\dot{}$The plot assumes all running is in the LE beam. The contribution from the flux uncertainty is comparable to the statistical precision for this measurement. Reducing the flux errors will make the coherent cross section measurements statistics limited.

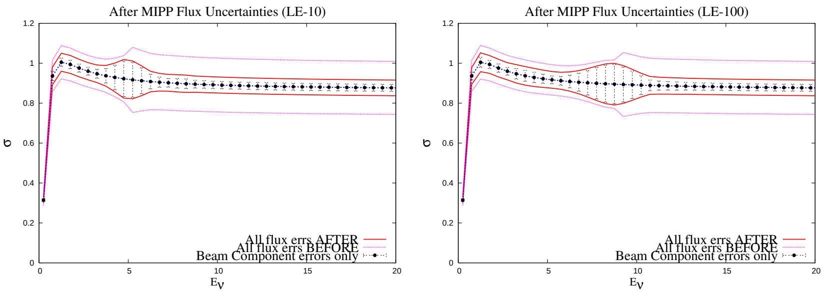

Figure 9: Estimate of flux uncertainties after MIPP data are incorporated into the flux prediction. Inner band (red) shows the total flux uncertainty assuming 4% production uncertainties (after MIPP) and beamline component uncertainties unchanged. The outer band (pink) shows the pre-MIPP total uncertainty band. Error bars on the points show the contribution to the flux uncertainty from beamline component tolerances (at the current level) only. The plots are LE beam (left) and sME beam (right).

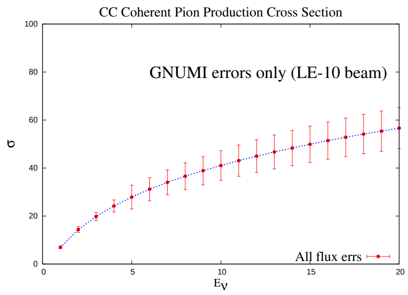

Figure 10: Size of contribution to uncertainty on the charged-current coherent cross section from flux uncertainties only (at the current level of precision pre-MIPP).

Part II
MINERνA Physics Goals and Detector Design Drivers

2 MINERνA Physics Goals and Detector Design Drivers

The MINERνA neutrino scattering experiment in the NuMI beam offers a unique opportunity to explore a broad spectrum of physics topics. Some have never been studied systematically, while others are plagued by sparse data with large statistical and systematic errors. The complete MINERνA physics program will include high-statistics studies of all the topics listed below. These studies are important for both the elementary particle and nuclear physics communities, providing information complementary to JLab studies with charged leptons in the same kinematic range.

1. Precision measurement of the quasi-elastic neutrino–nucleus cross-section, including its E_ν and q^2 dependence, and study of the nucleon axial form factors. Over **800 K** events are expected in the fiducial volume during a four-year MINERνA run.
2. Determination of cross-sections in the resonance-dominated region for both neutral-current (NC) and charged-current (CC) interactions, including study of isospin amplitudes, measurement of pion angular distributions, isolation of dominant form factors, and measurement of the effective axial mass. A total of **1.6M** one-pion events make up the low-W resonance sample.
3. Precision measurement of coherent single-pion production cross-sections, with particular attention to target A-dependence. NC coherent pion production is a significant background for next-generation of neutrino oscillation experiments probing $\nu_\mu \to \nu_e$ oscillation. A sample of **85 K** CC events is expected off carbon. The expected NC sample is roughly half the CC sample.
4. Examination of nuclear effects in neutrino interactions, including final-state modifications in heavy nuclei, by employing carbon, iron and lead targets. These effects play a significant role in neutrino oscillation experiments measuring ν_μ disappearance as a function of E_ν. It has recently been suggested that, for a given Q^2, shadowing can occur at much lower energy transfer (ν) for neutrinos than for charged leptons. This effect is unaccounted for in neutrino event generators. With sufficient $\overline{\nu}$ running, a study of flavor-dependent nuclear effects can also be performed. Due to the different mix of quark flavors, this is another way in which neutrino and charged-lepton nuclear effects differ. MINERνA will collect over **1.5M** CC events off both iron and lead, in addition to the carbon sample.
5. Study of nuclear effects on $\sin^2\theta_W$ measurements, and the NC/CC ratio for different nuclear targets.
6. Exploration of the W (hadronic mass) transition region where resonance production merges with deep-inelastic scattering (DIS), testing phenomenological models like quark/hadron duality. A sample of **2.0 M** multi-pion events is expected with W $\leq$ 2.0 GeV.
7. With a sample of over **4.1 M** CC DIS events, a much-improved measurement of the parton distribution functions, particularly at large x_{Bj}, will be possible using a measurement of all three ν structure functions. Although we expect over **100 K** CC $\overline{\nu}$ events in the four year MINERνA ν run, an additional dedicated $\overline{\nu}$ run would be required to measure the three $\overline{\nu}$ structure functions with similar precision.
8. Examination of the leading exponential contributions of perturbative QCD.
9. With nearly **230 K** fully reconstructed exclusive events, precision measurement of exclusive strange-production channels near threshold. This will significantly improve our knowledge of backgrounds in nucleon-decay searches. Also, determination of V_{us}, and searches for

strangeness-changing neutral-currents and candidate pentaquark resonances will be undertaken Measurement of hyperon-production cross-sections, including hyperon polarization, is feasible with exposure of MINERνA to $\overline{\nu}$ beams.

10. Improved determination of the effective charm-quark mass (m_c) near threshold, and new measurements of V_{cd}, $s(x)$ and, independently, $\overline{s}(x)$.

These are worthy research topics in their own right, and improved knowledge in most is essential to minimizing systematic uncertainties in neutrino-oscillation experiments.

2.1 Physics Driven Detector Requirements

To accomplish these physics goals requires a detector with particular attributes. It is not sufficient to simply have a large sample of interactions on the various targets. The kinematics of the events have to be reconstructed with sufficient accuracy to be able to determine the dynamics of the interaction.

To meet the physics goals of the experiment, the required resolution of the detector in measuring such kinematic variables as momentum, energy and angle were studied in detail in terms of three physics channels: quasi-elastic scattering, coherent pion production and deeply inelastic scattering. For each of these channels the purity of the final sample of candidates as well as the efficiency for detecting true candidates was measured as a function of the resolution of the detector. Studied were the momentum and angular resolution in the measurement of the outgoing muon in the three charged-current channels, the momentum resolution of stopping tracks for the quasi-elastic channel, the resolution of the measurement of hadronic energy showers and finally the resolution in the total visible energy of the interacting neutrino.

The details of the studies will be found in the following sections covering each of the channels: section 2.1 on Quasi-elastic scattering, section 2.3 on coherent pion production and section 2.6 on deeply inelastic scattering. Table 2.1 is a summary of the resolution studies giving the results for all three channels.

Channel	$\Delta P_\mu/P_\mu$	$\Delta\Theta_\mu$	$\Delta p^{stop}/p^{stop}$	ΔE^{int}	ΔE_ν
Quasi-elastic (Sect. 2.1)		note (a)	$\leq$ 0.05	$\leq 0.3/\sqrt{E_H}$	$\leq$ 0.15, note (b)
Coherent (Sect. 2.3)		$\leq 0.5°$		$\leq 0.20/\sqrt{E_H}$	
DIS (Sect. 2.6)	≤ 0.12				≤ 0.12, note (c)

Table 6: Summary of Physics-driven kinematic variable requirements. Notes: (a) Limits low Q^2 reach, (b) at low E_ν, (c) at high y

The remainder of this section provides more detail, and illustrates the rich physics potential of MINERνA.

2.2 Quasi-Elastic Scattering

2.2.1 Introduction

Quasi-elastic scattering dominates the total ν–N interaction rate in the threshold regime $E_\nu \leq 2$ GeV. Precision measurement of the cross-section for this reaction, including its energy dependence and variation with target nuclei, is essential to current and future neutrino-oscillation experiments.

2.2.2 Nucleon Form-factors in Quasi-elastic Scattering

MINERνA's large quasi-elastic samples will probe the Q^2 response of the weak nucleon current with unprecedented accuracy. The underlying V-A structure of this current includes vector and axial-vector form-factors. The essential formalism is given in reference [12].

$$< p(p_2)|J_\lambda^+|n(p_1) >= \overline{u}(p_2)\left[\gamma_\lambda F_V^1(q^2) + \frac{i\sigma_{\lambda\nu}q^\nu\xi F_V^2(q^2)}{2M} + \gamma_\lambda\gamma_5 F_A(q^2)\right]u(p_1),$$

where $q = k_\nu - k_\mu$, $\xi = (\mu_p - 1) - \mu_n$, and $M = (m_p + m_n)/2$. Here, μ_p and μ_n are the proton and neutron magnetic moments. The pseudoscalar form-factor is not shown since it is small for ν_μ.

The vector part of this matrix element can be expressed using $G_E^p(q^2)$, $G_E^n(q^2)$, $G_M^p(q^2)$, and $G_M^n(q^2)$. It has been generally assumed that the q^2 dependence of these form-factors can be described by the dipole approximation:

$$G_D(q^2) = \frac{1}{\left(1 - \frac{q^2}{M_V^2}\right)^2}, \quad M_V^2 = 0.71 \text{ (GeV/c)}^2, \quad F_A(q^2) = \frac{g_A}{\left(1 - \frac{q^2}{M_A^2}\right)^2}$$

$$G_E^p = G_D(q^2), \quad G_E^n = 0, \quad G_M^p = \mu_p G_D(q^2), \quad G_M^n = \mu_n G_D(q^2).$$

As discussed below, the dipole parameterization is far from perfect. MINERνA will be able to measure deviations of F_A from this form. In general, the axial form-factor $F_A(q^2)$ can only be extracted from quasi-elastic neutrino scattering.[1]

2.2.3 Vector form-factors

Electron scattering experiments at SLAC and Jefferson Lab (JLab) have measured the proton and neutron electromagnetic (vector) form-factors with high precision. The vector form-factors can be determined from electron scattering cross-sections using the standard Rosenbluth separation technique[13], which is sensitive to (two-photon) radiative corrections, or from polarization measurements using the newer polarization transfer technique[14]. Polarization measurements do not directly measure form-factors, but rather the ratio G_E/G_M. Recently, discrepancies in electron scattering measurements of some vector form-factors have appeared; study of quasi-elastic reactions in MINERνA may help reveal the origin these discrepancies. Figure 11 shows the BBBA-2005 (Bradford, Bodek, Budd,

[1] At low Q^2, below 0.1 (GeV/c)^2, its behavior can also be inferred from pion electroproduction data.

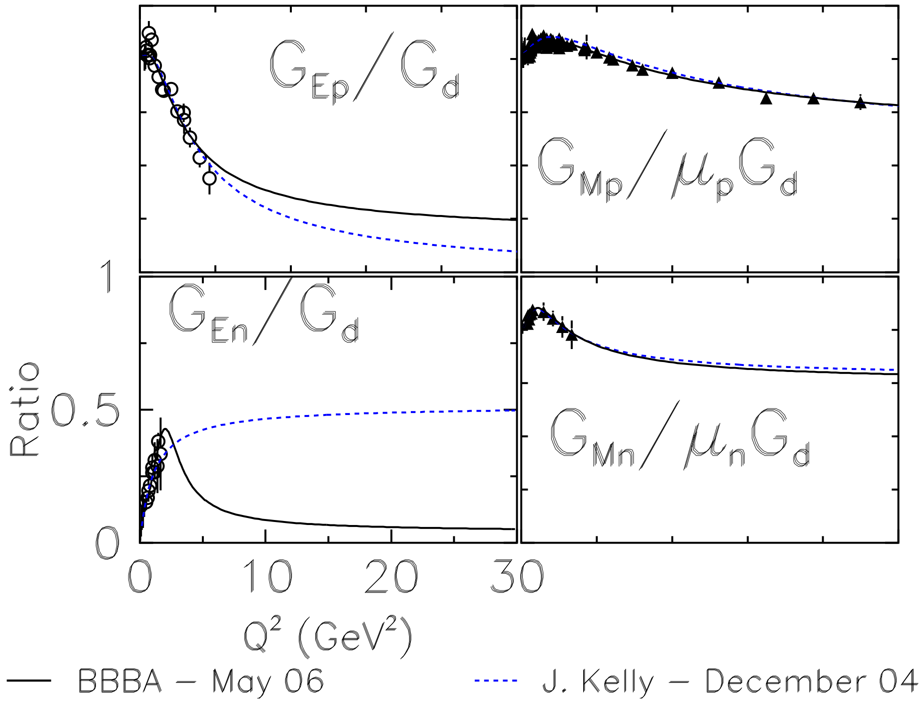

Figure 11: Deviations from dipole approximation are illustrated for two different nucleon form factor parameterizations - J. Kelly [15](dashed Blue) and BBBA05 [16] (solid black). Data are taken from [15].

Arrington 2005) fits. There appears to be a difference between the two methods of measuring this ratio. The newer polarization transfer technique yields a much lower value at high Q^2 and indicates a difference between the electric charge and magnetization distributions. The polarization transfer technique is believed to be more reliable and less sensitive to radiative effects from two-photon corrections. In addition, Figure 11 shows that dipole amplitudes provide only a first-order description of form-factor behavior at high Q^2.

If the electric charge and magnetization distributions of the proton are indeed different, accurate measurement of the axial form-factor's high-Q^2 shape in MINERνA can provide important new input to help resolve differences in electron scattering data.

To obtain the correct neutrino cross-sections [17], the input form-factors must be correct. The Q^2 distribution measured in neutrino scattering is sensitive to both the vector and axial form-factors. However, using an incorrect *axial* form-factor to match the the Q^2 distribution in neutrino scattering (to compensate for old dipole *vector* form-factors) results in a 6–8% error in the calculated neutrino cross-section. Therefore, updated vector form-factors *and* better-measured axial form-factors are required. MINERνA will measure the Q^2 dependence of F_A in neutrino scattering and compare the calculated cross-section with the measured cross-section.

2.2.4 Axial form-factor

Neutrino scattering provides the only practical route to precision measurement of the axial form-factor above $Q^2 = 0$, and the functional form of $F_A(Q^2)$. The fall-off of the form-factor strength with increasing Q^2 is traditionally parameterized (approximately) using an effective axial-vector mass M_A. Uncertainty in the value of M_A contributes directly to uncertainty in the total quasi-elastic cross-section. Earlier neutrino measurements, mostly bubble-chamber experiments on deuterium, extracted M_A using the best vector form-factors, other parameters, and models available at the time. Changing these input assumptions changes the extracted value of M_A. Hence, precision extractions of M_A and F_A require using the best possible vector form-factors and coupling constants. The value of M_A is $\approx$ 1.00 GeV/c^2, to an accuracy of perhaps 5%. This value agrees with the theoretically-corrected value from pion electroproduction[20], 1.014 ± 0.016 GeV$/c^2$.

The fractional contributions of F_A, G_M^p, G_M^n, G_E^p, and G_E^n to the Q^2 distribution for quasi-elastic neutrino and anti-neutrino scattering cross-sections in energy range of the NuMI beam are shown in Figure 12. The contributions are determined by comparing the BBA-2003 [17] cross-sections with and without each of the form-factors included. MINERνA will be the first systematic study of F_A, which accounts for roughly half of the quasi-elastic cross-section, over the entire range of Q^2 shown in the figure.

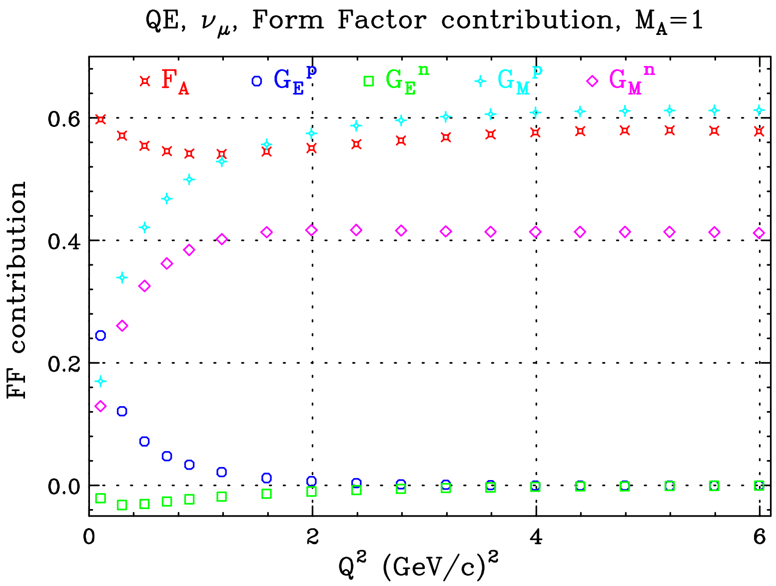

Figure 12: Fractional contributions of G_M^p, G_M^n, G_E^p, G_E^n, and F_A to the Q^2 distributions for quasi-elastic neutrino samples in the energy range of the NuMI beam. Because of interference terms, the sum of the fractions does not necessarily add up to 100%.

2.2.5 Physics of vector and axial form-factors

In deep-inelastic charged-current scattering from quarks, the vector and axial couplings are equal (V-A). Similarly, in electron scattering from quarks (vector current), there is a well-defined ratio between electric and magnetic scattering from point-like Dirac quarks. At low momentum transfers, all of these relations break down. For example in quasielastic and resonant production at very low momentum transfers, the charge and anomalous magnetic moments of the neutron and proton mean the ratio of electric and magnetic scattering for the vector current is not the same as for free quarks. Similarly, from neutron decay, we know that $g_a(Q^2 = 0) = 1.267$ instead of 1.0, so vector and axial scattering differ at $Q^2 = 0$.

There are efforts in progress by lattice gauge programs to calculate the anomalous vector and axial magnetic moments of the proton and neutron, and the Q^2 dependence of all the form-factors in the low- and high-Q^2 regions. The normalization of the magnetic form-factors at Q^2=0 are constrained to equal the charge and anomalous (vector and axial) magnetic moment. The slope at low Q^2 is related to the mean square charge radius of the proton and neutron. The dipole form assumes that the charge and magnetization distributions of the various types of quarks and antiquarks have an exponential form. For Q^2 above 0.5–1.0 (GeV/c)^2 this non-relativistic picture breaks down. The ratio $G_E/\mu G_M \approx 1.0$ (at low Q^2) implies that the charge and magnetization distribution of the proton are the same, but at higher Q^2 the ratio becomes much smaller, and more sophisticated models are required (e.g. lattice gauge theories). Therefore, measurement of the axial form-factor over a wide range of Q^2 is of great interest. In this section, we show MINERνA's sensitivity to three different models of the axial form-factor:

- Model 1: A simple dipole approximation currently used for the magnetic form-factor of the proton, with different axial and vector radii. This is the current standard assumption.
- Model 2: A constitutuent quark model preformed by Wagenbrunn *et al.*[18].
- Model 3: A model based on duality, which requires the axial and vector parts of $W_1^{elastic}$ to be equal above Q^2=0.5 (GeV/c)^2, and therefore increase with Q^2, as described briefly in the next section.

2.2.6 Quark/hadron and local duality

In modern language, the concept of quark-hadron duality can be related to the momentum sum rule in QCD, and various other moments of the structure functions. It has been shown by Bodek and Yang that with inclusion of target mass corrections, NNLO QCD describes deep-inelastic scattering and the average resonant cross-section down to $Q^2 = 0.5$ (GeV/c)^2. The concept of local duality implies that the integral of the QCD predictions (including target mass) in the threshold region up to pion threshold, should be equal to the integral of the elastic peak. Since for QCD, the vector and axial contributions to W_1 and W_2 are equal, local duality predicts that vector and axial part of the quasi-elastic form-factors should become equal around $Q^2 = 0.5$ (GeV/c)^2. This means that the dipole approximation must break down for both vector and axial form-factors.

The vector and axial components of $W_1^{elastic}$ become equal at $Q^2 \sim 0.5$ (GeV/c)^2 for both BBA and dipole form-factors. The requirement that this vector/axial ratio remains equal to 1.0 for higher

Q^2 yields a definite prediction that the axial form-factor is 1.4 times larger than the dipole prediction at higher Q^2.

2.2.7 Axial form-factor measurement in MINERνA

Figure 13 shows a typical quasi-elastic event, as simulated in MINERνA.

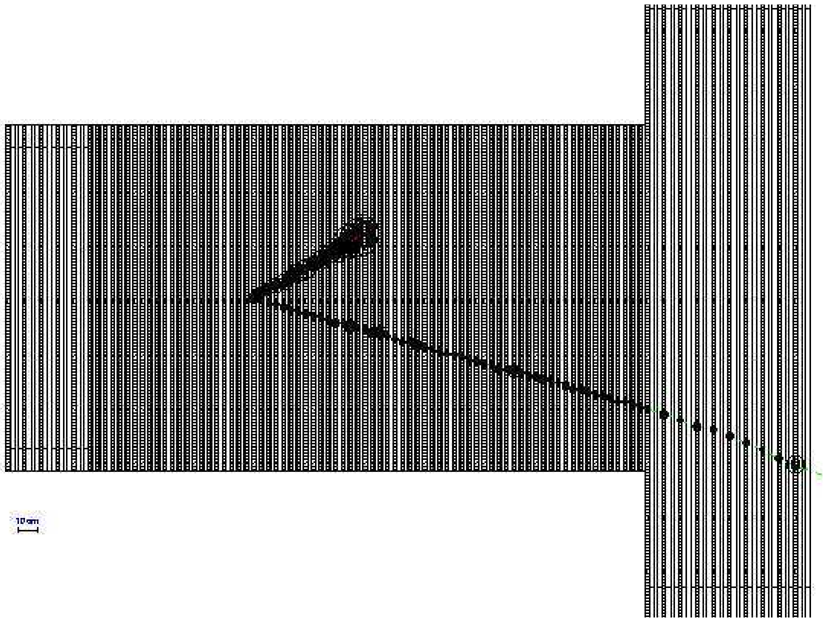

Figure 13: A simulated charged-current quasi-elastic interaction in MINERνA. The proton (upper) and muon (lower) tracks are well resolved. In this display, hit size is proportional to energy loss within a strip. The increased energy loss of the proton as it slows and stops is clear. For clarity the outer detector is not drawn.

In $\nu n \to \mu^- p$, the outgoing proton carries kinetic energy of approximately $Q^2/2M_N$. So for low Q^2, the challenge is identifying events with a very soft recoil proton; for high Q^2, this proton is high energy and may interact in the detector, making particle identification more challenging. The main strategies of the current analysis are:

- At low Q^2, we accept quasi-elastic candidates with a single (muon) track, and require kinematic consistency with $x = 1$.
- At higher Q^2, we reconstruct both the proton and the muon, and require kinematic consistency with $x = 1$ and $p_T^{tot} = 0$

Simple cuts based on these ideas yield reasonable efficiency and good purity, even at high Q^2.

This analysis uses the NEUGEN generator and the hit-level MINERνA detector simulation and tracking package to model signal selection and background processes. The generator uses Fermi smearing and INTRANUKE[19]. INTRANUKE is the procedure used by NEUGEN to simulate the passage of a hadron through dense nuclear matter. It includes the empirically measured phenomena of π and p re-scattering within the nucleus that can change the momentum vector of the exiting π or p and even eliminate a produced initial-state particle from the observed final state.

Initial event identification requires one or two tracks in the active target. One of these tracks must be non-interacting long range (80 g/cm^2) particle, as expected for a muon. We keep this range requirement low to keep the low energy quasi-elastic events. If a second track forms a vertex with this track, it is assumed to be the proton. No other tracks may be associated with this vertex. If the muon does not range out in the MINERνA , we require the muon to enter MINOS to be able to reconstruct the muon momentum. The main effect of the MINOS requirement is to reduce the acceptance for high Q^2 quasi-elastic events. The muon track momentum is reconstructed with a fractional uncertainty of 5% for muons which range out either in MINERνA or in MINOS and 12% for those muons measured by the magnetic spectrometer in MINOS.

The energy of the proton for the high-Q^2 sample (where the proton almost always interacts) is reconstructed calorimetrically from hits. To get the expected error, we use an expected fractional energy resolution of $4\%/E_{proton} + 18\%/\sqrt{E_{proton}}$. Note that this is only used to calculate the expected error used on Figures 14 and 15.

Although muons are identified by requiring a single long track, no attempt was made to improve particle identification by requiring a dE/dx consistent with the muon or proton tracks. This requirement should be particularly effective for protons of $\mathcal{O}(1)$ GeV momentum[2], and such a requirement can be imposed to optimize the analysis in the future.

If a quasi-elastic interaction is assumed, one can reconstruct the event kinematics from just the momentum and direction of the final state μ. Neglecting the binding energy of the final-state proton,

$$E_\nu^{QE} = \frac{M_N E_\mu - \frac{m_\mu^2}{2}}{M_N - E_\mu + p_\mu \cos\theta_\mu}.$$

If a proton track is identified and its angle and energy are also measured, one can additionally require consistency with the quasi-elastic hypothesis. Two constraints are possible, one on the x of the reconstructed interaction and one on the total p_T of the observed final state.

If the interaction is truly quasi-elastic, then $x = 1$, and therefore $Q^2 = 2M_N\nu$ where ν = E_{had} - M_N, and E_{had} is the energy of the hadronic final state. In this analysis, we test this by comparing Q^2 reconstructed from the lepton kinematics under the quasi-elastic hypothesis to $2M_N\nu$. We form $dx = (Q^2_\mu - 2M_N\nu)/\sigma$ where the σ is the expected 1σ error for dx from the event kinematics. The dominant part of the calculated error σ comes from the smearing of hadronic final-state energy. Figure 14 shows the significance of this Q^2 difference for four Q^2 bins for quasi-elastic, resonant, and deep-inelastic events. This cut can be applied without identifying a proton track if the visible energy, less the muon energy, is assumed to be ν. The efficiencies and purities for the dx cut are shown on the plot for the different Q^2 bins. We note physics from Fermi smearing and INTRANUKE smear dx as much as the detector smearing.

The Q^2 significance cut, dx cut, does not use information on the proton direction. Hence, we impose a second kinematic cut on the total transverse momentum p_T relative to the incoming neutrino direction. If a proton track is identified, we cut on the significance of the difference from $p_T = 0$:

[2]See Chapter 6

Figure 15 shows the significance of this p_T difference for four Q^2 bins for quasi-elastic, resonant and deep-inelastic events. The p_T cuts for the different Q^2 bins are shown on the plot. For $Q^2 < 1$ the p_T cut is not imposed if only one track is found.

2.2.8 Unfolding the Quasi-elastic Q^2 and E_ν Distributions

We have estimated the increase in the statistical errors due to resolution smearing. The limited resolution of the MINERνA detector smears out the measured values of E_ν and θ_μ and hence Q^2. The cross section plot and form factor plots should be in terms of true E_ν and Q^2. The scheme to unfold these distribution is described in [34], and we will use his notation. The quanity we minimize is

$$\chi^2 = (R\mu - n)V^{-1}(R\mu - n) + \alpha * S[f]$$

where $R_{i,j}$ is the response matrix (i - smeared, j - true); n_i is a vector of the data (smeared distribution); μ_j is vector of the true distribution; V is the covarience matrix of the data, $V_{i,j} = \delta_{i,j} n_i$; $S[f]$ is a regularization function; and α is the regulatization parameter. The χ^2 is minimized using Minuit by varing μ_j, the unfolded distribution. The unfolded error increase is the "minos" error in Minuit divided by the unsmeared errors. Without $S[f]$, the solution is $\mu = R^{-1}n$. However, this solution does not give the best answer, as the answer tends to oscillate around. The regularization function, $S[f]$, is added the χ^2 to dampen the oscillations, since physics distributions are supposed to be smooth. This function introduces a bias in the unfolding which one makes smaller than the final statistical error. We use $S[f]$ = sum of $(f''(x))^2 \Delta x$, where f is the true distribution, and Δx is the bin width. Given a unfolded histogram, we determine f with spline fit.

For quasi-elastic events the energy and Q^2 can be calculated from just the muon energy and angle. One can show:

$$\Delta Q^2/Q^2 = (1 + E_\nu/E_\mu)(\Delta E_\mu/E_\mu) + (E_\nu/E_\mu)cot(\theta/2)\Delta\theta$$

$$\Delta E_\nu/E_\nu = (E_\nu/E_\mu)(\Delta E_\mu/E_\mu) + (E_\mu/m)sin(\theta)\Delta\theta$$

and with $E_\nu/E_\mu \sim 1.15$:

$$\Delta Q^2/Q^2 = 2.15(\Delta E_\mu/E_\mu) + 1.15cot(\theta/2)\Delta\theta$$

$$\Delta E_\nu/E_\nu = 1.15(\Delta E_\mu/E_\mu) + (E_\mu/m)sin(\theta)\Delta\theta$$

For this unfolding result, the muon momentum smearing is given as 5% for $E_\mu < 10GeV$ (for rangeout measurement) and 12% $E_\mu > 10GeV$ (for MINOS magnetic spectrometer measurement). The ΔE_μ terms dominate the smearing as $\Delta\theta \sim .009$. Using the above techniques, we determine the increase in statistical error due to unfolding the smeared distributions.'

2.2.9 Results

Figure 16 shows predictions for the cross-section assuming the BBA-2003 form-factors, with $M_A = 1.00$ (GeV/c)^2. The predicted MINERνA points are shown along with their expected errors. The MIPP experiment will measure particle production off the NuMI target, and from this, we expect an additional overall uncertainty of 4% from the flux. Figure 16 summarizes current knowledge of neutrino quasi-elastic cross-sections. Among the results shown, there are typically 10–20% normalization uncertainties from knowledge of the fluxes. This plot shows that existing measurements have large errors throughout the E_ν range accessible to MINERνA and especially in the threshold regime crucial to future oscillation experiments.

Figure 17 shows the expected values and errors of F_A in bins of Q^2 for the MINERνA active carbon target, after a four-year exposure in the NuMI beam. The method to extract F_A from $d\sigma/dq^2$ is given in [35]. Clearly the high-Q^2 regime, which is inaccessible to K2K, MiniBooNE and T2K, will be well-resolved in MINERνA. Figure 17 shows these results as a ratio of F_A/F_A(Dipole), demonstrating MINERνA's ability to distinguish between different models of F_A. We effectively show the three different models (described earlier) for F_A as a function of Q^2 . Model 3 (based on duality) is a factor of 1.4 higher than the dipole approximation. Note that resolution effects are included in understanding the statistical error in this extraction of F_A,

Figure 17 shows the extraction of F_A from Miller, Baker, and Kitagaki, using their plots of $d\sigma/dq^2$. For $Q^2 > 2$ (GeV/c)^2 there is essentially no measurement of F_A. Even the measurements of $F_A(Q^2)$ below 2 (GeV/c)^2 have significant errors, hence one cannot assume F_A is a dipole for low Q^2. The maximum Q^2 values that can be achieved with incident neutrino energies of 0.5, 1.0, 1.5 and 2 GeV are 0.5, 1.2, 2.1 and 3.0 (GeV/c)^2, respectively. Since K2K, MiniBooNE, and T2K energies are in the 0.7–1.0 GeV range, these experiments probe the low $Q^2 < 1$ (GeV/c)^2 region where nuclear effects are large (see Figures 18). The low-Q^2 ($Q^2 < 1$ (GeV/c)^2) MiniBooNE and K2K experiments have begun to investigate the various nuclear effects in carbon and oxygen. However, higher Q^2 data are only accessible in experiments like MINERνA, which can span the 2–8 GeV neutrino energy range. MINERνA's measurement of the axial form-factor at high Q^2 will be essential to a complete understanding of the vector and axial structure of the neutron and proton.

2.2.10 Fermi gas model

There are three important nuclear effects in quasi-elastic scattering from bound targets: Fermi motion, Pauli blocking, and corrections to the nucleon form-factors due to distortion of the nucleon's size and its pion cloud in the nucleus. Figure 18 shows the nuclear suppression versus E_ν from a NUANCE[36] calculation[21] using the Smith and Moniz[37] Fermi gas model for carbon. This nuclear model includes Pauli blocking and Fermi motion but not final state interactions. The Fermi gas model uses a nuclear binding energy $\epsilon = 25$ MeV and Fermi momentum $k_f = 220$ MeV/c. Reference [37] shows how the effective k_f and nuclear potential binding energy ϵ (within a Fermi-gas model) for various nuclei is determined from electron scattering data.

2.2.11 Bound nucleon form-factors

The predicted distortions of nucleon form-factors due to nuclear binding are can be as large as 10% at $Q^2 = 1$ (GeV/c)^2 to 15% at $Q^2 = 2$ (GeV/c)^2. With carbon, iron and lead targets, MINERνA can compare measured form-factors for a range of light to heavy nuclei. Figure 16 shows the cross-section suppression due to bound form-factors. As is described in [22], these effects can cause variations up to 10% in the differential cross-sections at MiniBooNE, K2K and T2K energies.

Requiring vector and axial contributions to W_1 be equal for $Q^2 > 0.5$ (GeV/c)^2 introduces further suppression at low Q^2. Changing the various assumptions in $d\sigma/dq^2$ as calculated with dipole form-factors introduces 5–10% effects on the Q^2 distributions these experiments will see.

2.2.12 Intra-nuclear rescattering

In neutrino experiments, detection of the recoil nucleon helps distinguish quasi-elastic scattering from inelastic reactions. Knowledge of the probability for outgoing protons to reinteract with the target remnant is therefore highly desirable. The NEUGEN Monte Carlo used by MINERνA uses the INTRANUKE procedure to estimate this intra-nuclear re-scattering as described earlier in this section. Similarly, quasi-elastic scattering with nucleons in the high-momentum tail of the nuclear spectral function needs to be understood. More sophisticated treatments than the simple Fermi gas model are required. Conversely, inelastic reactions may be misidentified as quasi-elastic if a final-state pion is absorbed in the nucleus. With its constrained kinematics, low-energy neutrino-oscillation experiments use the quasi-elastic channel to measure the (oscillated) neutrino energy spectrum at the far detector; uncertainty in estimation of non-quasi-elastic background due to proton intra-nuclear rescattering is currently an important source of systematic error in K2K.

The best way to study these effects is to analyze electron scattering on nuclear targets (including the hadronic final states) and test the effects of the experimental cuts on the final-state nucleons. MINERνA can address proton intra-nuclear rescattering by comparing nuclear binding effects in neutrino scattering on carbon to electron data in similar kinematic regions. Indeed, MINERνA members will be working with the CLAS collaboration to study hadronic final states in electron scattering on nuclear targets using existing JLab Hall B data. This analysis will allow theoretical models used in both electron and neutrino experiments to be tested. Other work in progress, with the Ghent[38] nuclear physics group, will develop the theoretical tools needed to extract the axial form-factor of the nucleon using MINERνA quasi-elastic data on carbon. The ultimate aim is to preform nearly identical analyses on both neutrino and electron scattering data in the same range of Q^2.

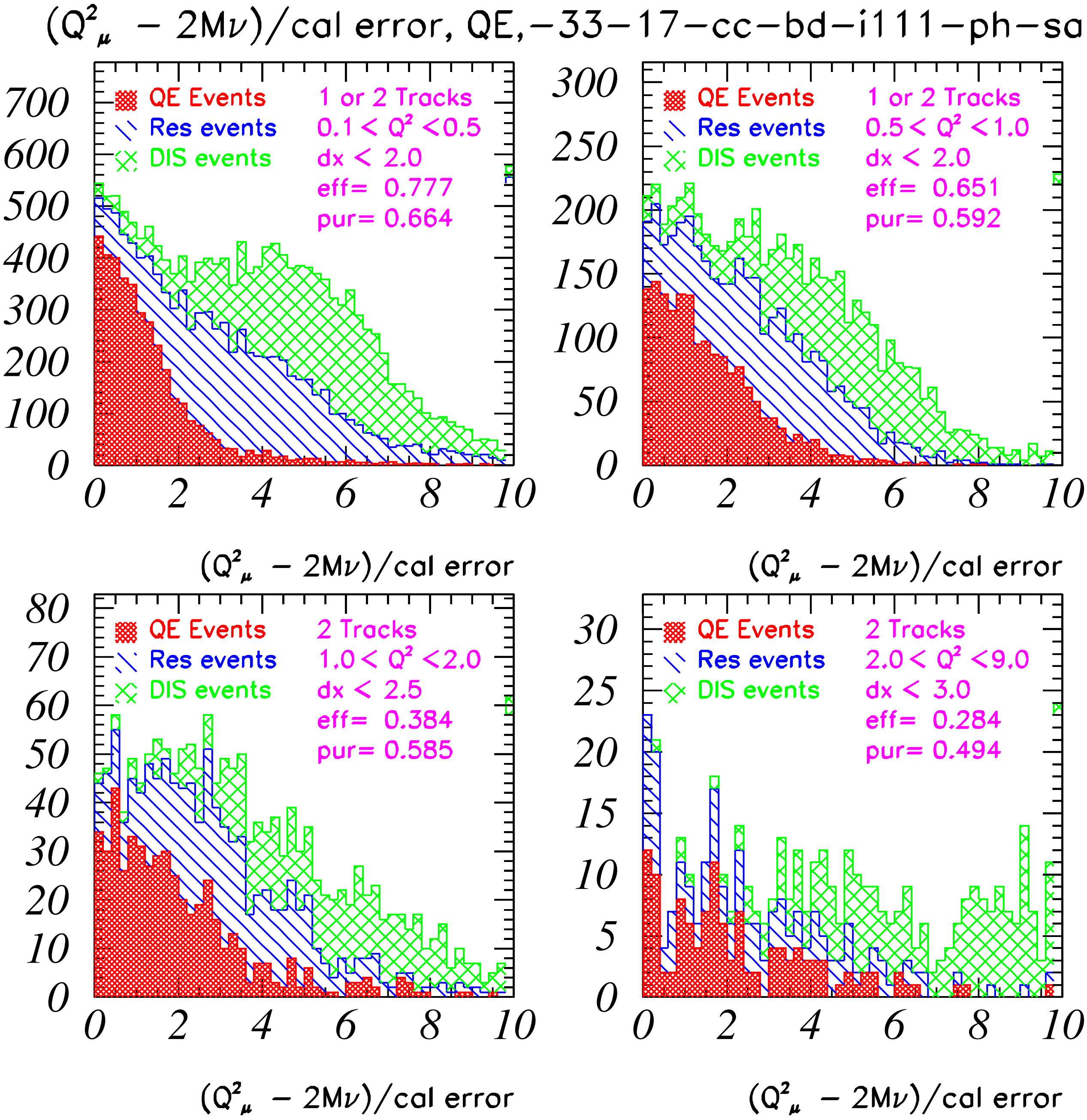

Figure 14: Significance of the difference between Q^2 from the quasi-elastic hypothesis and Q^2 from the final state energy, for quasielastic candidates. "cal error" on the plot is the expected error for $Q^2_\mu - 2M\nu$ from smearing of the kinematic quantities. The efficiency and purity are stated on the plots when the Q^2 difference is less than the amount given by dx. The purity and efficiency for $Q^2 < 1\ GeV$ require 1 or 2 found tracks. The purity and efficiency for $Q^2 > 1GeV$ require 2 found tracks.

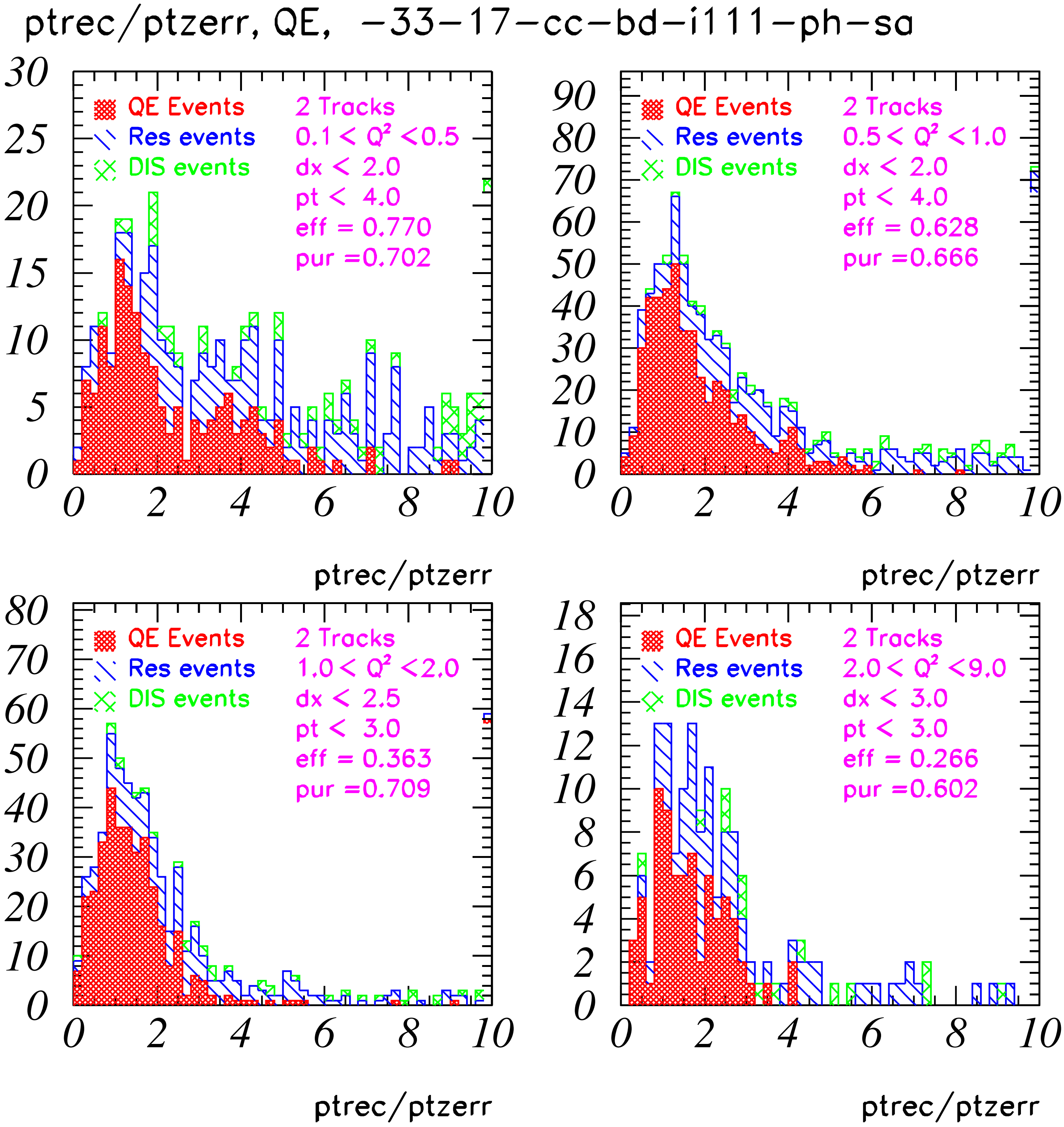

Figure 15: Significance of the difference between p_T from the quasi-elastic hypothesis for 2 track events. "ptzerr" is the expected error in p_T from smearing of the kinematic quantities. The efficiency and purity are stated on the plots when the Q^2 difference is less than the amount given by dx. and p_T is less than the amount given in the plot. The purity and efficiency for $Q^2 < 1\ GeV$ require 1 or 2 found tracks. The purity and efficiency for $Q^2 > 1\ GeV$ require 2 found tracks.

The pt

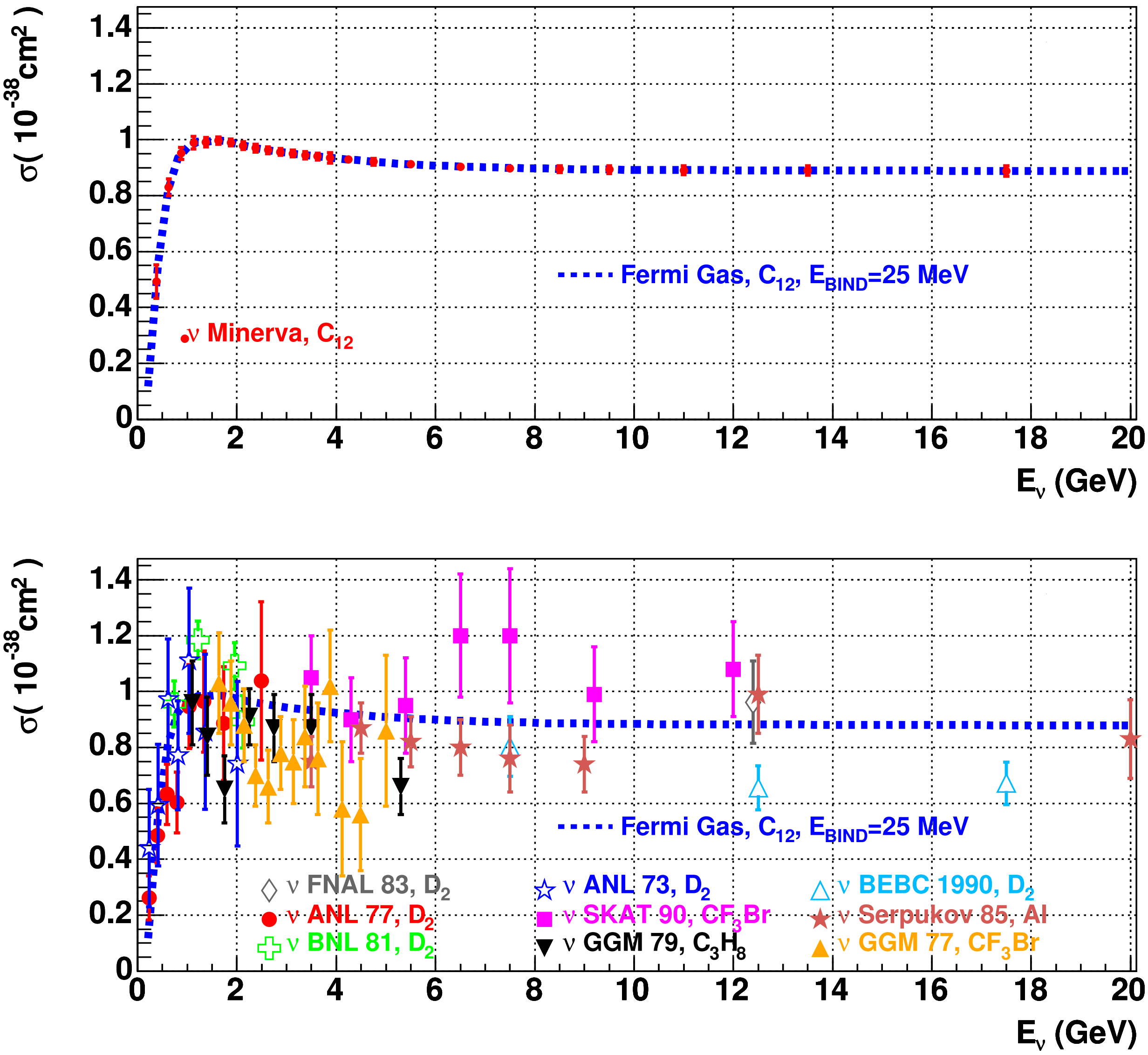

Figure 16: The quasi-elastic neutrino cross-section along with data from various experiments. Representative calculations are shown using BBBA-2006 form-factors with $M_A = 1.014$ GeV/c^2. The dashed curve [21] uses a Fermi gas model for carbon with 25 MeV binding energy and 220 MeV/c Fermi momentum. The predicted MINERνA points, with errors, are shown. The data shown in the bottom plot are from FNAL 1983 [23], ANL 1977 [25], BNL 1981 [26], ANL 1973 [27], SKAT 1990 [28], GGM 1979 [29], BEBC 1990 [30], Serpukov 1985 [31], and GGM 1977 [32]. The data have large errors and are only marginally consistent throughout the E_ν range.

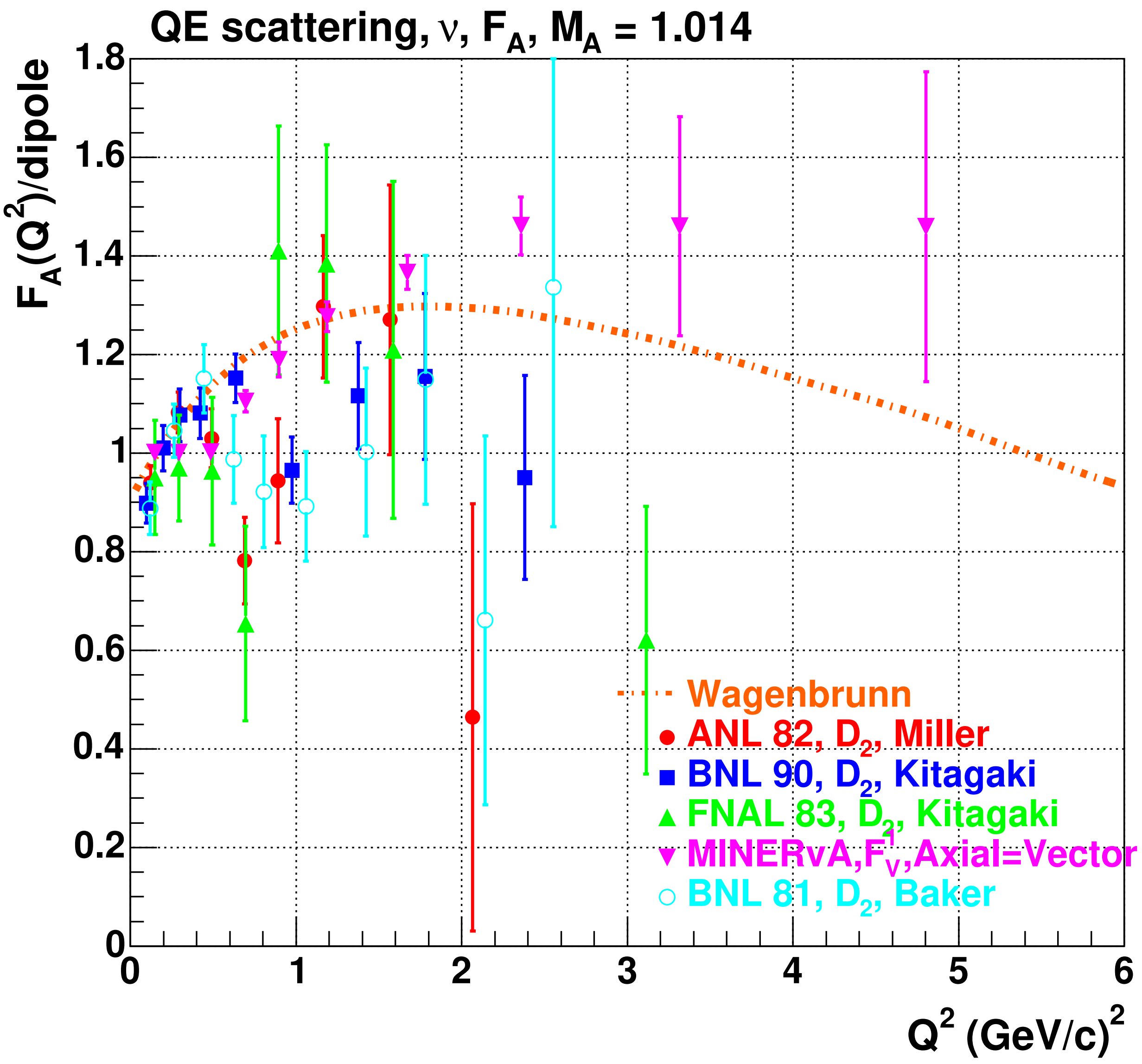

Figure 17: Estimation $F_A/$dipole for a four year MINERνA run using the quasielastic analysis described in the text. The MINERνA points are plotted assume the Model 3 axial form-factor. Also shown is F_A extracted from deuterium bubble chamber experiments using the $d\sigma/dq^2$ from the papers of FNAL 1983 [23], BNL 1990 [48], BNL 1981 [26], and ANL 1982 [33]. Also shown is the expectations from Model 2 for the axial form-factor.

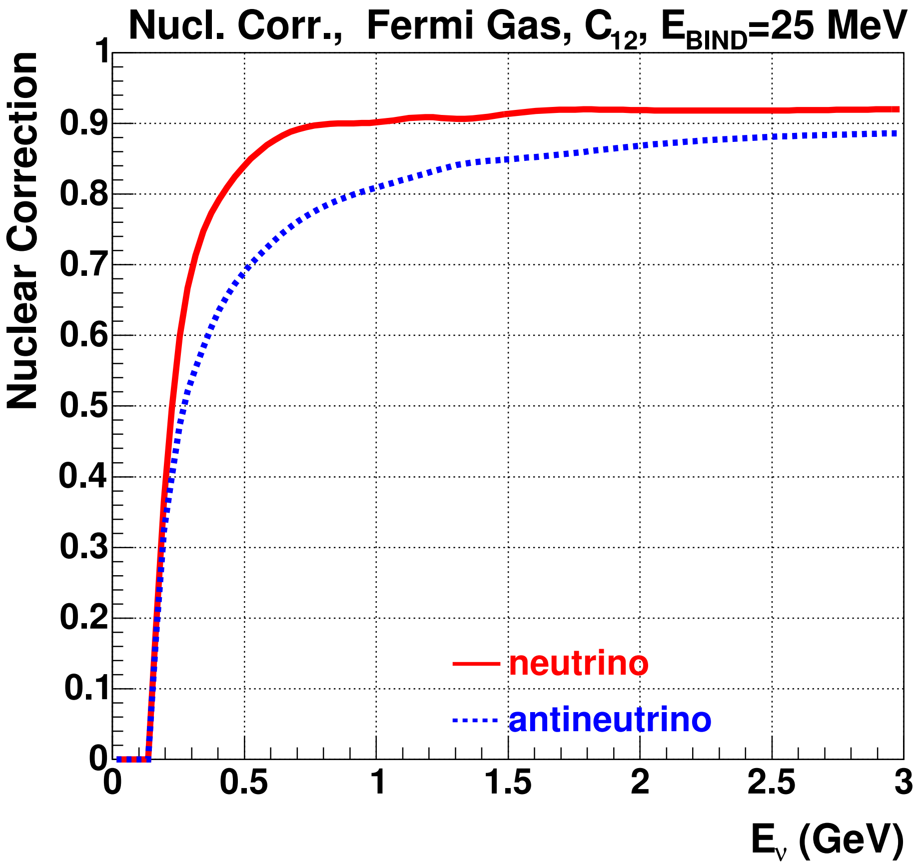

Figure 18: Pauli suppression in a Fermi gas model for carbon with binding energy $\epsilon = 25$ MeV and Fermi momentum $k_f = 220$ MeV/c. A similar suppression is expected for quasi-elastic reactions in MINERνA.

2.3 Resonant Pion Production

2.3.1 Introduction

The production and decay of nucleon resonances in neutrino interactions is a significant part of the total neutrino cross section in the few GeV region. These resonances have been explored using electron scattering experiments, but different form factors contribute in the neutrino case, and simulations rely on an early theoretical model by Rein and Sehgal [39]. Because the structure of the model is not as simple as either quasi-elastic or deep inelastic scattering, and because existing neutrino data does not provide significant constraint, there are large uncertainties on the contribution to the total cross section value and its shape.

Resonance production is the least certain part of the neutrino cross section picture, yet it may be the most important. Current and recent neutrino programs (K2K, MiniBooNE and MINOS) and upcoming experiments such as NOνA and T2K expect these interactions to be a large portion of the cross section in the energy region in which they are most interested. The use of similar near and far detectors serves to partially cancel detector systematic errors. However, since there are different incoming neutrino spectra at the near and far detectors and these mostly unknown resonance cross sections are energy dependent, the neutrino cross section errors do **not** cancel and there is a vital need for the systematic and detailed studies MINERνA can provide.

High statistics muon neutrino disappearance experiments are particularly sensitive to the hadronic final state, in particular the number, charge, and kinematics of the final state pions. The lack of knowledge of these final states contributes to an uncertainty in the total hadronic energy, and therefore to the estimate of the incident neutrino energy and the parameter Δm^2. For electron neutrino appearance experiments, constraints on the cross sections of neutral current and charged current single π^o production are needed. In the expected signal region, the former could enter as background from higher energy resonance and DIS interactions, while the latter would primarily be high E_{had} resonance events. In both cases, some kinematic combinations of the resulting decay photons could be indistinguishable from charged current electron neutrino interactions.

For MINERνA the combination of cross section, nuclear effects, and proton and pion final state interaction measurements will require the tracking and calorimetric abilities of a fully active, fine-grained detector.

2.3.2 Cross Section Models and Existing Data

Scattering of electrons and neutrinos off nucleons with hadronic invariant mass $W < 2$ GeV is dominated by resonance excitation. A complete description of the resonance region would require a map of all resonances and the non-resonant processes that contribute. About two dozen resonances are known and each has form factors. Even with much larger statistical accuracy, interpretations of electron scattering data have not reached this laudable goal. The lowest energy states are most easily separated; the most prominent resonance is the $P_{33}(1232)$ (often called the Delta), and most calculations also include the $S_{11}(1535)$, $P_{11}(1440)$, and $D_{13}(1520)$.

Using the Rein and Sehgal formalism, some simulation authors [40] include up to 18 resonances in neutrino simulations. In electro-production, the Delta is most important at low W and the the magnetic dipole term in the cross section dominates. This form factor has a particularly rapid Q^2

falloff (more steep than the nucleon dipole form factor) and emphasizes the C_3^V vector form factor. For neutrino induced resonances, the contribution of C_5^A (due to the axial form factors) is important and these two may be sufficient for a qualitative picture. The axial form factor is determined by the PCAC condition, and is also steeper than the dipole shape. The Delta has received a lot of attention in the medium energy community. Current wisdom is that the mesonic cloud surrounding the quark core dominates the low Q^2 response. That model has been extended to neutrino-nucleon excitation of $P_{33}(1232)$ by Sato, Uno, and Lee [41, 46]. Another model has been developed by Paschos, Sakuda, and Yu [42, 43] and applied to nuclei. Other work on form factors has been done by Lalakulich, Paschos, and collaborators [44, 45], but not yet applied to nuclei. Examples of both models are shown in Fig. 19 compared with data from the Brookhaven deuterium bubble-chamber experiment [47, 48]. In the plot on the left, the authors show the axial and vector contributions to the total cross section; the latter is well constrained by electron scattering experiments. These models describe existing data through most of the region shown, though that data has large uncertainties and does not provide much constraint. There are also large inconsistencies at very low $Q^2 < 0.2$ (GeV/c)^2. The lack of agreement at very low Q^2 has been seen in various interactions and has important consequences for the estimation of the coherent π^o background [49] for ν_e appearance experiments.

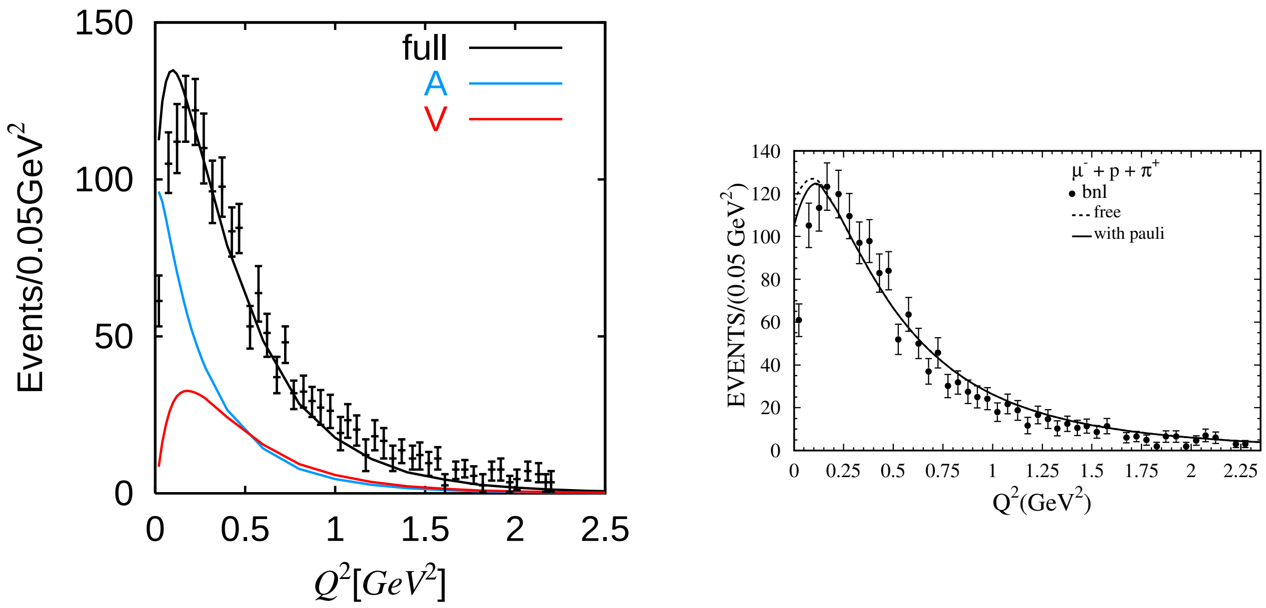

Figure 19: The cross-section $d\sigma/dQ^2$ from BNL compared with the work of Sato, et al. [46] on the left and shows their calculation and breaks down the Axial and Vector contributions to the cross section. A comparison to the same BNL data by Paschos, et al. [43] in the right plot. The full lines are for $M_A = 1.05$ GeV/c^2, the dashed line has no explicit Pauli blocking included.

The Q^2 dependence is determined by these form factors as well as nuclear effects, and in turn determines the outgoing angular distribution of the lepton as well as the hadronic final state particles.

One concern, for both resonance and quasi-elastic scattering off nuclei, are nuclear effects (especially Pauli blocking) which certainly play a large role at very low Q^2; this corresponds to more forward going final state leptons, a kinematic region which is difficult to access in electron beam experiments. This uncertain region accounts for a significant fraction of the total cross section. MINERνA with its variety of nuclear targets, can start to disentangle nuclear effects from form factors.

The poor understanding of the resonance cross section also impacts quasi-elastic cross section measurements. Experiments with relatively high thresholds for recoil nucleons and pions, such as Cerenkov detectors or coarse grained tracking detectors will frequently see only the outgoing lepton, and will tag it as a QE candidate. Any measurements of these interactions, or measurements which depend on the kinematic simplicity of a purified QE sample, will benefit from the improved measurement of the resonant background.

There are concerns, even when the outgoing pion can be seen, such as the π^o decay to two photons, or charged pions which are above detection threshold. The kinematics of these pions are often modified as they pass through the nucleus, sometimes even being completely absorbed. There will be a reduction of approximately 30% of pions with the same charge as the exchange current (π^+ for neutrino CC interactions) produced in a light target such as C or O. This is due to a combination of charge exchange (to π^o or π^-, for example) or absorption. These final state nuclear effects will change the visible energy, requiring corrections to estimate the true neutrino energy, the quasi-elastic cross section, or where π^o backgrounds are important such as ν_e searches. Again, MINERνA's integral nuclear targets and low tracking thresholds are designed to isolate exclusive single pion production and to disentangle these nuclear effects.

2.3.3 MINERνA performance

MINERνA will be able to improve the above situation with precision measurements of the total resonance cross sections, of the $d\sigma/dQ^2$ and $d\sigma/dW$ differential cross sections, and measure exclusive final states on a variety of nuclei to constrain the form factors and final state interaction models. One major goal is to provide a characterization of the final states and the energy dependence of the cross sections for the many contributing processes (pion production and nucleon knockout). With a fully active detector, MINERνA will be able to measure almost all final states. The angular distributions can be determined in most cases. The second goal is to study the details in special cases when individual resonances can be isolated. Building on experiences with electron scattering experiments, we will be able to isolate $P_{33}(1232)$ and $S_{11}(1535)$ by taking advantage of their decay processes.

Unlike inclusive charged lepton scattering (e,e'), measurements of neutrino inclusive scattering with wide-band neutrino beams can not rely solely on the outgoing lepton kinematics, since the incident neutrino's exact energy is not *a priori* known. Reconstruction of inclusive resonance production requires the measurement of W; for the dominant Delta resonance this will be at 1232 MeV. For charged current interactions this is accomplished by measuring the lepton energy and angle (which is easy for muons) and also either the hadronic energy or its angle. Measuring these also gives estimates for Q^2 and E_ν.

The hadronic energy can be estimated by tracking and identifying every particle emerging from an interaction vertex, or by summing up the dE/dx energy deposited by all the reaction products other than the muon. Both methods will be important for the study of resonances. Because the primary vertex multiplicities for resonance production will usually be low, a single pion and recoil nucleon, tracking (momentum from range) will be a viable technique for low efficiency, high resolution samples. However, the pions have a significant probability to interact or decay before stopping, and MINERνA's calorimetric abilities will be required to get inclusive cross sections. The correlation between the reconstructed and true E_h is shown in Fig. 20.

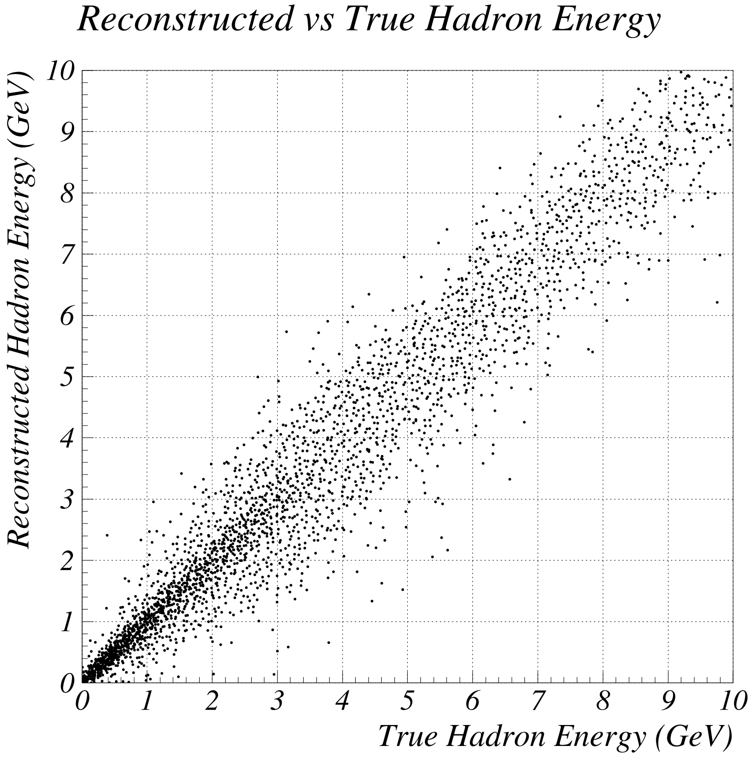

Figure 20: Correlation between true and reconstructed hadron energy.

When the kinematics of resonance events are reconstructed using E_h and an assumed muon momentum resolution $\delta P/P$ of 9%, we obtain the correlation of the reconstructed and true W and Q^2 shown in Fig 21. The W resolution is around 100 MeV in the region of the Δ(1232), and the Q^2 resolution is slightly better than 0.2 (GeV/c)^2. Even with this smearing, the Δ peak is still visible in the W spectrum in both Fig. 21 and also in the histogram in Fig. 22. Note, the smearing is largely due to detector effects, but there is a smaller, but still significant smearing due to nucleon Fermi motion for interactions taking place in carbon.

With the resolution on W described above, we will be able to make a simple selection to isolate a resonance enhanced sample. Isolating a sample with one muon and two visible hadrons, then choosing values of $1.1 < W < 1.5$ GeV yields a sample with enhanced $\Delta^{++}_{(1232)}$. With this selection, we estimate a 70% purity and 20% efficiency. There is a model dependence to the purity estimate coming from the DIS-Resonance transition region which will have to be settled by the data. In this case, we can reconstruct Q^2 assuming that a Δ was produced, which yields excellent resolution of

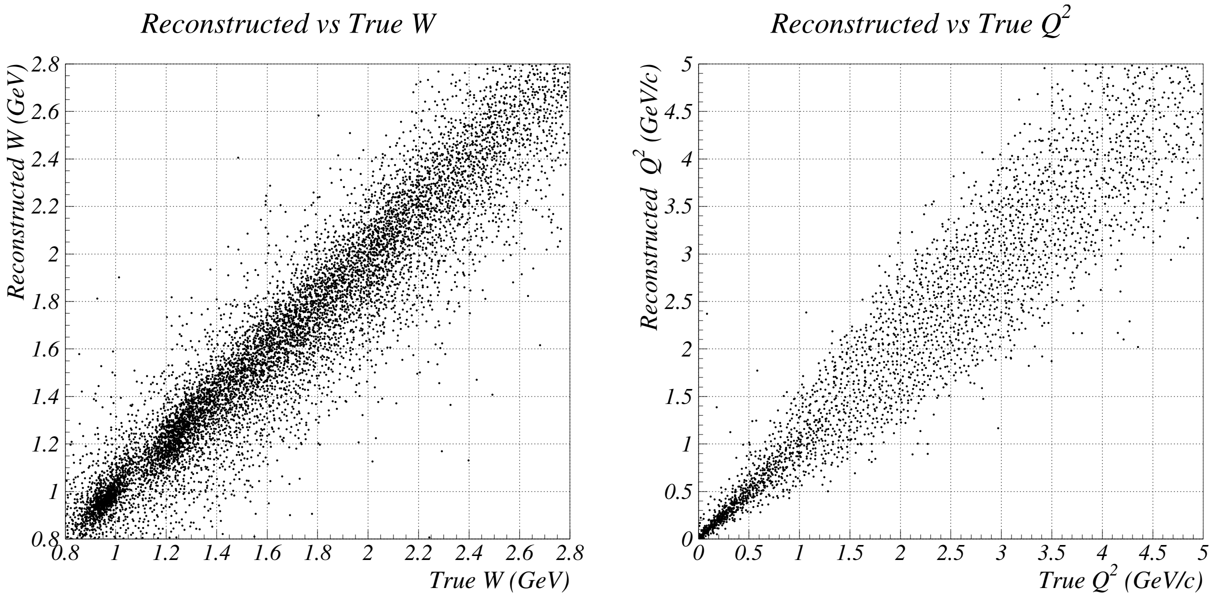

Figure 21: Correlation between true and reconstructed W (left) and Q^2 (right).

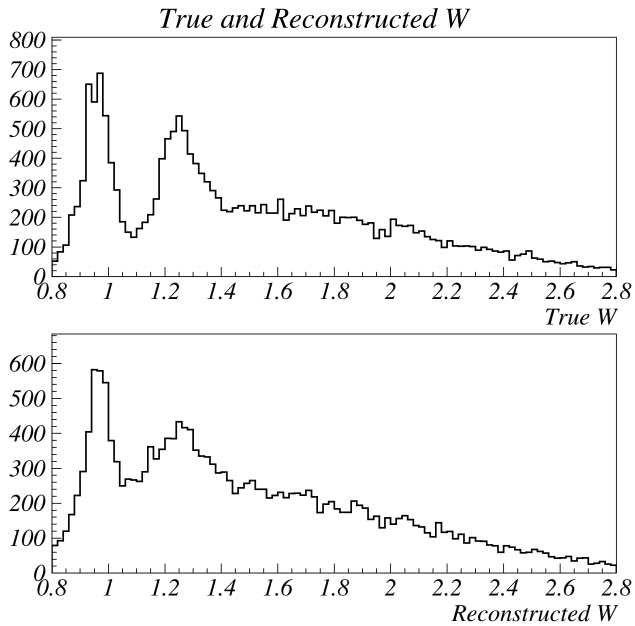

Figure 22: Top: true W distribution for resonant events with $Q^2 < 1$ (GeV/c)^2. Bottom: reconstructed W distribution for the same Q^2 range.

0.05 (GeV/c)^2 for the Δ signal. A sample of the resulting resonstructed Q^2 distribution, with no further selections is shown in Fig. 23. A substantial fraction of that efficiency (and access to lower

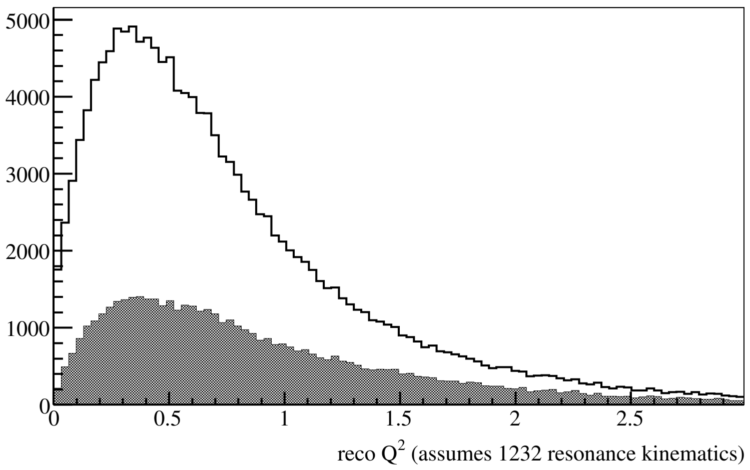

Figure 23: Estimate of the reconstructed Q^2 distribution for the two visible hadron enhanced Δ^{++} selection. The shaded region shows the expected background after this selection. This also shows the statistics for the estimated sample for three years running in the medium energy beam.

Q^2 events) can be regained by lowering the tracking thresholds and/or including events with only one reconstructed hadron track. For the estimate above, the tracking requirement was high: three XUXV layers. The purity may be improved by selecting events with little extra vertex activity.

2.3.4 Identifying specific final states

Previous neutrino studies have focused on charged particles because they are easier to track. However, the best physics interest in the resonance region might come from neutral particles such as π^0, η, and ω. That is because there is a preponderance of strongly excited baryon resonances close to their thresholds. The strong coupling of $\pi^0 p$ to the $\Delta(1232)$ resonance is well-known and the strong ηp coupling to $S_{11}(1535)$ is now also very well established. There is also a resonance at the ωN threshold, $P_{13}(1720)$, but its properties are not well-determined. Isolation of either of the higher mass states would be a major accomplishment. Then, it becomes possible for ν beams to add to the knowledge of these states.

Each of these mesons must be detected through decays. The π^0 decays almost solely to $\gamma\gamma$; that is also the largest decay branch for η. The signature would be clean: two photons of half the meson mass at large opening angle. The next largest decays for η are 3 pions, with charged ($\pi^+\pi^-\pi^0$) and neutral modes ($3\pi^0$) both prominent, but the latter will be difficult to reconstruct in MINERνA. The primary decay of ω is also to $\pi^+\pi^-\pi^0$. This mode should also be seen in the MINERνA detector because low energy particles will be contained very well. In each case, the invariant mass of a proton+meson pair could be constrained to be near the mass of the appropriate resonance as an additional way to suppress background. Studies of these modes are just beginning.

2.3.5 Error budget

The significant errors to some of the above analyses have been estimated; what is important depends on the measurement. For absolute cross section measurements, we expect a 5% absolute error for most parts of the energy spectrum when the MIPP hadron production results are incorporated into the NuMI beam flux. It is important to maintain access to the monitoring data and systematic studies that constrain errors due to beamline fluctuations, targeting, and alignment.

At this level, uncertainties in background subtraction and efficiency modeling will be comparable. This is certainly an improvement over the previous bubble chamber results where $> 20\%$ errors are reported (for a recent discussion see [50]). For relative cross sections, the relative flux error between neighboring energy bins will be 2%, and those measurements will be dominated by background, resolution, and calibration errors.

For the analysis of the shape of Q^2 or other distributions, such as in Fig. 19, the largest error will likely be from bias in the energy reconstruction. For example, a 2% uncorrectable bias in the muon momentum translates to an uncertainty in the shape of the Q^2 distribution that is about half as large as the apparent discrepancy in those plots, when you consider MINERνA's statistical error will be negligible for those distributions.

The extraction of pure nuclear effects from comparisons between the MINERνA nuclear targets, including the very low Q^2 region and the rescattering and absorption of final state pions, will probably be statistics limited. Because the detector surrounding the nuclear targets are the same, systematic uncertainties in the selection and backgrounds for the relative measurements will partially cancel. Thus, the limiting factor will be the maximum practical size for these targets.

2.3.6 Conclusion

MINERνA will significantly improve current measurements of resonance production of pions in neutrino interactions due to the large event samples, variety of nuclear targets, low detection thresholds, and excellent tracking and calorimetry. These measurements will be able to constrain the total cross section, relative cross sections, and the shape of the Q^2 distributions, and allow the first direct comparisons of neutrino interactions on different nuclei. These physics goals are consistent with the expected systematic and statistical errors. Better data on these processes will be of vital importance to current and future oscillation experiments as well as nucleon decay experiments. They will also lead to better understanding of the axial form factors of the nucleon and the effects of the nuclear medium.

2.4 Coherent Pion Production

MINERνA's high rates, range of nuclear targets, fine granularity, strong pattern recognition capabilities, and good electromagnetic calorimetry will make it possible to study charged- and neutral-current coherent neutrino-nucleus scattering with unprecedented precision. In this section we will briefly review the capabilities of the detector in this area focusing on the requirements placed on the detector design.

2.4.1 Introduction

Coherent neutrino-nucleus reactions, in which the neutrino scatters coherently from an entire nucleus with small energy transfer, leave a relatively clean experimental signature and have been studied in both charged-current ($\nu_\mu + A \to \mu^- + \pi^+$) and neutral-current ($\nu_\mu + A \to \nu + \pi^0$) interactions of neutrinos and anti-neutrinos. Although the coherent interaction rates are typically an order of magnitude or more lower than other single-pion production mechanisms, the distinct kinematic characteristics of these events allow them to be cleanly identified. Because the outgoing pion generally follows the incoming neutrino direction, this reaction is an important background to searches for $\nu_\mu \to \nu_e$ oscillation, as these events can easily mimic the oscillation signature of a single energetic electron shower.

A unique strength of the experiment is the ability to study both neutral and charged current channels from a variety of nuclear materials ranging from carbon to lead in the same experiment. Kinematic predictions from models can be explored in the charged current sample where the kinematics are fully reconstructed. The comparison of angular and energy distributions for produced pions in neutral and charged-current events will provide useful constraints on the various models, several of which predict CC/NC ratios differing by around 20% [51, 52]. A systematic comparison of charged- and neutral-current coherent production is currently a topic of considerable interest. While data on single π^0 production from the K2K and miniBoone experiments are in reasonable agreement with predictions [53, 54], a search for coherent CC production in the K2K experiment found only 7.6 ± 50.4 events where 470 were expected. This large difference between NC and CC production has been the subject of considerable theoretical work [55, 56, 57, 58] and could also account for the depletion at low Q^2 of inelastic events as compared with Monte Carlo predictions [59, 60].

2.4.2 Charged-current cross-section

The kinematics of coherent scattering are quite distinct compared to the more common deep-inelastic and resonant interactions. Because the coherence condition requires that the nucleus remain intact, low-energy transfers to the nuclear system, $|t|$, are needed. Events are generally defined as coherent by making cuts on the number of prongs emerging from the event vertex followed by an examination of the t distribution, where t is approximated by:

$$-|t| = -(q - p_\pi)^2 = (\Sigma_i(E_i - p_i^{||}))^2 - (\Sigma_i(p_i^{\perp}))^2 \quad (1)$$

With its excellent tracking capabilities, MINERνA's inner detector can measure this kinematic variable well.

To quantify MINERνA's ability to measure the charged-current coherent cross-section, a Monte Carlo study was carried out using the GEANT detector simulation described in Chapter 6. Analysis cuts were tuned on a sample of coherent interactions corresponding to a four-year run with the three-ton fiducial volume. Events were generated according to the appropriate mix of low and medium energy beams. This study used the Rein-Seghal [51] model of coherent production, as implemented in NEUGEN3. A low-energy beam sample containing all reaction channels was used for background determination. Based on published bubble chamber analyses, charged-current reactions should be the largest background contributor, in particular quasi-elastic and Δ-production reactions where the baryon is mis-identified as a pion or not observed. To isolate a sample of coherent interactions, a series of cuts are placed on event topology and kinematics. The detector response is parametrized based on measurement smearing of 0.5^o angular resolution for reconstruction of muon and pion tracks, $18\%/\sqrt{E_{had}}$ hadronic energy resolution, and 10% muon energy resolution.

Topological cuts An initial set of topological cuts are applied to isolate a sample of events which contain only a muon and charged pion. These cuts are based on the hit-level and truth information as provided by the GEANT simulation.

1. **2 Charged Tracks:** The event is required to have 2 visible charged tracks emerging from the event vertex. A track is assumed to be visible if it produces at least 8 hit strips in the fully active region of the detector which are due to this track alone.

2. **Track Identification:** The two tracks must be identified as a muon and pion. The muon track is taken to be the most energetic track in the event which does not undergo hadronic interactions. The pion track is identified by the presence of a hadronic interaction. The pion track is required not to have ionization characteristic of a stopping proton (which is assumed can be identified 95% of the time).

3. **π^0/neutron Energy:** Because MINERνA is nearly hermetic we also assume that neutral particles will produce visible activity which can be associated with the event and used to exclude it. Events with more than 500 MeV of neutral energy (π^0 or neutron) produced in the initial neutrino interaction are rejected.

4. **Track Separation:** To make good measurements of the two tracks, the interaction point of the pion must be more than 30 cm from the primary vertex, and at this interaction point, at least 4 strips must separate the two tracks in at least one view.

Kinematic cuts Because coherent and background processes have very different kinematics, cuts on kinematic variables are effective in isolating the final sample. Kinematic quantities are estimated from the smeared measurements of muon energy, pion energy, and muon angle measurement under the assumption that the event in question is CC-coherent. Kinematic cuts are as follows:

1. **$x_{Bj} < 0.2$:** Requiring Bjorken-x (as reconstructed from the observed pion and muon 4-momenta) less than 0.2 eliminates much of the background from quasi-elastic reactions with $x_{Bj} \sim 1$.

2. $\boldsymbol{t < 0.2}$ **(GeV/c)^2:** The most powerful variable for the identification of coherent events is the square of the 4-momentum transfer to the nucleus. Equation 1 relating t to the observed particles in the event is used as the estimator of this quantity.

3. $\boldsymbol{p_\pi > 600}$ **MeV:** Requiring $p_\pi > 0.6$ GeV effectively eliminates background from Δ excitation, which tends to produce lower energy pions.

Signal and background distributions for several of the important cut variables are shown in Figure 24. The relative normalizations of the two distributions in the initial plot is arbitrary; subsequent plots show the effect of the applied cuts.

Applying this set of cuts to our signal sample (85k events) we find that 25.5k signal events pass all cuts, which gives an overall efficiency of 30%. The expected purity of the sample is 67$\pm$3%, where the error bar is the statistical error on the Monte Carlo sample used for the study. We note that in this analysis other important variables for background rejection, related to associated activity around the vertex, were not used. Figure 25 shows the expected precision of the MINERνA measurement as a function of neutrino energy. Here we have only included the statistical error on the signal and assumed that the measured value is that predicted by Rein-Seghal. No attempt has been made to quantify the systematic errors on this measurement other than that resulting from the background subtraction. Previous measurements of the coherent cross-section were statistics limited. Of particular interest is the energy dependence of the cross section. Figure 26 compares the predictions of the Rein-Sehgal and Paschos-Kartavtsev models for charged current coherent scattering from carbon. Sizable differences are evident, particularly near threshold.

2.4.3 Detector requirements

Figure 27 shows the efficiency and purity of the CC-coherent selection as a function of the assumptions about the measurement resolution of the detector. This study indicates that to maintain high efficiency and purity for this analysis good hadronic energy resolution (<20% / $\sqrt{E_{had}}$) and angular resolution are required. In addition, good particle ID by dE/dx is crucial to distinguish protons which interact from pions.

2.4.4 Error Budget

The charged current cross section will be measured in bins of energy. In this section we perform a rough error analysis based on the assumption that the data will be divided into 20 energy bins with equal statistics. In each bin there will be around 1900 events of which 1275 are signal and 628 background. The statistical uncertainty on the cross section will therefore be 3.4%. We factorize the systematic errors into beam and analysis/detector related quantities. For the beam we find that the uncertainty in absolute cross section due to the flux uncertainty is 5%. The error on the background subtraction is 2.0% and is dominated by the statistical error on the subtraction. The error due to the uncertainty in the muon and pion energy scales, 2% and 3% respectively, is 1%. This value was determined by shifting the reconstructed energies by the stated amounts and determining the change in number of events accepted. The systematic uncertainty on the efficiency correction is hard to estimate without access to a variety of models as the correction is large and will be model

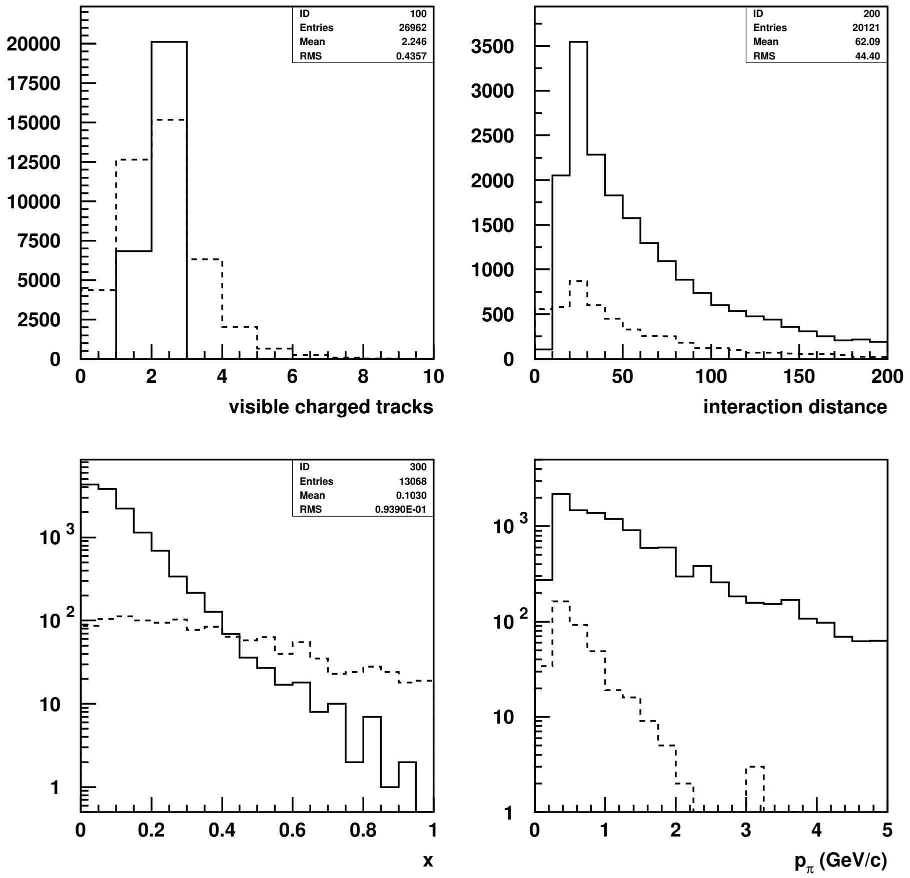

Figure 24: Topological and kinematic quantities for signal (solid) and background (dashed) processes. Top Left: Visible charged tracks. Top Right: Distance between the event vertex and the location of the pion interaction (in cm). Bottom Left: Bjorken-x. Bottom Right: Charged pion momentum.

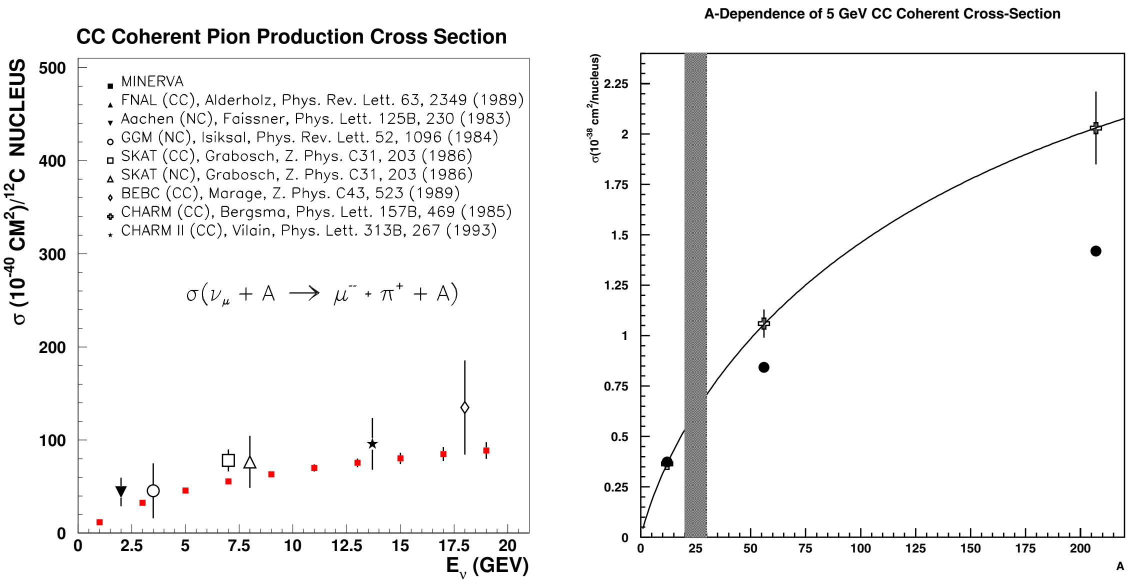

Figure 25: Left: Coherent cross-sections measured by MINERνA compared with existing published results. MINERνA errors here are statistical only. Right: Measurement of the coherent cross-section as a function of atomic number in MINERνA.The shaded band indicates the range of previous measurements. Error bars indicate the size of the experimental errors in a single 1-GeV bin. The curve shows the prediction from the Rein-Seghal model. Crosses are the prediction of the Rein-Seghal model for scattering from carbon, iron, and lead, circles are the predictions of the Paschos-Kartavtsev model.

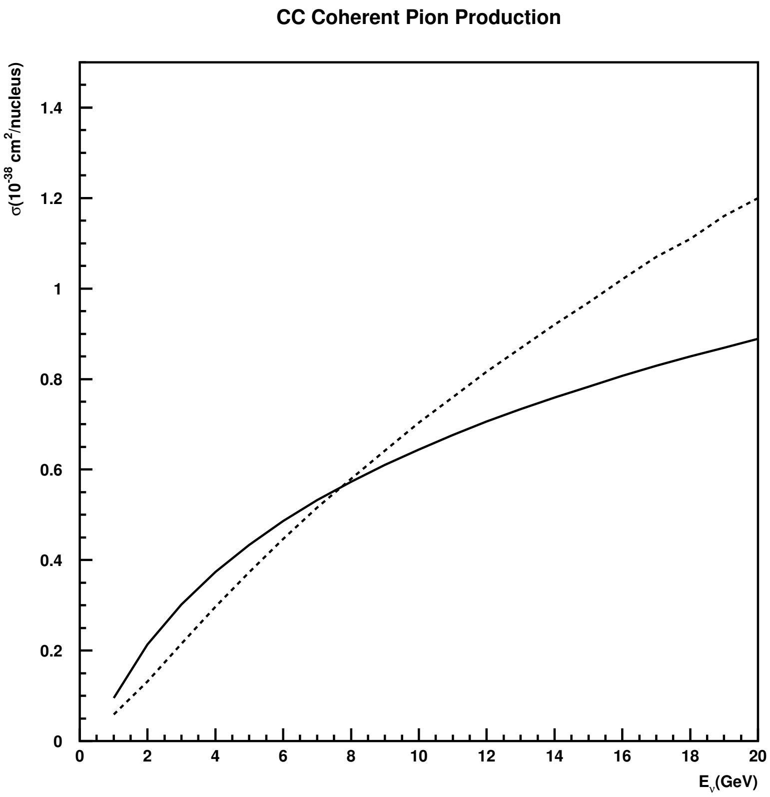

Figure 26: Predictions for charged current coherent production from carbon from the Rein-Sehgal model (solid) and the Paschos-Kartavtsev model (dashed).

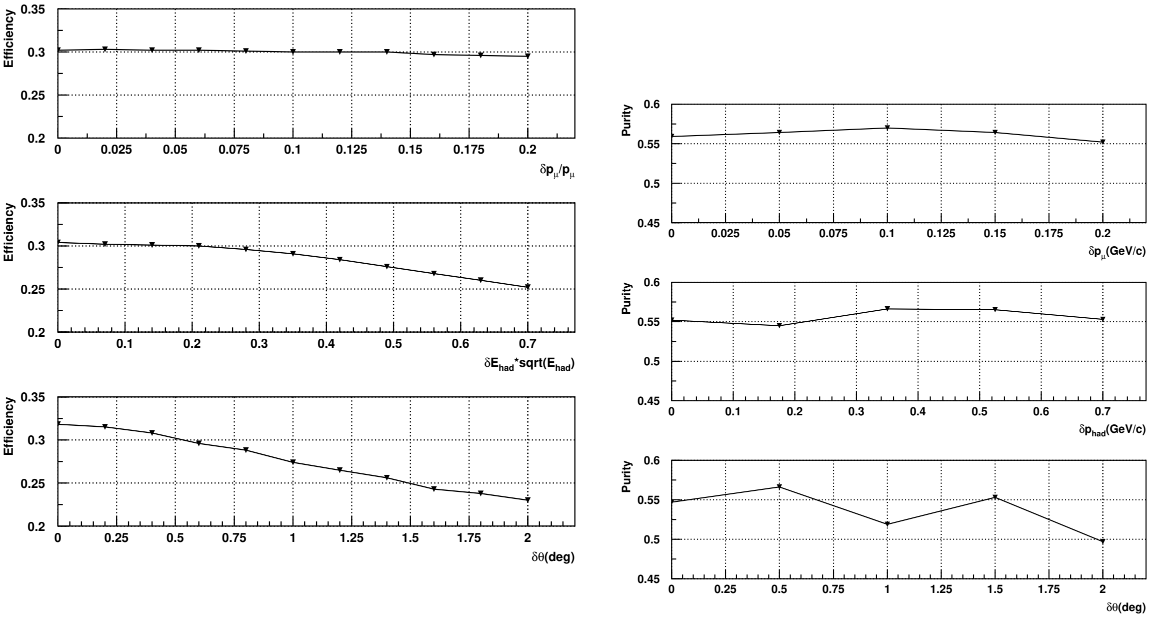

Figure 27: Left: Efficiency of CC coherent selection as a function of angular resolution, muon energy resolution, and hadronic energy resolution. Right: Purity of CC coherent selection as a function of the same variables. Note that in the hadronic energy resolution plots the x-axis is the coefficient of the $1/\sqrt{E_{had}}$ term.

dependent. We estimate this uncertainty to be 5% and will be data-driven to some extent since our sample will provide full kinematic distributions with which existing and future models must agree. Understanding the efficiency of the topological cuts will require good testbeam calibration over a range of charged pion and proton energies. In summary, the statistical error will be 3.4%, the systematic uncertainty (beam-related) is 5%, and the systematic uncertainty (analysis/detector-related) is 5.5%.

2.4.5 A-dependence of the coherent cross-section

Another task for MINERνA will be comparison of reaction rates for lead and carbon. The expected yield from lead will be $\approx$ 1800 charged-current events, assuming the same efficiency. The A-dependence of the cross-section depends mainly on the model assumed for the hadron–nucleus interaction, and serves as a crucial test for that component of the predictions. No experiment to date has been able to perform this comparison. For reference, the predicted ratio of carbon to lead neutral-current cross-sections at 10 GeV in the Rein-Sehgal and Paschos models are 0.223 and 0.259, respectively [56]. Figure 25 shows the predicted A-dependence according to the model of Rein and Sehgal.

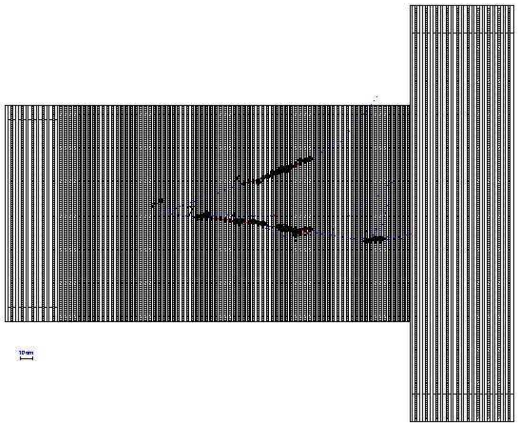

Figure 28: A simulated neutral-current coherent π^0 production event in MINERνA. The position of the π^0 decay vertex can be determined accurately by extrapolating the two photons backward. Notice that both photons pass through a number of planes before beginning to shower, distinguishing them from electrons.

2.4.6 Neutral-current cross-section

Neutral-current π^0 production can occur through a number of mechanisms - resonant production, coherent production, and deep-inelastic scattering. Figure 28 shows a striking example of MINERνA's response to coherent π^0 production.

By requiring two well-separated electromagnetic clusters that shower in the scintillator target, and extend at least 6 scintillator planes, about 30% of the coherent π^0 events produced in the detector are retained. Furthermore, by requiring the ratio of the energy in the two clusters to that of the total event energy to be above 90%, and requiring any extra energy to be less than 100 MeV, reduces both the ν_e (ν_μ) charged-current contamination to a few (less than one) events. Figure 29 shows these two last variables, where the coherent π^0 peak is clearly visible in the plot on the right. The resulting sample in this simple analysis (1000 events per year in 3 tons of fiducial mass) is roughly half resonant π^0 production and half coherent π^0 events, which can be separated by studying the angular and energy distribution of the events, as well as the presence or absence of additional particles at the production vertex identified by the two photon showers.

Neutral pions from resonance excitation are neither as energetic nor as collinear as those produced coherently. Resonant π^0 are particularly susceptible to final-state nuclear interaction and rescattering, which will be studied in detail by MINERνA using charged-current reactions.

As a proof-of-concept, a sample of neutral-current single-π^0 events has been selected using simple cuts. For events with two well-separated electromagnetic clusters ($E_\pi \equiv E_1 + E_2$), each passing through at least six planes of the fully-active region, requiring $E_\pi/E_{tot} > 90\%$ and $E_{tot} - E_\pi < 100$ MeV efficiently isolates a neutral-current π^0 sample, as shown in Figure 30. After these cuts, the contamination of ν_e and ν_μ charged-current interactions (combined) is less than 1%. The resulting sample contains about 2400 neutral-current π^0 events per 3 ton-yr, of which half are resonant and half coherent.

Coherent and resonant interactions can be cleanly separated by cutting on the π^0 angle to the beam direction, as shown in Figure 31, which also highlights MINERνA's excellent π^0 angular resolution. The overall efficiency for selecting coherent neutral-current π^0 is about 40%.

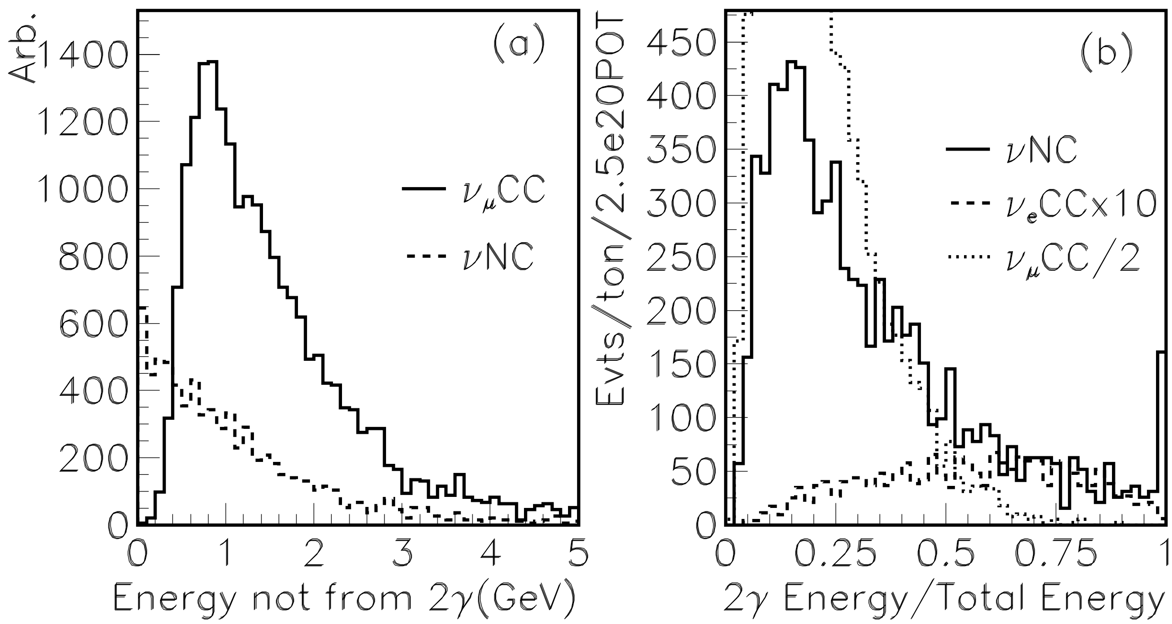

Figure 29: Variables that reject backgrounds to coherent π^0 measurements: (a) Other energy in the event for ν_μ charged- and neutral-current events, and (b) Ratio of two photon energy to total event energy for ν_μ charged-current sample (reduced by factor of 2), ν_e charged-current (increased by a factor of 10) and the neutral-current sample (normalized per ton per year, acceptance calculated for 3 tons fiducial volume)

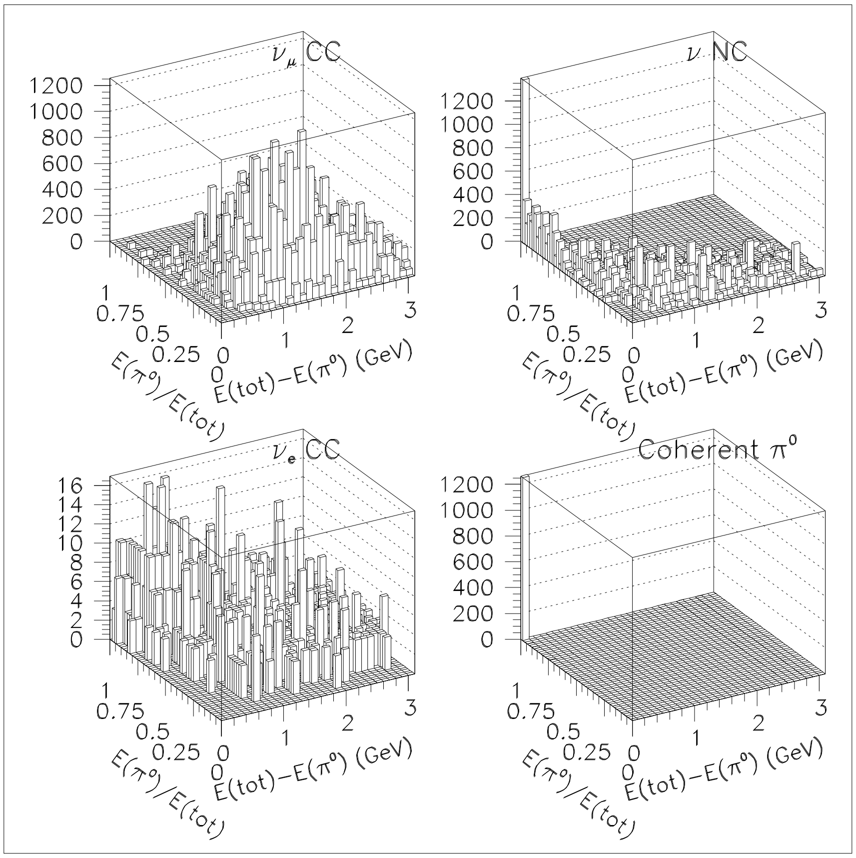

Figure 30: Selection of neutral-current single-π^0 production. The variables plotted are the fraction of visible energy carried by the π^0 candidate (E_π/E_{tot}) and the residual energy $E_{tot} - E_\pi$. The left-hand plots show backgrounds from ν_μ(top) and ν_e(bottom). The plot at top right shows the same distribution for true neutral-current π^0 production, and the lower right shows the subset from coherent scattering. In the neutral-current plots, notice the dramatic concentration of the coherent π^0 signal in a single bin, in the left-most corner of the graph. All samples shown are normalized to a 3 ton-yr exposure of MINERνA.

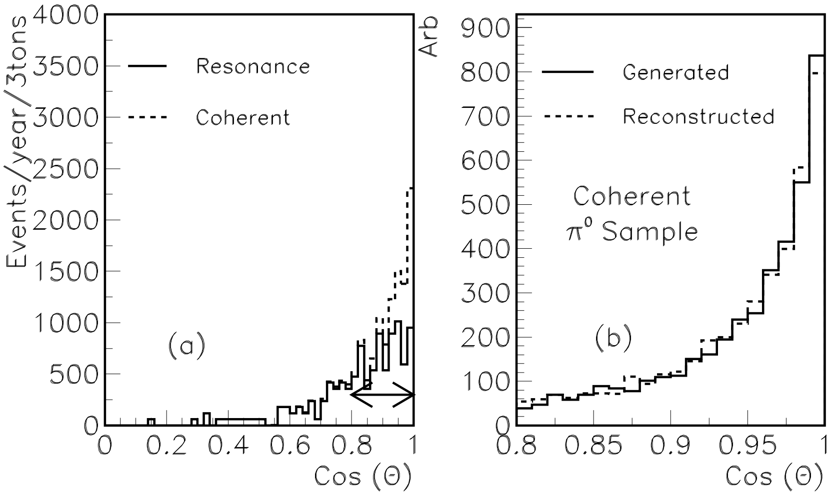

Figure 31: Angular distribution of neutral-current single-π^0 sample. The plot at left shows all events passing the cuts on E_π/E_{tot} and $E_{tot} - E_\pi$ described in the text, broken down into coherent and resonant reactions. The coherent sample is strongly forward-peaked. The plot at right is a close-up of the forward region comparing the true and reconstructed π^0 angular distributions from the beam direction. The distributions are nearly identical, highlighting the MINERνA's excellent angular resolution.

2.5 Strange and Charm Particle Production

High-statistics studies of exclusive strange-particle production by neutrinos will be possible for the first time in MINERνA. Sample sizes for several channels accessible to MINERνA in a four-year ν_μ run are summarized in Table 2.5.3. Cross section measurements afforded by these samples will impact other areas of particle physics, for example in estimation of atmospheric neutrino ΔS backgrounds to nucleon-decay searches. MINERνA's physics program will also include searches for new processes, *e.g.* strangeness-changing neutral-current reactions and unusual baryon resonances. Extended running of the NuMI beam with $\bar{\nu}$ exposures will provide valuable data for many neutrino topics. Anti-neutrino exposure will facilitate study of $\Delta S = 1$ single-hyperon production (Λ, Σ, Y^*), and would permit a novel measurement of CKM matrix elements. Selected topics and their motivations are summarized below.

2.5.1 Backgrounds to Nucleon Decay

Current lifetime limits for nucleon decay ($\tau/\beta \geq 10^{33}$ years) have not diminished hopes for the eventual success of supersymmetric grand unification (SUSY GUTs). Indeed, there is strong motivation to proceed with more ambitious experimental searches. For the near future, improved searches will be carried out by Super–Kamiokande. Eventually these will be taken up by a next generation of underground detectors. Continued progress, either by improving limits to 10^{34} year lifetimes or discovering nucleon decay, hinges upon improved knowledge of certain neutrino interactions which, when initiated by atmospheric neutrinos, can imitate nucleon-decay signals. The most problematic of background reactions to SUSY GUT modes arise with neutral-current associated production of strangeness at threshold energies.

2.5.2 Measurement of $\sigma(\nu\Lambda K^+)$

/minerva/ will measure the exclusive $\Delta S = 0$ neutral-current channel

$$\frac{d\sigma}{dE_\nu}(\nu_\mu p \rightarrow \nu_\mu K^+ \Lambda), \tag{2}$$

from its threshold at ≈ 1 GeV through its rise and plateau at E_ν between 10-15 GeV. For purposes of comparison and as a valuable check on systematics[61], we will simultaneously measure the the $\Delta S = 0$ companion charged-current reaction

$$\frac{d\sigma}{dE_\nu}(\nu_\mu n \rightarrow \mu^- K^+ \Lambda). \tag{3}$$

2.5.3 Strangeness-changing Neutral Currents

Strangeness-changing neutral-current reactions have never been observed. Their occurrence at rates accessible in NuMI would imply new physics beyond the Standard Model. Existing limits on NC $\Delta S = 1$ processes are based upon searches for rare K decays. Although there are experimental difficulties with unambiguous identification of such processes in neutrino reactions, there is nevertheless

Reaction Type	Exclusive Channel	No. Events ($\geq$ 0 constraint)
$\Delta S = 0$ CC	$\nu_\mu n \rightarrow \mu^- K^+ \Lambda^0$	23,100
	$\nu_\mu n \rightarrow \mu^- \pi^0 K^+ \Lambda^0$	20,400
	$\nu_\mu n \rightarrow \mu^- \pi^+ K^0 \Lambda^0$	13,800
	$\nu_\mu n \rightarrow \mu^- K^- K^+ p$	11,200
	$\nu_\mu p \rightarrow \mu^- K^0 K^+ \pi^0 p$	3,300
$\Delta S = 1$ CC	$\nu_\mu p \rightarrow \mu^- K^+ p$	34,900
	$\nu_\mu n \rightarrow \mu^- K^0 p$	5,200
	$\nu_\mu n \rightarrow \mu^- \pi^+ K^0$	4,600
$\Delta S = 0$ NC	$\nu_\mu p \rightarrow \nu K^+ \Lambda^0$	7,900
	$\nu_\mu n \rightarrow \nu K^0 \Lambda^0$	2,400
	$\nu_\mu n \rightarrow \nu K^0 \Lambda^0$	6,100

Table 7: Event samples for kinematically constrainable exclusive strangeness production reactions, in a four-year exposure of MINERνA's three-ton inner fiducial volume.

an opportunity for a search in the neutrino sector. A search for strangeness-changing neutral-current neutrino interactions can usefully clarify the extent to which new physics parameters may be missing from the analysis of weak radiative hyperon decays. It is plausible that neutrino reactions, in contrast to hyperon weak decays, may provide cleaner signals for a new weak current, since multi-loop quark-gluon diagrams which complicate hyperon decay analysis would be absent.

2.5.4 Hyperon Beta-decay and Exotic Quark States

Hyperon beta-decay $A \rightarrow B\, e^-\, \bar{\nu}_e$ provides a window onto weak hadronic current form-factors and their underlying structure. Recent high-statistics measurements of these form-factors using KTeV Ξ^0 hyperon beta-decays have been reported[62]; the results show that the level of SU(3) breaking is very small compared to expectations of modern theories[63]. These new results have been used to extract the CKM matrix elements V_{us}[64] [65]. Similar studies are possible using anti-neutrino interactions that produce hyperons. The hyperon decays have the added feature of a self-analyzing power of the polarization vector. In hyperon production via anti-neutrinos,the fundamental form-factors and CKM matrix elements will be accessible without the hindrance (encountered in hyperon beta-decay) of double solutions due to the missing neutrino energy.

Searches for $\Delta S = 1$ production of pentaquark states such as those reported[66], could be greatly extended in MINERνA. In neutrino-nucleus interactions wherein hyperons and mesons are produced together, a wealth of combinations can be examined to search for the full spectrum of the pentaquark family[67] of particles and for other exotic quark combinations such as di-baryons as well.

2.5.5 Charm Production

Charm production in MINERνA is suppressed by the relatively low energy of its beams, hence the reach will be limited. Nevertheless, the cross-section turn-on just above threshold is very sensitive to the bare charm quark mass and MINERνA can still make a valuable contribution. With the proposed beam running schedule for MINERνA we expect $\sim 23,000$ of inclusive charm production events in the fiducial volume in the standard four year run.

2.6 The Perturbative and Non-Perturbative Interface

2.6.1 Quark Distributions at Large x

One of the most fundamental properties of the nucleon is the structure of its valence quark distributions. Valence quarks are the irreducible kernel of each hadron, responsible for its charge, baryon number and other macroscopic properties. Sea quarks, which at high Q^2 are largely generated through gluon bremsstrahlung and subsequent splitting into quark-antiquark pairs, represent one source of the nonperturbative dressing of the valence quarks at low Q^2. At higher x values these quark / anti-quark contributions drop away, and the physics of the valence quarks is cleanly exposed. Although a large body of structure function data exists over a wide range of x and Q^2, the region $x > 0.6$ is not well explored.

Knowledge of the valence quark distributions of the nucleon at large x is vital for several reasons. Measurements of structure functions at large x will bring insights into the mechanisms responsible for spin-flavor symmetry breaking. In addition, quark distributions at large x are a crucial input for estimating backgrounds in searches for new physics beyond the Standard Model at high energy colliders [68].

The uncertainties in the current nucleon parton distribution functions at high x are of two predominant types: the ratio of the light quark pdf's, $d(x)/u(x)$, as $x \to 1$ and the role of leading power corrections (higher twist) in the extraction of the high x behavior of the quarks. The measurement of quark densities at high-x_{Bj} is closely related to the question of the leading power corrections known as "higher twist effects". The n^{th} order higher twist effects are proportional to $1/Q^{2n}$ and reflect the fact that quarks have transverse momentum within the nucleon and that the probe becomes larger as Q^2 decreases, thus increasing the probability of multi-quark participation in an interaction. Different analyses of higher twist corrections in current data leave some unresolved issues that would benefit from new experimental information.

The only actual measurements of a higher-twist term in neutrino experiments have been two low-statistics bubble chamber experiments: in Gargamelle [69] with freon and in BEBC [70] with NeH_2. Both bubble chamber analyses are complicated by nuclear corrections at high-x. However, both analyses found a twist-4 contribution that is smaller in magnitude than the charged leptoproduction analysis and, most significantly, is preferentially negative.

Higher twist components of the structure functions may be obtained from deviations of measured data from the calculable expectations from perturbative QCD. As indicated in Figure 32, showing one of the dominant systematic errors, the expected uncertainties in the structure functions obtained in the MINERνA experiment will be such that this type of higher twist analysis may be performed precisely for the first time with neutrino measurements. In this case, it is crucial also to understand the effects arising from nuclear medium modifications to the nucleon structure functions, which will also be measured by MINERνA.

2.6.2 Quark-Hadron Duality

The description of hadrons in terms of their fundamental quark and gluon constituents is one of the major challenges in nuclear physics today. While at present we cannot describe the structure and interactions of hadrons directly utilizing the quark and gluon degrees of freedom of QCD, we know

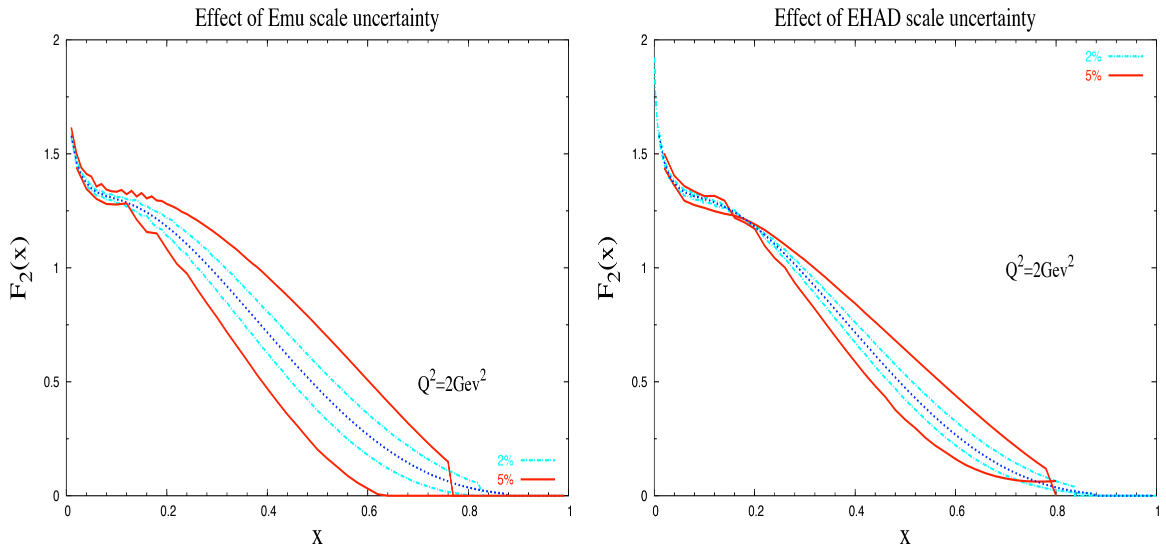

Figure 32: The effect of the (dominant) energy scale uncertainties, muon on left and hadron on right, on the x dependence of the F_2 structure function is shown for the transition region at at $Q^2 = 2$ GeV^2. Here, for instance, x = 0.7 corresponds to $W^2 = 1.7$ GeV^2 in the resonance region.

that in principle it should just be a matter of convenience in choosing to describe a process in terms of quark-gluon or hadronic degrees of freedom. This fact is referred to as *quark-hadron duality*, and means that one can use either set of complete basis states to describe physical phenomena. At high energies, where the interactions between quarks and gluons become weak and quarks can be considered asymptotically free, an efficient description of phenomena is afforded in terms of quarks; at low energies, where the effects of confinement make strongly-coupled QCD highly non-perturbative and the final state is guaranteed to be made of hadrons, it is more efficient to work in terms of collective degrees of freedom, the physical mesons and baryons. The duality between quark and hadron descriptions reflects the relationship between confinement and asymptotic freedom, and is intimately related to the nature of the transition from non-perturbative to perturbative QCD. It has been said that (short of the full solution of QCD) understanding and controlling the accuracy of the quark-hadron duality is one of the most important and challenging problems for QCD practitioners today [71].

Although the duality between quark and hadron descriptions is formally exact in principle, how this reveals itself specifically in different physical processes and under different kinematical conditions is a key to understanding the consequences of QCD for hadronic structure. The phenomenon of duality is in fact quite general in nature and can be studied in a variety of processes, such as $e^+e^- \rightarrow$ hadrons, or semi-leptonic decays of heavy quarks. Duality in lepton–nucleon scattering, historically called Bloom-Gilman duality, links the physics of resonance production to the physics of deep inelastic scaling. Duality is manifested here in the observation that the hadronic (resonance) and quark (scaling) strengths are, on average, equivalent. Moreover, this is true for all Q^2 observed above $Q^2 \approx 1$ GeV^2, and thus a perturbative behavior apparently describes the average Q^2 dependence of the hadronic, non-perturbative, resonance enhancement region.

The MINERνA experiment is uniquely poised to provide a wealth of data to answer where duality works, in what structure functions, in what reactions, and at what kinematics. Duality has been well-verified [73] for the proton F_2 structure function [74], observed recently in the separated longitudinal and transverse unpolarized structure functions [75], on nucleons and in nuclei [76], and in polarized structure functions [77]. While it's fundamental cause remains a mystery, duality appears experimentally to be a non-trivial property of nucleon structure. It is, therefore, crucial to test it in a variety of reactions – including neutrino-nucleon and nucleus scattering and the structure function xF_3.To accomplish such a study, high precision structure function data are needed in both the deep inelastic and in the resonance regimes. As can be seen in Figure 33, MINERνA will have high statistics in both of these regions.

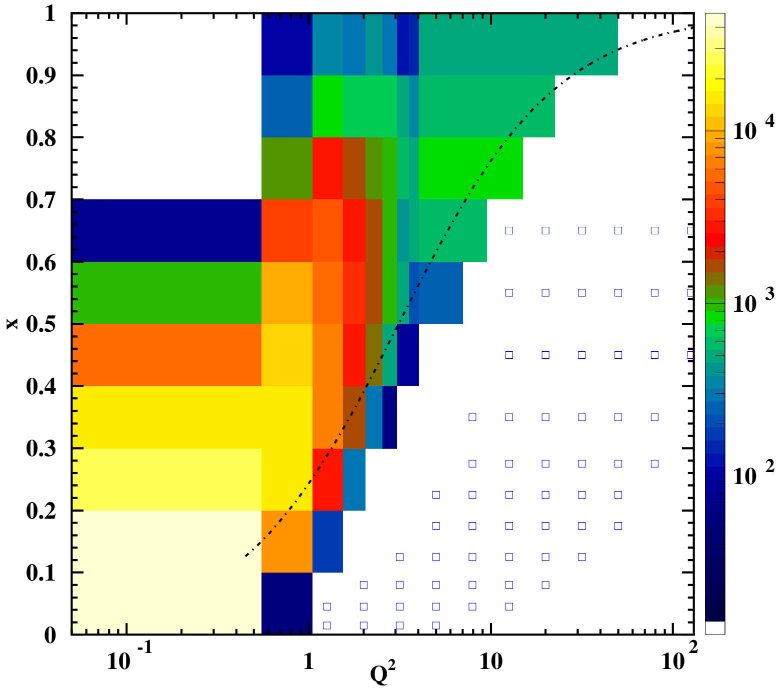

Figure 33: Available xF$_3$ data (open symbols) and the anticipated (resonance region) MINERνA data (colored distributions in x and Q^2. The curve indicates the commonly-utilized W^2 $= 4$ GeV^2 boundary between the deep inelastic and resonance regimes. The color key to the right indicates anticipated MINERνA statistics.

Duality studies of electron-deuteron scattering at low Q^2 reported a resemblance to deep inelastic neutrino-nucleus scattering at much higher Q^2, indicating a potential sensitivity of duality to the valence quarks [78]. The proposed experiment will allow this observation to be verified and tested for the first time, as data from like kinematic regimes but differing in probe and interaction (from MINERνA and Jefferson Lab) may be compared directly. As shown in Figure 34 in Section 2.6, the kinematic regimes of these facilities are quite complementary.

2.6.3 QCD Moments

Figure 34 from Section 2.6 depicts the substantial kinematic range enhancement in both x and Q^2 made possible by the MINERνA experiment. This broad range of the data will allow for accurate moments of the structure functions to be obtained. To obtain a structure function moment, it is necessary to integrate over the full range in x at a fixed value of Q^2. These moments are fundamental quantities, calculable in QCD and recently calculated in lattice QCD at $Q^2 = 4$ GeV^2 for valence distributions [80]. If duality is shown to hold, the proposed data may provide one of the few available quantities which can be directly compared to lattice QCD calculations – that is, a valence–only structure function moment.

At $Q^2 = 4$ GeV^2, MINERνA will measure the range $0.1 < x < 1$. These data combined with existing world data will allow for moments of structure functions to be obtained with about a 5% precision. It is important to note two things in this case – first, nuclear effects are not expected to play a role in the integrated moments, as it has been shown that the momentum sum rule is preserved in nuclei [81]. Next, uncertainties in kinematics play only a reduced role in moment extractions, which are integrated in x, or in W^2.

Large x (resonance region) data become increasingly important for higher order moments. At n=6, for example, the resonance and large x region above $x = 0.7$ make up 70% of the Cornwall-Norton moment of F_2 at $Q^2 = 10$ (GeV/c)^2. The contribution is larger at $Q^2 = 4$ GeV^2, where lattice calculations are available. As noted above and clear in Figure 33, there currently exist little to no neutrino cross section data in the resonance region or at larger x, while such data will be easily obtainable with MINERνA.

2.7 Deep Inelastic Scattering and QCD

Neutrino scattering plays a crucial role in extraction of fundamental parton distribution functions (PDFs). These PDFs describe parton constituents of protons and other hadrons, and (in the $\overline{MS}$ convention) are precisely defined in terms of operator matrix elements. The necessity of neutrino measurements is obvious, because only neutrinos can resolve the flavor of the nucleon's constituents: ν interacts with d, s, $\overline{u}$ and $\overline{c}$ while the $\overline{\nu}$ interacts with u, c, $\overline{d}$ and $\overline{s}$. The weak current's unique ability to "taste" only particular quark flavors significantly enhances the study of parton distribution functions. MINERνA's high-statistics measurement of the nucleon's partonic structure, using neutrinos, will complement on-going studies with electromagnetic probes at other laboratories.

With the addition of large samples of nub, and dedicated effort to minimizing beam-related systematics, MINERνA will be able to independently isolate all the structure functions $F_1^{\nu N}(x, Q^2)$, $F_1^{\bar{\nu} N}(x, Q^2)$, $F_2^{\nu N}(x, Q^2)$, $F_2^{\bar{\nu} N}(x, Q^2)$, $xF_3^{\nu N}(x, Q^2)$ and $xF_3^{\bar{\nu} N}(x, Q^2)$ for the first time. By taking differences and sums of these structure functions, specific parton distribution functions in a given (x, Q^2) bin can in turn be determined. With the manageable systematic uncertainties expected, this experiment will dramatically improve the isolation of individual PDFs by measuring the full set of ν and $\bar{\nu}$ structure functions.

Extracting this full set of structure functions will rely on the y-variation of the structure function coefficients in the expression for the cross-section. In the helicity representation, for example:

$$\begin{aligned} \frac{d^2\sigma^\nu}{dxdQ^2} &= \frac{G_F^2}{2\pi x}\Big[\frac{1}{2}\left(F_2^\nu(x, Q^2) + xF_3^\nu(x, Q^2)\right) + \\ &\quad \frac{(1-y)^2}{2}\left(F_2^\nu(x, Q^2) - xF_3^\nu(x, Q^2)\right) - \\ &\quad 2y^2 F_L^\nu x, Q^2)\Big]. \end{aligned} \tag{4}$$

By analyzing the data as a function of $(1-y)^2$ in a given (x, Q^2) bin, all six structure functions can be extracted.[3]

MINERνA has the important feature to allow measurement of the neutrino cross section and structure function from a variety of nuclear targets. This will be important both to connect with previous measurements which will overlap the MINERνA result on the high Q^2 end and to allow, for the first time, a precision determination of nuclear effects in neutrino scattering.

2.7.1 Structure Functions

The structure function F_2 has been precisely measured over a large range of Q^2 using charged-lepton probes. Figure 34 illustrates the kinematic coverage for measurements of F_2 using charged-lepton and neutrino probes. Neutrino measurements have been limited so far to moderate Q^2's. MINERνA will provide complimentary information from neutrinos in the high-x low-Q^2 regime which overlaps precise measurements using charged-lepton probes.

[3]Note that for this type of parton distribution function study, anti-neutrino running will be essential.

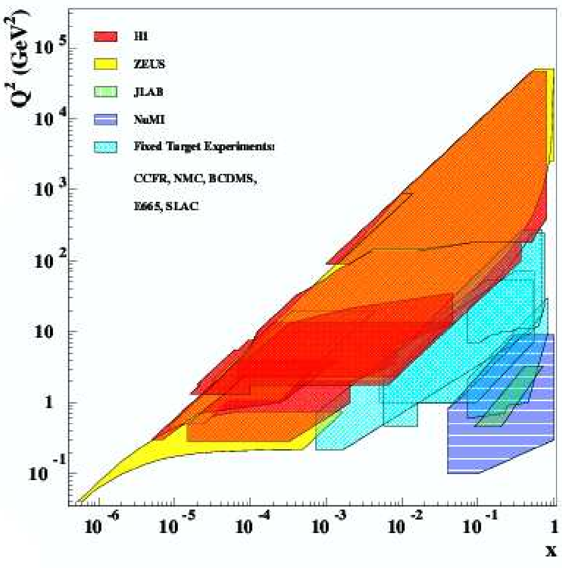

Figure 34: Kinematic coverage of structure function measurements.

While the structure function F_2 is precisely measured with charged-lepton probes, the parity-violating structure function xF_3 can best be determined using a weak-interaction probe. Neutrino measurement have been limited to moderate x and Q^2. As Figure 35 illustrated MINERνA will provide new kinematic coverage for the structure function xF_3.

2.7.2 Physics Driven Detector Requirements: Structure Function Measurement

There are several components of the MINERνA detector design that impact DIS physics. In a deeply inelastic event, the probing particle breaks apart the nucleus and a hadronic shower is present in the final state. The detector must have sufficient mass to contain the shower and measure the energy at the hadronic vertex. In MINERνA the calorimeters serve the function of stopping hadrons and measuring their energy. The design of the calorimeters was optimized to provide adequate hadronic shower energy resolution and good hadron containment.

The measurement of the neutrino differential cross section and structure functions relies on accurate determination of the event kinematic variables. Figure 36 shows the effect of hadron energy resolution on the measured kinematic variable distributions, x, y, and Q^2, for the nominal resolution of $22\%/\sqrt{E_H}$. The hadronic energy resolution has a large impact on the measured y distribution. Figure 37 shows how the smearing changes as the hadron energy resolution is varied from $11\%/\sqrt{E}$ (half the nominal value) up to $44\%/\sqrt{E}$ (twice nominal). Clearly a resolution of twice nominal significantly degrades the measured y distribution, which decreases significantly the ability of MINERνA to precisely measure the y dependence of the differential cross section.

To fully determine the kinematics of a charged-current neutrino scattering event, the momentum of the outgoing muon track must be measured. This adds a requirement that the calorimeters be thick enough to identify tracks exiting the inner detector and to track them into the minos near detector

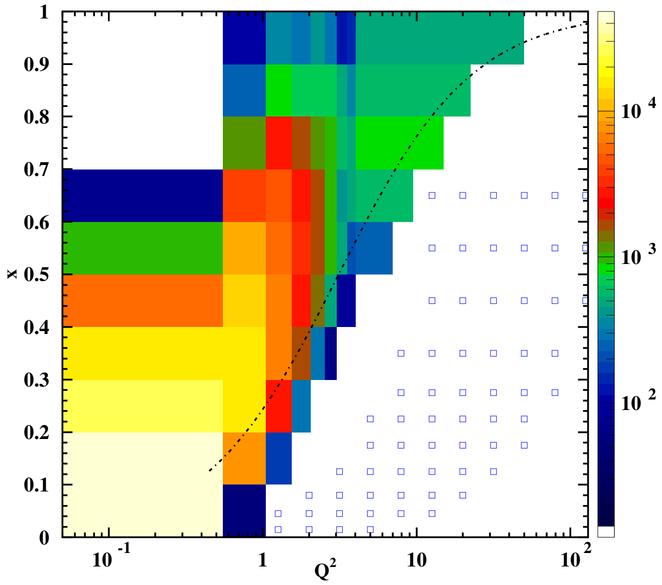

Figure 35: Available xF_3 data (open symbols) and the anticipated (resonant region) MINERνA data (colored distributions) in x_{Bj} vs. Q^2. The curve indicates the commonly-accepted W^2 = 4 GeV^2 boundary between the resonant and deep-inelastic regimes. The color key to the right shows the corresponding, expected MINERνA statistics.

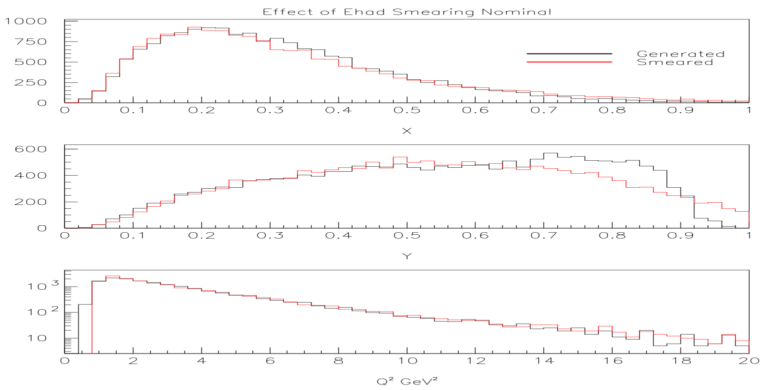

Figure 36: Effect of hadron energy resolution on the measured kinematic variable distributions (x, y, and Q^2) for the nominal resolution of 22%/$\sqrt{E_H}$.

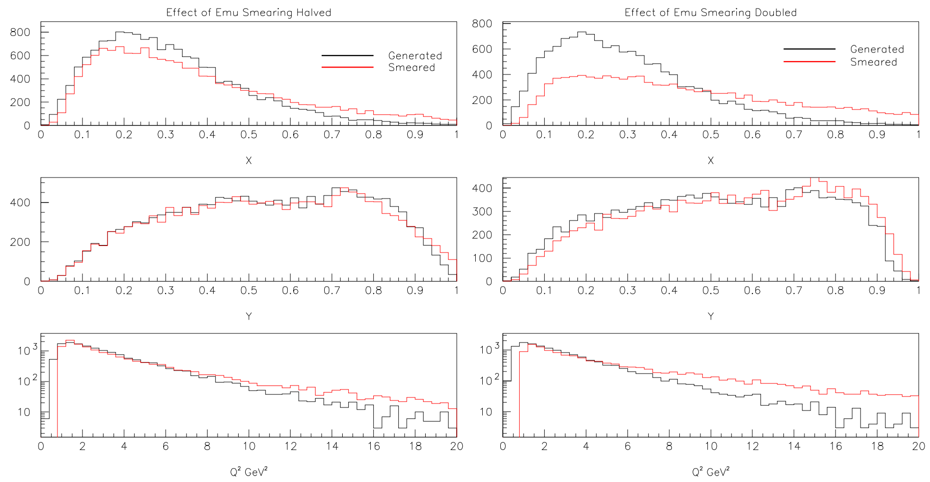

Figure 37: Effect of hadron energy resolution on the measured kinematic variable distributions (x, y, and Q^2) for the resolution of $11\%/\sqrt{E}$ (left) and $44\%/\sqrt{E}$ (right).

where their momentum is measured. The MINERνA design, which uses the minos near detector as a muon spectrometer, has adequate acceptance and momentum resolution for muons. Figure 38 shows the effect of muon momentum resolution on the measured kinematic variable distributions for the nominal muon momentum resolution of 12% for the minos near detector. Figure 39 shows how

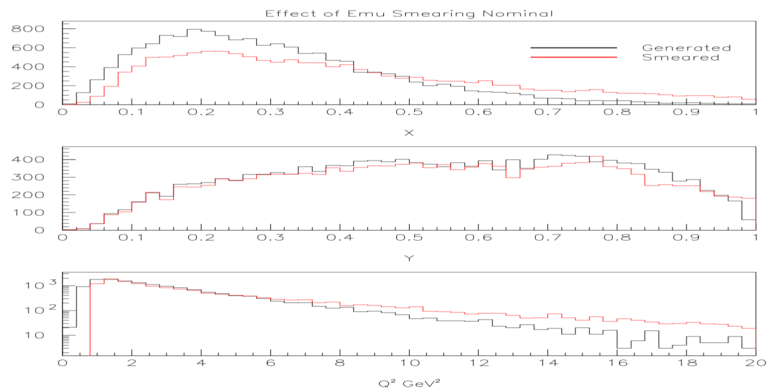

Figure 38: Effect of muon momentum resolution on the measured kinematic variable distributions (x, y, and Q^2) for the nominal muon momentum resolution of 12% for the minos near detector.

the smearing changes as the muon momentum resolution is varied from 6% (half the nominal value) up to 24% twice nominal. Clearly the resolution of 24% has significantly degraded the measured x and Q^2 distributions, which decreases significantly the ability of MINERνA to measure structure functions.

Accurate measurement of the structure functions also requires precise control of systematic uncertainties. The largest systematic uncertainties arise from knowledge of the experiement's absolute

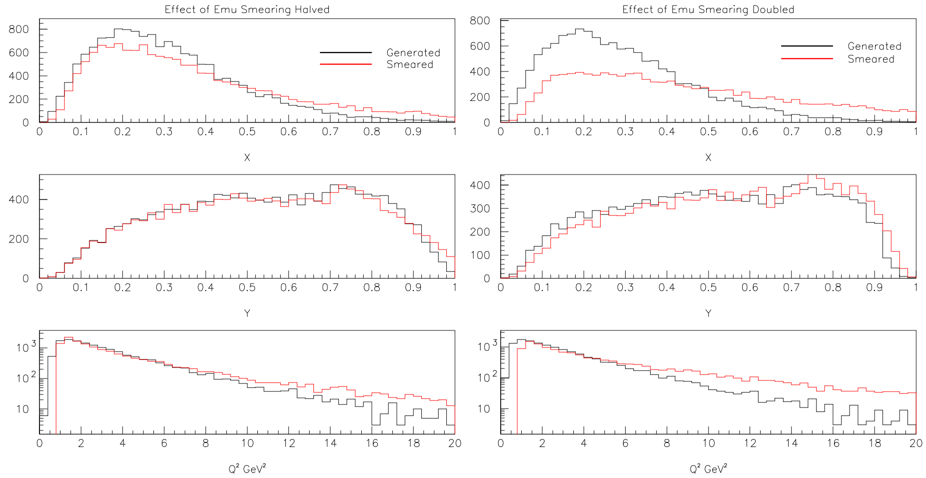

Figure 39: Effect of muon momentum resolution on the measured kinematic variable distributions (x, y, and Q^2) for the muon momentum resolution of 6% (left) and 24% (right).

energy scale. This affects measurement of the kinematic variables and limits how well the Q^2 dependence of the structure functions can be determined. Figure 40 shows the effect of two values of energy scale uncertainty on measurement of the structure function F_2.

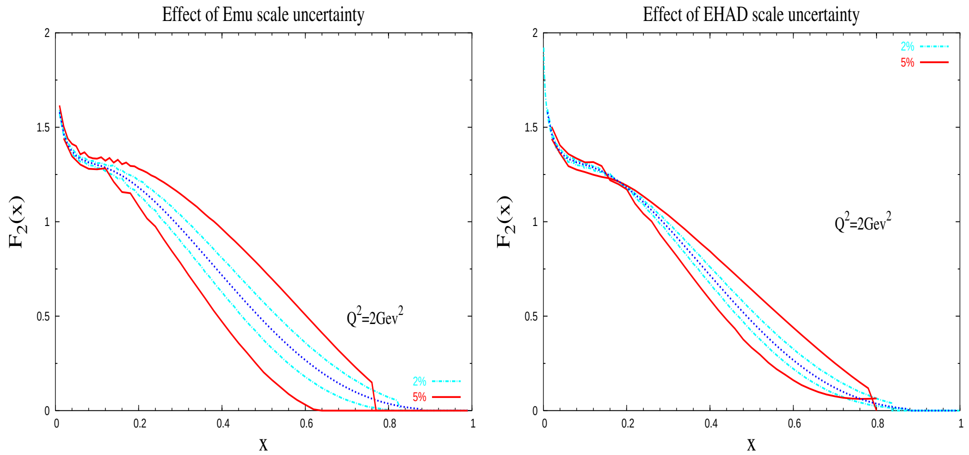

Figure 40: Effect of energy scale uncertainties on x-dependence of F_2 at Q^2=2GeV^2. Uncertainty due to muon energy scale is shown on the left for 2%(blue) and 5% (red) scale uncertainties. The same curves for hadron energy scale are shown on the left.

2.8 Generalized Parton Distributions

One of the main goals of subatomic physics is to understand the structure of hadrons, and in particular the structure of the nucleon. The primary approach to this problem has been measurement of the nucleon form-factors, with (quasi-)elastic scattering (for Q^2 up to a few (GeV/c)^2), parton densities, through inclusive deep-inelastic scattering (DIS), and distribution amplitudes, through exclusive processes. However, the usual parton densities extracted from DIS are only sensitive to the longitudinal component of the parton distributions and do not give information on the transverse component, or other contributions to the nucleon angular momentum.

2.8.1 The Nucleon Spin Puzzle and GPDs

In the late 1980's, results from polarized DIS showed that a relatively small fraction, about 20%, of the nucleon spin is carried by the valence quarks. The obvious candidates for the missing spin were the quark and gluon orbital momentum and gluon helicity. However, information on those quantities cannot be extracted from DIS.

In 1997, Ji [82, 83] showed that a new class of nucleon observables, which he called "off-forward parton distributions", could be used to determine the spin structure of the nucleon. This work, along with developments by others, especially Radyuskin [84, 85] and Collins [86] showed that these distributions, now called generalized parton distributions (GPDs), had the potential to give a full three-dimensional picture of the nucleon structure. This exciting development has led to an immense amount of theoretical work in the last few years. Short reviews can be found in [87, 88] and a comprehensive review can be found in [89].

Ji showed that in leading twist there are four GPDs, which he called H, $\tilde{H}$, E, and $\tilde{E}$, for each quark flavor. H and $\tilde{H}$ are nucleon helicity-conserving amplitudes and E and $\tilde{E}$ are helicity-flipping amplitudes. The GPDs are functions of x, ξ (a factor determining the "off-forwardness" of the reaction), and the total momentum-transfer squared, t. The GPDs can be accessed experimentally through reactions proceeding via the "handbag" diagram shown in Figure 41.

2.8.2 Deeply-virtual Compton Scattering

The most promising reaction to measure GPDs identified so far is deeply-virtual Compton scattering (DVCS). The DVCS reaction is shown in Figure 42a. An interesting feature of DVCS is that it can interfere with the Bethe-Heitler process, Figure 42b, which is completely calculable in terms of the nucleon elastic form-factors. This interference causes an asymmetry in the azimuthal distribution of the scattered proton allowing some quantities to be determined that would otherwise require a polarized target. However, DVCS involves a combination of the four GPD amplitudes, which cannot be separated using DVCS alone. Some complementary information can also be obtained from nucleon form-factor measurements and deep exclusive meson electroproduction.

Neutrino scattering provides a very similar reaction to DVCS. In this case, the virtual mediator is a $W^{\pm}$ with the production of an energetic photon, a $\mu^{\pm}$, with either a recoiling nucleon or nucleon resonance, as shown in Fig. 43. This "weak DVCS" reaction is very promising theoretically because it provides access to different GPDs than DVCS. It will help resolve the individual flavors, e.g. d

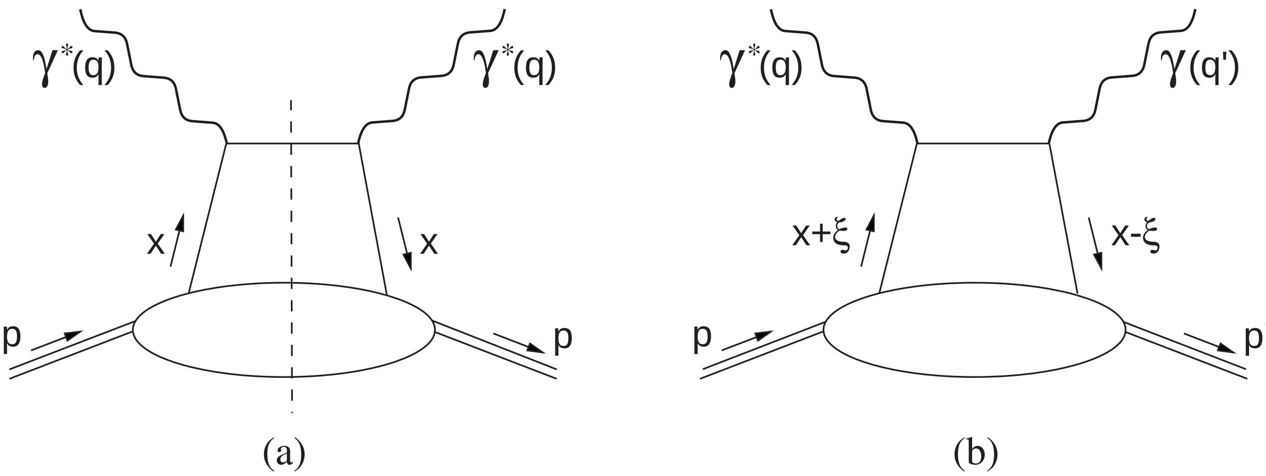

Figure 41: (a) Forward virtual Compton amplitude which describes the DIS *cross-section* via the optical theorem ($x_B = x$); (b) Handbag diagram occurring in the DVCS *amplitude*.

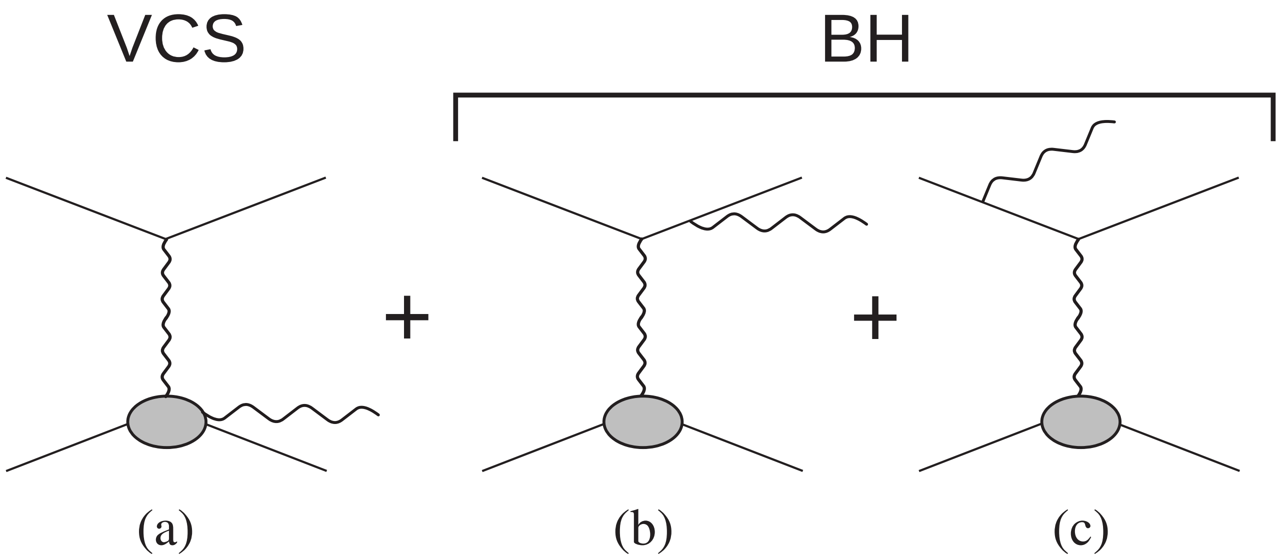

Figure 42: The DVCS process (a) along with the interfering Bethe-Heitler diagrams (b) and (c).

in neutrino scattering and u in anti-neutrino scattering, and the interference of the V and A currents will give access to C-odd combinations of GPDs.

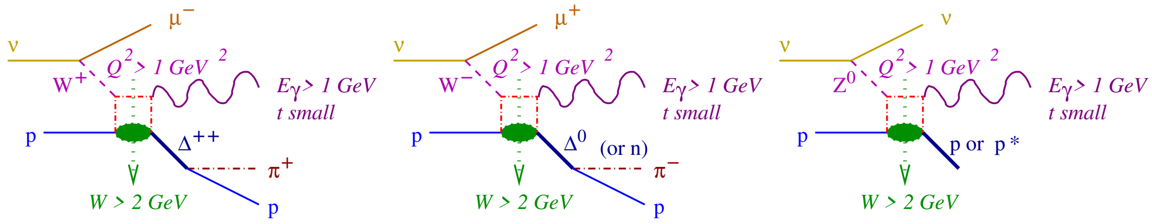

Figure 43: Reactions sensitive to GPDs in neutrino scattering.

2.8.3 Measurement of GPDs in MINERνA

Measurement of the GPDs requires measurement of exclusive processes. In addition, certain kinematic limits must be imposed to allow reliable calculations. In particular, the reaction should be above the resonance region ($W^2 > 4$ GeV^2), the momentum transfer should be small ($t < 0.2$ (GeV/c)^2), and Q^2 should be large ($Q^2 > 2$ (GeV/c)^2), which implies a high-energy photon and low-energy nucleon in the final state. Although this does present certain experimental difficulties, it should be possible to detect these for charged currents in MINERνA. A. Psaker, a student of A. Radyuskin, has made detailed calculations of the weak DVCS process for neutrinos in the 5-20 GeV range with the above kinematic constraints. He finds a cross-section of about 10^{-41} cm^2/neutron for CC reactions, with a relatively small energy dependence (the useful cross section increases slightly from 5 to 20 GeV). The cross section for protons (giving a $\Delta^{++} \to p\pi^+$ in the final state would be about half the neutron cross section. This would yield $\approx$ 10,000 events for the full four-year run with a 3 ton active target.

Additionally, recent work at JLab studying GPD's using DVCS have given promising results [90] for the prospects of measuring GPD's with few GeV neutrinos. The JLab results show a clear signal for GPD's measured at modest Q^2 - 1.5-2.3 GeV^2 - with a 5.75 GeV electron beam, in rough agreement with theoretical expectations. Detailed calculations for neutrino scattering are currently being done W. Melnitchouk and A. Psaker [91] which will give more precise predictions for expectations of measuring GPD's with MINERνA.

Background studies have not yet been performed, but the most significant background should be events with a photon radiated by the out-going muon. It should be pointed out that these will be primarily for reactions on neutrons in carbon, not free nucleons. We are still studying this reaction to assess the effect of extracting GPDs from a bound nucleon.

2.9 Nuclear Effects in Neutrino Interactions

2.9.1 Introduction

Most neutrino experiments, including neutrino oscillation experiments, require massive nuclear targets/detectors to obtain useful reaction rates. Analysis of neutrino reactions with nuclear media requires understanding the nuclear environment's effect on the process [92]. There are two general categories of such nuclear effects:

- The neutrino interaction probability on nuclei is modified relative to free nucleons. Nuclear effects of this type have been extensively studied using muon and electron beams, but have not been explored with neutrinos. Depending on the kinematic region, these nuclear effects can be quite different for neutrinos [93], and are important for neutrino energies typical of oscillation experiments.

- Hadrons produced in a nuclear target may undergo final-state interactions (FSI), including re-scattering and absorption. These effects may significantly alter the observed final-state configuration and measured energy [94, 95], and are sizable at neutrino energies typical of current and planned neutrino oscillation experiments [136].

The hadron shower observed in neutrino experiments is actually the *convolution* of these two effects. FSI effects are dependent on the specific final states that, even for free protons, differ for neutrino and charged-lepton reactions. The suppression or enhancement of particular final states by nuclear effects also differs for neutrino and charged lepton reactions. For these reasons, measurements of nuclear effects with charged leptons cannot be applied to neutrino-nucleus interactions without considerable care.

In addition to the above effects, there is strong evidence that hadron properties are modified in the nuclear medium [124]. Extraction of any nucleon properties from nuclear targets, even as light as ^{4}He, requires understanding such modification.

To study these questions in MINERνA, carbon, iron and lead targets will be installed upstream of the pure scintillator active detector, with tracking detectors surrounding them, and a liquid ^{4}He target will be installed upstream of the main detector. To measure the overall effect of the nucleus, the observed interaction rate, hadron spectrum and multiplicity will be measured for all four targets.

2.9.2 Modified Interaction Probabilities

Pronounced nuclear effects have been measured in *charged-lepton* scattering from a number of nuclear targets. The experimental situation is discussed in review papers [97, 98].

The mechanisms of nuclear scattering have also been studied theoretically. These mechanisms appear to be different for small and large Bjorken x as viewed from the laboratory system. Bjorken x is defined as $x = Q^2/2M\nu$, where ν and $\boldsymbol{q}$ are energy and three-momentum transfer to the target and $Q^2 = \boldsymbol{q}^2 - \nu^2$. The physical quantity discriminating between large and small x regions is a characteristic scattering time, which is also known as Ioffe time (or length) $\tau_I = \nu/Q^2$ [99]. If τ_I is smaller than the average nuclear separation between nucleons, the process can be viewed as incoherent scattering off bound nucleons. This occurs for larger $x(> 0.2)$.

At small Bjorken x the space-time picture is different. The underlying physical mechanism in the laboratory reference frame can be sketched as a two-stage process. In the first stage, the virtual photon γ^* (or W^* or Z^* for neutrino interactions) fluctuates into a quark-antiquark (or hadronic) state. This hadronic state then interacts with the target. The uncertainty principle allows an estimate of the average lifetime of such a fluctuation as

$$\tau = 2\nu/(m^2 + Q^2), \tag{5}$$

where m is the invariant mass of the hadrons into which the virtual boson converts. The same scale τ also determines the characteristic longitudinal distances involved in the process. At small x, τ exceeds the average distance between bound nucleons and coherent multiple interactions of this hadronic fluctuation in a nucleus are important. It is well known that the nuclear shadowing effect for structure functions results from coherent nuclear interactions by hadronic fluctuations of virtual intermediate bosons (for a recent review of nuclear shadowing see, e.g., [98]).

2.9.3 Nuclear effects in the incoherent regime at large x

If x is large enough to neglect coherent nuclear shadowing, lepton scattering off a nucleus can be approximated as incoherent scattering from bound protons and neutrons. The most pronounced nuclear effects in this region are due to Fermi-motion, nuclear binding [100, 101, 102, 103, 104, 105, 106], and off-shell modification of nucleon structure functions [105, 106, 107, 108, 111].

A widely used approximation in description of nuclear structure functions is to neglect the final state interactions of resulting hadrons with the recoiling nucleus. In this approximation the nuclear structure functions can be written as the bound nucleon structure function averaged (convoluted) with the nuclear spectral function (for derivation and more details see [102, 105, 111]). Since bound nucleons are off-shell particles their quark distributions generally depend on nucleon virtuality k^2 as an additional variable. Off-shell effects in structure functions can be viewed as a way to describe in-medium modification of structure functions. This effect was discussed in terms of different approaches in the literature [104, 108, 105, 107, 110, 111].

Predictions of the convolution approach are compared to data on charged-lepton deep-inelastic scattering in Figure 44. Model calculations of nuclear structure functions use realistic nuclear spectral functions. Data seem to indicate that some off-shell modification of bound nucleon structure function is necessary [111]. The right panel of Figure 44 displays the ratio of lead and carbon structure functions calculated within the same approach. It appears nuclear effects at large x are practically saturated in carbon. Similar effects are predicted for neutrino structure functions F_2 and xF_3. MINERνA will provide valuable information on nuclear effects in this region.

2.9.4 Nuclear effects at small x

Nuclear shadowing effects have been discussed extensively in the literature. A recent paper [98] reviews both experimental data and theoretical models of nuclear shadowing for charged-lepton scattering. This effect is interpreted as the coherent interaction of a hadronic component of the virtual photons with the target nucleus. The structure functions at small x can be represented as a superposition of contributions from different hadronic states.

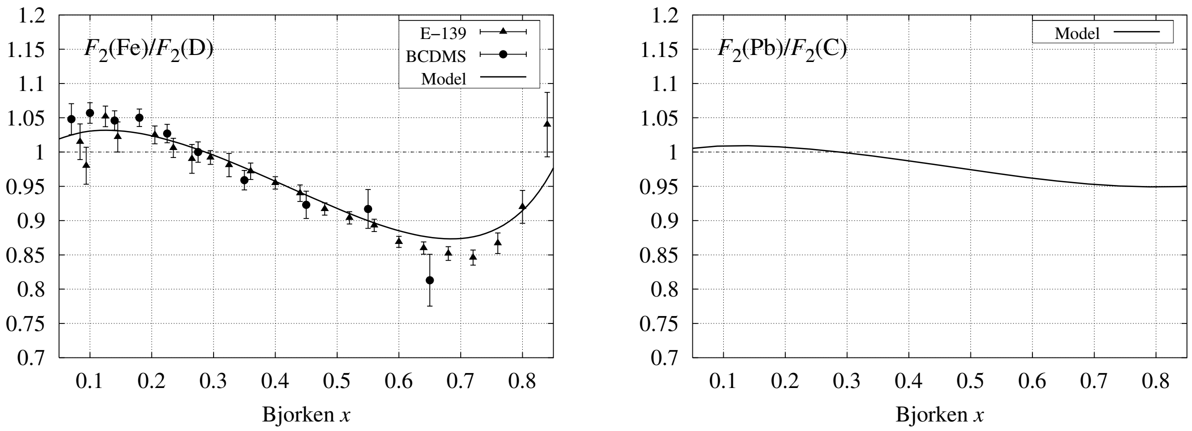

Figure 44: The ratio of iron to deuterium structure functions as measured by SLAC E-139 and CERN BCDMS collaborations in experiments with electron and muon beams (left panel). Also shown are the results of model calculation at fixed $Q^2 = 10\ \mathrm{GeV}^2$ which account for binding, Fermi-motion and off-shell effects in nuclear deep-inelastic scattering [111]. The ratio of lead and carbon structure functions calculated at fixed $Q^2 = 10\,\mathrm{GeV}^2$ within the same approach is presented in the right panel.

In fixed-target experiments events with small Bjorken x are correlated with low four-momentum transfer (Q^2). At low Q^2 the vector meson dominance model (VMD) appears to be a good tool to study nuclear corrections to structure functions [98, 112]. In VMD the structure functions are saturated by contributions from a few low-mass vector meson states. For the interactions driven by the electromagnetic current usually only the isovector ρ and the isoscalar ω and ϕ mesons are important at low $Q^2 < 1\ \mathrm{GeV}^2$ [112]. The structure functions in this model have strong Q^2 dependence. In the generalized versions of VMD, higher-mass states including the continuum have also been considered, making the model applicable at higher Q^2 [98, 112].

The VMD approach has also been applied to weak interactions [113]. The vector current, in close analogy with the electromagnetic current, is assumed to be saturated by ρ meson contribution at low Q^2. The axial-vector channel requires inclusion of contributions from the axial-vector meson a_1. There are still a number of interesting physics questions related to the analysis of the axial-vector channel for neutrino interactions.

It should be emphasized that neutrino scattering at low Q^2 is dominated by the axial current. Indeed, contributions to the structure functions (and cross-sections) from the vector current vanish as $Q^2 \to 0$ due to vector-current conservation. The axial current is not conserved and for this reason the longitudinal structure function F_L does not vanish at low Q^2. It was observed long ago by Adler that neutrino cross-sections at low Q^2 are dominated by the contribution from the divergence of the axial current [114]. The latter, because of PCAC, is saturated by the pion contribution, so low Q^2 neutrino cross-sections and structure functions are determined by pion cross-sections. For the longitudinal structure function at low Q^2 the Adler relation is

$$2xF_L^{\mathrm{PCAC}} = \frac{f_\pi^2}{\pi}\sigma_\pi(s, Q^2), \tag{6}$$

where $f_\pi = 0.93 m_\pi$ is the pion decay constant (m_π is the pion mass) and $\sigma_\pi(s, Q^2)$ the total pion cross-section at the center-of-mass energy $s = Q^2(1/x-1) + M^2$ for an off-shell pion with mass $\sqrt{Q^2}$. Equation (6) determines the dominant contribution to F_2 and neutrino cross-sections at small Q^2 for nucleon and nuclear targets.

It is important to realize that Eq. (6) is not a consequence of the pion dominance of the axial current, i.e. fluctuation of the axial current to a pion which interacts with the target [117]. Indeed, the single-pion fluctuation of the axial current gives a vanishing contribution to the neutrino cross-section. Instead, the axial current in neutrino interactions can produce heavy states such as the a_1 meson and $\rho\pi$ pair, which interact with the target. The overall contribution of all such states is described by the PCAC relation. The detailed mechanism of this phenomenon is not fully understood and MINERνA can provide new insights on physics driven by the axial current in neutrino interactions.

The strength of nuclear shadowing is controlled by mesonic cross-sections σ_v for the vector current. In the axial-vector channel the relevant quantity is the pion cross-section. To quantitatively understand nuclear effects, the multiple scattering effect on the cross-section is calculated using Glauber–Gribov multiple scattering theory [115, 116, 112, 117]. If l_f is small compared with the nuclear radius, as is the case for heavy nuclei, then multiple scattering effects are important. It should be emphasized that the multiple scattering correction is negative because destructive interference of the forward scattering amplitudes on the upstream nucleons causes *shadowing* of virtual hadron interactions on the back-face nucleons.

The onset of coherent nuclear effects can be estimated by comparing the coherence length of hadronic fluctuation L_c with the average distance between bound nucleons in the nucleus d. For hadronic fluctuation of the vector current L_c is similar to the fluctuation time τ from Eq. (5), where m is the mass of hadronic state in question. Coherent nuclear effects occur if the fluctuation time is large enough $\tau > d$. This condition requires high energy transfer ν and, as is clear from Eq. (5), the coherent region begins at lower energy for smaller masses m. Since $\tau < 2\nu/Q^2$ for any intermediate state, the region of coherent nuclear effects is limited to small x for any Q^2, $x < 1/Md$. Nuclear shadowing saturates if $L_c \gg R$, which happens at small x, and the condition $L_c \sim R$ defines the transition region with strong x dependence of the ratio $\delta\sigma_A/\sigma_N$.

For the axial-vector current, the fluctuation time τ is also given by Eq. (5). However, as argued in [117], the fluctuation and coherence lengths are not the same in this case. In particular, the coherence length is determined by the pion mass m_π in Eq. (5) because of the dominance of off-diagonal transitions like $a_1 N \to \pi N$ in nuclear interactions. Since the pion mass is much smaller than typical masses of intermediate hadronic states for the vector current (m_ρ, m_ω, etc.), the coherence length L_c of intermediate states of the axial current at low Q^2 will be much larger than L_c for the vector current. A direct consequence of this observation is early onset of nuclear shadowing in neutrino scattering at lower energy and Q^2 compared to charged-lepton scattering.

Figure 45 shows the calculated ratios of iron to nucleon and lead to carbon structure functions at two different Q^2 values as a function of x. We also compare the nuclear shadowing effect for muon and neutrino scattering. The basic reason for the earlier onset of nuclear shadowing in neutrino scattering and different behavior in the transition region is the difference in correlation lengths of hadronic fluctuations between the vector and axial-vector currents. This is also illustrated by the

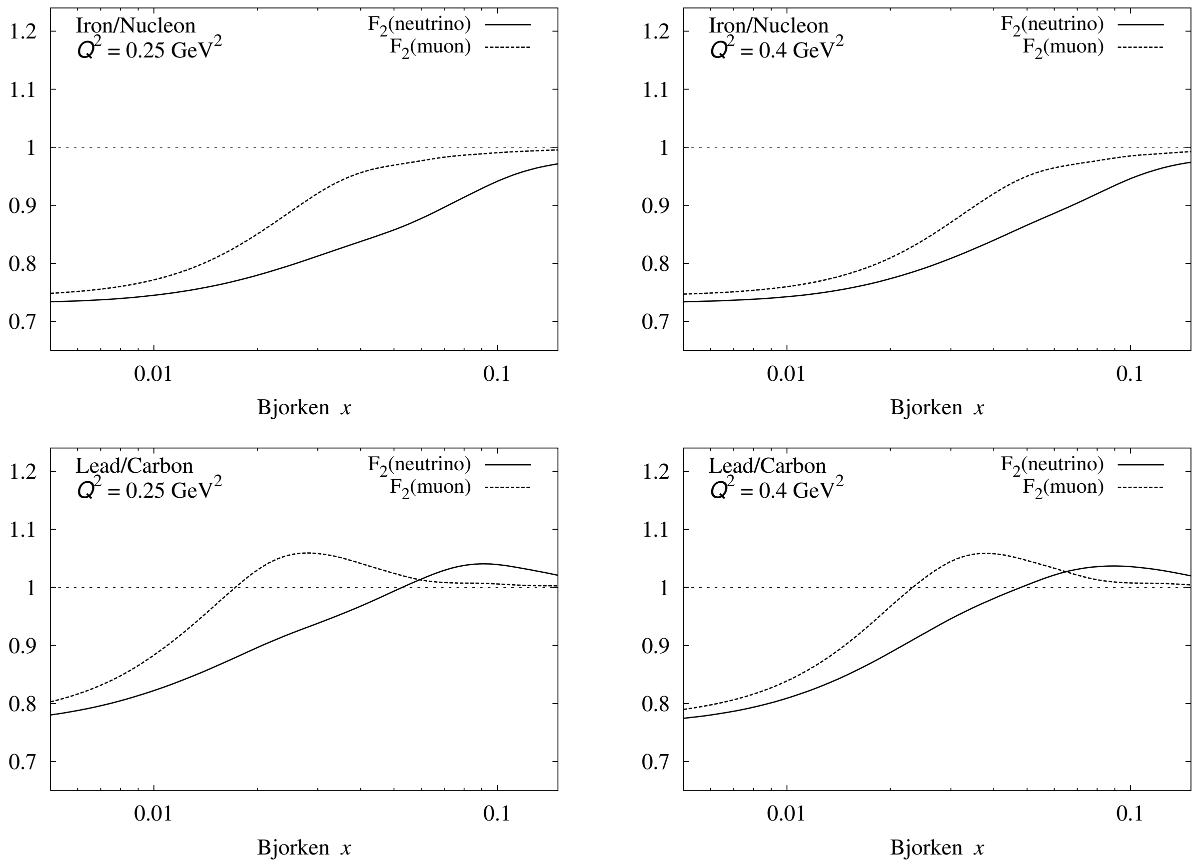

Figure 45: The ratio of iron to nucleon (upper row) and lead to carbon neutrino CC structure functions F_2^ν calculated at two different Q^2 within an approach based on PCAC and VMD (solid line). The dashed line shows similar ratios for the muon structure function F_2^μ.

observation that for a given Q^2 the cross-section suppression due to shadowing occurs for much lower energy transfer (ν) in neutrino interactions than for charged leptons.

The relative nuclear shadowing effect for the structure function xF_3 should be substantially different than that of F_2 [118]. This is because xF_3 describes the correlation between the vector and the axial-vector current in neutrino scattering. In terms of helicity cross-sections, xF_3 is given by the cross-section asymmetry between the left- and right-polarized states of the virtual W boson. It is known that such a difference of cross-sections is strongly affected by Glauber multiple scattering corrections in nuclei. This leads to enhanced nuclear shadowing of xF_3.

The resulting ratio of lead and carbon structure functions are shown in Figure 46. Unlike nuclear effects at large Bjorken x (Figure 44), there are substantial, structure-function dependent nuclear effects at small x. MINERνA can provide a unique tool to study these effects.

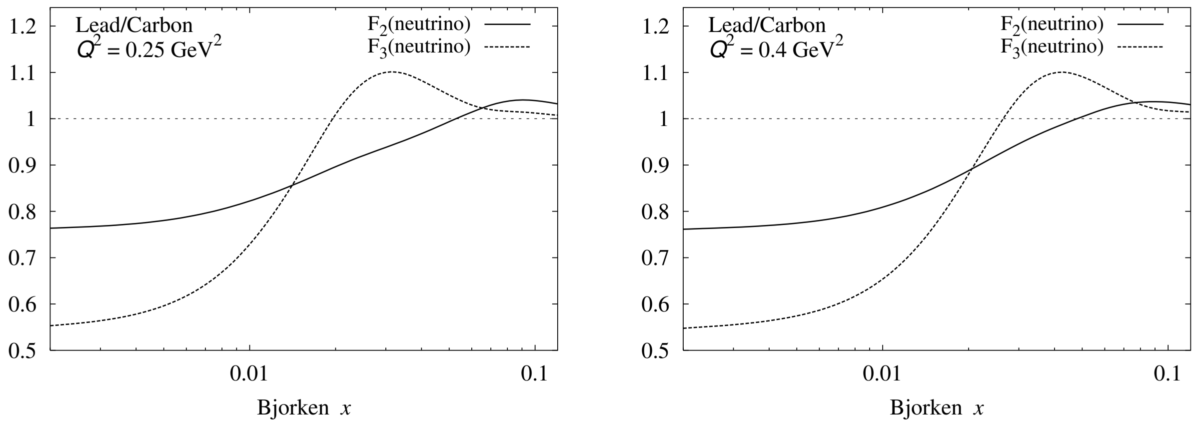

Figure 46: The ratio of lead to carbon neutrino charged-current structure functions F_2 calculated in an approach based on PCAC and VMD at two different Q^2 (solid line). The corresponding ratio for xF_3 is shown by the dashed curve.

2.9.5 Determination of $\sin^2\theta_W$

The rates of neutral-current (anti-)neutrino scattering are directly determined by $\sin^2\theta_W$. Therefore the measurement of NC/CC ratios of neutrino cross-sections provides a valuable tool for determination of $\sin^2\theta_W$. For an isoscalar target (e.g. the isoscalar combination of proton and neutron, or for deuterium) a relation between neutrino–antineutrino asymmetries in the NC and CC DIS cross-sections was derived by Paschos and Wolfenstein [119]

$$R^- = \frac{\sigma^{\nu}_{\rm NC} - \sigma^{\bar\nu}_{\rm NC}}{\sigma^{\nu}_{\rm CC} - \sigma^{\bar\nu}_{\rm CC}} = \frac{1}{2} - \sin^2\theta_W, \tag{7}$$

where θ_W is the weak mixing angle. A similar relation also holds for the NC/CC ratio of structure functions

$$F_3^{\rm NC}(x,Q^2)/F_3^{\rm CC}(x,Q^2) = 1 - 2\sin^2\theta_W, \tag{8}$$

where $F_3^{\rm CC}$ is the neutrino and antineutrino averaged structure function, $F_3^{\rm CC} = (F_3^{\nu} + F_3^{\bar\nu})$.

If only the contributions of light quarks are taken into account, the PW relationship is a direct result of isospin symmetry. This ensures that various strong interaction effects, including nuclear effects, cancel out in R^- for an isoscalar target, making Eq. (7) a powerful tool for measurement of the mixing angle in neutrino scattering.

The targets used in neutrino experiments are usually heavy nuclei, such as iron in the NuTeV experiment [120]. Heavy nuclei typically have an excess of neutrons over protons and therefore are not isoscalar targets. For a non-isoscalar target the relations (7) and (8) are violated by contributions from isovector components of nuclear parton distribution functions. Nuclear corrections to relations (7) and (8) were recently studied in [121, 122, 123], which showed that nuclear effects enter through non-isoscalar effects in the target. These studies suggest that nuclear corrections should be greatly reduced for isoscalar targets like carbon. MINERνA, with its lead, iron, and carbon targets, can directly measure the NC/CC ratio for several nuclear targets to explore these effects experimentally.

2.9.6 Modification of the nucleon form factors

The question of whether the structure of a bound nucleon differs from the structure of a free nucleon has long been of interest. The change in nuclear structure functions are known to be modified (the EMC effect) [125], the axial vector coupling constant is quenched in nuclear β decay [126], and studies of the electromagnetic form factors in ^{4}He at Jefferson Lab indicate that the ratio of the electric to magnetic form factor is about 10% smaller in ^{4}He than for the free proton [127].

Recent calculations by Tsushima *et al.* based on the quark-meson coupling model predict over a 10% reduction in the axial form factor in nuclei compared to the free nucleon [124], for Q^2 below 1.5 GeV^2, where the model is expected to be valid. The average density of nuclei increases quickly, so the effect is substantial even in a nucleus as light as ^{4}He. Because the axial form factor will be extracted from measurements on nuclei, it is essential that the any nuclear effect be determined.

Since we will not have a hydrogen or deuterium target in our initial run, it is not possible to make a direct study of nuclear effects on the form factors. Fortunately, the work of Tsushima has shown that the ratio of the form factors in lead to carbon, as shown in Fig. 47, is about 5% lower than unity for the axial form factor.

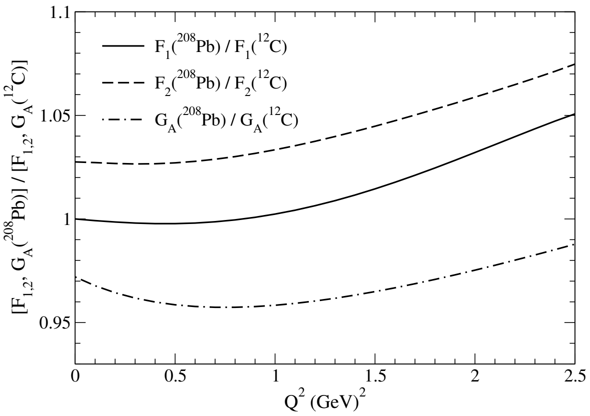

Figure 47: Predicted ratio of the axial form factor as measured in Pb to C, from Ref. [124].

The statistical uncertainties on this measurements will be small. In the Q^2 range of 0.75-1.25 GeV2, where the effect is largest, we expect about 330,000 events in Pb, 1.1 million events in C, and about 100,000 events in He. About 80,000 events will be in the pure C target, which will allow a comparison with comparable systematics to both iron and lead. The comparison with He will be extremely valuable in this case because of the ability to compare with the high precision JLab measurements of experiment E03-104 [128], which is measuring the ratio of the electric to magnetic form factor of the proton in ^{4}He near a Q^2 of 1 GeV2. The protons produced at Q^2 near

1 GeV2 will have an energy of about 500 MeV and are produced at an angle of about $45°$, which will allow coincident detection with the muon. In addition, complicating factors such as final state interactions are much smaller in helium than heavier nuclei, which will facilitate the comparison with measurements on hydrogen and deuterium when those do take place.

2.9.7 Final-state Interactions

Overview - Pion Absorption Interactions of few-GeV neutrinos with nuclei often produce resonances which decay to pions. Any attempt to reconstruct the incident neutrino energy based on the total observed energy must account for pion interactions within the target nucleus. Existing neutrino interaction Monte Carlos (such as INTRANUKE [19]) handle intra-nuclear pion interactions crudely and have generally not incorporated the latest knowledge of pion interactions.

The concern is mainly with pions in the 100–500 MeV range, where the interaction cross-sections are highest. In this range the pion/nucleon cross-section is dominated by the strong $\Delta(1232)$ resonance. The Δ is a fairly narrow (about 100 MeV) resonance, and the pion-nucleon cross-section reflects this, with a peak near 200 MeV pion energy which drops quickly above and below this. The pion/nucleus cross-section exhibits a similar behavior, with a less pronounced drop-off at higher energy. The charged-pion/nucleus cross-section has four important components in the intermediate energy range: elastic scattering (nucleus left in the ground state), inelastic scattering (nucleus left in an excited state or nucleon knocked out), true absorption (no pion in the final state), and single charge exchange (neutral pion in the final state).

Neutrino detectors are mainly iron (absorber), oxygen (water) and carbon (scintillator). The total pion–carbon cross-section is 600 mb, with elastic and inelastic cross-sections about 200 mb each, and absorption about 160 mb. The total pion-iron cross-section is about 1700 mb, with elastic and absorption about 600 mb each, and inelastic about 400 mb. Cross-sections for positive and negative pions are nearly the same because nuclei contain about the same number of protons and neutrons. These very large cross-sections mean that many pions will undergo some nuclear reaction within the target nucleus. In elastic and most inelastic reactions the scattered pion will not, because of its small mass, lose much energy. However, absorbed pions will lose all of their kinetic and mass energy. Of the four components of this intra-nuclear cross-section, the absorption probability within the interaction nucleus is roughly 30%. Figure 48 [137] shows absorption cross-sections for various nuclei as a function of pion energy.

Pion absorption cannot occur on a single nucleon due to energy and momentum conservation. The simplest absorption mechanism is on two nucleons. Because absorption appears to proceed mainly through $N - \Delta$ intermediate states, an isospin zero (np) pair is the primary candidate. Such an absorption for a positive pion would give two energetic protons whose kinetic energy nearly equaled the total pion energy. However, early studies of pion absorption found this was not the most probable mechanism.

In the 1990's two large solid angle detectors, the LAMPF BGO Ball and the PSI LADS detector, were built to study pion absorption. The somewhat surprising result from both experiments was that pion absorption is dominated by three body absorption [129]. For positive pions, the absorption on a pnn triplet (leading to a ppn final state) was the most common. This was observed even in ^{4}He. The absorption in heavier nuclei also appears to proceed mainly through a three-body mech-

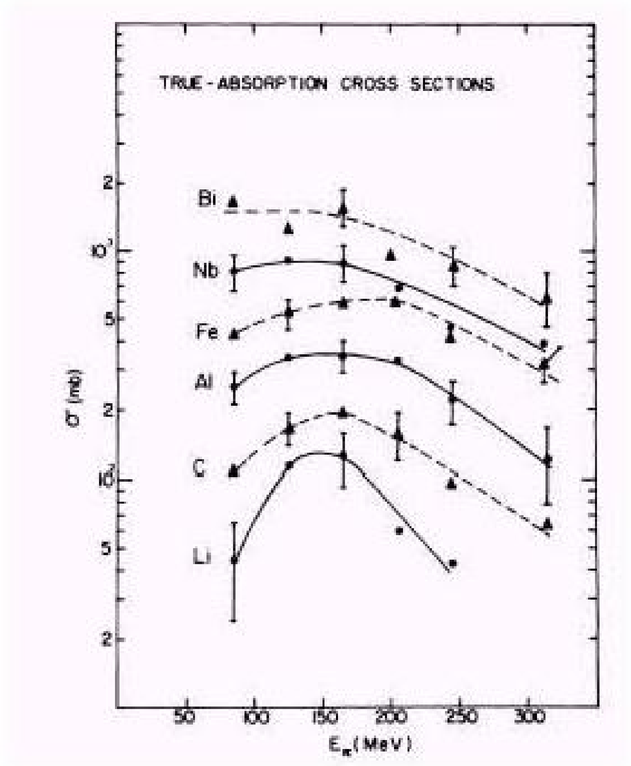

Figure 48: The absorption cross-sections for various nuclei as a function of pion energy.

anism, although increased initial state interactions (pion re-scattering) and final-state interactions (nucleon re-scattering) result in four to five nucleons being emitted. Typically the final-state contains more neutrons than protons. The absorption process, which is still not well understood theoretically, largely fills the available phase space thus giving a wide range of nucleon energies with little angular dependence. Because much of the energy is in neutrons, the visible energy is well below the total pion energy. Even in carbon more than half the energy is lost to unobserved particles, a fraction which increases with pion energy and with A [130].

The situation is worse for negative pions. Charge symmetry would indicate that the primary absorption should be on a ppn triplet leading to a pnn final state. In this case, most of the pion energy would be in neutrons, and hence effectively invisible. However, if the interaction vertex and one proton energy is known, and the angles of the outgoing neutrons are known, the total energy of the three nucleons can be estimated. Monte Carlo studies with realistic absorption models will be needed to determine the accuracies of such estimates.

Although neutral pions escaping the nucleus will decay, usually to two photons, the mean distance traveled before decay is a few nanometers, much greater than the size of the nucleus. Thus the absorption of neutral pions in the interaction nucleus must also be accounted for in any study of resonance production.

For MINERνA, studies with INTRANUKE have begun to explore the sensitivity to the probability of pion absorption in the interaction nucleus. Monte Carlo routines are being modified to treat pion absorption more realistically. Unfortunately there are essentially no measurements of pion absorption above 500 MeV. The fine spatial resolution and 4π acceptance of MINERνA will allow study of these interactions, especially in carbon.

Nuclear transparency A second nuclear interaction process which affects the observed energy is final state interaction of a nucleon in the struck nucleus. An outgoing nucleon has a substantial probability of interacting in the nucleus. These probabilities have been measured, most recently at Jefferson Lab, with some precision. The experiments used $(e, e'p)$ coincidence reactions, and the cross-section for finding the scattered electron in the quasi-elastic peak was compared to the cross-section for finding the coincident proton.

Unlike pion absorption, there is little available information on what happens to the scattered nucleon. Of course, most either scatter from a single nucleon quasi-elastically or produce a pion (for protons above 600 MeV). Improving Monte Carlo routines to model this interaction should allow us to better estimate the total final state energy. As for pion absorption, the good resolution, neutron detection capability, and full solid angle coverage of MINERνA should allow measurement of the actual final states and help constrain the Monte Carlo models.

2.9.8 Nuclear Effects in MINERνA

To study nuclear effects in MINERνA, helium, carbon, iron and lead targets will be installed upstream of the pure scintillator active detector. The planned configuration involves a total of 5 planes, with planes being mixtures of the various solid targets, as will be described in Section 3.3, and the ^{4}He target upstream. For the standard four-year run described in the proposal, MINERνA would collect about 2 million events on Fe and Pb, 500 thousand events in He, and 1 million events on C as well as 8.4 M events on the scintillator in the fiducial volume.

2.9.9 Measuring modified interaction probabilities

To measure this nuclear effect, the cross-section and resulting structure functions $F_2(x,Q^2)$ and $xF_3(x,Q^2)$ will be measured for the four target nuclei of He, C, Fe and Pb. For an A-dependent comparison in the DIS region ($W \geq 2$ GeV and $Q^2 \geq 1$ (GeV/c)^2) we would expect abour 450 K events in the Pb and Fe targets, 100 K events in He, and 220 K events from the pure carbon target. About 4% of the events are expected to be in the shadowing region ($x \leq 0.1$) and 7% of the events in the high-x region ($x \geq 0.5$).

To study the axial-vector nuclear shadowing effects expected at low Q^2 (non-DIS events) and high ν we need to compare lead to carbon to get a statistically significant result. The expected number of events with Q^2 less than 0.5 GeV^2 in lead is listed in Table 8, along with the statistical uncertainty on the ratio. The number of events in carbon will be much greater than in lead, because the carbon in the fiducial volume can be used. With these samples, MINERνA can measure the expected difference in lead to carbon shadowing for charged leptons compared to neutrinos to under three standard deviations (statistical).

Table 8: Estimated uncertainty on shadowing ratio for Pb to C.

ν GeV	Events in Pb	Uncertainty on Ratio
6-7	1700	2.7%
7-8	940	3.6%
8-9	720	4.1%
9-10	400	5.4%
10-12	560	4.7%
12-14	410	5.4%
14-20	320	6.1%

2.9.10 Measuring final state interactions

The NEUGEN Monte Carlo has been used to study MINERνA's sensitivity to nuclear effects. Nuclear effects in NEUGEN are controlled by the INTRANUKE processor. This processor incorporates a probability for pion absorption based on earlier electroproduction absorption studies and lower-statistics Ne/H_2 neutrino bubble chamber data. The observed phenomenon of hadron formation length, which increases the transparency and reduces final-state interactions, is incorporated. The particular model used for pion absorption, which is currently being improved and updated, assumes that absorption eliminates a pion and the resulting nucleons are themselves either absorbed in the nucleus or are too low in energy to be observed.

To determine MINERνA's sensitivity to the predictions of this model, the assumed probability for pion absorption in INTRANUKE has been increased by three standard deviations and then decreased by the same amount, which essentially turns off pion absorption completely. The multiplicity and a simple, crude estimate of the visible hadron energy have been examined under these extreme conditions. Other nuclear effects such as intra-nuclear scattering and hadron formation length have not been altered from their nominal values. Figure 49 shows both the true and reconstructed multiplicity distributions for carbon. Unfortunately, the available tracking software fails to reconstruct many of the tracks. We expect this problem to be resolved when full pattern recognition and a more robust tracker become available. For the present study, we will use the true multiplicities.

The next series of figures show the predicted "asymmetry" of the true multiplicity and visible hadron energy. The asymmetry is defined as the percentage change under these extreme assumptions. That is, the bin contents at plus three standard deviations minus the bin contents at minus three standard deviations, divided by bin contents at minus three standard deviations. Figure 50 shows the asymmetry of the true multiplicity for carbon and iron. There is a dramatic effect for carbon, as the high absorption value increases the number of 0-track events by over a factor of six compared to the no-absorption case. This is because the other nuclear effects, being unchanged, are minimal for carbon. Since intra-nuclear rescattering increases as $A^{1/3}$ and the suppression due to hadron formation length decreases as $A^{1/3}$, non-absorption nuclear effects are minimal for carbon and already sizable for lead. If this model is realistic, the carbon multiplicity distribution should be quite sensitive to the probability of absorption.

Final determination of the visible hadronic energy will be an involved process for this experiment.

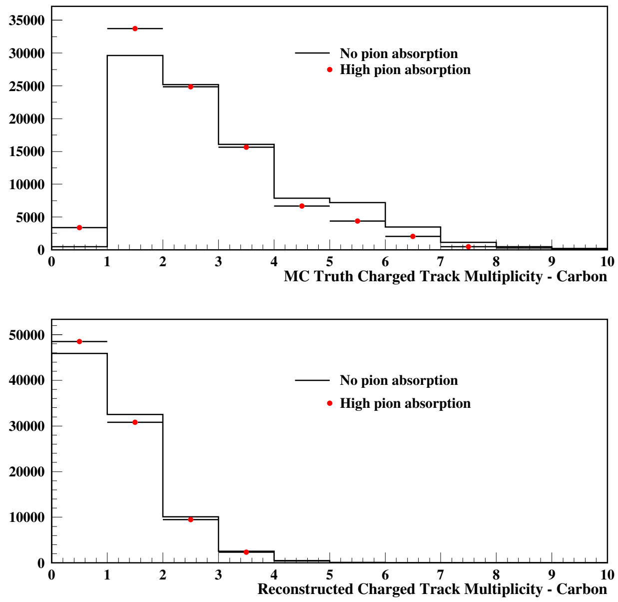

Figure 49: The shift in the true and reconstructed multiplicity distributions between the two values assumed for pion absorption on carbon described in the text.

For now, we use the most primitive estimate of this quantity, an uncorrected version derived from the total light output of the hadron shower. In the real data analysis this can be refined through measurements of stopping/decaying particles. With this crude estimate, the change in hadron energy for iron and lead are shown in Figure 51. There is a significant increase in the number of events with E_H less than 3 GeV and a corresponding decrease in the number of events with higher E_H, as one would expect. MINERνA will collect several times these statistics and should be able to measure this effect at even higher hadron energy.

Since the incoming neutrino energy is not known *a priori*, the measured **muon** kinematics will be tested as a basis for comparing the visible hadron shower across nuclear targets to determine whether a nuclear correction-factor can be parameterized as a function of the observed muon angle and energy. The muon is relatively free from nuclear dependent effects and serves well as an A-independent normalization. For example, the quantity:

$$Q' = E_\mu \sin^2(\theta/2) \tag{9}$$

is representative of the 4-momentum transfer to the nucleon or quark (divided by E_ν) and reflects the energy-momentum transferred to the hadronic vertex. The distribution of events in this quantity is peaked toward low Q'. with half the events below $Q' = 1.0$ GeV.

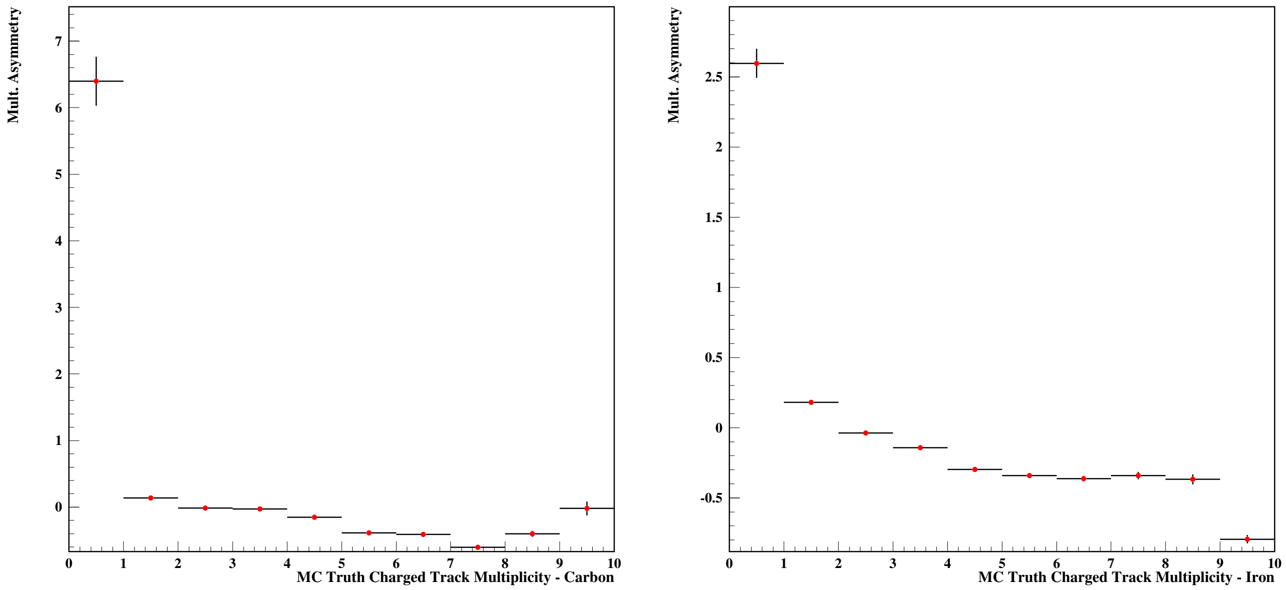

Figure 50: The fractional change in true multiplicity distributions between the two values assumed for pion absorption on carbon (left) and iron (right), as described in the text.

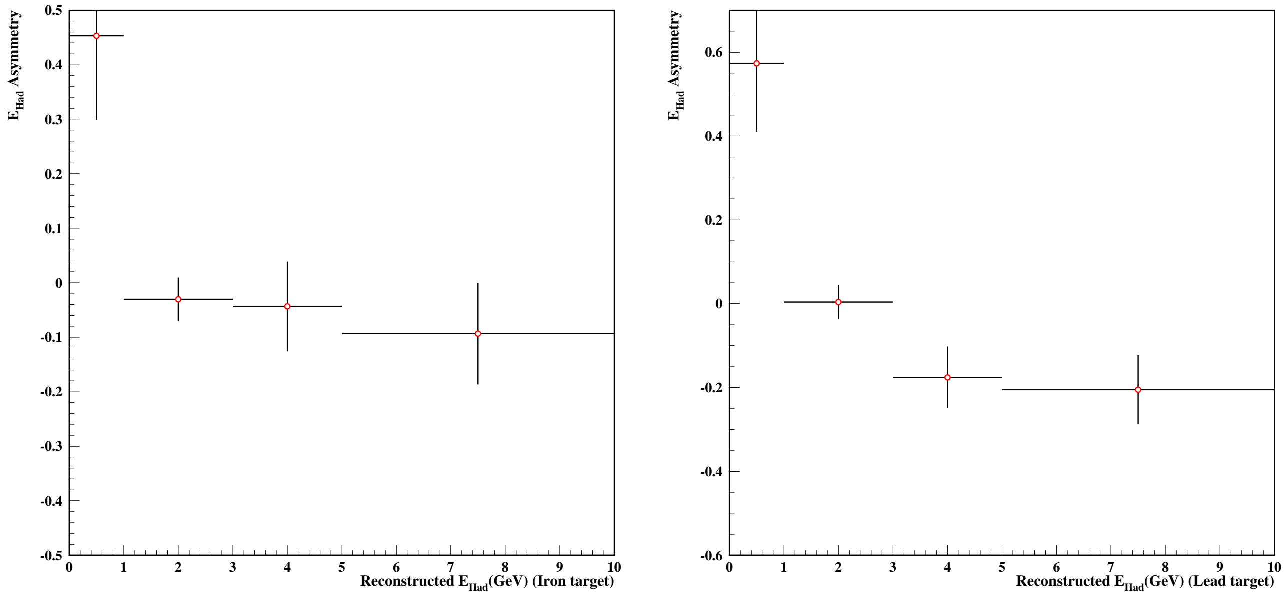

Figure 51: The fractional change in the visible hadron energy distributions between the two values of pion absorption on iron (left) and lead (right), as discussed in the text.

2.10 Neutrino Scattering and Long-Baseline Oscillation Experiments

The field of oscillation physics is about to make an enormous leap forward in statistical precision: first with MINOS in the coming year, and later in T2K and the proposed NOνA experiment. Unfortunately, our relatively poor understanding of neutrino interaction physics in the relevant energy range of these experiments gives rise to systematic uncertainties that could be as large as, or even larger than, their corresponding statistical uncertainties. We have studied the origin of some of these systematic effects, and how MINERνA's measurements can reduce them to well below the statistical level.

2.10.1 Introduction

Over the past five years the field of neutrino oscillations has moved from seeing decades-old anomalies in cosmic ray [142] and solar [143] neutrino data to powerful cross checks of these anomalies (SNO data [144] and angular distributions in atmospheric neutrino data [145]), and most recently to terrestrial confirmation of the oscillation hypothesis (Kamland [146] and K2K [147]). The next steps in this field are to move to precision measurement of the mass splittings and mixing angles already observed, and search for other non-zero off-diagonal elements in the neutrino mixing matrix.

New, extremely-intense beams have been or are being built to greatly increase the statistical reach and ultimate measurement precision for oscillation parameters. With these tremendous improvements in statistical accuracy, however, come new concerns about systematic uncertainties that until now have been a secondary concern. In particular, uncertainties in neutrino cross-sections and nuclear effects lead to systematic uncertainty in the extraction of mixing parameters. Although near detectors are a critical part of precision long-baseline oscillation measurements, they are often ill-suited to make the needed cross-section measurements because they tend to be similar to the coarse and massive far detectors. A near detector can at best constrain the convolution of the near flux, cross-section and detection efficiency. Uncertainties on all of these quantities must be incorporated into the analysis. The cross-section uncertainties we consider are only a subset of the whole, but when flux and efficiency are also taken into account, near-detector performance must be worse than we estimate here.

This chapter is divided into two sections. The first addresses uncertainties relevant for ν_μ disappearance experiments, whose aim is to precisely measure the mass splitting Δm^2_{23}, and the mixing angle which has already been determined to be large, θ_{23}. To achieve these goals the experiments must measure oscillation probabilities as a function of neutrino energy. Two important concerns here are uncertainties in charged-current inelastic processes, and the scale of nuclear effects. Both inelastic channels and the nuclear environment alter the relationship between the true and measured neutrino energies. The second section discusses searches for ν_e appearance, which if observed at accelerator energies would indicate a non-zero value of θ_{13} or more exotic new physics. Because the size of the signal is unknown, the final sample may be dominated by signal (charged-current) cross-sections, and/or background (neutral- and charged-current) processes. In both cases, the experiments of the past are inadequate to precisely predict the far detector event samples.

2.10.2 ν_μ Disappearance

Precision measurement of the mass splitting between two neutrino eigenstates requires analysis of the oscillation probability as a function of neutrino energy (E_ν) divided by baseline (L). The muon neutrino disappearance probability (in the standard 3-generation oscillation parameterization [148]) is

$$P(\nu_\mu \to \nu_\mu) = 1 - \cos^4\theta_{13}\sin^2 2\theta_{23}\sin^2\left(\frac{1.27\Delta m^2_{23}(eV^2)L(km)}{E_\nu(GeV)}\right) - ... \tag{10}$$

where the additional terms are $\mathcal{O}(\sin^2 2\theta_{13})$ or smaller. Currently Δm^2_{23} is known to within a factor of two and $\cos^4\theta_{13}\sin^2 2\theta_{23}$ must be larger than 0.9, at 90% confidence level [149]. Since $\sin^2 2\theta_{13}$ has been constrained below 0.1 by the CHOOZ reactor experiment[150], this means $\sin^2 2\theta_{23}$ itself is very close to 1. The fact that θ_{23} is close to $45°$ has been cited as a hint of the underlying symmetry that generates neutrino mass and mixing. Precise measurement of this angle is important because the level at which the mixing deviates from maximal may again give hints about the mechanisms responsible for the breaking that symmetry [151].

More precise measurements of Δm^2_{23} are required to extract mixing angles from eventual ν_e appearance experiments. The challenge of Δm^2_{23} lies in measuring the true neutrino energy in both near and far detectors. Even if the two detectors have an identical design, any uncertainty in the "neutrino energy scale" of the ν_μ charged-current signal translates directly into an uncertainty in the extracted value of Δm^2_{23}.

There are two different ways of measuring neutrino energies: kinematic or calorimetric reconstruction. We discuss both techniques here, and then explain how uncertainties in neutrino interactions lead to energy scale uncertainties and ultimately Δm^2_{23} uncertainties.

The first experiment to provide a precision measurement of Δm^2_{23} will be MINOS [152], which has finished its first year of beam data and presented preliminary results. MINOS uses both far and near detectors, which are magnetized steel-scintillator calorimeters with approximately 6 cm total longitudinal segmentation. The transverse segmentation of the 1 cm thick scintillator planes is 4 cm. MINOS uses Fermilab's NuMI beam, with a baseline of 735 km, which can provide a variety of broad-band neutrino spectra. MINOS does most of its running in the lowest-energy configuration where the peak neutrino energy is about 3.5 GeV, but a long tail extends into tens of GeV.

T2K will use Super-Kamiokande, a water Cherenkov detector, and focus on single-ring muon-like events, for which the neutrino energy is reconstructed kinematically under the hypothesis of two-body scattering. T2K will use a narrow band off-axis neutrino beam from J-PARC in Tokai, whose peak flux is close to 700 MeV, and which originates some 295 km away [154]. The design of the near detectors has not been finalized, but should include a fine-grained tracker and a water Cherenkov detector.

The proposed NOνA experiment will use a calorimetric detector to improve measurement of Δm^2_{23}. Because NOνA is optimized for ν_e appearance rather than ν_μ disappearance, it will use near and far calorimeters made of scintillator planes interspersed with particle board or other scintillator planes. The longitudinal segmentation should be about 1/3 to 1/6 of a radiation length, and the transverse segmentation of the scintillator will be about 4 cm[153]. NOνA will also use the NuMI beam, but will place its detectors 12–14 mrad off the beam axis, to receive a narrow-band neutrino spectrum. NOνA with a baseline of 810 km, will run with a peak neutrino energy of about 2 GeV.

Kinematic neutrino energy recontruction

Kinematic reconstruction assumes that a given event was produced by a particular process (for example, quasi-elastic scattering) and determines the neutrino energy based on a sufficiently constraining subset of the final-state particles under that hypothesis.

This technique is well-suited to water Cherenkov detectors, which perform best for single-ring topologies. In Super-Kamiokande detector, for example, the ν_μ charged-current signal consists of single-ring, muon-like events, which are primarily quasi-elastic interactions. The energy of the incoming neutrino in that case can be determined using only the outgoing muon momentum (p_μ) and direction (θ_μ):

$$E_\nu = \frac{m_N E\mu - m_\mu^2/2}{m_N - E_\mu + p_\mu \cos\theta_\mu} \tag{11}$$

Since the absolute energy scale for muons can be fixed to within 2–3% by a variety of calibration techniques [131], and the reconstruction algorithms measure ring directions extremely well, it seems plausible that the neutrino energy scale could be determined with comparable precision. However, not all events producing a single muon-like ring are quasi-elastic interactions. Resonant excitation, and even deep-inelastic scattering, where pions are absorbed in the oxygen nucleus or emerge below Cherenkov threshold can lead to the same topology. Such events will have a reconstructed energy well below the true neutrino energy, because the recoiling hadronic mass is larger than assumed. The effect of this inelastic background could be corrected, if the energy-dependent ratio of quasi-elastic and resonant cross-sections were perfectly known, but since it is not, an uncertainty in the effective neutrino energy scale of the detector results.

Because the ν_μ disappearance probability is nearly 100% for T2K, the relative abundance of quasi-elastic and inelastic events will be very different at Super–K than for the unoscillated beam sampled by a near detector.

Precision measurement of the differential cross-sections for single- and multi-pion production, as a function of neutrino energy, will reduce uncertainties in the subtraction of inelastic background, improving T2K's neutrino energy resolution, and ultimately the precision of its oscillation measurements. Since the event samples are so different between near and far detectors, and because water Cherenkov technology cannot entirely eliminate the inelastic background, additional measurements with fine-grained detectors are required. Ideally, these measurements would include not only exclusive inelastic reactions, but also quasi-elastic scattering, with a well-modeled efficiency relative to the inelastic channels. Because the reconstructed energy for inelastic background is lower than the true neutrino energy (the background "feeds down"), it is essential to measure these cross-sections both at and above the T2K beam energy. Chapters 2.2 and 2.3 discuss MINERνA's measurements of quasi-elastic and resonant cross-sections.

Calorimetric neutrino energy reconstruction

At neutrino energies above 1 GeV, calorimetric energy reconstruction is more efficient than kinematic reconstruction. In a low-threshold calorimetric device, the reconstructed or visible neutrino energy is simply the sum of all observed secondary particles' energies. For a ν_μ charged-current interaction, the muon energy can be determined by measuring its momentum by either range or curvature (if the calorimeter is magnetized), and the remaining activity can be summed to estimate the hadron energy. Scintillating calorimeters have a lower charged-pion detection threshold than Cherenkov detectors, so more of the total kinetic energy is visible for multi-pion interactions, which dominate the cross-section above a few GeV. As a result, neutrino energy reconstruction is less susceptible to bias from inelastic reactions than Cherenkov detectors.

For MINOS, the absolute energy scale for muons is fixed by knowledge of the steek plate thickness and muon energy loss processes. The thickness of each plate has been measured to better than 0.1% and they vary with an RMS of 0.4% [132]. In a muon test beam at CERN a 2% absolute scale calibration was achieved [133]. The hadronic and electromagnetic energy scales have been calibrated with test beams on a prototype detector at CERN, and have been measured relative to the muon scale within better than 5% [134, 135]. It is still necessary to translate from the raw response to pions and muons to the energy of interacting neutrinos, however.

At neutrino energies of a few GeV and below, three effects become significant in translation between visible and and neutrino energies. Uncertainties in these effects must be understood and included in any precise measurement of Δm^2_{23}. One effect, independent of the target nucleus, is the rest masses of the secondary charged pions. Since MINOS lacks the granularity to measure the multiplicity of final state particles, a hadron-energy dependent multiplicity distribution must be assumed. The second and third effects are due to secondary particle scattering or complete absorption in the nucleus. All three effects reduce the visible hadronic energy, which in turn lowers the reconstructed neutrino energy. Importance of these effects grows larger as the parent neutrino energy decreases,[96] due to strong enhancement of the pion–nucleon cross-section near the $\Delta(1232)$ resonace [137].

To quantify the magnitude of nuclear effects on measurement of Δm^2_{23} in a MINOS-like detector, a simple detector simulation was combined with the NEUGEN event generator [138] and NuMI fluxes at 735 km [139]. In this simulation the visible energy is simply defined as the sum of kinetic energies for all charged final-state particles, plus the total energy for the neutral pions, and photons, which are assumed to deposit all their energy as electromagnetic showers.

Figure 52 shows the variation of the ratio of visible to total neutrino energy for changes in nuclear absorption and scattering separately. In the plot on the left the target is assumed to be steel, and the parameter controlling pion absorption is set to zero or doubled. In the plot on the right all pion absorption is turned off, and the differences that remain are due to rescattering effects in steel, carbon, and lead. These rescattering effects have not been measured with neutrinos on high Z nuclei, so the rescattering variation can be considered as an error on extrapolation from the low-Z measurements that do exist. Because the ν_μ disappearance probability should be large, the far and near detector energy spectra will be very different, and these effects will only partially cancel in a ratio between near and far detectors. The extent to which they do not cancel represents a systematic error on Δm^2_{23}.

If these pion absorption Z extrapolation effects are treated as the total systematic uncertainty due to nuclear effects, we can compare it to the expected MINOS statistical error. In this more complete

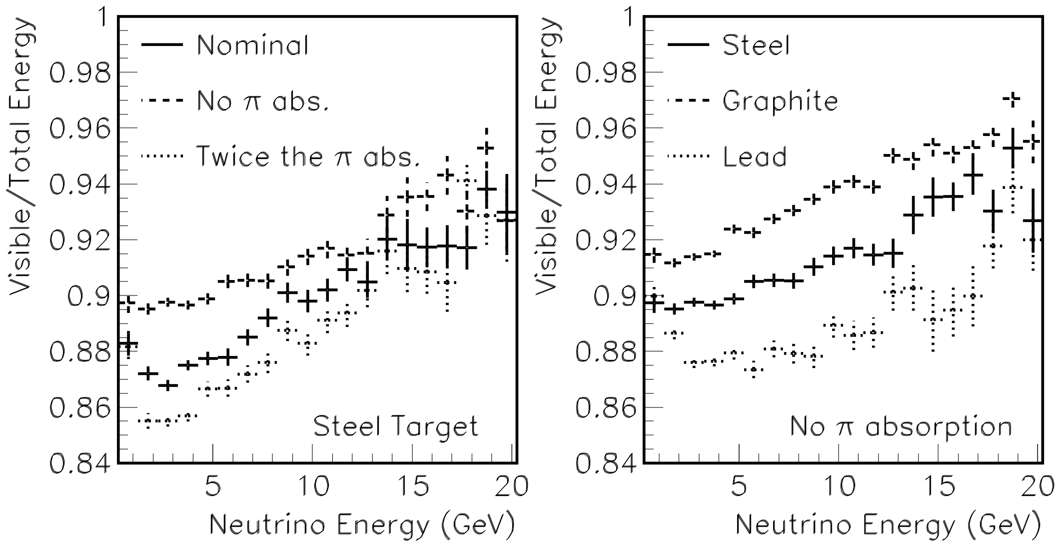

Figure 52: Ratio of visible (reconstructed) to true neutrino energy for several different models of nuclear effects. The left plot shows the ratio for steel (solid) with the nominal pion absorption, as well as the same ratio for the pion absorption turned off or doubled from what is expected. The right plot shows the differences the ratio for three different target nuclei, where pion absorption is turned off to isolate the effects of pion rescattering.

analysis, the detector acceptance must also be taken into account. One cut which could reduce the error due to nuclear effects significantly would be to require a minimum muon energy. The less visible energy attributable to hadrons, the smaller the relative effect of nuclear uncertainties on the total neutrino energy measurement. Requiring the muon to take up most of the energy in an event lowers efficiency, of course, and reduces the statistical power of the far-detector data sample. Here a minimum muon energy of 0.5 GeV was required, in an attempt to approximate the acceptance of a real analysis.

If the uncertainties from nuclear effects correspond to the differences in Figure 52, then for a 0.5 GeV muon momentum cut they induce a Δm^2_{23} error only slightly smaller than the statistical error expected by MINOS with 9×10^{20} protons on target (POT) (see Figure 53). This figure includes an estimate for the total systematic error that was made before the current MINOS result, where they report an additional large systematic due to the neutral current background [155]. We are currently reviewing how the NC error profile might be reduced with additional effort by MINOS and/or input from MINERνA.

MINERνA's contribution to reducing the rescattering errors would be very significant if the other large NC systematic error is reduced. It would have the same effect on the total error as obtaining 40% more protons on target. This is illustrated in the bottom plot in Figure 53, which shows the increased *effective* protons on target as a function of the true value for Δm^2. For a mass splitting near the MINOS best fit value of 2.7×10^{-3} eV^2, this is nearly 4×10^{20} POT, roughly an extra year of beam operation.

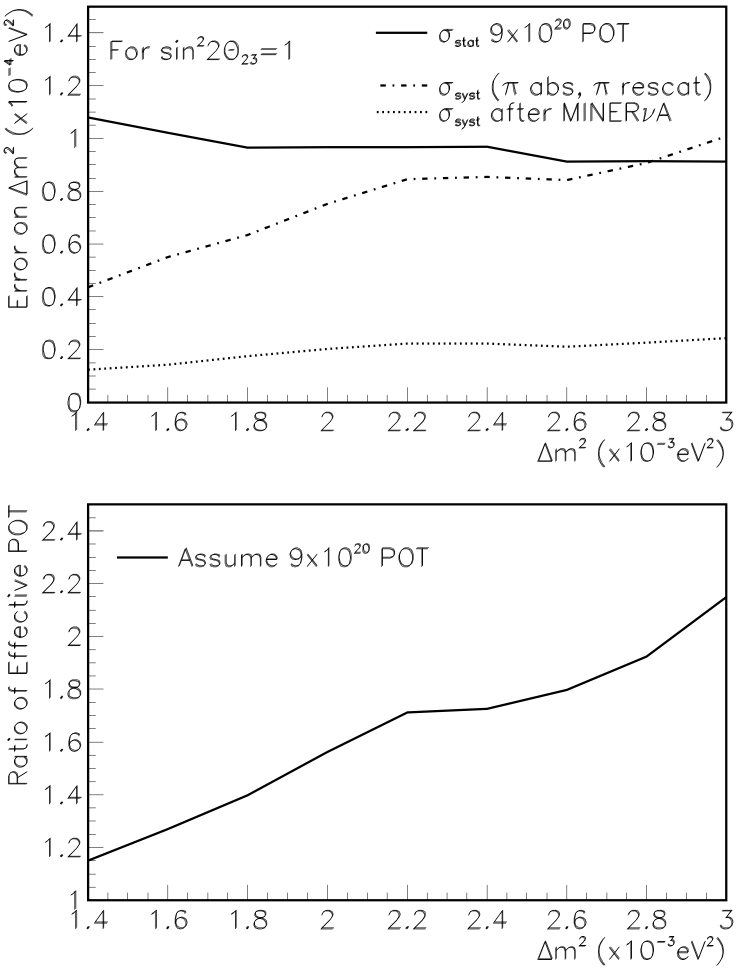

Figure 53: Top plot: projected size of errors on Δm^2 when MINOS has 9×10^{20} POT. Solid line is the expected statistical error. The other lines are estimates for the total systematic error before and after the reduction of the pion rescattering and absorption errors. Bottom plot, for the range of mass splittings near the MINOS value of 2.7×10^{-3} eV^2, this has the same effect on the total error as 40% more protons on target. These estimates were made before the current MINOS result, which reports an additional large systematic due to the neutral current background.

As described in Chapter 2.9, MINERνA will measure neutrino interactions on steel, carbon, and lead and collect between 400k and 2.5M events on each target (in addition to events on plastic CH) over a four year run. This represents an enormous improvement in both the statistics and the range of target nuclei over previous experiments, and would improve our level of understanding of nuclear effects dramatically. This is true with only a single year of operation, which would be the one relevant for the result from the full MINOS data. With sufficient data on several different nuclei, the error on Z extrapolation would be reduced since the nuclear models would be better constrained. The remaining uncertainties on the detector energy scale are likely due to uncertainties in pion rescattering in steel. Systematic uncertainty in Δm^2_{23} with this new data in hand would be small compared to the statistical error.

2.10.3 ν_e Appearance

Signal and backgrounds

The goal of the next generation of neutrino oscillation experiments is to determine whether the last unmeasured neutrino mixing matrix element, (called $|U_{e3}|$ or $\sin\theta_{13}$) is non-zero. If θ_{13} is in fact non-zero future experiments could measure the neutrino mass hierarchy search for CP violation in the lepton sector. T2K and NOνAwill probe this matrix element by measuring the $\nu_\mu \to \nu_e$ oscillation probability at a "frequency" corresponding to Δm^2_{23}. The oscillation probability for $\nu_\mu \to \nu_e$ in vacuum can be expressed [148]

$$P(\nu_\mu \to \nu_e) = \sin^2\theta_{23}\sin^2 2\theta_{13}\sin^2\left(\frac{1.27\Delta m^2_{23}(eV^2)L(km)}{E_\nu(GeV)}\right) + ... \tag{12}$$

where the additional terms not shown are due to small effects from the solar mass splitting, Δm^2_{12}.

Identifying ν_e appearance in a ν_μ beam is quite challenging for several reasons. From the CHOOZ reactor neutrino limit on $\sin^2 2\theta_{13}$ [150] the appearance probability must be less than about 5% at 90% confidence level. Also, the beams contain an intrinsic ν_e contamination as large as a few per cent. Finally, neutral-current and high-y charged-current ν_μ interactions can produce energetic π^0, leading to electromagnetic showers that may resemble a ν_e charged-current event.

T2K and NOνA will reduce some of these backgrounds significantly below the level in current long baseline experiments by using detectors optimized for electron appearance, and by placing those detectors off the beam axis. In two-body decay of the charged pion, the neutrino energy spectrum at small angles from the beam axis are narrower than the on-axis spectrum. Also, at these small angles the peak energy itself is reduced. The narrowest neutrino energy spectrum occurs when the far detector is placed at an angle corresponding to 90° in the pion center of mass. In this configuration, the ν_e flux comes from the three-body muon decays, so the intrinsic ν_e flux at lower energies does not increase at higher angles like the ν_μ flux does. Also, the neutral-current background is always a steeply falling function of visible energy because the outgoing neutrino always takes some fraction of the incoming neutrino's energy.

With this "off-axis" strategy, T2K and NOνA still expect some background after all analysis cuts, even in the absence of $\nu_\mu \to \nu_e$ oscillation. Measurement of the $\nu_\mu \to \nu_e$ probability requires accurate knowledge of this remaining background, and the cross-section and detection efficiencies for the ν_e signal.

Cross-section uncertainties with a near detector

Both T2K and NOνA will use near-detector measurements to predict the expected backgrounds at the far detector. In T2K, an on-axis near detector 280 m from the proton target will measure the spectrum and transverse beam profile, and at least one other off-axis detector will be focused on cross-section measurements. There are also plans to build a water Cherenkov detector 2 km from the proton target, but even then near- and far-detector efficiencies may not be identical. For NOνA, the near detector will be very similar in design to the far detector, and can be placed in a wide range of angles with respect to the beam. By making the near detector similar, NOνA hopes to minimize uncertainties in the detector response and efficiency. However, because the near detector will be as coarse as the far, it is not optimized for cross-section measurements.

To see how any uncertainties (cross-section, detector acceptance, or flux) will arise in the far detector prediction based on the near detector data, it is useful to think about how the event samples are likely to change between near and far. At a near detector, the flux of muon neutrinos will have a very strong peak at a particular energy, while at the far detector that peak will (by design) have oscillated to mostly ν_τ. At these energies, ν_τ cannot produce charged-current interactions, only neutral-current. Neutral-current samples are likely to be similar from near to far, provided the near detector is at a similar off-axis angle. Electron neutrino events at the peak are primarily from muon decays in the beam, which occur on average substantially farther downstream than the pion decays. Therefore, the extrapolation from the near to far detector tends to be different for all three event samples. If the relative population of the background sample among different categories cannot be predicted accurately (due to cross-section, detector or flux uncertainties), the far detector extrapolation will be wrong.

The MINOS and NOνA near detectors will both provide important constraints on neutrinos coming from NuMI. However, neither will be able to measure the charged- and neutral-current near detector backgrounds precisely. A finer-grained detector with improved timing resolution will be extremely useful to distinguish these two contributions which change so dramatically between near and far detectors.

A quantitative case study of how cross-section uncertainties may not completely cancel between near and far detectors, was performed using the simulation for an early design [140] of NOνA. Although NOνA's final design will be different, the fundamental arguments remain unchanged: the mixture of contributing cross-sections at the far detector cannot, even in principle, be identical to the mixture at the near detector.

		QE	RES	COH	DIS
		cross-section Uncertainty			
		20%	40%	100%	20%
Process	Statistics	Composition after all cuts in far detector			
Signal ν_e	175 ($\sin^2 2\theta_{13} = 0.1$)	55%	35%	n/I	10%
NC	15.4	0	50%	20%	30%
$\nu_\mu CC$	3.6	0	65%	n/I	35%
Beam ν_e	19.1	50%	40%	n/I	10%

Table 9: Rate of signal and background processes in an earlier 50 kton NOνA far detector design, assuming $\Delta m^2_{23} = 2.5 \times 10^{-3}$ eV^2. Also listed are the present cross-section uncertainties for those processes. Charged-current coherent production was not included since it is should be unimportant compared to other charged-current processes.

The signal and background samples for the nominal 5 year run are listed in Table 9 along with the fractional contribution of each process to events of a given type passing all cuts, and the relative cross-section uncertainties [141]. Without a near detector, the total error on the background prediction from cross-section uncertainties, in the absence of ν_μ oscillation, is 16%, which is equal to the statistical error. For oscillation at the level indicated in the table, the statistical error on the probability would be 8%, while the errors from cross-section uncertainties alone are 31% .

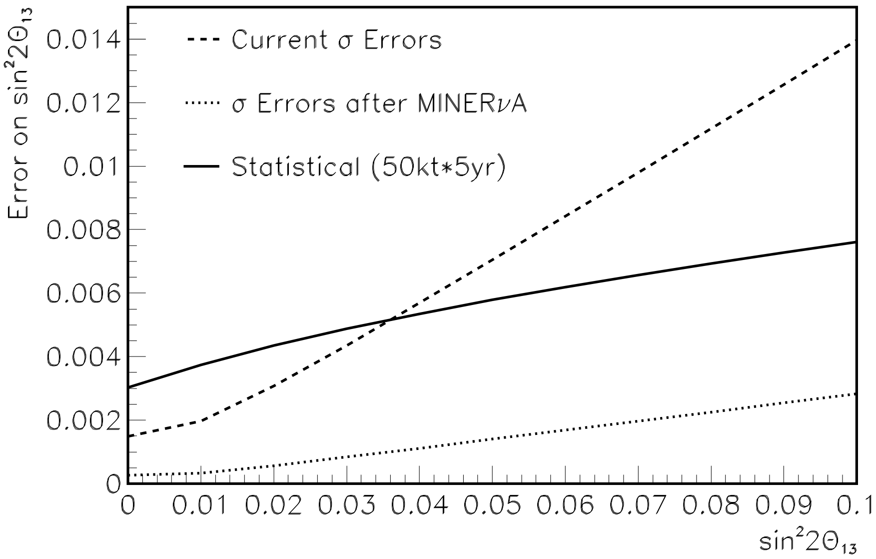

Figure 54: Statistical error, present cross-section systematic error, and post-MINERνA cross-section systematic error in NOνA measurement of $\sin^2 2\theta_{13}$, as a function of $\sin^2 2\theta_{13}$.

Figure 54 shows the projected error on $\sin^2 2\theta_{13}$ as a function of $\sin^2 2\theta_{13}$ itself, for present cross-section uncertainties. Should NOνA find a large signal, even in its first phase the measurement will be systematics limited with existing knowledge of relevant cross-sections. Chapters 2.2, 2.3 and 2.5 explain how different channels will be isolated, and give the size of the expected samples. MINERνA should be able to reduce cross-section uncertainties for NOνA to about 5% for all charged- and neutral-current deep-inelastic scattering processes, 10% for neutral-current resonant processes, and 20% for neutral-current coherent π^0 processes. If these uncertainties were achieved, then systematic errors due to cross-section uncertainties would be well below the statistical errors, as shown in Figure 54.

2.10.4 Conclusions

It is clear from even these preliminary studies that MINERνA will play an important and potentially decisive role in helping current and future precision oscillation experiments reach their ultimate sensitivity. To get the most precise values of Δm^2_{23} (which is eventually necessary to extract mixing angles and the CP-violating phase) our field must better understand and quantify the processes that occur between interaction of an incoming neutrino and measurement of the outgoing particles in a detector. Although the issues are different depending on whether the detector is a water Cherenkov or calorimetric devices, in both cases more information is needed. Extracting mixing parameters like θ_{13} and ultimately the neutrino mass hierarchy and CP-violation requires much better understanding of resonant cross-sections. Even setting limits on these parameters will require better measurements of neutral-current processes. The cost of curing our present ignorance pales in comparison to the possibility that an entire generation of oscillation experiments might miss out on an exciting discovery or end in a morass of inconclusive, ambiguous, contradictory or even wrong results because we have failed to invest the effort needed to understand the most basic interactions of the particle whose exotic behavior they were built to study. Precision measurement of exclusive cross-sections and nuclear effects will finally put a field making tremendous strides in luminosity and statistical power on a sound systematic foundation.

Part III
The MINERνA Project

3 The MINERνA Detector

Chapters 3 and 4 describe, respectively, the detector components and the assembly and installation of these components into the MINERνA detector. This chapter will begin with an overview of the MINERνA detector, and will then describe the active detector elements which are constructed from scintillator-fiber assemblies (Section 3.2, read-out by multi-anode photomultiplier tubes (Section 3.3 and digitized by custom electronics and a data acquisition system (Section 3.5). Also described here are the absorbers used as calorimetric absorbers and nuclear targets in MINERνA (Section 3.4). Finally, we conclude with a discussion of results from the prototype vertical slice test (VST) in Section 3.6.

As a note to the reader, reference to the MINERνA project structure is made frequently in Chapters 3 and 4 since it is the construction of these components that the MINERνA project seeks to complete. For the reader's reference, we note that a listing of the gross work-breakdown structure (WBS) of the MINERνA project can be found at the start of Chapter 8.

3.1 Detector Overview

For MINERνA to meet its physics goals (Section 2.1), the detector must break new ground in the design of high-rate neutrino experiments. With final states as varied as high-multiplicity deep-inelastic reactions, coherent single-π^0 production and quasi-elastic neutrino scattering, the detector is a hybrid of a fully active fine-grained detector and a traditional calorimeter.

At the core of the MINERνA design is a solid scintillator-strip detector, similar in principle to the recently commissioned K2K SciBar [5]. The plastic inner detector serves as the primary fiducial volume, where precise tracking, low density of material and fine sampling ensures that some of the most difficult measurements can be performed. These include multiplicity counting in deep-inelastic scattering, tracking of photons, detection of recoil protons in low-Q^2 quasi-elastic events, and particle identification by dE/dx. A side view of the detector is shown in Figure 55.

The scintillator detector cannot contain events due to its low density and low Z, and therefore, the MINERνA design surrounds the scintillator fiducial volume with sampling detectors. At the low energies needed to study cross-sections of interest to neutrino-oscillation searches, many of the events contain energetic sideways-going particles, so these sampling detectors extend to the sides of the detector. Finally, energetic forward muons will enter the MINOS near detector, where their momentum can be measured magnetically and/or by range.

Except for the upstream veto, the entire MINERνA detector is segmented transversely into an inner detector with planes of solid strips and an outer picture frame (OD)[4]. For construction and handling convenience, a single plane of MINERνA incorporates both the inner detector and OD, which serves as the support structure. Two planes of scintillator are mounted in one frame, called a "module", as illustrated in Figure 57. There are three distinct orientations of strips in the inner detector, offset by 60°, and labeled X, U, and V. The different strip orientations enable a three-dimensional reconstruction of tracks, and the 60° offset makes the hexagon a natural transverse

[4]The OD detector steel and portions of the support geometry were so that the OD steel may be magnetized as a future upgrade to MINERνA. This would improve focusing of sideways muons into MINOS or help them to range out in the OD; however, this option is not part of the baseline design.

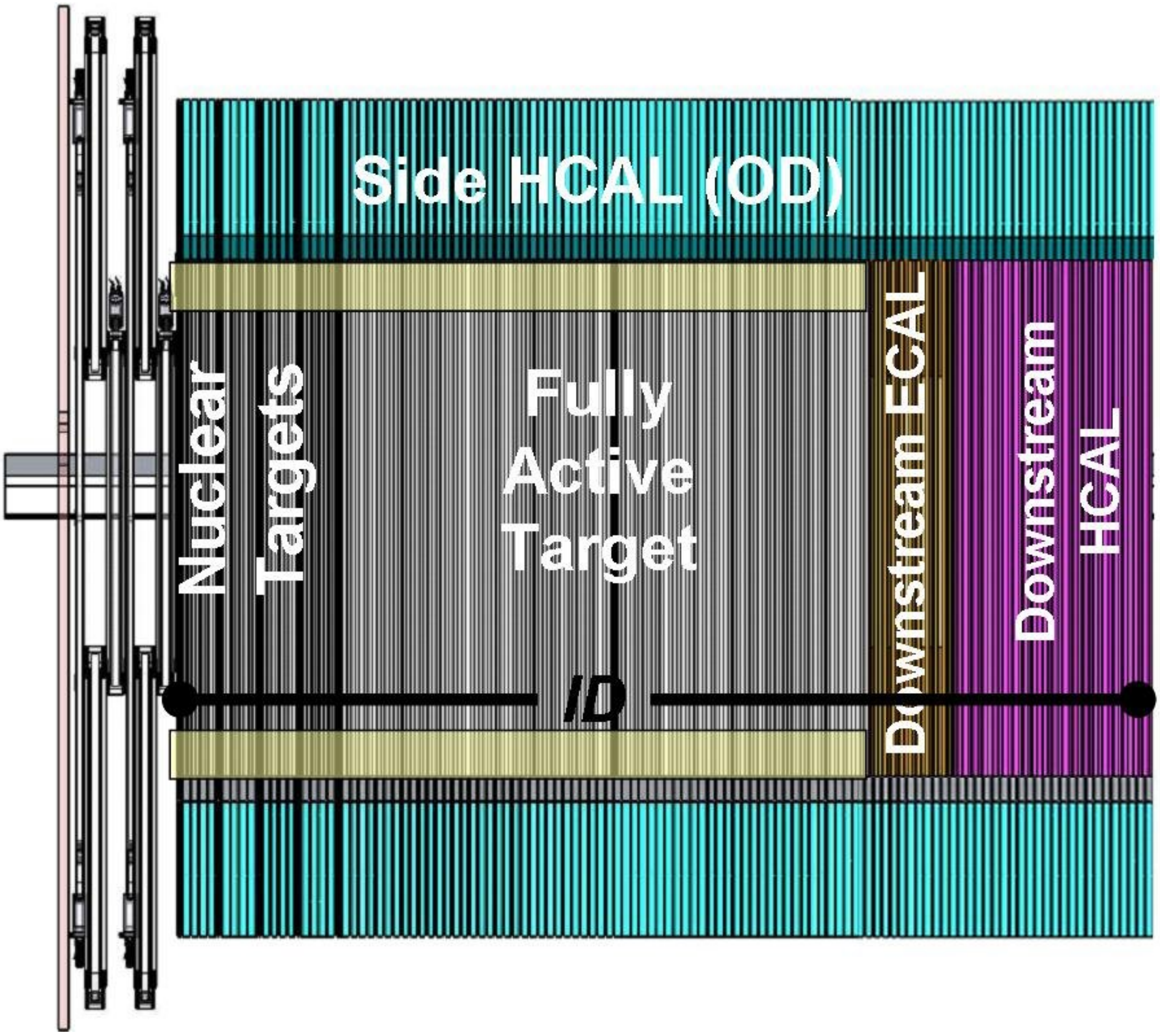

Figure 55: A side view schematic of the MINERνA detector

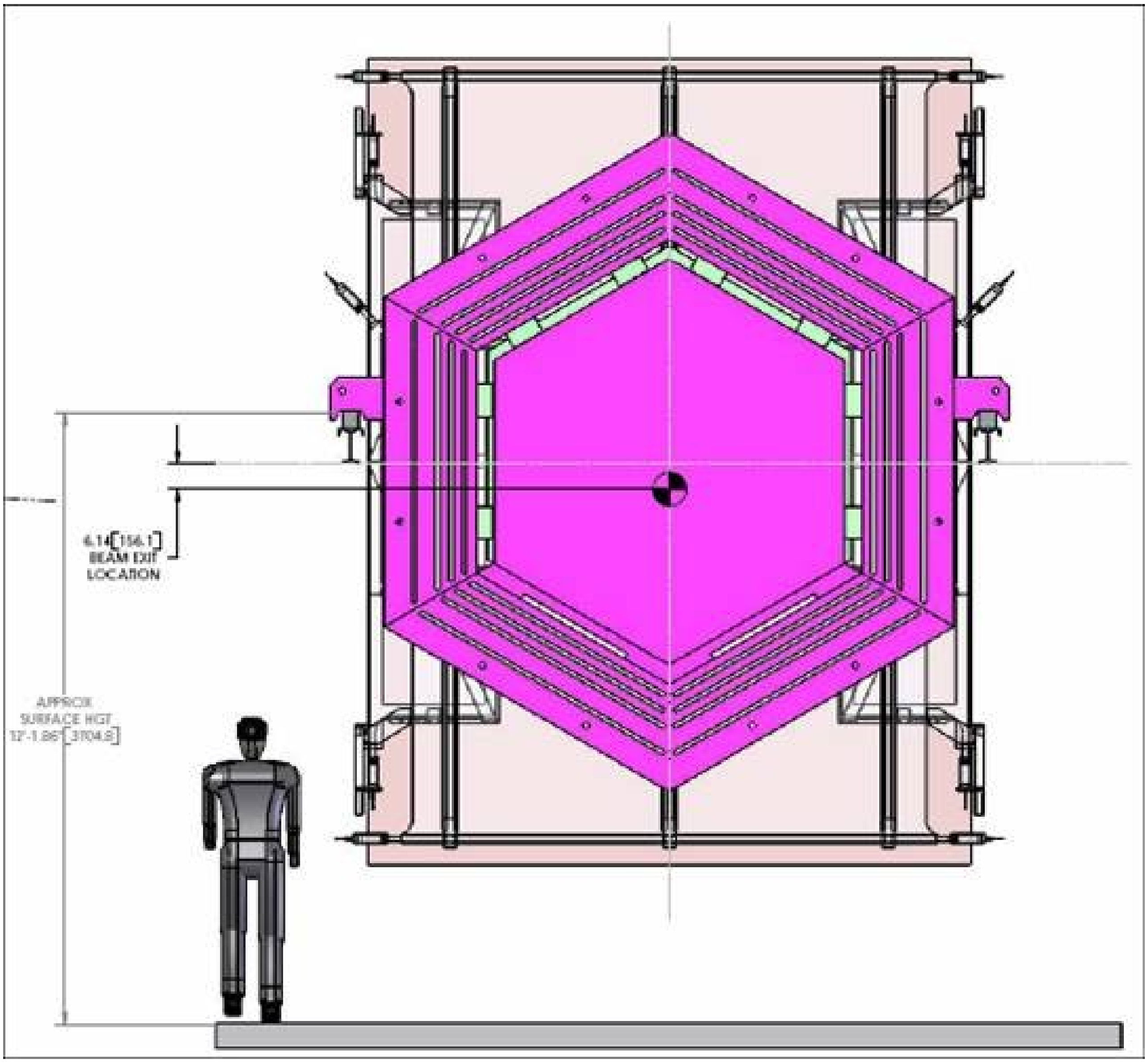

Figure 56: View from the back of the MINERνA detector to illustrate shape and scale. The tall structure at the far end of the view is the veto wall; the detector stand is not shown for ease of viewing.

cross-section for the detector. As shown, the scintillator strips extend the full length of the hexagon and range between 205 and 400 cm in length.

The center of the detector is the fully active inner detector (ID), whose plastic core represents the fiducial volume for most analyses in MINERνA. Calorimetric detectors in the central region of the detector are constructed by inserting absorber between adjacent planes as shown in Figure 57. Lead alloy absorbers, 30 cm from the edge of the ID and 0.2 cm thick, are inserted between layers of scintillator and at the front of each module to serve as a side electromagnetic calorimeter. This part represents the largest part of the detector in length, and the outer calorimeter surrounding the fully active planes are the largest part of the detector in mass.

The inner detector is surrounded by the picture frames of absorber and scintillator strips that make up the outer detector (OD). The OD consists of six "towers" (one sixth of a hexagon). Note that the strips in the OD run only in one direction in each tower: along the direction of the longest side in a tower. Three-dimensional tracks must therefore be matched from the inner detector and extrapolated outwards for an energy measurement or muon momentum measurement. A complication of the design is illustrated by the fact that the inner detector strips, which range in length from 120 to 240 cm, end inside the OD, and therefore bundled WLS fibers must travel through the gap between the OD planes of each module to the detector edge. The scintillator strips in the towers are rectangular in cross-section, $\sim 1.9 \times 1.5$ cm^2, and are arranged in rectangular layers of two strips per OD slot.

In the inner detector, MINERνA's sensitive elements are extruded triangular scintillator strips, 1.7 cm height with a 3.3 cm base, with embedded wavelength-shifting fibers. To improve coordinate resolution while maintaining reasonably large strips, these elements are triangular and assembled into planes (see for example Figure 99); this allows charge-sharing between neighboring strips in a single plane to interpolate the coordinate position.

The most downstream detectors are the hadronic calorimeters (HCALs) with a 1 inch steel absorber per scintillator plane, as shown in Figure 58. Next are the electromagnetic calorimeters, shown in Figure 59. The electromagnetic calorimeters (ECALs) have one 0.2 cm Pb alloy absorber per scintillator plane. The absorbers only overlap the inner detector and not the outer detector where it would represent a negligible fraction of the absorber material. The fine granularity of the ECAL ensures excellent photon and electron energy resolution as well as a direction measurement for each. Finally, in the region labeled "nuclear targets" in Figure 55, there are sparsely placed absorbers in between active target modules to allow study of events on different nuclear targets. These targets are described in Section 3.4.

3.2 Scintillator Detectors

This section describes the MINERνA scintillator components for the Inner (ID) and Outer (OD) Detectors, and related systems such as the Vertical Slice Test (VST). Section 3.2.1 addresses the requirements and performance criteria for the scintillator system. Section 3.2.2 provides an overview on the extruded scintillator preparation (MINERνA project WBS 1). Section 3.2.3 describes the wavelength shifting (WLS) fibers (WBS 2) that will be used in the detectors. Section 3.2.4 discusses in detail the clear fiber cables (WBS 4).

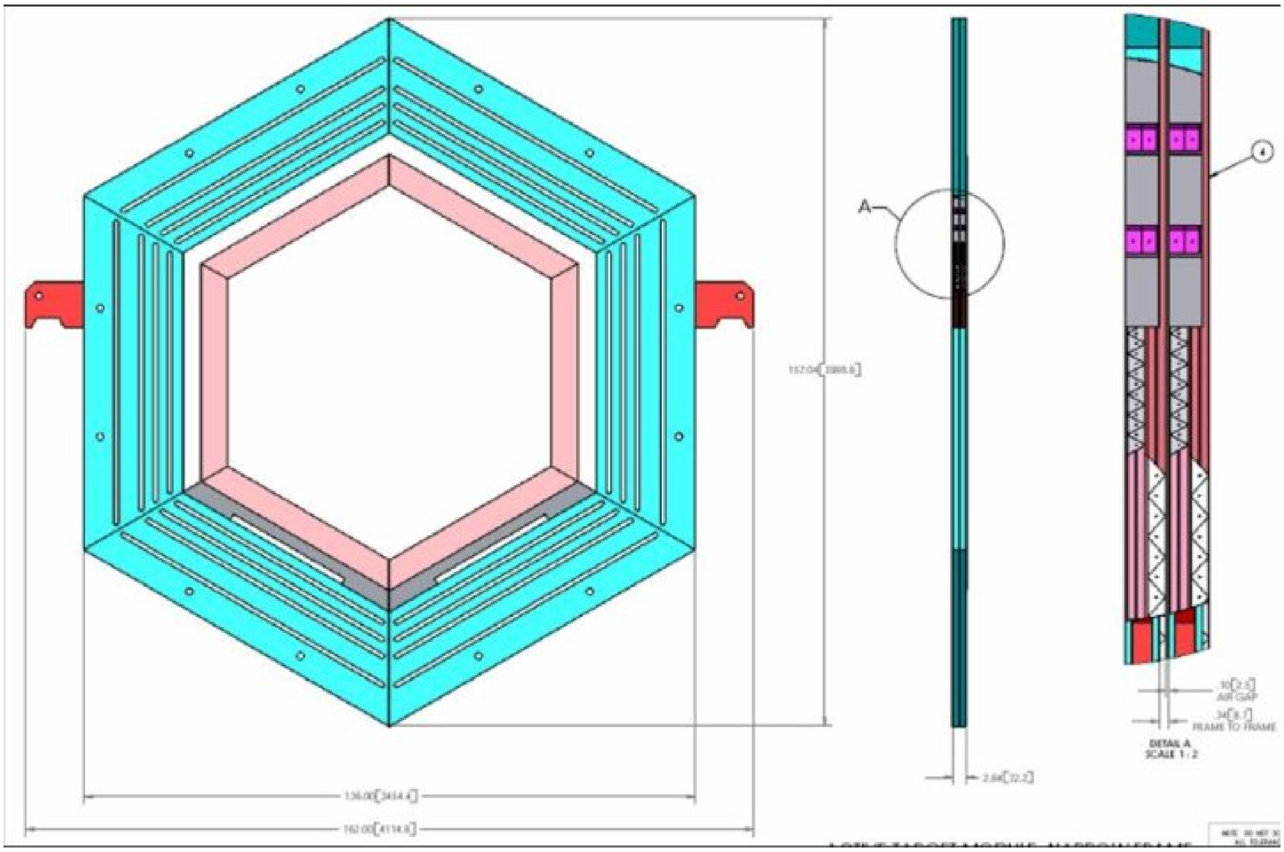

Figure 57: View of an active detector module. The figure at right shows a cut-away view from the side.

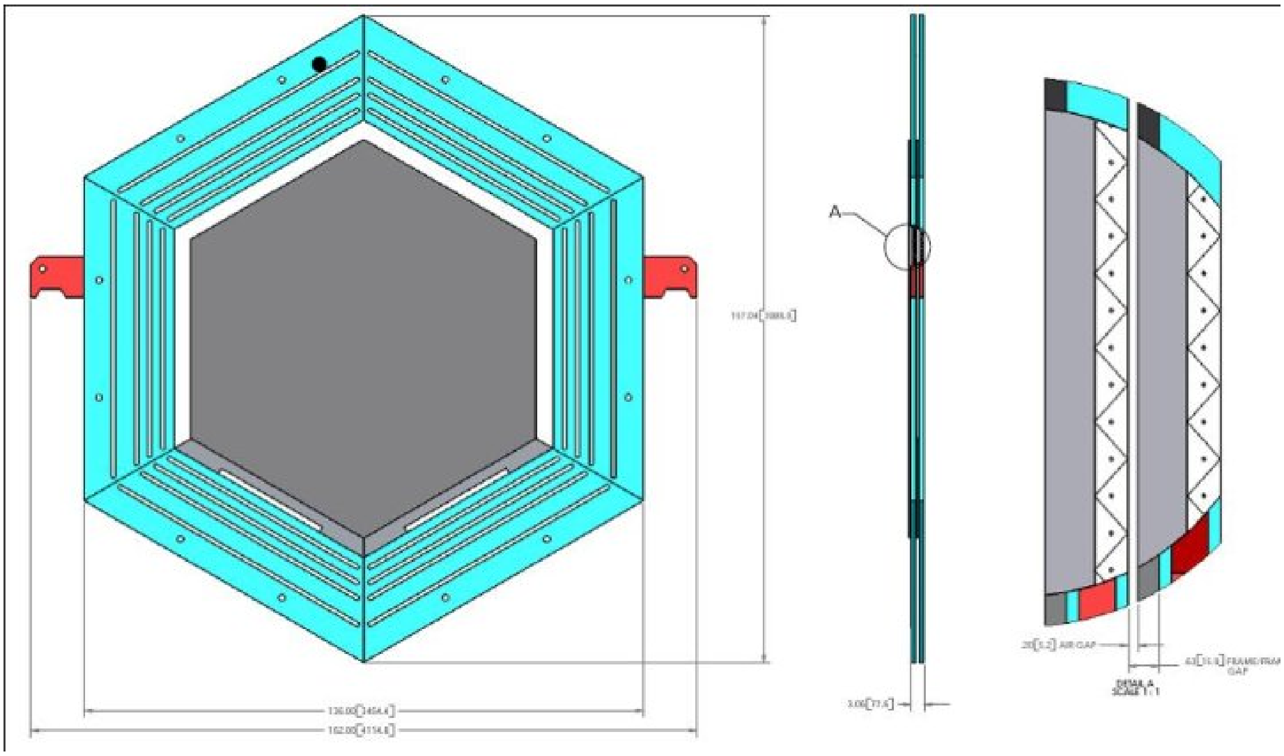

Figure 58: View of an HCAL detector module. The figure at right shows a cut-away view from the side.

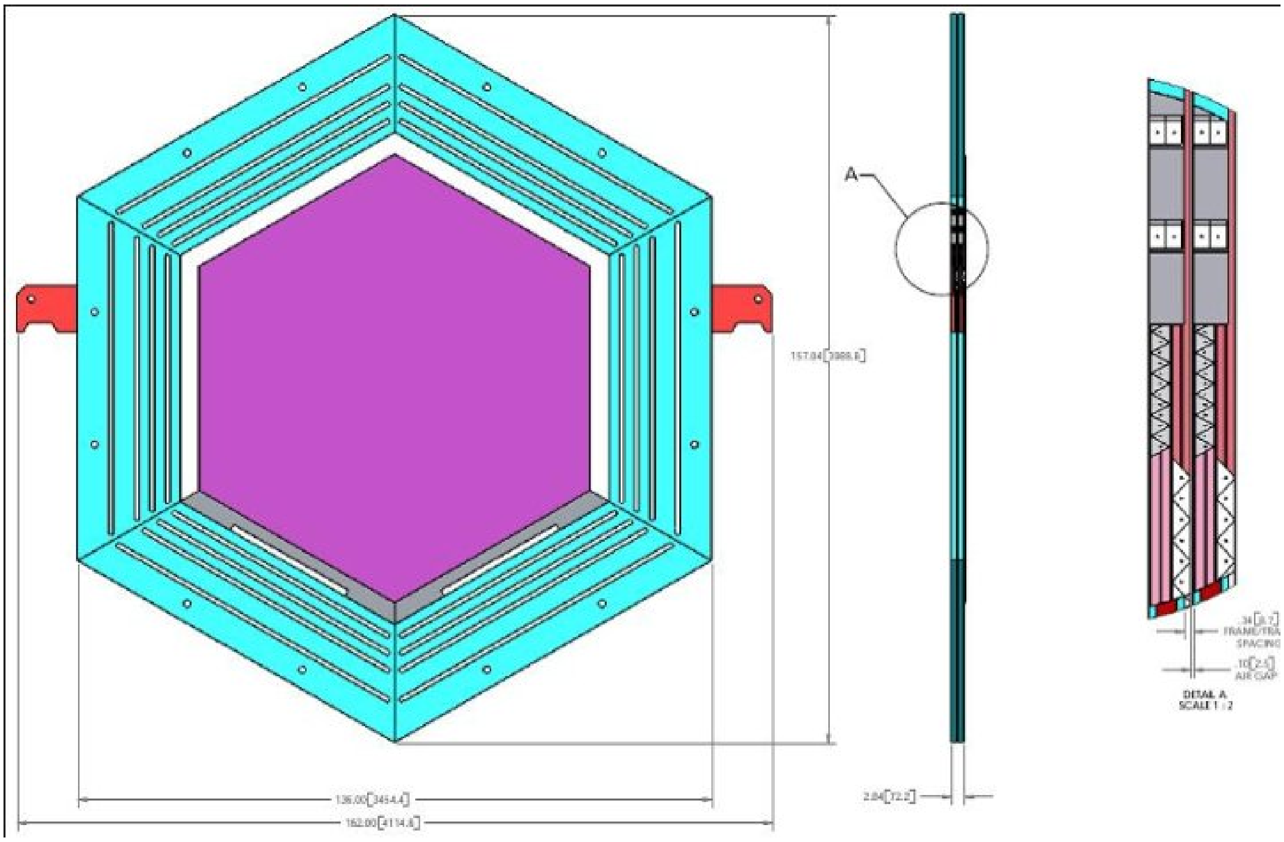

Figure 59: View of an ECAL detector module. The figure at right shows a cut-away view from the side.

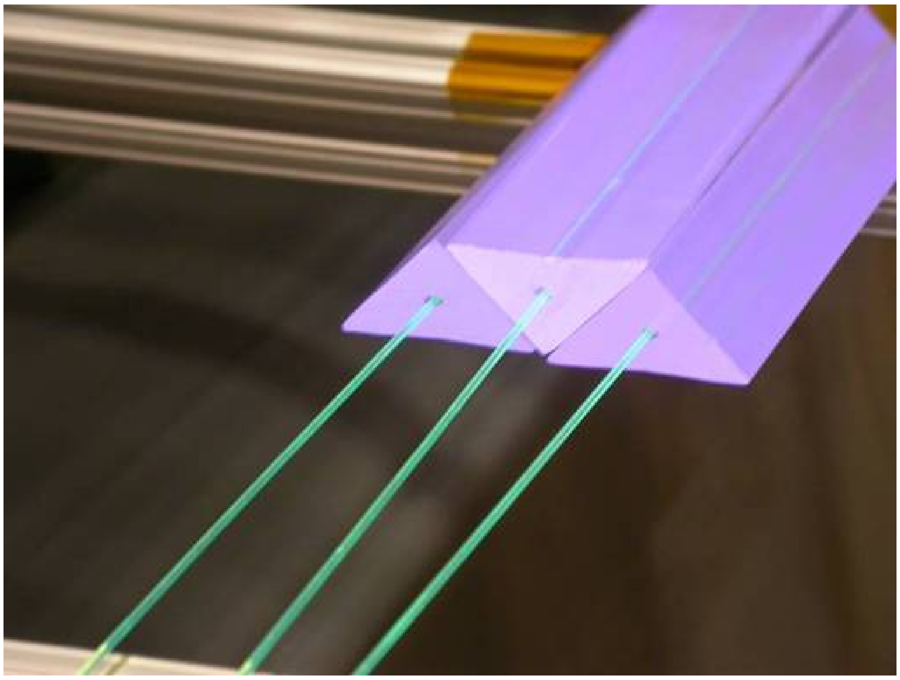

Figure 60: Prototype MINERνA scintillator bars, with wavelength-shifting fibers inserted.

3.2.1 Requirements and Performance Criteria

The MINERνA detectors utilize extruded plastic scintillator which is read out by wavelength shifting (WLS) fibers coupled to multi-pixel photodetectors. Figure 60 shows early prototypes of the scintillator and WLS fiber system. This technique provides excellent energy and spatial resolutions. The baseline design relies on existing technology for which performance measurements have been made. This same system is being used in the MINOS experiment. The major components that will be discussed in this Chapter are:

- The scintillator strips which consist of an extruded polystyrene core doped with blue-emitting fluorescent compounds, a co-extruded TiO_2 outer layer for reflectivity, and a hole in the middle for a WLS fiber. These strips are prepared with a triangular cross-section (3.3 cm base and 1.7 cm height) for the Inner Detector (ID) and with a rectangular profile (1.9 cm base by 1.5 cm height) for the Outer Detector (OD). Figure 60 shows an early prototype ID scintillator strip without the white reflective coating and with WLS fibers inserted in the holes.

- The WLS fibers which consist of Y11 fibers with 175 ppm of dopant, multi-cladded with a 1.2 mm diameter. These fibers, which are glued into the hole of the scintillator strips, are manufactured by Kuraray using an optical epoxy (Epon resin with TETA hardener). The fibers are read from one single end. The other end is mirrored.

- The clear fiber cables which consist of ribbons of 8 clear fibers (1.2 mm diameter, 109 cm maximum length) to carry the light from the detector modules to the photodetectors. Optical connectors are used for all fiber optics connections.

The technical requirements on the scintillator system have been established from a combination of physical studies and practical considerations. The technical requirements for the Inner Detector scintillator are more stringent than those for the Outer Detector scintillator. However, in order to save time and money the same scintillator will be produced for both applications. The same co-extrusion procedure with the same raw materials will be utilized. Therefore only the specifications of the Inner Detector Scintillator-WLS-Clear Fiber system are listed here:

Scintillator Bar Specifications:

Cross-sectional uniformity: $\pm$ 0.5 mm base and height both, measured with a caliper to within 0.1 mm.

Length uniformity: 5%, must be cut at 1% precision later.

Minimum TiO_2 thickness: 0.13 mm for efficient light reflection (based on MINOS tests).

Scintillator Light Output Uniformity: 5%, measured to within 1%.

Attenuation Length: 5-6 cm or longer (with capstocking) or 25-30 cm or longer (without capstocking).

Light Output: The light output must be sufficient for measuring event vertices and multiplicities. We have determined that the required number of photoelectrons (pe) per layer, per minimum ionizing particle is 13.2 pe at normal incidence for the full fiber readout chain.

Fiducial Mass: The total mass in the fiducial volume of the Inner Detector varies for different physics analyses, but there should be a minimum of 3 tons fiducial mass for each analysis. A minimum transverse (longitudinal) distance of 35 cm (50 cm) is required for containment. For the MINERvA detector, the minimum transverse distance cut translates to a cut of 75 cm maximum distance from the center of the detector.

Uniformity: The light output at the end of the clear fiber should vary by no more than 30% over the length of the bar. When combined with our measurements of expected light yield, our expected light yield stability with time, our expected variations in all parts of the light production, collection and transmission chain, this ensures that over 99% of the bars will meet the 13.2 photoelectron requirement.

WLS Fiber Attenuation and Mirroring: The light output at the far end of the scintillator bar must be above the minimum 13.2 photoelectrons per layer.

Clear Fiber Cable Transmission: The clear fiber transmission should be high enough that the minimum number of photoelectrons at the far end of the scintillator bar is 13.2 photoelectrons per layer.

Stability: The detector is expected to be able to operate for approximately 10 years, over that time the scintillator-fiber assembly light output is expected to decrease roughly $3 \pm 1\%$ per year [156]. Due to this degradation, a safety factor of > 1.3 should be included in the light output requirement in order to allow operations over 10 years. Short-term variations must be measurable, at the few per cent level over a month.

Calibration: The detector energy levels must be absolutely calibrated at the 2% level.

Transverse Position Resolution: In order to do exclusive channel reconstruction and make precise vertex measurements the transverse coordinate resolution must be 3 mm.

Linearity: The non-linearity of the Inner Detector scintillator bar system should be less than 15%, and should be known to better than 5% (or 33% of itself).

Cross-talk: The cross-talk between adjacent bars should contribute no more than 10% of the intrinsic position resolution of 3 mm. Given the transverse dimensions of the scintillator triangle base, this translates to a requirement that the cross-talk between adjacent bars be less than 2%.

Longitudinal Vertex Resolution: In order to measure nuclear effects we require less than 10% contamination for any given nuclear target region. This requires that the longitudinal vertex resolution is no worse than 1 cm.

Cost: The cost should be as low as possible given the above requirements.

3.2.2 Scintillator Extrusion

Particle detection using extruded scintillator and optical fibers is a mature technology. MINOS has shown that co-extruded solid scintillator with embedded wavelength shifting (WLS) fibers and PMT readout produces adequate light for minimum ionizing particle (MIP) tracking and that it can be manufactured with excellent quality control and uniformity in an industrial setting. MINERνA intends to use this same technology for the active elements of its detectors. While in terms of size MINERνA pales in comparison to MINOS, its system is similar in scale to other successful applications such as the K2K SCIBAR detector. Extrusion will also enable the use of different cross-sections throughout the detector to better address the experiment needs.

The extruded scintillator elements will be produced at Fermilab using the extrusion line jointly operated by Fermilab and the Northern Illinois Center for Accelerator and Detector Development (NICADD) at Northern Illinois University (NIU). NIU physicists and mechanical engineers have formed a collaboration to support development of the next generation of detectors at Fermilab's Scintillator Detector Development Technical Center. The extrusion line was purchased by NICADD in 2003. The co-extruder line was purchased by Fermilab in 2005. Fermilab and NICADD support and operate the extruder to ensure that the High Energy Physics community has access to high-quality extruded scintillator. Fermilab and NICADD personnel have been responsible for commissioning the extruder; simulations, production and prototyping of dies associated with specific detectors; and productions of extrusions for prototypes and detector construction.

MINERνA has chosen a scintillator bar with a triangular profile and a hole in the middle for the Inner Detector (ID). The triangle has a 3.3-cm base and a 1.7-cm height, and a 2.6 mm hole for the WLS fiber. A drawing with the specifications and tolerances for this part is available (FNAL Drawing Number: 9291.000-MB-241845). A rectangular cross-section with a hole in the middle was selected for the Outer Detector (OD). The rectangle has a 1.9-cm base and a 1.5-cm height, and a 2.6 mm hole for a WLS fiber. A drawing with the specifications and tolerances for this part is available (FNAL Drawing Number: 9219.000-MB-241843).

Figure 61 shows the die for the ID scintillator strips mounted on the extruder. Figure 62 shows the die sections to produce the OD scintillator strips. Only the last sections of the die and the sizing tooling need to be changed to produce either strip type. All scintillator strips have the same composition: a polystyrene core (Dow Styron 663 W) doped with PPO (1% by weight) and POPOP (0.03% by weight). Both strips have a white, co-extruded, 0.25 mm thick TiO_2 reflective coating. This layer is introduced in a single step as part of a co-extrusion process. The composition of this capstocking is 15% TiO_2 (rutile) in polystyrene. In addition to its reflectivity properties, the layer facilitates the assembly of the scintillator strips into modules. The ruggedness of this coating enables the direct gluing of the strips to each other and to the module skins which results in labor and time savings for

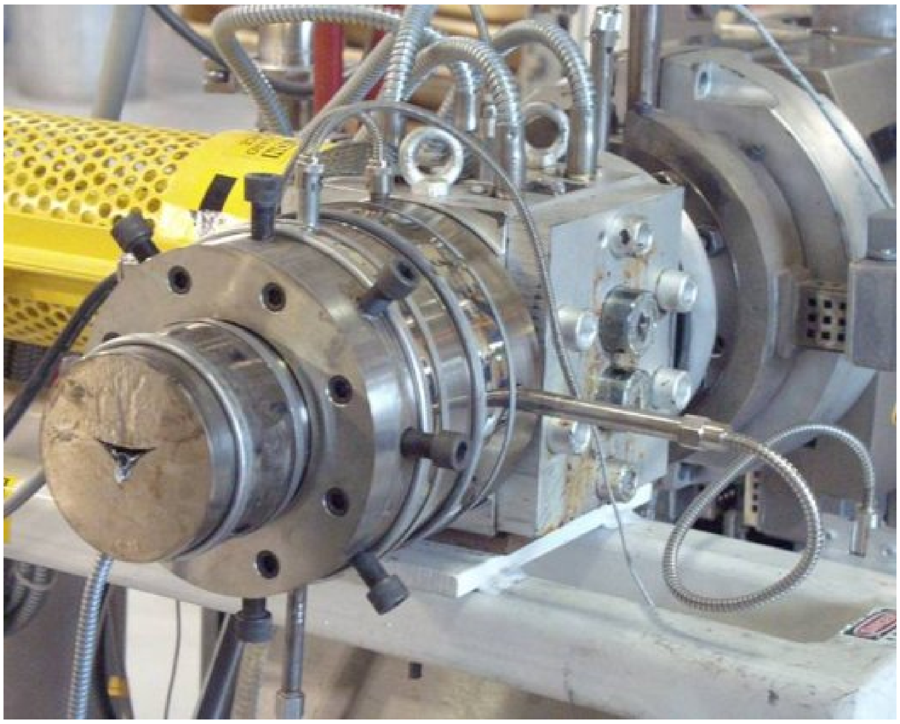

Figure 61: Die to produce MINERνA's triangular strips for ID scintillator.

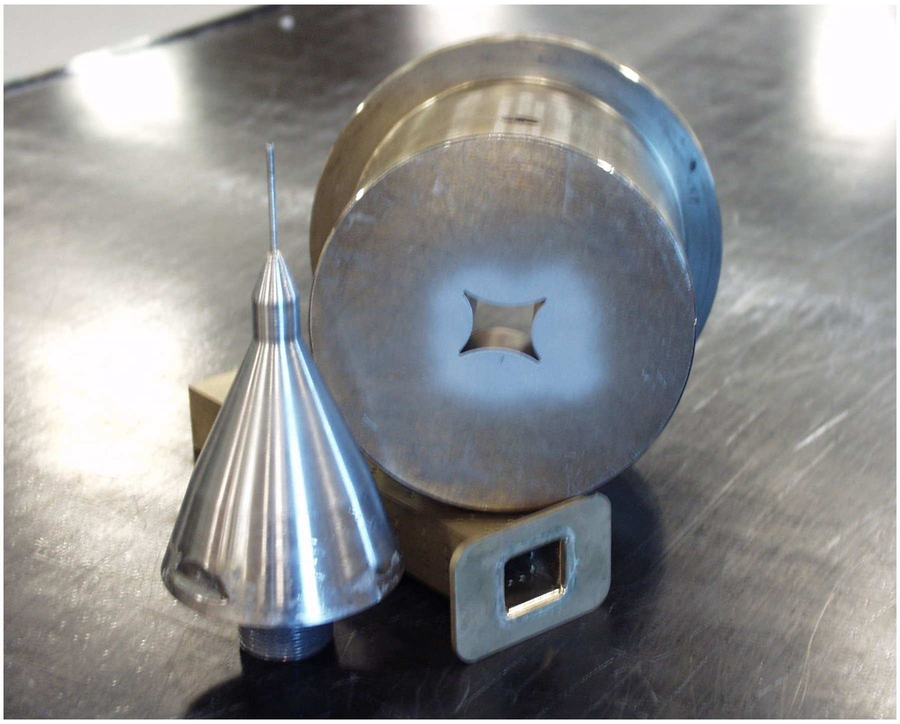

Figure 62: Die to produce MINERνA's rectangular strips for OD scintillator.

the experiment.

The scintillator bar production process is characterized by an "in-line", continuous extrusion process as opposed to a batch process. The polystyrene pellets are dried in a nitrogen atmosphere and automatically conveyed to a gravimetric feeder. The dopant mixture is added periodically to a different gravimetric feeder that works surrogated to the pellet feeder. These feeders have the necessary precision and reliability to ensure a constant ratio delivered. The pellet feeder is controlled by computer to the output of the twin-screw extruder to ensure the correct composition and processing. The extruder is responsible for melting and mixing the polystyrene pellets and the dopants. A twin-screw extruder will provide the highest degree of mixing to achieve a very homogeneous concentration. The outer reflective coating is added through material injected from a second extrusion machine (co-extruder) which mixes the polystyrene and TiO_2 pellets. Currently the co-extruder is manually operated to start-up and to vary the thickness of the reflective coating. As the plastic emerges from the die, it goes directly into the cooling tank. There it is formed into the final shape using the sizing tooling and vacuum. It continues to be cooled with water and air until it can be handled.

A total of 13,312 triangular strips and 2,736 rectangular strips will be produced for the ID and OD, respectively. The ID bars will be cut at 3.8 m long and the OD bars at 3.5 m long. Each strip will contain two strips for the final detector module. By cutting a single strip into two sections, it is possible to minimize the amount of waste material and still have each strip of exactly the right length for its hexagon location.

The extrusion rate for both scintillator strips is of 75 Kg/h. The dies have also been tested at 50 and 100 Kg/h. There is little difference in the quality of the extruded bars at any of these three rates. However, it becomes harder to cool down the extruded part as the extrusion rate increases. The best compromise is reached with the 75-Kg/h extrusion rate. The schedule was developed with the possibility of using the lower rate (50 Kg/h) in case that either the overall process (extrusion and quality control activities) or the quality of the material would require it. The higher rate (100 Kg/h) could be used if the production is delayed or if there are personnel shortcomings as a means to keep within the projected schedule. The 23 metric tons of extruded scintillator for the full MINERνA design will require a production run of approximately 18 weeks.

Quality Assurance and Quality Control (QA/QC) procedures to ensure the light yield of the finished product will be established and maintained by Fermilab and NIU personnel throughout production. Figure 63 shows the quality control (QC) measurements for seven of the R&D extrusion runs to prepare co-extruded scintillator bars. Two main parameters will be checked during production at the Extrusion Facility: dimensions and light yield. Dimensions will be checked every 60 minutes using a caliper. The data will be entered in a computer and the file submitted daily to the experiment's electronic document database, MINERνA-docDB. Light yield will be tested using a radioactive source. A reference sample will also be measured to monitor the stability of the equipment as well as to provide a minimum acceptable value. The results will also be uploaded into MINERνA-docDB. These measurements will be carried out on a QC sample (15 cm long). This short QC sample will be cut once every five full length scintillator strips. These two tests will be the basis of the Quality Control program. Additional testing will be performed if a problem is encountered. Measurements to determine the attenuation length of the material may be conducted at weekly intervals as a secondary proof of material quality and equipment stability.

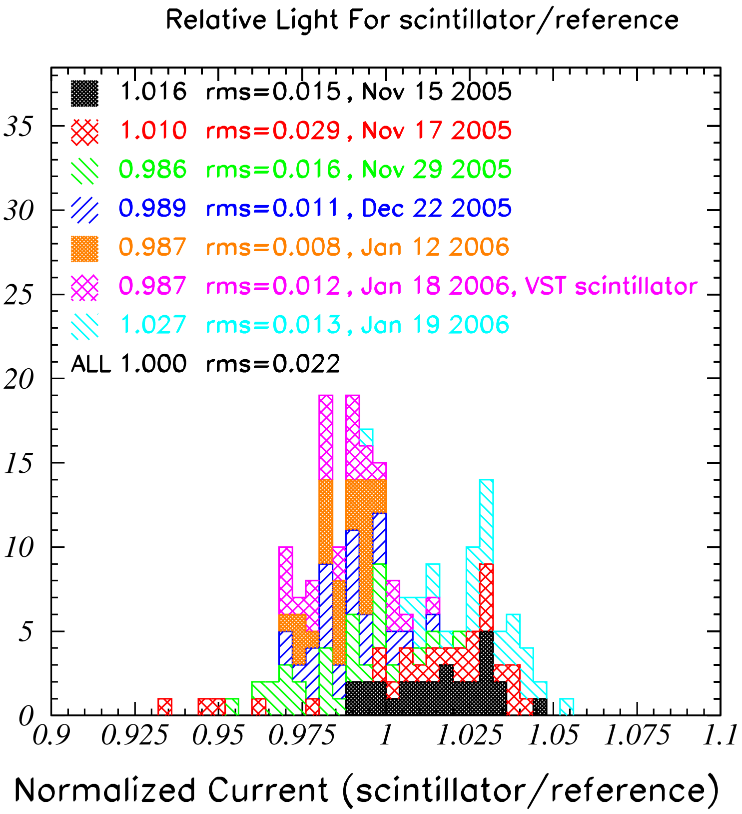

Figure 63: Light yield quality control measurements of the MINERνA scintillator bars. The plot shows the sample measurement divided by the control measurement. The normalization is set to 1. The VST scintillator is labeled. The bottom number shows the RMS of all the bars.

3.2.3 Wavelength-shifting fibers

The MINERνA optical system uses 1.2 mm diameter, 175 ppm Y-11 doped, S-35 multiclad fiber from Kuraray. Kuraray fibers have a proven track record in many HEP experiments including the CDF Plug Upgrade, CMS HCAL, and MINOS. The S-35 denotes a more flexible fiber than non-S fiber which MINOS and the CDF Plug Upgrade used in their scintillator planes.

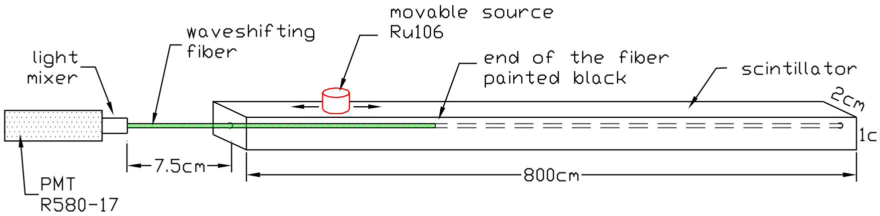

Figure 64: A schematic of the MINOS Scanner used to measure the WLS fibers.

The fibers will be manufactured in batches. (A batch is technically called a preform.) Five 3.2 m fibers from each batch will be tested using a fiber scanner called the MINOS Scanner, see Figure 64, to determine if the attenuation length is acceptable. The fiber is inserted into a long scintillator, a source moves over the scintillator, and the fiber is read out using a R580-17 Hamamatsu PMT. The PMT is read out by a picoammeter. The data are fit to a double exponential. Figure 65 shows the same fibers measured with mirrored and blackened ends. The quality control will be based on the amount of light at 320 cm from the readout end and the attenuation length. (Note, the longest WLS fibers in MINERνA are about 320 cm.) A light pulser consisting of americium in sodium iodide will be used to maintain the calibration of the PMT. Each of these is determined by extrapolating a fit to 320 cm. Figure 66a shows the relative light outputs among the fibers at 320 cm. The three batches we have received are shown. Figure 66b shows the light loss after 320 cm of fiber. Figure 66 shows that the 3 batches appear to be equivalent.

MINERνA will read out only one end of its wavelength-shifting (WLS) fibers. To maximize light collection, we will mirror the unread end of each fiber using techniques developed at Fermilab. "Mirroring" consists of 3 steps: polishing the end to be mirrored, depositing the reflective surface on the fibers (a process called sputtering), and protecting the mirrors.

A technique called ice-polishing is used to prepare the fibers prior to applying the reflective coating. Ice-polishing can give a very good finish to many fibers at once. This technique is described in detail in [157].

The reflective coating is applied in a vacuum system dedicated to optical fiber mirroring at Fermilab. The number of fibers that can be sputtered per load depends on the diameter, but typically 1000–2000 fibers per pumpdown per unit can be coated. A 99.999% chemically pure aluminum coating is a applied for good reflectivity. The coating is approximately 2500 Angstroms thick and is monitored using an oscillating quartz crystal sensor device. The aluminized ends are protected with a coat of epoxy.

After this process, MINERνA will do a destructive measurement of the mirror reflectivity with 5 fibers from each sputtering session. Light output is measured through the unmirrored end of a fiber

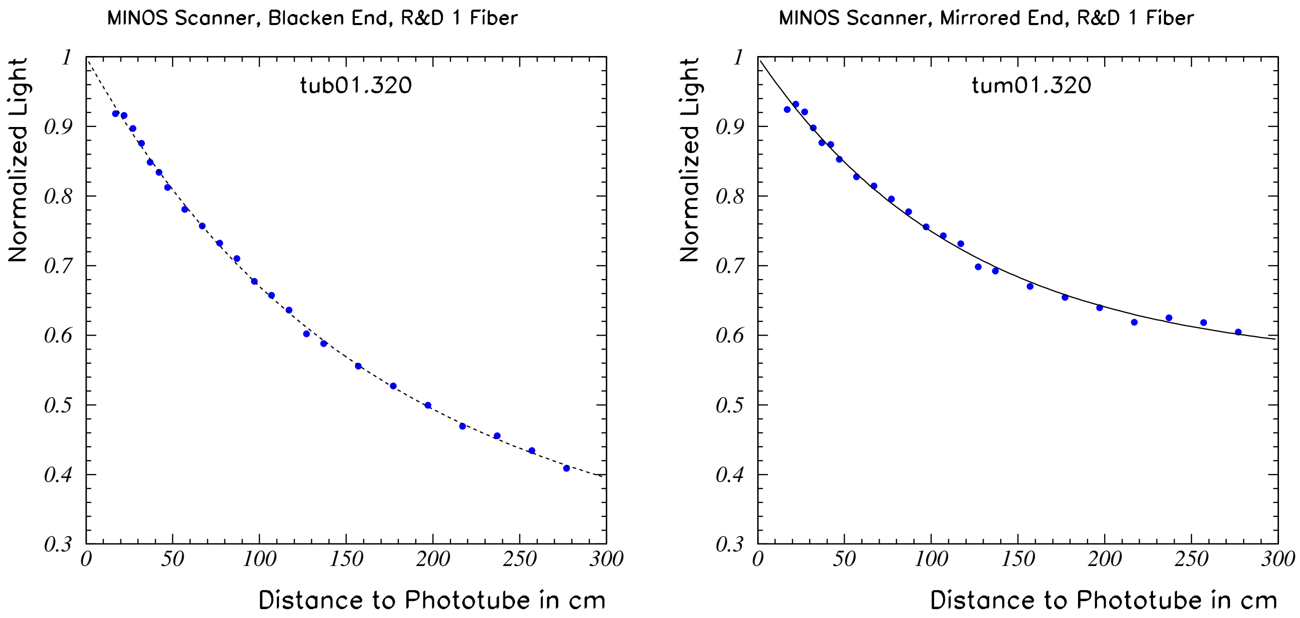

Figure 65: The measurement of the same fiber using the MINOS Scanner. The fiber is first measured with the mirror on. Next, the mirror is cut off and the end painted black. The fiber is remeasured. The fit is a double exponential, $p(1)e^{-x/p(2)} + p(3)e^{-x/p(4)}$, where x is the distance to the phototube and p(i) are the parameters. The mirror reflectivity is determined by using these 2 fits extrapolated to the fiber end.

with ultra-violet light incident on the fiber near the mirrored end. Then, the mirrored end is cut off at 45°, painted black, and the light yield is remeasured with the UV light at the same place. Figure 67 shows the mirror reflectivity by scanning with the MINOS Scanner the same fiber with and without the mirror. The mirror reflectivity is measured to be about 80%. RMS of the mirroring is 5.5%, while the RMS of the mirroring for the CDF Plug Upgrade was 5.4%.

3.2.4 Fiber connectors and optical cables

We are using optical connectors from Fujikura/DDK (generically referred to as DDK connectors). These connectors were originally developed for the CDF Plug Upgrade by DDK, in consultation with Tsukuba University. Since then, they have been used by several other experiments such as FOCUS, STAR, and D0.

The DDK connectors consist of a ferrule, clip, and box (Figure 68). They snap together without screws or pins. These connectors were chosen for their ease of use. DDK has made a new ferrule die for our 1.2 mm diameter fibers, keeping the outside dimensions of the ferrule identical to the current model; thus, other parts of the connector do not need to be redesigned.

The hole position, diameter, and outer dimensions of the new ferrule have been precisely mea-

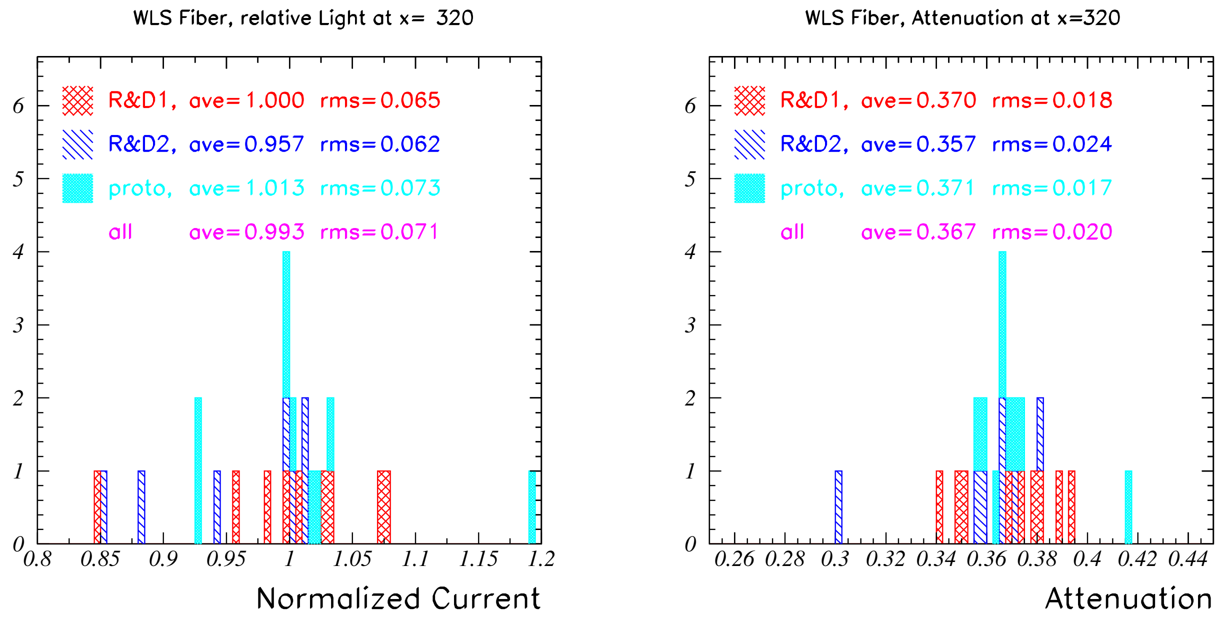

Figure 66: The left figure shows the relative light output for the WLS fibers measured with the MINOS Scanner. Three batches were measured; R&D-1 Fibers (purchased May 2005), R&D-2 Fibers (purchased Aug 2006), and Prototype Fibers (purchased Dec 2006). The relative light was normalized to the R&D 1 Fibers, the fibers used for the VST. The right figure shows the light loss at 3.2m

sured. These measurements were done at SCIDET using the Coordinate Measuring Machine (CCM) and the Optical Gaging Products (OGP). The CCM measure objects mechanically, while the OGP measures objects optically. When the connectors are mated, the fiber holes line up to < 25 microns. The hole diameters are very similar, with the differences < 12 microns. The ferrules fit very tight in the box.

The transmission was measured using the new connectors. Figure 69 is a schematic which shows how the connector transmission is measured. We injected light into a pigtail using 1 m WLS fiber inserted into 0.5 m long coextruded scintillator. (By ”pigtail”, we mean a set of fibers put in one DDK optical connector with no DDK optical connector on the other end.) A source in a lead cone excited the scintillator. The light was readout using a PMT and a picoammeter. We measured the light before and after inserting a connector into a 2 m cable. Figure 70 shows transmission for 3 cables.

We have measured the light loss from a 1 m clear cable to be about 30% without optical grease between the connections. We injected light into a WLS pigtail using the same procedure as used to test the cable transmission, see Figure 71. We connected the DDK connector on a WLS pigtail to DDK connector on a clear pigtail with the other end going to a PMT. We then inserted a 1 m cable between the 2 DDK connectors and remeasured the system. Figure 72 shows the light loss for 3

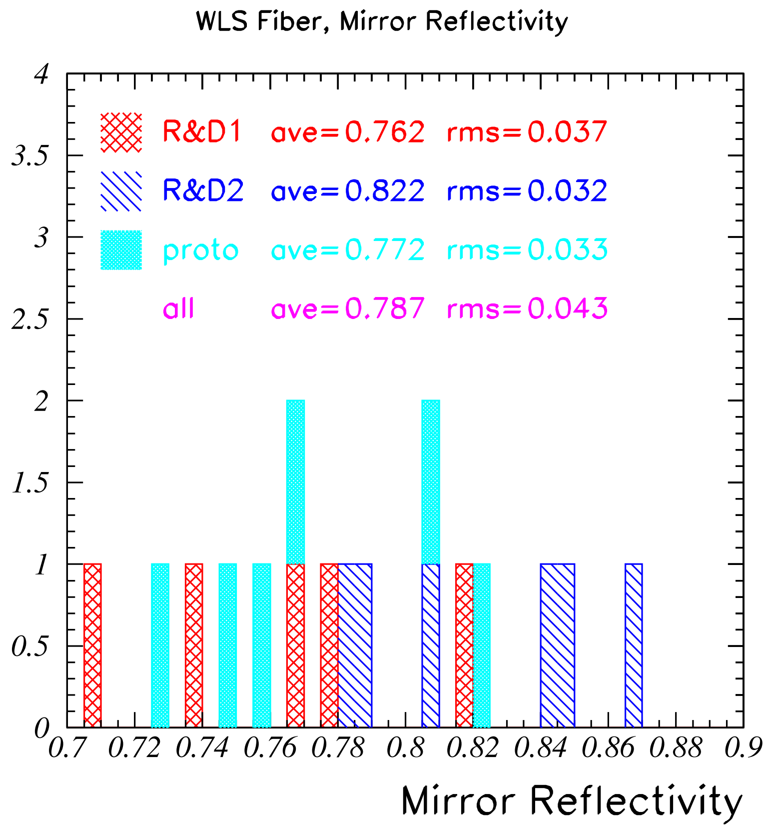

Figure 67: Plot shows of the mirror reflectivity for the 3 batches of fiber. Each batch was mirrored at a different time. Each entry is the ratio between the mirrored-end fiber fit and the blackened-end fiber fit extrapolated to the fiber end.

cables by taking the ratio of light after the inserted cable to light without cable. We are planning on using optical grease between the connectors to increase the transmission. We have measured the light increase from optical grease to be about 16%. In order to determine the lifetime of optical grease, we have measured the transmission of 2 greased connections after 6 weeks. We have seen no change in the light transmission.

For the cables, we are using 1.2 mm, S-35 multiclad fiber from Kuraray to match the Kuraray WLS fiber. The S-35 denotes a more flexible fiber than non-S fiber. Five fibers from each batch will have their attenuation length checked using a cut-back test developed by CMS. The test uses a source, scintillator, and WLS fiber to inject light into the clear fiber. A 6.8 m attenuation length was measured for the R&D fibers using this procedure.

We will be manufacturing 2 kinds of optical cables; referred to as ODUs (optical decoder units) and cables. The ODUs are meant for the PMT boxes. ODUs are built the same way as cables, but they are not made light tight. Hence, they undergo the same cable QC procedure as cables do. At the

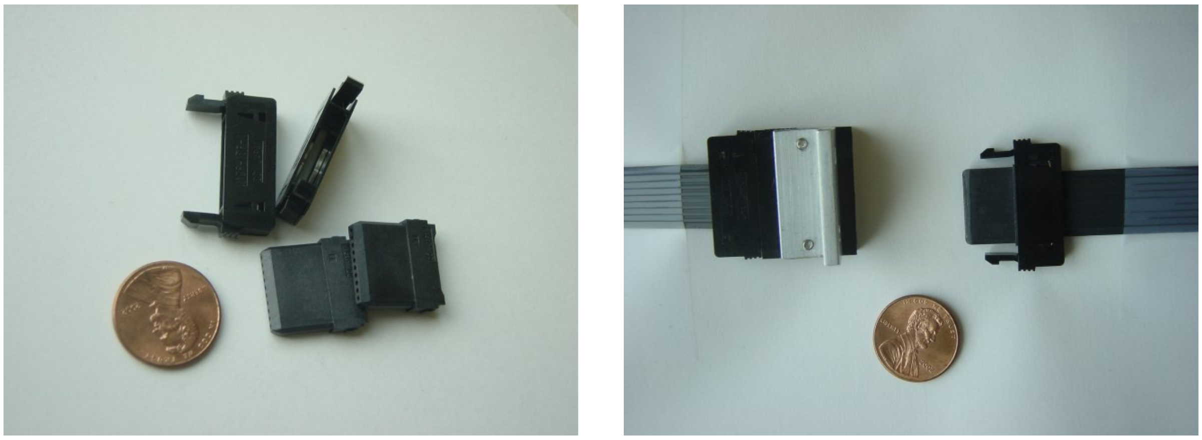

Figure 68: DDK connector parts. At the left, examples of the ferrules (bottom) and the clip (top). At the right, two completed CDF cables with the box to which they connect. The aluminum angle bolted onto the box is used to hold the box on an aluminum cover.

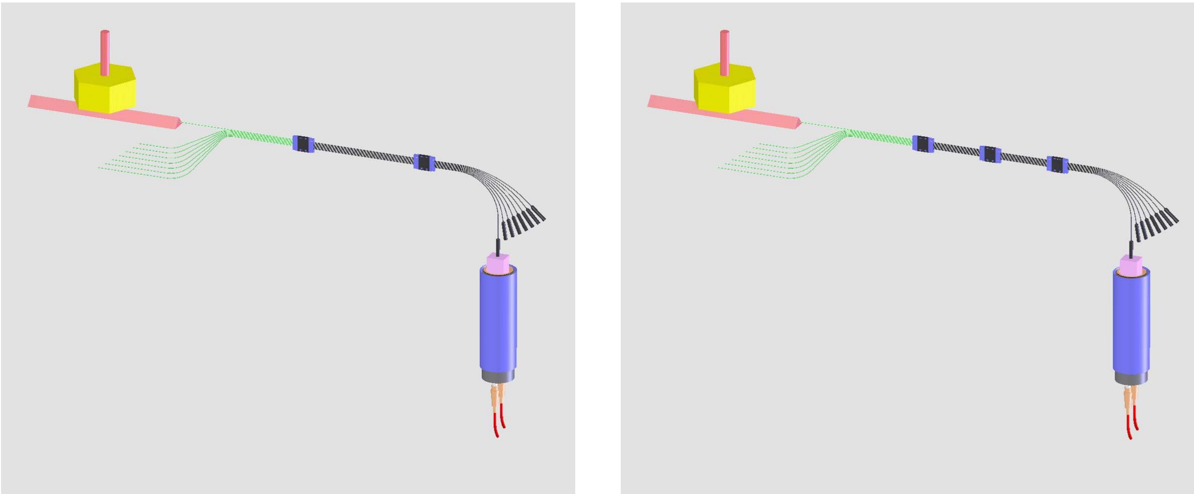

Figure 69: Schematic of apparatus used to measure the connector transmission. The left picture shows the light being measured with an optical cable inserted between 2 pigtails. The right picture has the connector inserted into the cable.

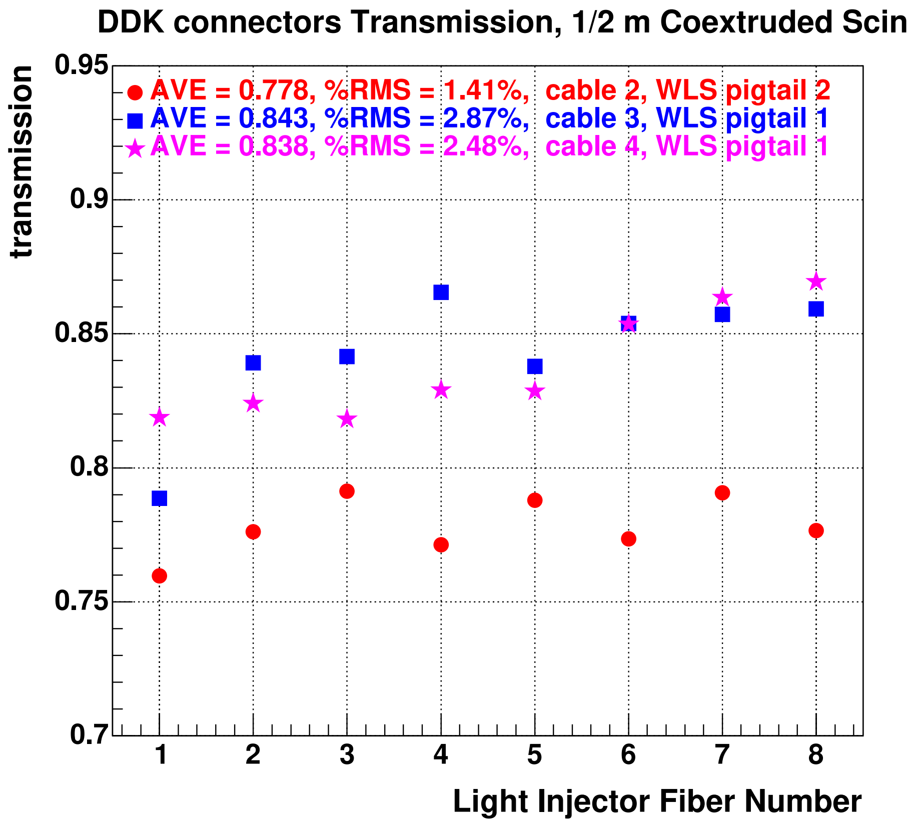

Figure 70: The light transmission for 3 DDK connectors.

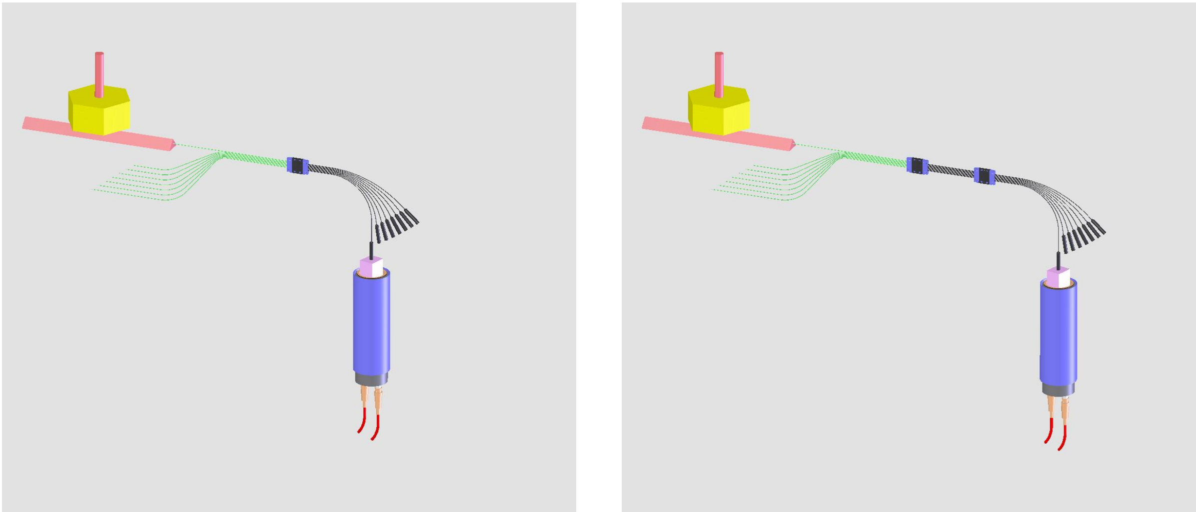

Figure 71: Schematic of the apparatus used to measure loss from a 1 m cable. The left picture shows the light being measured before the insertion of the cable. The right picture has a cable inserted between the 2 pigtails.

PMT box factories the ODUs are cut in 2 and weaved into the cookie for the PMT box.

The fabrication and polishing procedure we plan to adopt was used by the CDF collaboration on DDK cables. Initially, the fibers are cut to the correct length. Then, the fibers are inserted into a ferrule oriented vertically and taped in place, with the mating end pointing down. The top of fibers are taped against a horizontal piece of metal. BC600 epoxy is then placed in the pocket of the ferrule with a syringe. After the epoxy cures (the next day), two clips are placed on the fibers, one for the ferrule that was just epoxied and the other to fit over the ferrule yet to be fixed to the other end of the cable. A light-tight tube is placed over the entire length of the fibers except for approximately 5 cm near the ends where the fibers enter the ferrules. The end of the fibers not glued in the first ferrule are then placed in a second ferrule and epoxied in place. After curing, the fibers on both ends of the cable are trimmed to about 1/8" at the connector in anticipation of the polishing. After the ferrules and fiber ends are polished, the clips are pushed up onto the two ferrules.

For the CDF Plug Upgrade, a significant Fermilab effort was devoted to developing a method to polish the DDK connectors [157]. Since then, Fermilab has developed a machine which can polish multiple optical connectors simultaneously. Fermilab has designed a fixture for this machine to hold 6 DDK connectors. We have used this machine to polish the R&D cables which have been used for a variety of measurements, including the transmission measurement described above.

We have developed a light-tightening scheme similar to one developed by the Michigan State University nuclear physics group, who used DDK connectors in a large electromagnetic calorimeter. The fibers are surrounded by an 1/4" opaque sheath, INSUL #4900/3. We have developed a mold to surround the region at the connectors with a light-tight urethane boot. Figure 73 shows a light tight cable. Both the boot material and the tubing have passed the FNAL fire safety review. The urethane boot takes about 1/2 hour to cure, so that only $\sim$ 5 molds are needed for production.

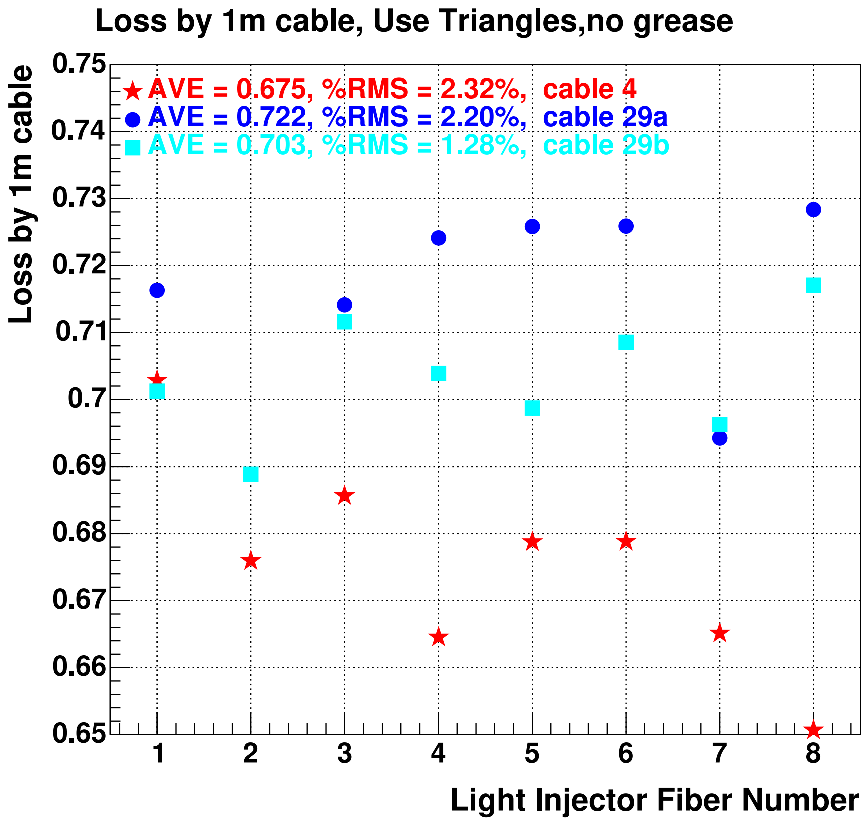

Figure 72: The measurement of the light loss from a 1 m clear cable. The average light loss from a 1 m cable is 30%

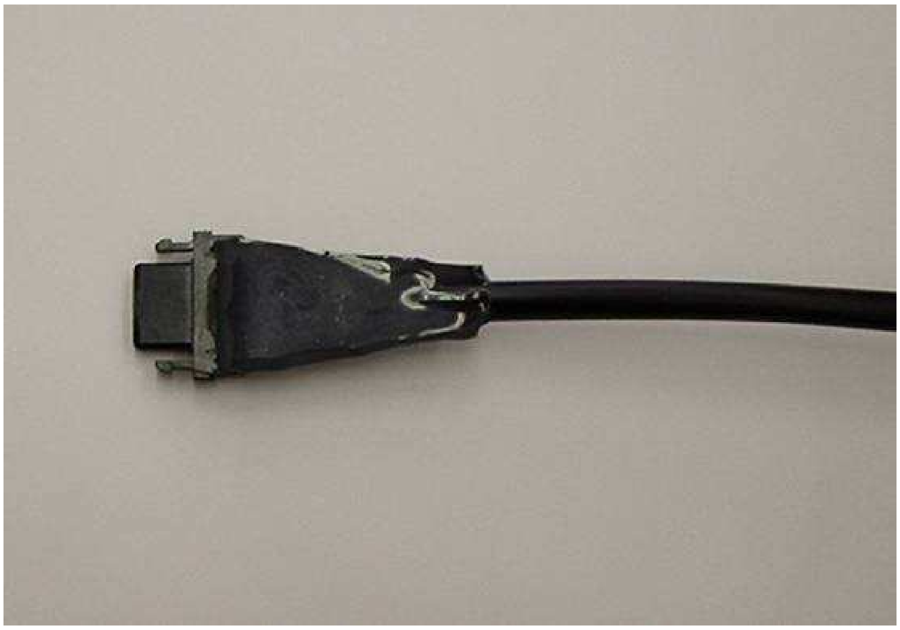

Figure 73: The light-tight boot for DDK connectors.

The final QC measurement tests the light transmission for each fiber in the connectors. This test uses a light injector box. This box has a LED with a pin diode for normalization. The LED shines on the fibers in a consistent way which can be normalized by the pin diode. Each cable is connected from this box to a readout box using optical jumper cable on both boxes. The jumper cables help to preserve the optical surface of both boxes by reducing the number of box connections. Fibers in the readout box go to individual pin diodes which are read out using a Keithley 6485 digital picoammeter. In order to bring the individual pin diodes to the Keithley we will use the Keithley 7001 high density switch system and a Keithley 7058 low current scanner card. A LabView program controls the automated readout procedure. Figure 74 shows the output of the cable QC for 14 R&D ODUs. The average of each channel is set to 1. Fibers varying more than certain amount from the average will have their cable rejected. In this case all fibers were fine. Note that, measuring 2 jumper cables connected together without the test cable will give us an additional handle. Fibers will be visually checked for breaks or cracks during and at the end of assembly.

For cables, two additional QC procedures are done. We check that the cables are light tight and check the fibers are connected in the correct order. The box which checks if the cables are light tight consists of a PMT inside a light tight box. The PMT is readout by a picoammeter. The box has connections for both ends of the cable. We check to see if the PMT sees any light. A box with 8 different color LEDs checks the fiber order. Each fiber is lit up by a different color LED. We visually check that the fiber order is correct.

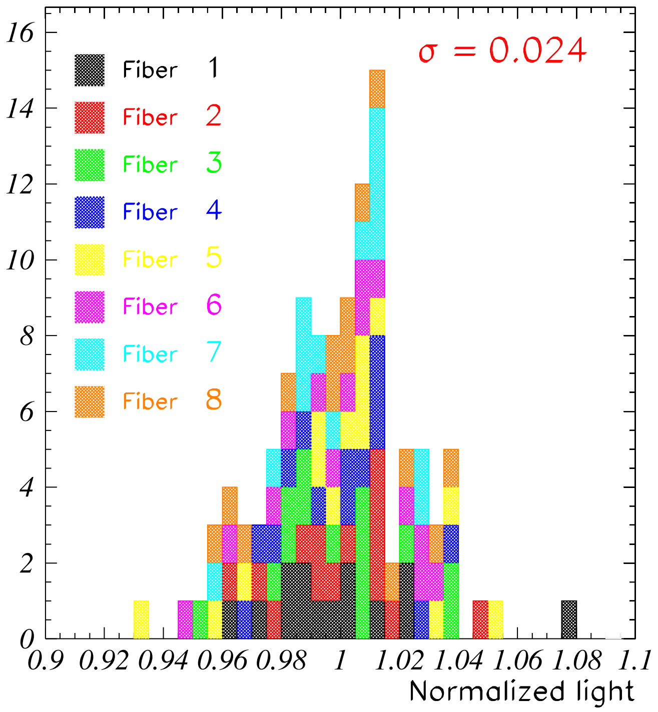

Figure 74: The QC results for R&D ODUs is shown. This uses the final Light Injector Box and Cable Tester Readout Box. A intermediate version of the final DAQ is used. Fourteen ODUs are tested. The normalization of the light for each fiber channel is determined by averaging each fiber channel and setting the average to 1 for each channel. The individual colors show the distribution of each fiber channel.

Parameter	Description/Value	Unit
Spectral Response	300–650	nm
Peak Wavelength	420	nm
Photocathode Material	Bialkali	
Photocathode Min. Effective Area	18×18	mm
Window Material	Borosilicate Glass	
Dynode Structure	metal channel dynodes	
Number of Stages	12	
Weight	30	g
Operating Ambient Temperature	-30–50	^{o}C
Storage Temperature	-30–50	^{o}C
Supply Voltage	900	V
Average Anode Current	0.1	mA

Table 10: General properties of the R7600U phototube

3.3 Photomultiplier Tubes

Light from each of the ~30,000 scintillators in MINERνA must be converted to an electrical pulse which carries accurate timing information and has an amplitude proportional to the energy deposited. This is done with photomultipliers (PMT's) of moderate gain and good linearity. To save cost, multi-anode PMT's with 64 pixels are used. The MINERνA detector requires 473 PMT's. Each PMT sits in a steel tube called a PMT box (Sect. 3.3.1). The inputs to this box are the clear signal fibers (WBS 2) bringing light from the scintillators and 2 light injection fibers (Sect. 3.3.3) which will track the gain during the experiment. Fast analog signals are fed to front end boards (FEB's) which sit on top of the PMT box. There, the signals are amplified, digitized, and converted to a fast timing signal (WBS 7).

We will use the R7600-00-M64 multi-anode photomultiplier tubes from Hamamatsu Photonics. These are 2 cm x 2 cm, 8 x 8 pixel PMTs, i.e. 64 pixels with effective dimensions 2 x 2 mm^2. The general properties of and manufacturer specifications for the R7600U PMT are listed in Tables 10 and 11. Additional specifications on the PMTs set for the MINERνA application are listed in Table 12.

Since this is the successor to the PMT's used by MINOS, we have good experience on which to build. For the overall system, we require standard properties of mechanical strength, isolation from light, electronic noise, and magnetic fields, and excellent calibration techniques. Standard concerns with PMT's include dark current and gain uniformity. With multianode PMT's, linearity and cross talk must be carefully considered. Finally, alignment of the fibers with respect to the pixels is also very important. Selection criteria will be imposed based on the dark count rate, and pixel gain uniformity. Alignment methods and performance testing method will be discussed in Sect. 3.3.2.

3.3.1 PMT optical boxes of the MINERνA detector

In MINERνA, optical cables must carry the light signals from the inner and outer regions of the

Parameter	Min	Typical	Max	Unit
Luminous (2856 K) Cathode Sensitivity	60	70	–	μ A/lm
Quantum Efficiency at 420 nm	–	20	–	%
Blue Sensitivity Index	7	8	–	–
Luminous Anode Sensitivity	4	140	–	A/lm
Gain	5×10^5	2×10^6	–	
Anode Dark Current	–	2	20	nA
Anode Pulse Rise Time	–	1.4	–	ns
Electron Transit Time	–	8.8	–	ns
Transit Time Spread (FWHM)	–	0.26	–	ns
Pulse Linearity ($\pm 2\%$)	–	30	–	mA

Table 11: R7600U phototube characteristics at 25^{o}C.

Parameter	Min	Max
Single Anode Dark Rate		5000 Hz
Quantum Efficiency at 510nm	12%	
Ratio of Gains of highest to lowest gain pixel		3

Table 12: Additional specifications for MINERνA R7600U MAPMTs

tracking spectrometer and transport them to pixels of the detector's readout array of photomultiplier tubes (PMTs) [158]. Each PMT is housed in an individual light-tight cylindrical enclosure ("box") made of steel. Each box provides the optical connection of fibers to PMT pixels in a way which ensures the crucial alignment. The boxes facilitate the routing of signal and voltage cables to-and-from the PMTs. Moreover they provide mechanical protection as well as significant shielding from ambient magnetic fields - the latter arising as result of proximity to the magnetized Near Detector of MINOS.

A new PMT box design has been developed for MINERνA, the essential features of which are described below. The design incorporates features of two optical box implementations which have been serving the MINOS experiment very well. As will be elaborated, MINERνA boxes accommodate one M64 phototube per box and so are more similar to "Alner boxes" of the MINOS Near Detector, rather than MINOS MUX boxes of the Far Detector (which serve three M16 PMTs per box). However, in contrast to Alner boxes, the MINERνA design utilizes construction-standard steel extrusions to achieve fabrication economy and improved magnetic shielding. Fabrication and quality assurance testing of a total set of 550 optical boxes is required to fulfill MINERνA's immediate deployment need (473 boxes) plus its operational maintenance needs upon extended operation. (The latter includes the experiment's need for hot spares and spare components, plus a small allowance for production wastage.) Manufacture of the optical box array and its delivery to the staging area at Fermilab will be carried out using two coordinated, independently operating assembly "factories" which are being set up at Tufts and Rutgers universities.

Functions of PMT boxes

PMT box functions addressed by the design developed for MINERνA are listed below. Design aspects which relate to these functions are elaborated in the Sections following.

1. *Boxes provide precise alignment of signal fibers to PMT pixels:* Alignment is made using machined mounting cookies which capture the input fibers and press them onto the face of each M64 PMT; the PMT is held via a machined holder, to which the cookie mates in a precise way and with unique orientation.

2. *Boxes provide light-tight enclosures for the PMTs:* Each box consists of a hollow cylindrical steel hull with endplates at either end; each endplate is augmented with a gasket and RTV seals which ensure that no light can leak in from the outside.

3. *Boxes provide mechanical protection for the delicate and valuable M64 PMTs:* Construction-standard Fe extrusions are used to provide rugged and inexpensive enclosures.

4. *Boxes provide magnetic shielding for the PMTs:* Ambient magnetic fields exceeding 5 gauss can degrade PMT efficiency; ambient fields in spaces to be occupied by the detector have been measured and are in the range of 2 to 16 gauss. In the deployed orientation, axes of MINERνA boxes will be nearly transverse to residual B-field from MINOS and will provide a factor ten field reduction from the box exterior to the inner, central location of the PMT.

5. *Boxes provide optical fiber and electronic voltage and signal routes to the PMT:* Routing of fibers and cables to/from the box interior is made via connectors and ports which breach the endplates.

6. *Boxes provide mounting surfaces for circuits of the Front-End Board (FEB):* Within a MINERνA PMT box, a part of the FEB plugs directly into an electronics endplate feed-through board, while the remaining circuitry is housed in an aluminum tray positioned axially along the outside the the cylindrical hull.

7. *MINERνA boxes provide the interface between the PMTs and the light injection (LI) calibration system:* Light from a reference LED is routed via optical fiber through the fiber feedthrough endplate of each box and terminates within the box in a diffuser piece. The PMT response to diffused light which is propagated through the narrow area around the optical fibers as they threaded through the cookie, is used to monitor its performance.

MINERνA PMT box mechanical design In the Alner boxes build for MINOS, the box enclosures were made from thin-wall plate, creased and welded into a rectangular box. In MINERνA, an equivalent structure is obtainable more economically by utilizing construction-standard hollow steel extrusions of circular cross-section. These can be capped by spot-welding of flanges onto each end, to which flat steel endplates can be screw-mounted.

A highly useful feature of the Alner boxes is that the metallic enclosure forms an outer shell from which the inner components can be separated. The latter are mounted on a rigid structural frame which is inserted along the axis of the rectangular enclosure. Using this arrangement, easy access to all pieces which must eventually reside within the box, is available during assembly and alignment, e.g. the loaded cookie and its fiber bundle and the PMT-holder-base assembly. This same fabrication stratagem has been adapted for MINERνA. In the latter implementation, four rigid mounting rods are attached to the interior side of the fiber feed-through endplate. The PMT-holder assembly has a receiving hole pattern which allows it to be slipped to the center of the rod frame. The unit thusly mounted can then be inserted axially into the cylindrical hull. These mechanical aspects are readily discerned in the photo of Fig. 75 which shows a partially assembled MINERνA box prior to insertion of the frame.

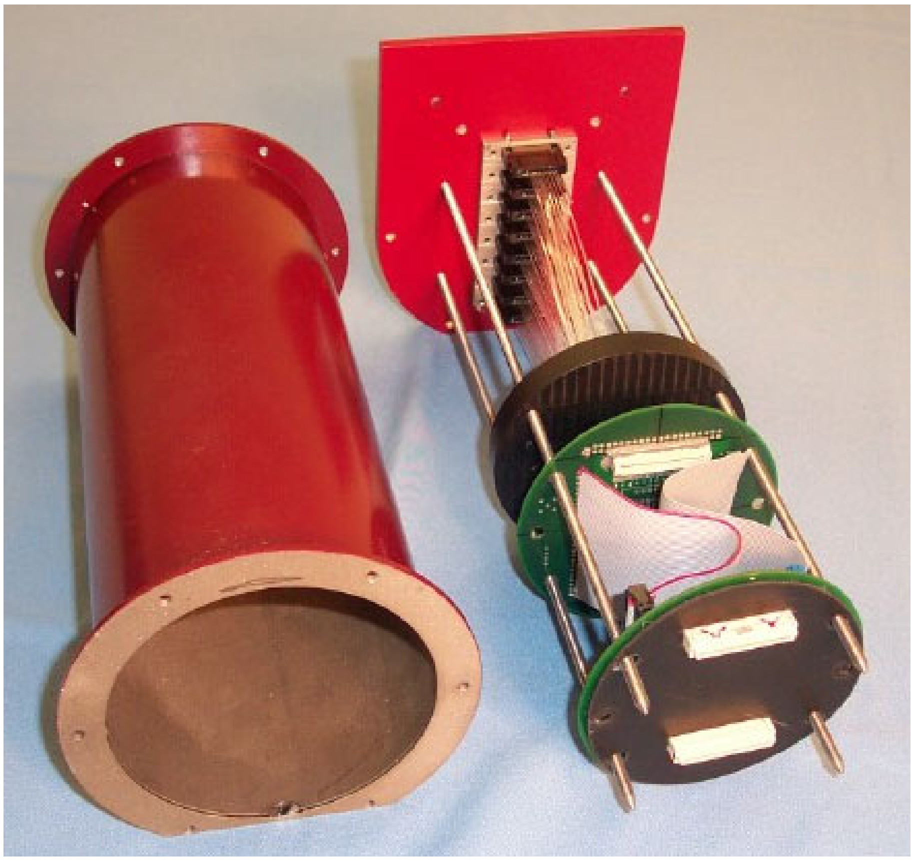

Figure 75: MINERνA PMT optical box prior to assembly. The rod frame which holds the fiber cookie plus holder plus PMT (right) is inserted axially into the surrounding steel enclosure (left).

By using construction-standard steel extrusions, it is possible to have a relatively thick-walled box at modest cost; for MINERνA boxes, wall thickness of 2.36 mm has been chosen. The result is a box which provides a useful degree of magnetic shielding for the inner region occupied by the PMT.

Alignment of fibers to pixels

Within each box, the enclosed PMT will be in optical contact with the polished ends of the bundled fibers which it reads out. This contact is made possible via termination of the fiber bundle with a precisely machined fiber mounting "cookie" - shown in Fig. 76 - which holds the polished

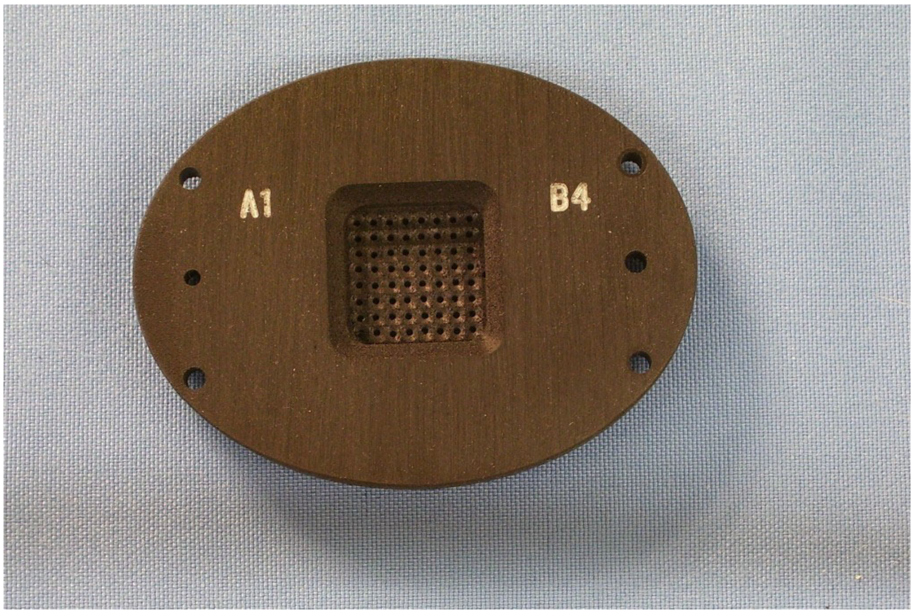

Figure 76: Optical fiber “cookie”. The hole pattern accommodates the sixty-four fibers which are routed to the box by eight fiber cables.

fiber ends. Registration of the fiber-loaded cookie to the PMT is mechanically precise. This is made possible by a precision mounting “holder” which captures the PMT and which receives the cookie; the correct positioning of fiber ends onto the PMT pixel pattern is assured via alignment pins on the holder. A holder piece is shown in Fig. 77. The fiber mounting cookie and the PMT holder are precision pieces CNC-milled from Noryl plastic. The cookie, precision holder, and their relation to the PMT, are indicated in the photograph of Fig. 78.

It is highly desirable to ensure that at the PMT pixel grid, signals originating at neighboring locations within the detector receive a degree of isolation; otherwise, pixel to pixel cross-talk can obscure the assignment of pulse heights to track hits. In order to provide a degree of isolation, a simple weave pattern is used in the routing of fibers onto the cookies. The weave pattern is a “row-pair interleave weave”; the fiber-to-pixel association which it introduces is shown in Fig. 79.

Box endplates

As indicated previously, each end of the box hull is closed off with a steel endplate. Connections to the box interior are made via various connectors and ports which breach the endplates. The box interior layout with endplate connections can be seen in the cutaway view of Fig. 80.

All of the electrical connections are brought through one endplate (the “electronics endplate”), whereas the optical fiber connections and also the connection to the LI diffuser are brought through the opposite endplate (the “fiber feedthrough endplate”). Consequently the endplates are quite different, and the implementation of light-sealing is different. At the electronics endplate, the light seal is made via a thin-rubber gasket. The fiber feedthrough endplate however, is mechanically more complicated due to the port arrangement needed for eight separate fiber cables. On the interior surface

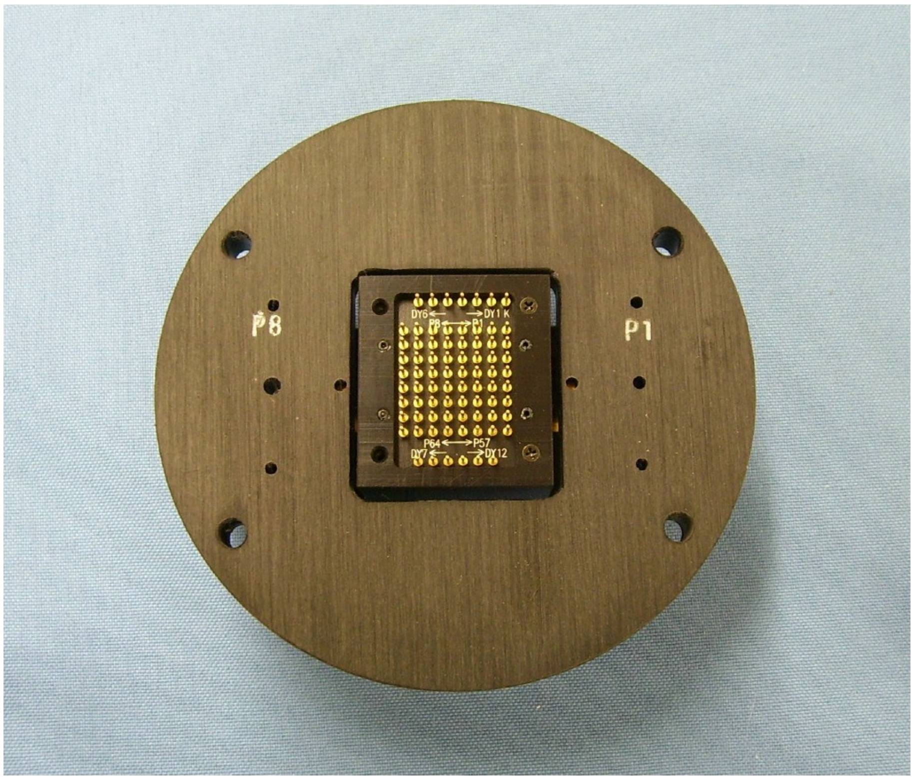

Figure 77: The precision PMT holder. The PMT is held so that its pixel grid relates to the holder locating pins in a precise and reproducible way.

of this endplate, sets of small aluminum clips with pins are used to secure the eight plastic box connectors. Light sealing of the plate is accomplished using a sealing compound which is poured into a cavity on the outside of the endplate. The feed-through box connectors can be seen in the foreground of the photograph of Fig. 81. The sealing cavity, prior to epoxy-loading, is also clearly visible.

Box magnetic shielding of the PMT Measurement of the magnetic fields in Near Hall regions immediately upstream of MINOS was carried out by M. Bonkowski [159]. An ambient magnetic field of five gauss exists throughout the area to be occupied by the MINERνA detector. In the space immediately downstream of MINERνA and in front of the first magnetized plane of MINOS, the ambient field will be larger; the measurements show ten gauss at the downstream end of MINERνA, increasing to 21 gauss within a few inches of the MINOS front plane. Ambient field of the latter magnitude, if it were to be allowed to pervade the volume occupied by MINERνA's M64 PMTs within their optical boxes, could be deleterious to phototube performance. Measurements of M64 response to magnetic field are provided by Hamamatsu; it is observed that PMT output is reduced to 92% in the presence of an axial magnetic field of five gauss (Hamamatsu curves are reproduced in Ref. [160]. Consequently it is required that MINERνA PMT boxes provide, in addition to a light-tight enclosure, an environment for the PMT which is well shielded magnetically.

This goal is achieved in the MINERνA design as the result of two features: Firstly, the wall of the

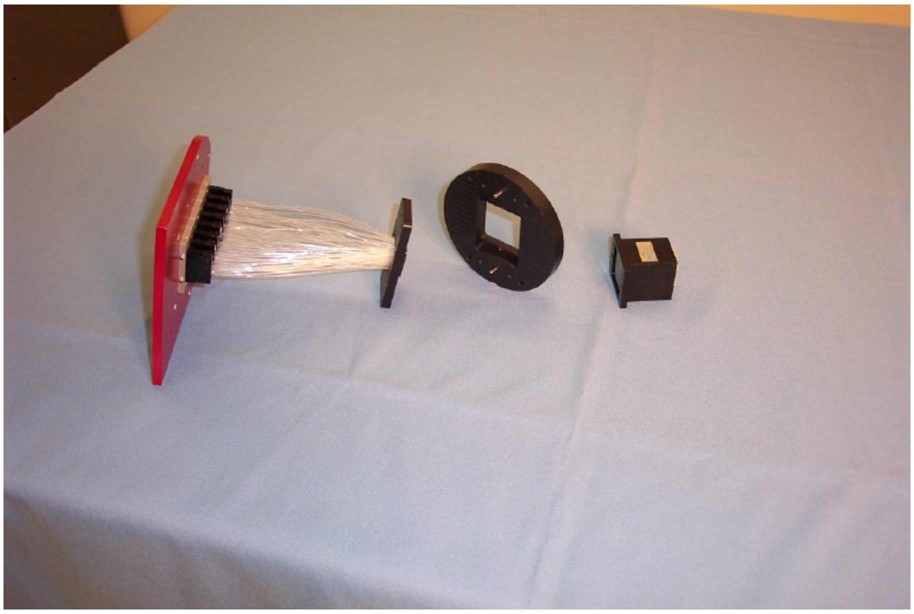

Figure 78: Photograph shows a fiber-loaded cookie, oriented towards the face of the precision holder onto which it is to be mounted using alignment pins. The PMT plus its holder - shown on the right - is affixed into the holder (at the PMT testing sites) in a way which relates the PMT pixel grid to the locating pins of the holder.

box cylindrical hull is made of 2.36 mm steel; this is distinctly thicker than either of the MINOS box implementations which have adequately provided magnetic shielding for PMTs deployed in environments similar to MINERνA's Near Hall location. Secondly, cylindrical containers are especially effective in shielding from ambient fields provided that the cylinder axis is tranversely oriented relative to the ambient field direction. The latter situation is in fact the case for deployment configuration planned, wherein the cylindrical box axes are oriented transversely and radially with respect to the spectrometer's central axis. In this orientation, PMT box axes are everywhere roughly transverse to the ambient toroidal field arising from the MINOS coil current. An additional design feature, which has been thoroughly explored using Hall probe measurements (see below), is the capability of each box to readily accommodate a mu-metal foil insert should it prove necessary. The foil insert is to be wrapped cylindrically, so that it defines an interior volume within which each PMT resides. The foil acts like a conducting path for B-field lines, drawing them away from the PMT and routing them around it.

Magnetic shielding capabilities of the MINERνA PMT box were examined by placing an assembled box in various orientations within 20 gauss ambient B-fields created using Helmholtz coils. A Gaussmeter with axial and transverse Hall probes was used to measure the leakage field pervading the box interior. It is observed that the MINERνA box provides a field reduction factor (outside/inside-center) of about ten when the box axis is oriented transversely to the external B-field; in the most unfavorable orientation - box axis parallel to ambient $\vec{B}$ - the reduction factor drops to four. With the introduction of a mu-foil inner surface, the reduction factor with unfavorable box orientation is increased from factor four to factor ten. Fortunately, the magnetic shield provided to MINERνA

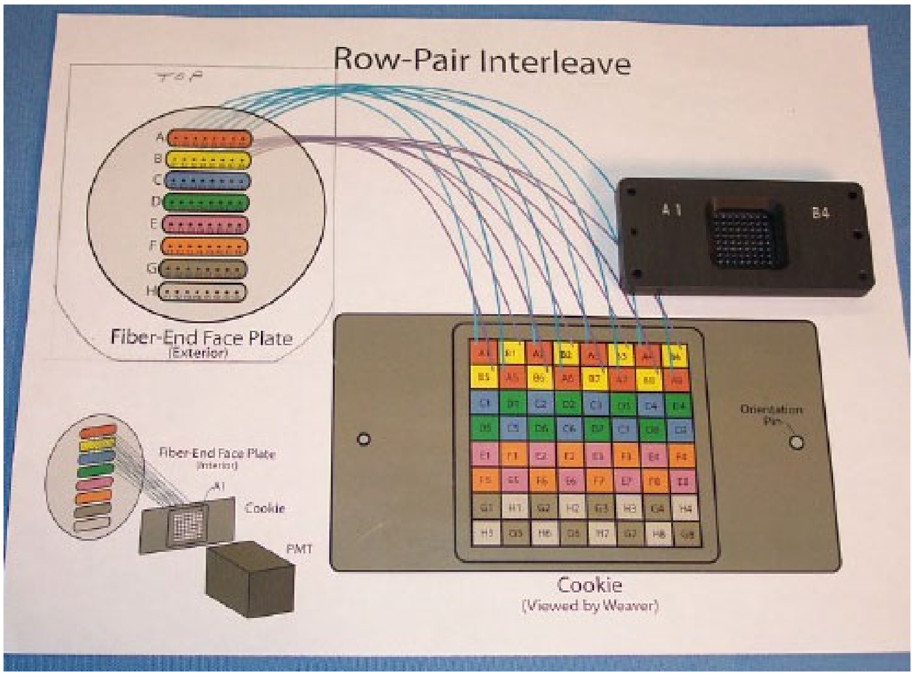

Figure 79: The weave used in placing optical fibers into the cookie grid. The resulting row-pair interleave pattern is designed to minimize signal reconstruction confusion arising from pixel-to-pixel cross-talk.

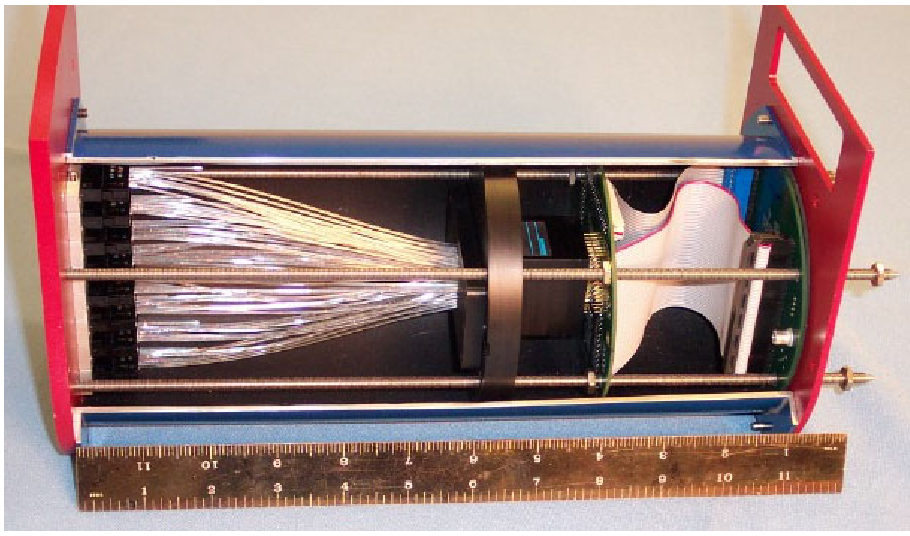

Figure 80: Interior structure of an optical box: Optical fibers enter from the outside via connectors through the fiber feedthrough endplate (left side) and terminate on the cookie. The pixel grid of the M64 phototube is registered to the cookie hole pattern via precision mounting pins which are part of the PMT holder. Cables provide voltage and signal connections to the PMT from connectors which breach the electronics endplate (right side).

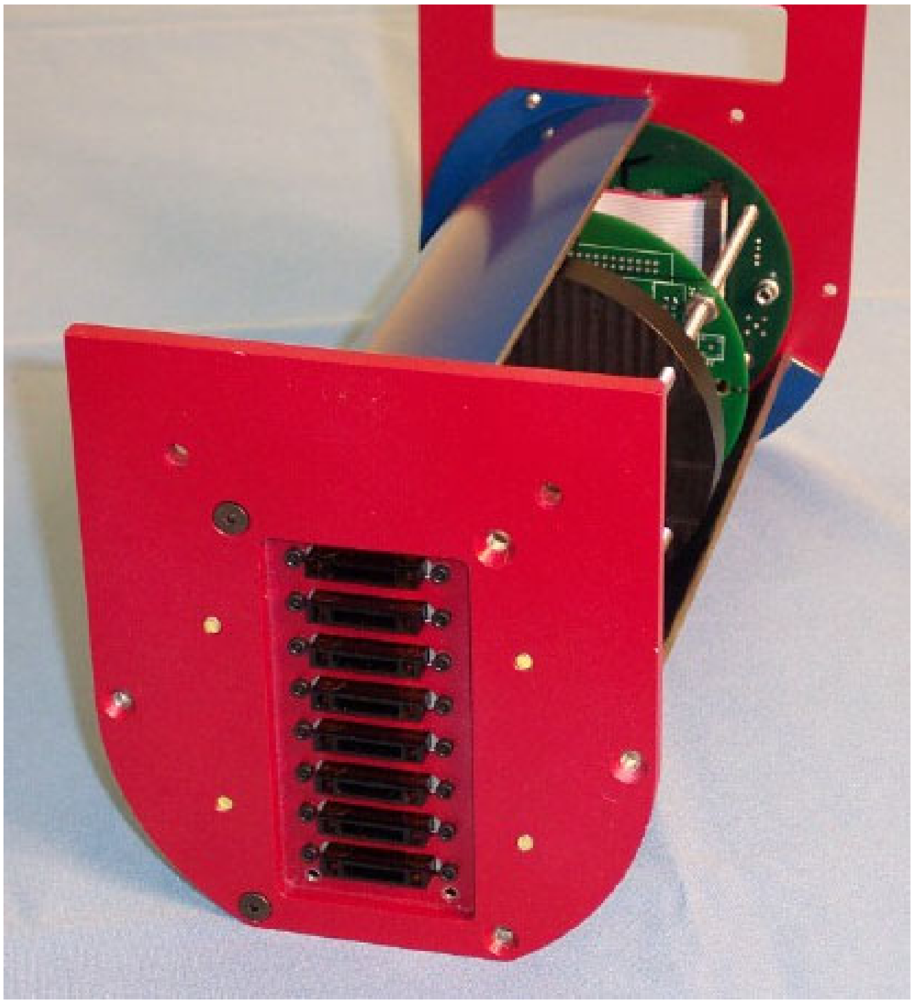

Figure 81: Fiber feed-through endplate - exterior view.

PMTs appears to be sufficient in either orientation and without the mu-foil augmentation, provided that the MINERνA detector is operated without its own magnetic field. Details of magnetic shielding measurements with the MINERνA box design can be found in Ref. [160].

Mounting the box array on the detector Each MINERνA box has two steel mounting pins which are welded to the fiber-feedthrough endcap. The pins allow each box to be loaded - with fiber connectors radially inward, electronics endcap radially outward - into a structural framework mounted atop the spectrometer's two upper/outer surfaces. The framework provides a standoff space from detector surfaces to facilitate fiber cable routing and their connections to the PMT box array. The mounting arrangement positions the circuits and connections of the signal Front-End boards on the elevated, outer surfaces of the boxes, thereby facilitating access to them for diagnostic work and for repair. The layout is designed to allow rapid removal and replacement of individual PMT boxes, should that be needed during running of the experiment.

Factory production Mass production and checkout of PMT boxes requires that dedicated factory fabrication areas be set up. Moreover, frequent utilization of modern, staffed machine shops is a prerequisite for timely box array manufacture. In MINERνA these resources - in the form of dedicated university shops - are available at two factory sites which are being developed at Tufts and Rutgers universities. The factory sites will operate concurrently and independently. In steady-state operation, each factory will produce functional boxes at a rate of approximately one box per two working days. Workstations are being deployed at the factories which will carry out the following:

1. Machining of precision PMT holders and fiber mounting cookies (Tufts).
2. Machining of box endplates and flanges.
3. Spot-welding of endplate flanges to cylindrical hulls.
4. Electrostatic painting of box cylinders and endplates.
5. Optical fiber weaving into cookies and epoxying.
6. Cutting and polishing of fiber-loaded cookies.
7. Quality assurance (QA) testing of assembled PMT boxes.

Figure 82: A loom rig is used to thread optical fibers into cookies according to the weave pattern of Fig. 5. The central assembly is mounted so as to maximize hand access. Vertical struts on either side accomodate stabilizing supports (preferred by some operators).

Instrumentation has been designed for each workstation to facilitate execution of the task at hand. For example, the weaving and epoxying of optical fibers into cookies (task 5 above) is greatly facilitated by use of a "loom rig"; the current prototype is shown in Fig. 82. The rig holds a set-of-eight ODU cables and their fibers optimally for ease in implementing a weave.

Tasks which involve weaving of cookies, mounting of components into the endplates and onto the internal frame, final assembly of boxes and their QA testing, will be carried out in clean room assembly areas. Factory daily operations, from arrival of parts to shipment of completed boxes, will be monitored and progress will be recorded in a web-accessible database.

Assembled optical boxes will be shipped by commercial trucking to Fermilab. For this purpose, shipping containers will be built which accommodate forklift handling and which will hold a convenient (large) number of boxes.

3.3.2 PMT Alignment and Testing

The Hamamatsu multianode PMT (R7600U-00-M64) was selected for use in MINERνA. This type of multianode PMT is an incremental design improvement from the R5900-00-M64 phototubes used in several high energy experiments, including the MINOS near detector. The R7600U-00-M64 PMT meets the design requirements of the experiment (to be elaborated below); the high density maximizes the channel/$ ratio.

Alignment The first task of the James Madison University (JMU) group is to align each PMT channel with its corresponding optic fiber. The actual part number delivered by Hamamatsu is H8804-MOD2, which consists of the actual PMT epoxied in a rigid jacket or housing. This packaging, while saving a couple of manufacturing steps (manufacturing the jacket and gluing the PMT in it), does not eliminate the need of aligning the PMT pixels with respect to the optical fibers. The MINERνA PMT optical boxes (see Sect. 3.3.1) contain precision–machined mounting cookies which capture the 8×8 array of optic fibers and press them on the face of the PMT. The optical fiber cookies are precision-mounted to the PMT holder using alignment pins. To ensure the unambiguous orientation of the cookie with respect to the PMT holder, different diameter pins are used. The only degrees of freedom allowed are between the PMT holder and the jacketed PMT.

Each PMT has 4 alignment "dots" provided by the manufacturer. Regular cookies are opaque making difficult to use for alignment purposes. A special, transparent cookie outfitted with cross-hairs will be used instead. A schematic of the alignment stand built at JMU is shown in Fig. 83. The PMT is held by the (green) holder shown in the middle of the picture, mounted on top of a set of X–Y–ϕ stages. The alignment cookie is fixed to the top plate of the device (shown in gray). The PMT can be moved using the stages with respect to the cookie–PMT holder assembly. A high resolution digital camera (Nikon...) is used to visually check the alignment. Based on the resolution of the camera we estimate that we can obtain a 10 μm alignment precision. The PMT holder has holes drilled and tapped for 4-40 screws that are used to "lock–in" the alignment once the PMT is properly positioned. These screws pass through slightly oversized holes drilled through the "ears" of the PMT jacket. A picture of the alignment station at JMU is shown in Fig. 84.

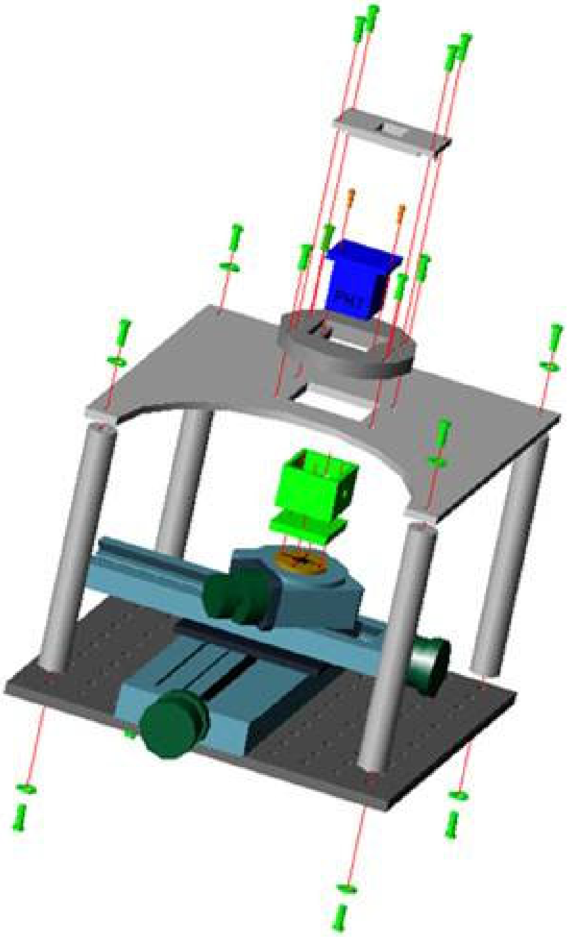

Figure 83: Schematic of the Alignment Stand

PMT Testing Once aligned, each phototube will be subjected to a series of tests to determine its suitability for use in the experiment. These tests are designed to complement and augment the testing done "in–house" by Hamamatsu and are driven by the physics requirements of the experiment.

To further understand the real meaning of some of the figures listed in Tables 10 and 11 we asked the Hamamatsu representatives to elaborate on the tests they conduct prior to delivery of PMTs. Hamamatsu tests all PMTs shipped and provides a data-sheet for each PMT that includes S_k (cathode sensitivity in μA/lm), S_p (anode sensitivity in μA/lm), dark current, Blue Sensitivity Index, and Gain (calculated from S_k, S_p). Dark current information is provided on our final test data sheet shipped with the PMTs and at no additional cost/delivery time. But, the dark current value is a total value and is not specific for each anode. Gain is calculated using the S_k and S_p values provided on the final test data sheet. Gain = S_k/S_p and this value is provided as well. Hamamatsu will provide a relative gain versus channel map and will guarantee no deviation outside the MINERνA specification of 3:1.

As seen from the above, Hamamatsu Photonics is mostly concerned with obtaining numbers that globally characterize their product. While this type of information is suitable for rejecting defective

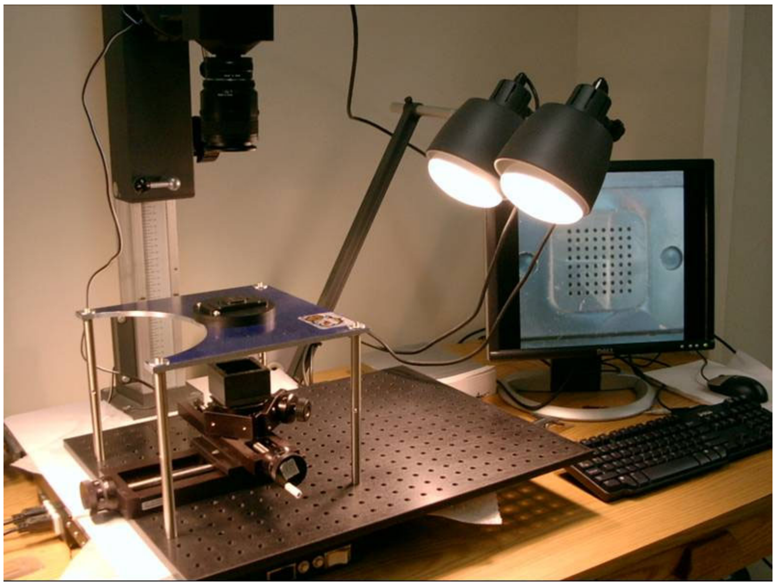

Figure 84: JMU Alignment Stand

PMTs, it does not provide the channel–by–channel data needed for MINERνA use. As outlined in the next section, the MINERνA collaboration will build a test stand enabling us to perform these more detailed tests.

The Test Stand The MINERνA test stand will be designed to test 5 PMTs at a time. Automation will allow a complete series of tests which will last less than 24 hours for a batch of 5 PMTs. The test stand will use 448 (= 7 x 64) channels of MINERνA electronics, and will assume a DAQ rate of 500 Hz and integration time of 12 microseconds. The conceptual design of the test stand is shown in Figs. 85 and 86.

The test stand will consist of:

- a) Frame: A relatively light frame which will consist of two separate sections that fit precisely together. Fig. 87 shows two views of the frame. The upper part will hold the light injection manifold. The lower one will have a plate on which several parts will reside: the traveling stages, the LED, the filter wheel, and the monitoring PMT. The relative alignment of the two frames is important to ensure that the light pen travels in x–y–z directions matching the positions of the fiber bundles. This arrangement of the support structure in two sections allows for easy transportation of the assembled test stand.
- b) Fiber optic light injection manifold: this is placed in the upper section of the frame. It will provide light from an LED to 6 M64s, one of which will be permanent and will serve as a reference PMT. The concept is shown in Fig. 86. The upper plate will hold 6 cookies+PMT's and the lower plate will route fibers illuminated by the LED to the PMT's. Each cookie will accept a bundle of 64 clear fibers, each 1.2 mm in diameter (same as will be use for scintillator

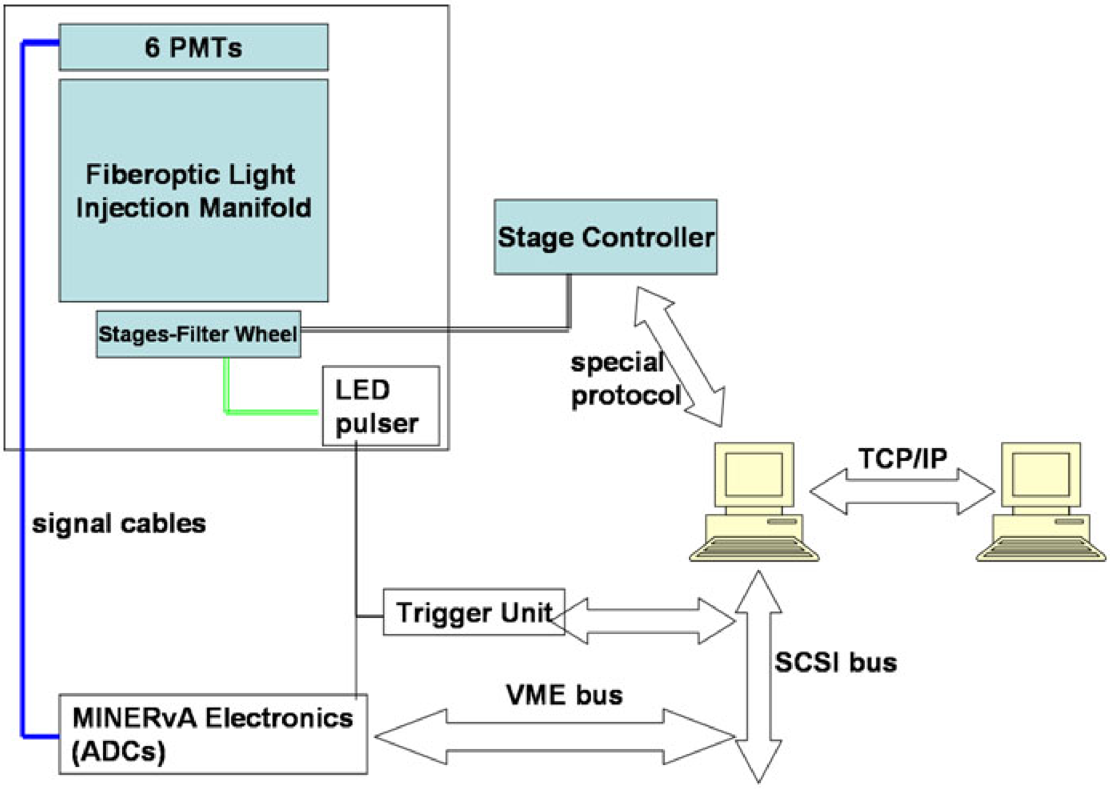

Figure 85: Schematic of the Test Stand

signals in the experiment). The lower plate has 64 holes, each of which can be illuminated by the LED. Each hole holds 6 fibers which are routed to the same pixel in each PMT in the upper plate. Thus, 64 bundles of 6 clear fibers each will emerge from the lower plate and they will get reorganized into 6 bundles of 64 fibers to match the PMT. Each LED position will send light to 6 pixels and when the LED has been in all 64 positions all 6 $\times$ 64 pixels will have been illuminated.

- c) A system of x–y–z stages carrying an LED light pen which injects light sequentially to all 64 fiber bundles. The LED travels with the system, so that no changes to the optical readout system (e.g. fiber bending) occur during the movement from bundle to bundle. The stage motion will be controlled by the DAQ PC. The LED light will go through several feet of WLS fiber to emulate the frequency distribution from the real detector. A light diffuser in each hole in the lower plate will send light uniformly to all 6 clear fibers. Before the light reaches the light pen it goes through a set of 7 neutral density filters mounted on a filter wheel controlled by a moving ϕ stage. This enables the study of the PMT response versus light intensity. A light monitoring PMT will sample the light intensity prior to injection.

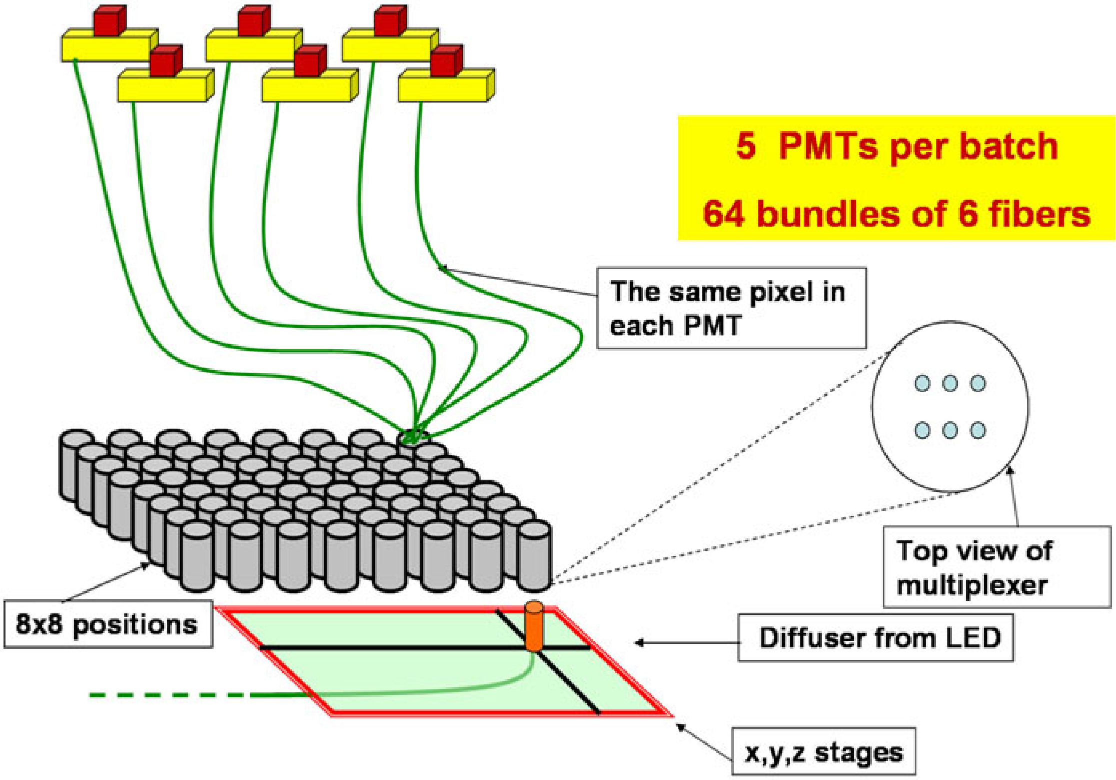

Figure 86: Schematic of the fiber optic injection manifold.

- d) MINERνA Electronics: The signals from the M64s are amplified and digitized in the same front end boards (FEB's) as will be used in the experiment. The data is then read out through VME. to the DAQ computer.

- e) Trigger: A computer controlled trigger unit will trigger the LED pulser and will provide an integration gate for the ADCs.

- f) Data analysis PC: this computer will receive the data from the DAQ computer via TCP/IP connection. Analysis done here will provide monitoring data, histograms, tables, and summaries; it will build the information that will be stored the data base.

Athens and Fermilab are responsible for the design of the test stand. The frame was constructed at Fermilab. The mounting plates and cookies were done by Tufts. The fiber-optic 64 to 6 distribution is will be done by Rutgers and is expected to be complete by the end of October, 2006. . The overall assembly of the system, including MINERνA electronics, DAQ, software, and commissioning will be done by Athens. After successful initial operation the test stand will be installed at JMU for the testing of the MINERνA PMTs. The PMT alignment will be done at JMU before the PMT's are

Figure 87: The test stand frame.

mounted to the test stand.

Initial Tests Each PMT will be subject to a series of short/quick tests. These tests will determine the optimum operating point via a high voltage scan. The optimum operating setting will have a gain of about 3×10^5 and a good one photoelectron resolution. Also at this stage we will look for dead pixels as well as grossly misaligned PMT assemblies.

Dark current The main concern is that high dark noise leads to unacceptable dead time and/or large event size. A dark noise pulse (defined as the signal produced by the PMT when no light input is present) produces a $\sim$300 ns dead time, evenly split between the integration time and the reset time. This represents a 3% dead time for the whole PMT (assume $10\mu s$ beam pulse). For a 1 kHz dark noise rate the probability of having a dark noise pulse during the $10\mu s$ beam pulse is 1%. Overall this amounts to a 0.03% dead time, assuming all tubes have the same dead time rate. Past experience (MINOS) with M64 phototubes shows that only 5% of tubes exceeded the 1 kHz rate. For MINERνA we propose to test/reject tubes that have a dark noise rate of 5 kHz in any pixel. The summed rate for the full PMT will have a higher limit.

Testing procedure The high voltage on the PMTs will be set to the nominal operating point and the system will be kept in the dark for 1 h. During this time (and the rest of the test) the temperature will be monitored/kept constant to within 2 ^oC. The DAQ will be pulsed and $\sim$10 M events will be accumulated. Counting how many times the integrated charge was greater than the 1/3 p.e. threshold will provide a measure of the dark current.

Linearity Non-linearity in the PMT response (energy vs. npe curve) leads to inaccurate energy measurement, possibly affecting particle identification. Observable non-linearities of the signal may result from space charge effects due to the small size of the M64 dynodes. One should expect to see non-linearities in the PMT response for large input signals. The MINOS experiment found non-linear effects starting at 70–300 pe, phototube dependent. Hamamatsu Photonics quotes a 5% deviation at 0.6 mA, which corresponds to $\sim$87 pe assuming typical MINERνA conditions ($\sim$7 ns pulse width and 3×10^5 gain). The typical MINERνA signal will produce $\sim$5 photoelectrons/MeV. Electromagnetic showers deposit about 20 MeV per detector element (extruded triangular prism), for a total of ~ 100 photoelectrons. The largest non-linear effects documented by MINOS were of the order of 10% at 300 pe. Even assuming a worse case scenario of 10% non-linear effects at the expected 100 pe, a modest measurement (20% accuracy) will help keep this uncertainty at a 1-2% level.

Testing procedure A remotely controlled filter wheel will vary the light intensity received from the LED. The data set will comprise of 10,000 pulses/pixel for each light intensity level. By first measuring the tube's response to a preselected reference level, say 12 p.e., the expected response, based on an assumption of linearity, may be calculated as a product of the incident light intensity, the gain, and the pixel efficiency. The incident light level is determined from the relative opacities of the filters between the reference and current points. The ratio of the measured/expected charge, when plotted over the expected dynamic range for MINERνA, will indicate the PMT's linearity.

For this test to be useful, the test stand setup must be a good match to the actual experiment. We will use the same cookie, PMT, and electronics as the experiment. The blue LED will be triggered with a fast pulser to match the experiment and a few meters of WLS fiber will shift the frequency spectrum to approximate what we will see in the experiment.

Phototubes are expected to be linear within 1% up to 80 pe. The accepted PMTs will be further tested up to 400 pe and the best tubes will be selected for the central region of the detector.

Inter–pixel cross talk For the purpose of this document cross talk is defined as the process in which one pixel of a PMT provides a measurable output when other/adjacent pixel(s) is/are illuminated. This mechanism gives incorrect energy measurements and deteriorates the position resolution (if between adjacent detector elements). Both of these affect pattern recognition/particle identification and further complicate tracking. The origin of cross talk are either electrical (charge leakage during amplification from one channel to another) or optical (light from one fiber ends up on a different pixel).

The MINOS experiment found the electrical cross talk to be small, consistent with the 2% value quoted by Hamamatsu Photonics. The amount of electrical cross talk to nearest neighbors is less than 0.5%.

Optical cross talk is potentially more damaging, as it affects the position resolution and thus tracking. Misalignments between the PMT and its holder would result in large cross talk effects, although gross misalignments should be easy to spot. This type of effect is more important for minimum ionizing particles, where the overall number of photoelectrons is small (10 pe for MINERνA). For these kind of yields an extra pe causes an error of about 10% in position resolution (about 2 mm). Optical cross talk is minimized in MINERνA using the weave-pattern described in Sect. 3.3.1 (adjacent triangles are mapped to diagonals on the PMT face).

Testing procedure Each individual pixel will be pulsed with an amplitude of about 30 pe for 10,000 pulses. The cross talk observed should be less than 5% of the primary signal for diagonally opposite pixels and less than 10% for adjacent pixels. The procedure will be repeated (with less counts/setting) for two more intensity levels.

Pixel–to–Pixel Uniformity The average gain for MINERνA will be around 3×10^5. Individual pixels will exhibit larger or smaller gains. These variations need to be contained so as to not exceed the dynamic range of the MINERνA electronics. It is anticipated that the MINERνA electronics could accommodate a 3:1 range. Previous testing done by MINOS found very few tubes exceeding this limit. The 3:1 pixel–to–pixel gain variation limit is explicitly requested in the contract with Hamamatsu Photonics and will be tested for each tube.

Efficiency Low efficiency tubes will adversely affect the photon statistics. This is especially important for minimum ionizing particles where the experiment cannot afford significant decreases in efficiency. Hamamatsu Photonics gives a typical value of 70 μA/lm, with a minimum efficiency of 60 μA/lm. Our preference would be to request that all tubes have at least 70 μA/lm luminous cathode sensitivity.

The MINERνA PMT test stand does not provide a method for measuring the absolute quantum efficiency (QE) of the PMTs. However, the procedure outlined below can measure an "effective efficiency", i.e. the product of the QE and charge collection efficiency, integrated over the whole light spectrum of the diode/fiber combination.

Testing procedure The monitor PMT will be used to correct for variations in the light input to 1 % or better. This correction will make possible comparisons between the numbers of photoelectrons detected on a pixel/phototube basis. These effective efficiencies can be subsequently normalized to one/few PMTs for which the manufacturer provides an absolute efficiency curve(s).

Summary The tests listed above will take an estimated 24 hours for 5 PMTs, including setup (loading and unloading PMTs) and data analysis.

3.3.3 Light Injection Calibration System

Any particle physics experiment with a large scintillator system such as MINERνA needs a rapid, simple, cost effective monitoring system. MINERνA has over 30,000 cintillators that must be installed, monitored, and at times replaced. The scintillators are read out with wavelength shifting (WLS) fibers which are joined to clear fibers that direct the light to Hamamatsu M64 phototubes. The PMT's sit in an iron PMT box. Confronted with the same problem, MINOS chose to inject LED light into the WLS fibers at the detector [161]. When injecting light directly into scintillators, nitrogen lasers are also used, e.g. at CDF. Our plan is to inject LED light into the PMT box, a simple and robust light injection (LI) calibrations system. The LI system is presently in the prototyping stage. Although we have a preliminary design, features are still being defined.

Function of Light Injection System

- The main application will be during installation and maintenance periods. A rapid check for dead channels and an accurate measurement of the gain of each PMT will be an important requirement.
- We also anticipate regular tests while taking data to supplement the calibration data coming from muons traversing the detector. In the MINOS near detector hall (where MINERνA will be located), the temperature is held constant to within a 6.5° range and the diurnal variation of about 1° is seen [162]. Thus, monitoring doesn't need to be continuous, but will be important whenever detector conditions change significantly (e.g. during dectctor maintenance, certainly when replacing phototubes.)
- A system such as this could also be used to measure the absolute gains non-linearities of each pixel in situ. This property will be measured as part of the PMT testing at JMU and Athens. The cost and complexity of doing a similar test with this system were deemed too large.
- As this is a moderate resolution experiment, the physics requirements are not thought to drive the design at present.

LI System Design Our design is a simplified version of the MINOS system. To keep costs down, we choose to inject LED light directly into the PMT box, some of which will be captured by the multianode PMT. Each PMT is serviced by 2 fibers to ensure that each pixel is uniformly illuminated. The light is spread out in the PMT box with a diffuser (see Fig. 88). This will enable a rapid and accurate gain check for the entire PMT.

The LED's sit in a Pulser Box near the detector; it is the most expensive part of the system. This box is presently being designed. It contains optical fanouts, the LED's and associated electronics. PIN diodes will be used initially to monitor the LED light output. They will be close to the Pulser Box. The output of this box will be 2*500=1000 fibers funneling light to the PMT boxes and the PIN diodes. The light from each LED will be fanned out to 50 PMT boxes in a cone/collar assembly similar to what MINOS used [161]. Thus, 20 LED's are expected to be enough to cover the full set

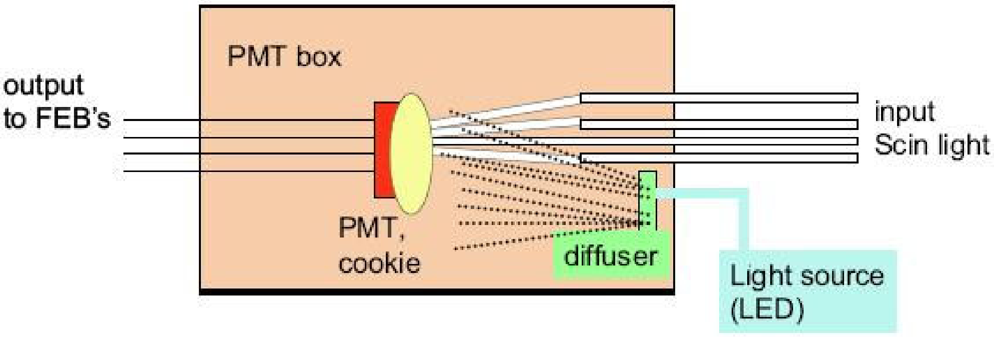

Figure 88: Conceptual picture of the way light will be injected into the PMT box. A simple prototype of this technique is discussed.

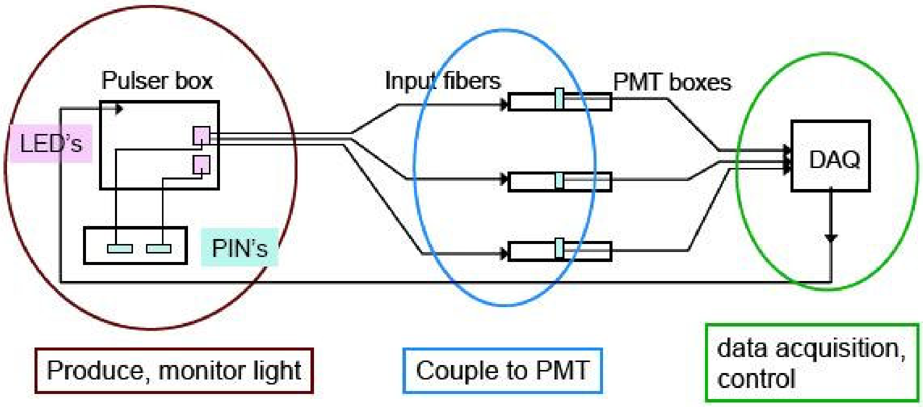

Figure 89: Design of the LI system. The DAQ computer will control the pulser box which will send out short pulses to each PMT. The repsonse will then be read out.

of 473 PMT's and the PIN diodes with a sufficient number of spares. It is clear that the mechanical stability of these components is essential.

A diagram of the system is shown in Fig. 89. The entire system will be controlled as part of the MINERνA experiment data acquisition program. Groups of PMT's will be pulsed together (like MINOS) and all PMT's and the PIN diodes will be read out each time the calibration system is triggered.

The electronics required to control the LED's are not complicated. MINOS made 3 cards for power, LED driver, and control functions. A microprocessor on the control card will determine how the LED is fired - e.g. pulse height and width. We will start with the MINOS electronics and adapt to our needs. A very fast pulser (width stable at $\sim$ 10 ns) will be required to simulate the scintillator output signals. The overall cost is low when compared with the MINOS system.

The MINOS light injection system achieves $\sim 2\%$ accuracy with careful attention to construction details and a PIN diode to monitor the LED output. Although we don't need as much accuracy, we can easily obtain few percent accuracy with the system envisaged. The main usage for this system will be to monitor the overall gain of each PMT. At present, we plan to inject green LED light into the ends of a clear fiber. This will provide a moderately good match to the frequency spectrum of light from the scintillators.

Construction Prototyping efforts to date have measured the ability to inject LED light into clear and WLS fibers. Green LED's couple well to either kind of fiber when the light is directed into the end of the fiber. For this test, the light transmitted through the fibers was measured with a PIN diode. We have also used the LED to trigger an M64 PMT in 2 realistic situations in a dark box(see Figs. 90 and 91). In the first test, light from the green LED triggered with a 4Vx100ns pulse produces a few pe signal in each PMT pixel using a prototype cookie. We have verified that at least 95% of the light reaching the PMT comes through the cracks between fiber and cookie. This test showed the need for small changes in cookie and PMT mount design to better protect the PMT from light other than what comes through the cookie. The second test (see Fig. 91) takes light from the same green LED as used in the first test. Using a cone/collar assembly from MINOS[164] (seen at the left side of the photo),light was fed through a clear fiber and aimed at the PMT in the approximate position the fiber will be located on the input plate to the PMT box. The light has to find its way through a 'forest' of 64 fibers simulating the real situation. The response for pixels on the far side of the forest was about a factor of 3 less than for pixels on the near side. When we added a diffuser (as seen on the right side of the photo), the response of all pixels showed less than 20% variation. This proves the concept in Fig. 88. Modifications to the PMT box are now complete.

Preliminary versions of the cone assembly are now being tested with the goal of defining properties of the LED and the density of clear fibers in the collar. We have purchased a fast pulser and will investigate LED's for speed, intensity, and stability. The light reaching the PMT's should not vary by more than a factor of 2 across the full set. We plan to complete prototyping efforts by end of 2006.

3.4 Calorimeters and Targets

One of the main goals of MINERνA is to improve the estimate of the incident neutrino energy based on the visible energy. The physics goals of MINERνA require measurement of the energies of charged ($p,\ \pi^{+/-},\ K^{+/-},\ \mu^{+/-}$ and neutral $\pi^0,\ K^0$ particles with energies up to a few GeV. The best way to do this would be with a fully active detector with 100% containment of the energy, but cost and location constraints prohibit a fully active detector of the required size. Instead, we have chosen a mixture of detectors with fairly standard elements.

The elements of MINERνA are: a central fully active detector, an array of alternating lead and scintillator downstream and surrounding the active detector for electromagnetic calorimetry, an array of alternating steel and scintillator downstream and on the outside of the detector for hadron calorimetry, and plates of lead, steel, and carbon upstream of the central detector for upstream electromagnetic and hadron calorimetry.

Another goal of MINERνA is to study the A dependence of neutrino interactions. The main detector is scintillator, which will serve as a carbon target. The upstream targets of iron, lead and some pure carbon, which serve as the upstream calorimetry, will do double duty as the nuclear targets.

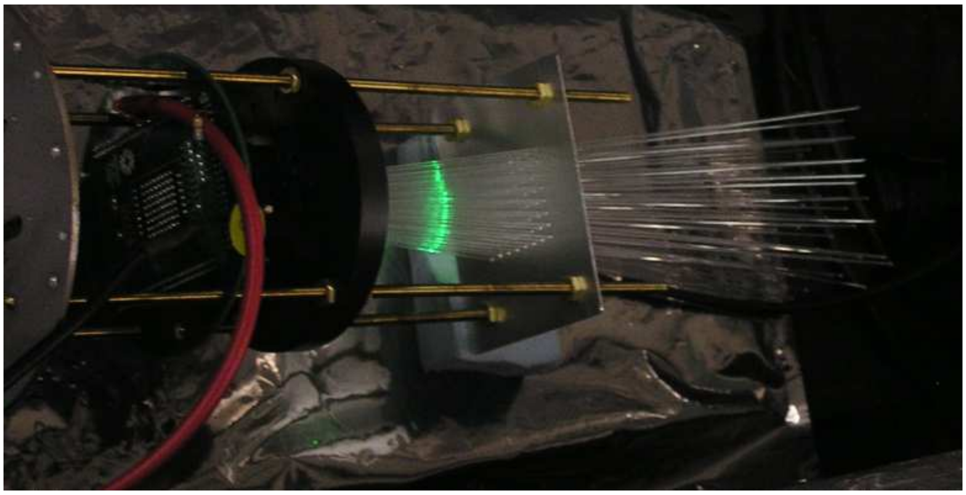

Figure 90: Prototype test of the light injection transmission to the PMT. The MINERνA PMT and prototype base (left) and cookie (hidden) are used. All 64 pixels have a fiber attached; the final design has a complicated weave, not used here. The green LED is in the approximate position of the light source for the final system. The frame, but not the iron shell, of the PMT box is used.

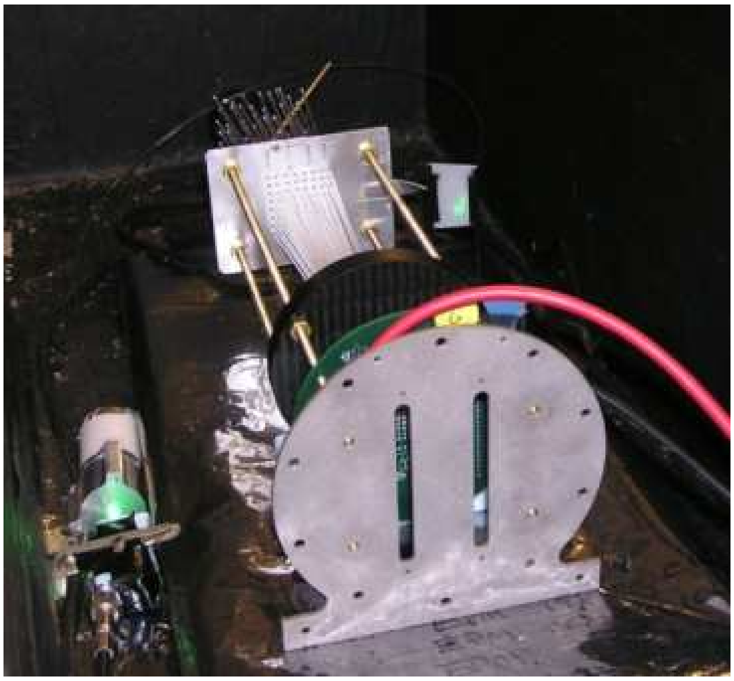

Figure 91: Prototype test of the light injection transmission to the PMT, an extension of the test shown in Fig. 90. Light is now injected into a clear fiber in a cone/collar assembly on the left of the photo. This assempty was borrowed from MINOS and is very similar to what will be in the full design. The fiber (not seen) loops around the apparatus and is aimed at the PMT (right). A diffuser is shown.

The general criterion for the calorimetry is that hadronic energy and electromagnetic showers originating in the central tracking region should be fully contained. This is most critical for the downstream calorimetry because for the neutrino energies of interest the particle production is strongly peaked in the downstream direction and those particles have the highest energy.

The requirement that the upstream elements do double duty as both calorimeters and nuclear targets, means that care must be taken to allow them to serve effectively in both roles.

3.4.1 Electromagnetic Calorimeters

The detection of high energy photons is through the pair-production/bremsstrahlung process leading to a shower of e^+, e^- and γ. Because the pair production cross section is proportional to Z^2, lead sheets are generally used to produce a shower of reasonable length. The characteristic length of the shower varies with energy, but for photons up to a few GeV, as expected in our energy regime, 99% of the energy will be contained within 4 cm of Pb (about 7 radiation lengths).

The downstream electromagnetic calorimeter will consist of 20 layers of Pb, each 2 mm thick, interleaved with one layer of scintillator, consisting of the standard 1.7 cm thick layer of triangular strips. Arrangements such as this have been widely used in the past. The expected energy resolution is approximately 6%/$\sqrt{E}$, with E in GeV.

The side calorimetry is quite similar. Trapezoidal sheets of Pb, also 2 mm thick, will be interleaved with each layer of scintillator. The sheets will extend 15 cm into the active area. Photons entering the side calorimeter will be fully contained for angles less than about 25° with respect to the neutrino beam axis. At larger angles the shower will not be fully contained, but will penetrate into the outer hadron calorimetry, where the remainder of the shower will be fully contained, but less well sampled, leading to a decline in resolution.

Because the primary purpose of the upstream Pb/Fe/C plates is to serve as nuclear targets, the design does not allow as efficient calorimetry as the downstream and side modules. The sampling is more coarse because the Pb/Fe/C plates are thicker than in the downstream calorimeter. The arrangement of targets means that the number of radiation lengths the shower sees before escaping from the upstream end will vary from 5 to 10. However, since the backward going photons will generally be much lower energy, showers starting in the active central region will be fully contained.

3.4.2 Hadron Calorimeters

The downstream hadron calorimetry will consist of 20 layers of iron, each 2.54 cm thick, interleaved with one layer of scintillator between plates, downstream of the electromagnetic calorimeter. The combined thickness of the 4 cm of Pb and 50 cm of Fe will stop muons up to about 600 MeV and protons up to about 800 MeV. One nuclear interaction length is 16 cm for Fe, so higher energy protons (or pions) will also generally be stopped.

The side hadron calorimeter consists of a plates of iron 55.9 cm thick, with fives slots, each 2.5 cm wide, filled with scintillator. The total iron thickness is 43.4 cm, or 340 g/cm^2, which can stop, from ionization losses alone, up to 750 MeV protons at 90° and nearly 1 GeV protons entering at an angle of 30°.

The resolution of the hadron calorimeter, based on studies by MINOS, is expected to be about $50\%/\sqrt{E}$ for hadron energies above 1 GeV. The resolution for lower energy particles is expected to be 50% or less, depending on the energy. The primary reason for the poor resolution is the likely interaction of the particle with a nucleus before stopping, which frequently produces one or more energetic neutrons whose energy is unobserved, making it difficult to get good energy resolution

As with the upstream electromagnetic calorimetry, the upstream hadron calorimetry relies on the nuclear targets, with a less efficient design than the downstream calorimeter. The upstream mass thickness is sufficient to stop protons originating in the active central region of at least 300 MeV.

Studies show that the visible hadronic component of quasi-elastic and resonant events originating in the fully-active central region of the detector are completely contained, apart from secondary neutrinos and low-energy neutrons. Figure 92 shows the fraction of escaping visible hadronic energy for deep-inelastic reactions in several hadronic energy ranges, and figure 93 shows the probability that a deep-inelastic event will leak visible energy as a function of the true hadronic energy. Only for hadronic energies greater than 8 GeV is there any significant probability of leakage and only above 15 GeV is the average fraction of escaping energy greater than 10%. The fraction of deep-inelastic interactions with hadronic energies over 15 GeV in the low-energy, medium-energy, semi-medium or semi-high energy beams is $< 1\%$, and so visible energy leakage should be insignificant. These estimates ignore downstream components beyond the forward hadron calorimeter, such as the MINOS detector, and are therefore conservative.

To study MINERνA's calorimetric E_h resolution, the detector response to a neutrino sample generated throughout the inner detector by NUANCE, on carbon and hydrogen targets, was simulated using GEANT3. From this simulated sample, events where all hadronic fragments were contained within MINERνA were used. Hits from lepton tracks in charged-current interactions are excluded from the following analysis.

In a fully-active scintillator calorimeter, the total light yield should be essentially proportional to E_h. (The proportionality is not unity due to escaping neutrinos, rest masses of charged pions, nuclear binding energy in the initial and secondary reactions and other nuclear effects such as pion absorption.) While the central inner detector volume is fully active, there are also regions with passive iron or lead absorber sandwiched between scintillators. In these sampling calorimeter regions, not all energy deposited results in scintillation light, so the light yield is corrected accordingly.

3.4.3 Nuclear Targets

The MINERνA nuclear targets will consist of carbon, iron, and lead. Hydrogen is also present as a component of the scintillator in the active target. However, separating reactions on hydrogen from those on carbon will be extremely difficult and dominated by systematics. Iron is chosen both as a relatively inexpensive medium mass target and as the absorptive material used in many neutrino detectors, such as MINOS. Lead is the highest nuclear mass material that is easily obtainable.

There are a number of criteria that determined the nuclear target design. The ideal arrangement of nuclear targets would have many thin targets with several tracking layers in between each target in order to determine multiplicity of final states and the amount of energy going into relatively low energy particles. There are a number of factors which limit the number and size of targets, as well as the number of tracking layers.

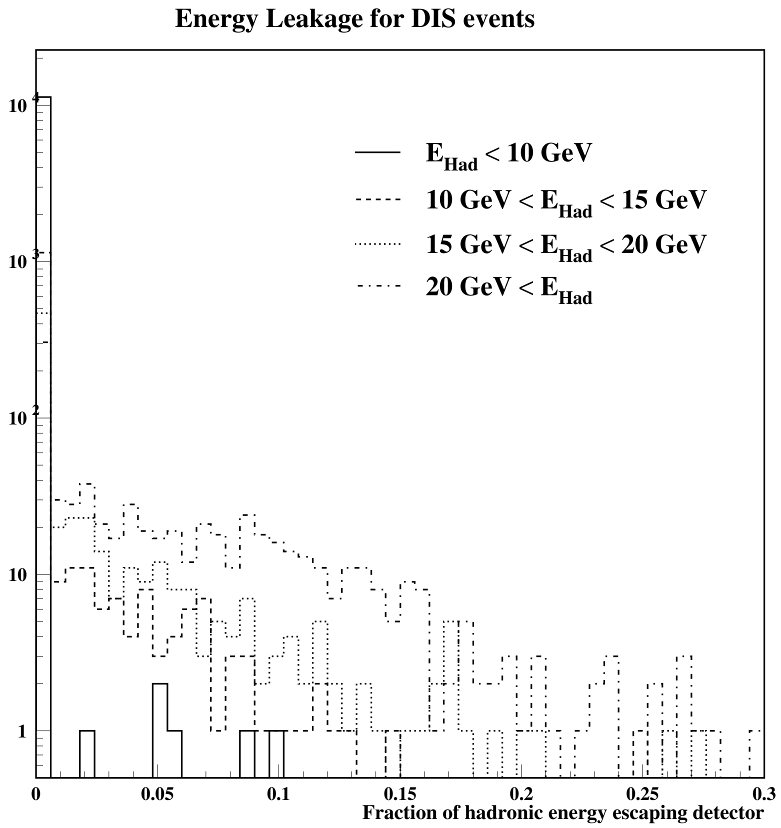

Figure 92: Fraction of hadronic energy escaping the detector for deep-inelastic scattering in the fully-active central region.

The intrinsic spatial resolution of the detector is of order 1 cm, so thinner targets will be inefficient. MINOS used 2.5 cm iron plates, so plates thicker than this will not allow significant improvement of the knowledge of the low energy particle spectrum, which is one of the goals of MINERνA. In order to get sufficient statistics over a wide range of kinematics, we would ideally like of order 1 ton of each target. The number of frames required to determine a single stereo point is two (an XU and an XV). We would at least two of these points, or four frames, between targets in order to determine the trajectory of short tracks before they enter the next detector. A thickness of 4 frames will stop a straight going proton of 200 MeV. However, because we wish to use MINOS for muon identification, we cannot put too many tracking planes between target plates or use too many plates since the upstream target will then be too far from MINOS a large fraction of the muons will miss MINOS. In addition, we would like to have similar detection configurations for each of the three materials.

The design we have decided on his shown schematically below, with the most upstream section on the left. Each "F" represents one frame, either an XU or XV, and an "FF" pair will be a set of XUXV.

FF Pb/Fe [1] FFFF Pb/Fe [2] FFFF Pb/Fe/C [3] FFFF Pb[4] FFFF Pb/Fe [5]

Targets [1] and [2] will be 2.5 cm thick Pb and Fe mounted in one plane. The areal coverage will

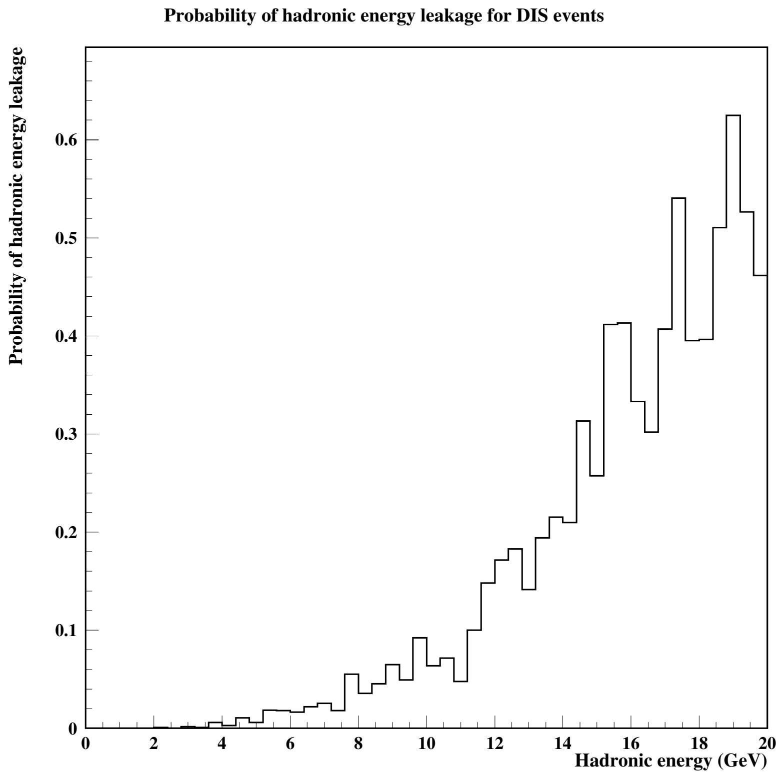

Figure 93: Probability that visible hadronic energy from a deep-inelastic event escapes undetected vs. total hadronic energy.

be 60% Fe and 40% Pb, which gives about 230 kg of Pb and Fe in each target within a radius of 80 cm. Target [3] will have areal coverage of 50% C, 30% Fe, and 20% Pb, which gives 140 kg of C and 110 kg each of Pb and Fe. The Pb and Fe targets will again be 2.5 cm thick, and the C target 7.5 cm thick. Target [4] will be 0.75 cm thick pure lead, with a mass of 170 kg. Target [5] is 1.25 cm thick Pb and Fe, again 60% areal coverage in Fe and 40% in Pb, with a mass of about 115 kg each. To illustrate the feasibility of these hybrid targets, Figure 94 shows engineering drawings of Targets [1] and [3].

The total mass of Fe and Pb are 685 kg and 855 kg, respectively. The expected number of CC events are about 2.0 million for Fe, 2.5 million for Pb, and 400,000 for C.

The first two frames will allow us to determine if a particle going through the upstream veto detectors originated in the first nuclear target or outside the detector. Targets [1] and [2] will have the Pb and Fe rotated with respect to each other to allow checks for differences in detection. Target [3] contains all three nuclei with essentially the same detection capability to allow detailed studies a the A dependence of interactions. Target [4] is pure lead to insure that any produced photons, either from the upstream or downstream targets, begin to shower. The Pb sheet is about 1.5 radiation lengths thick, which is enough to begin the shower but not enough to contain it. Target [5], directly upstream of the fully active central detector, will give allow us to study multiplicities and distributions of lower energy particles with good tracking and energy resolution.

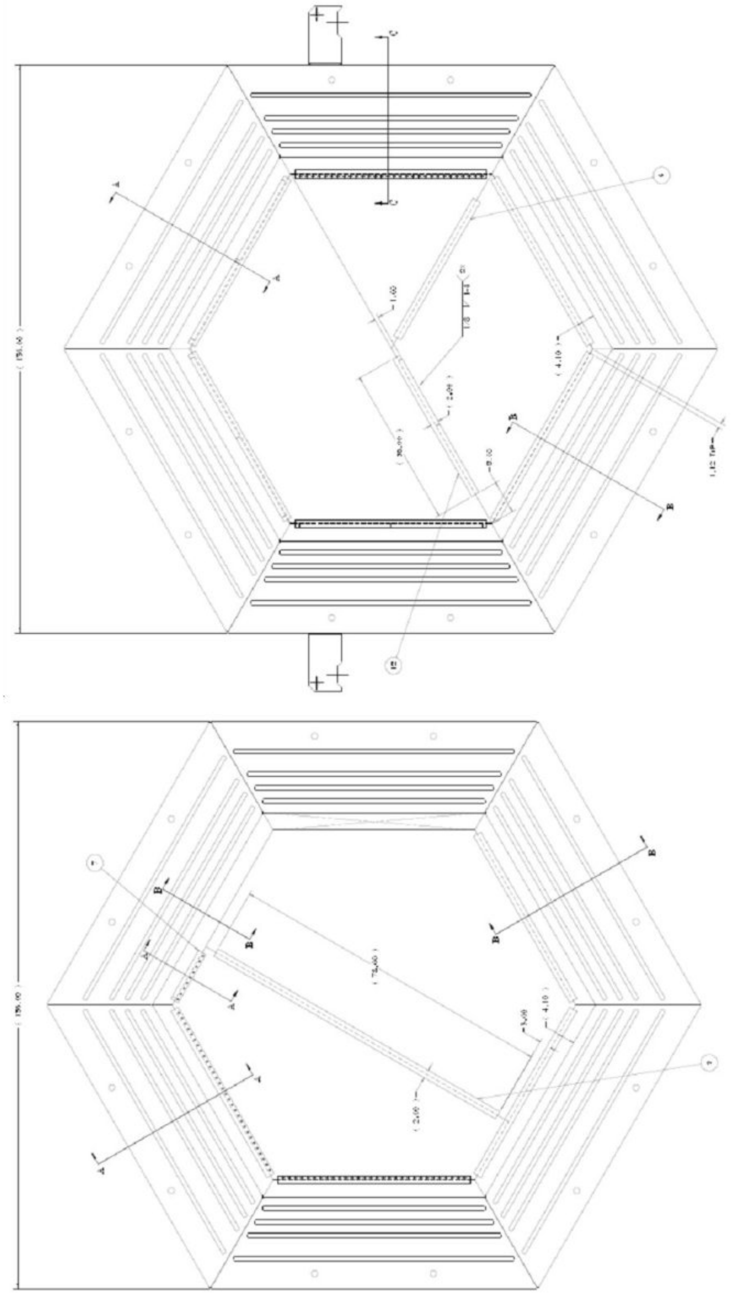

Figure 94: Engineering design of nuclear targets #1 and #3

We have studied this arrangement with our standard Monte Carlo. We find that it satisfies most of our requirements. Most importantly, energy containment for events originating in the central detector is good for upstream (backward) going particles despite there being less material, due to the fact that the backward going particles are lower energy. The energy of charged hadrons and photons from neutral meson decay resulting from quasi-elastic and resonance reactions is almost 100% contained, due to the very forward peaked nature of these reactions. For the most upstream nuclear target, energy confinement is worst for DIS reactions. The high multiplicity of these events produces some lower energy particles going upstream. However, over 90% of produced protons and charged pions are fully contained. Only photon containment is significantly worse than the central region. For incident neutrino energies above 2 GeV about 80% of the photon energy is contained. Thus we conclude that all targets can be used for studies of all interaction types at all energies with only moderate loss of resolution due to lack of confinement.

3.5 Electronics, DAQ, Monitoring and Slow Control

The requirements for the MINERνA electronics are summarized in Table 13. These requirements are motivated by the experiment's physics goals, which include:

- Fine-grained spatial resolution, exploiting light-sharing between neighboring scintillator strips,
- Identification of $\pi^{\pm}$, $K^{\pm}$ and p using dE/dx information,
- Efficient pattern-recognition, using timing to identify track direction and separate interactions occurring during a single spill,
- Ability to identify strange particles, and muon decay, using delayed coincidence, and
- Negligible deadtime within a spill.

The average data rate expected for MINERνA ($\sim$ 100 kByte/second) and the relatively modest duty-factor of the NuMI beam (one $\sim$ 10 μs spill every 2 seconds) are far from demanding, by the standards of modern high-energy physics experiments.

Electronics and DAQ systems are needed not just by the full MINERνA detector but in a number of other testing and measuring subsystems which will be commissioned earlier. The needs of the complete detector, the photomultiplier tube testing station and the module mapper are:

- PMT Boxes: All(473) Transition boards/cables (Interface between PMT base and FEB)
- PMT Testing: All(473) PMT bases, 7 FEB/FESB, 1 CROC, and stand-alone DAQ system for PMT testing
- Module Assembly/Mapping: 7 PMT bases, 7 FEB/FESB, 1 CROC, and stand-alone DAQ system for module scanning

3.5.1 Front-end Electronics

The front-end boards digitize timing and pulse-height signals and provide high-voltage for the photomultiplier tubes (PMTs), and communicate with VME-resident readout controller modules over an LVDS token-ring. For easy access in connection, testing and replacement, the boards are mounted *outside* the light-tight PMT housing assemblies. Pulse-heights and latched times will be read from all channels at the end of each spill.

The front-end board for MINERνA is designed around the D0 TriP-t ASIC which is a redesign of the readout ASIC for the D0 fiber tracker and preshower. The TriP-t chip has suitable capabilities for use in MINERνA. The most significant technical risks have already been addressed by our successful 2004 R&D program, using a prototype board fabricated using available TriP chips from D0.

Requirements and design features Each front-end board (FEB) will service one PMT (64 channels) which will require 6 TriP-t chips per board. The TriP-t chips will be controlled by a commercial FPGA (Field-Programmable Gate Array) using custom firmware. A prototype of this firmware has already been developed and successfully operated during our R&D studies. In addition to digitization of charge and timing information, the front-end boards will also supply high-voltage to the associated PMT and communicate with the downstream readout system over an LVDS (Low-Voltage Differential Signaling) link. The FEB will attach to the PMT box via the transition board that is mounted to the rear of the PMT box. Figure 95 shows the basic design of the board and the main components. Table 14 summarizes the channel counts for the final design.

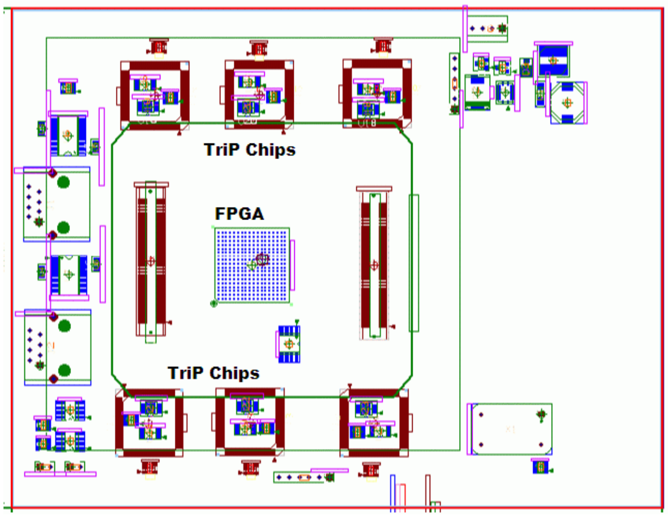

Figure 95: Simplified schematic of the front end electronics 2nd prototype board.

The TriP-t chip and digitization The heart of the system is the D0 TriP-t ASIC. The TriP-t chip was designed by Abder Mekkaoui of the Fermilab ASIC group and has undergone extensive testing by D0 [165]. Its analog readout is based on the SVX4 chip design. Each TriP-t chip supports 32

Parameter	Value	Comments
Active spill width	12 μsec	Spill plus $2\tau_\mu$
Repetition Time	$>$ 1.9 sec	
Number of channels	30272	
Occupancy per spill	2%	LE beam, 2.5E13 POT/spill
Front-end noise RMS	$<$ 0.2 PE	
Photo-detector gain variation	4.5 dB	Extremes of pixel-to-pixel variation
Minimum saturation	350 PE	Proton range-out or DIS event
Maximum guaranteed charge/PE	50 fC	Lowest possible charge at highest gain
Time resolution	3 ns	Identify backwards tracks by TOF
		Identify decay-at-rest $K^\pm$

Table 13: Electronics design requirements and parameters for MINERνA

Item	
Number of FEB boards including spares(15%))	545
Number of PMT's serviced per board	1
Number of PMT channels serviced per board	64
Number of ADC channels per board	192 (Low, Middle, High Gain)
Number of TDC channels per board	64
Number of HV channels per board	1

Table 14: MINERνA front-end board channel summary.

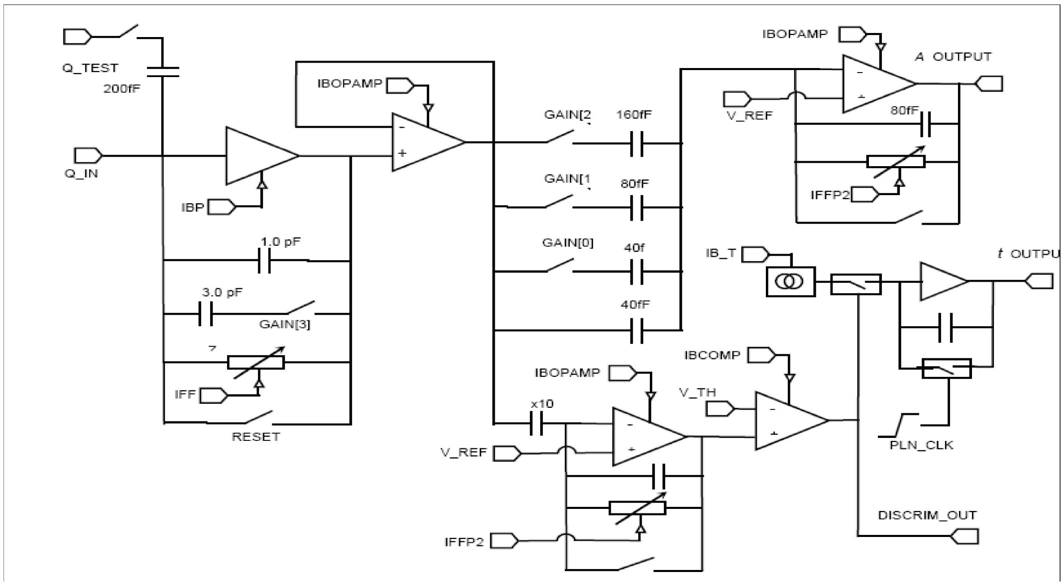

Figure 96: Simplified schematic of the front end electronics of the TriP-t chip.

channels for digitization, but only half that number of channels for discrimination and timing. A simplified schematic of the TriP-t ASIC is shown in Figure 96. The pre-amplifier gain is controlled by jumper GAIN(3) and has two settings which differ by a factor of four. The gain of the second amplifier stage is controlled by jumpers GAIN(2)-GAIN(0). We will set the chip to the highest gain setting for the preamp and lowest integration capacitor. This gives a linear range with a maximum charge readout of 1 pC. The "A OUTPUT" goes into a analog pipeline, which is identical to the one used on the SVX4 chip and 48 cells deep. To gain dynamic range, MINERνA will increase the input range of the electronics by using a passive divider to divide charge from a single PMT anode among three TriP-t channels. Each TriP-t channel will be digitized by a 10 bit ADC.

Based on Monte Carlo studies of proton identification by dE/dx, the MINERνA design requires no saturation below 350 photoelectrons (PE) and RMS noise well below 1 PE. Matching this to the 1 pC charge limit, the highest gain anodes in a tube would be set at 100 fC/PE and therefore the lowest gain anodes would be run at 33 fC/PE. In MINERνA the integration time for the ADC will be 10–12 μs, much less than the hold time for the charge in the capacitor of 100 μs. The prototype MINERνA board has been tested explicitly with a 10 μs gate, and pedestal RMS was found to be $<$2 fC. This will put a single photoelectron approximately a factor of 10 above the pedestal RMS, well within our requirements. The maximum PMT gain for the lowest gain anode will be 50 fC/PE, safely within the desired parameters above.

Timing Only one of every two input channels to the TriP-t chip have a latched discriminator output (latch) which can be used for timing information. Hence, only the lower range channels will feed the latch whose output will then go into an FPGA. With appropriate firmware, internal logic of the FPGA can be used measure timing with a granularity of 5 ns. To measure the time of the latch firing accurately, the RF/2 reference clock from the Tevatron (approximately 25Mhz) is multiplied by four in a PLL and phase shifted by 90deg to form a quadrature clock that is used inside the FPGA to form a digital TDC with least bit resolution of 2.5ns. This feature has also been tested on the prototype board and a timing resolution consistent with the 2.5 ns least count timing resolution of the TDC's has been achieved. The reset time for the latch is only 15 ns, so inside a spill the latch will be in the ready state by default. When the signal exceeds a threshold of 1.5 PE, the latch will fire. After storing the time, the latch is reset, incurring minimal deadtime.

Each board includes its own high-frequency phase-locked oscillator, which provides a local clock signal for the FPGA logic. Global synchronization is provided using an external counter-reset reference signal distributed over the LVDS interface from the VME readout boards once every second, and originating with a MINOS timing module which is, in turn, synchronized to the NuMI beam.

High-voltage and Front-End Support Board (FESB) A Cockroft-Walton(CW) high-voltage base supply will provide power to each board's PMT. The Cockroft-Walton high-voltage supply will be split between two boards: one that resides in the PMT box and contains passive components and a second board (Front-End Support Board - FESB) that will be attached to the outside of the PMT box and contain the CW oscillator elements. The CW card that resides in the PMT Box will also map the analog PMT pixel signals to connectors on the transition board. The auxiliary card (FESB) design will allow a malfunctioning high-voltage supply to be easily replaced without changing the main readout board. In addition the FESB will physically seperate the CW oscillator elements from the incoming analog signals from the PMT to reduce noise pickup and by reducing the physical size of the FEB improve its cooling capabilities. An existing Cockroft-Walton controller design (developed at Fermilab) will allow the PMT voltage to be monitored, adjusted or disabled over computer control, using the LVDS interface.

LVDS interface As detailed in Section 3.5.2 each front-end board will be a member of a chain (or token-ring) connected by LVDS to a VME-resident readout controller. As such, the front-end boards require two LVDS connections, one to receive data from the previous member, and another to transmit data to the next. The LVDS interface transmits all information to and from the board, including:

- Transmission of digitized timing and charge data from the front-end board to the VME readout controller,
- Write access to the front-end memory buffers, for diagnostics,
- Configuration of the TriP-t chip registers (thresholds, gains, etc) for data-taking,
- Reprogramming of the flash ROM containing the front-end board's FPGA firmware, and
- High-voltage control and monitoring messages.

The first prototype front-end board used in our 2004 R&D studies was designed to accommodate an LVDS interface, was commissioned and tested in late-2004/early-2005.[5] This subsystem represented the most significant remaining technical risk in the electronics (now that the TriP-t digitization and timing scheme has been successfully tested), as the latency in propagating signals from one front-end board to another via LVDS limits the number of boards that may be linked in a single chain, and hence the number of chains (and VME readout boards) required to service the full detector. The latency tolerance is constrained by the need to transmit a global timing synchronization signal to all front-end readout boards. As explained in Section 3.5.2, pending prototype testing we estimate approximately 100 ps jitter may be introduced by each link in the chain. As the least count of our TDCs is 2.5 ns (which is itself considerably better than required, since each track will have numerous timing measurements) we have conservatively limited the design length of each LVDS chain to 12 boards, which represents a factor of two safety margin ($12 \times 100\,\mathrm{ps} = 1.2\,\mathrm{ns}$) from a single TDC count. As LVDS is a mature technology, used in many consumer applications, this risk is a relatively mild one, which in the worst case would require fabrication of a small number of additional VME readout boards and/or a modest compromise in timing resolution which will not noticeably degrade the experiment's physics capabilities. Based on results from the first prototype, the final version of the LVDS interface will be designed and incorporated into the second (64-channel) prototype, and the full token-ring communication protocol defined, for testing together with a prototype of the VME readout controller.

FPGA and firmware The internal behavior of the front-end board is supervised by an FPGA operating as a finite-state machine, making the system programmable and highly flexible. As noted, during commissioning of the first prototype version of the board during 2004 R&D, the most mission-critical and timing-sensitive elements of the firmware (controlling the TriP-t chip's buffering and TDC functionality) have already been developed and successfully tested. For the production boards, logic to interpret commands and exchange data over the LVDS interface, and control the Cockroft-Walton high-voltage supply will also be required. This additional logic can be developed and tested using the full 64-channel prototype version to be built in the summer 2006.

Persistent storage for the firmware is provided by an onboard flash PROM, which is read by the FPGA on power-up and can be re-written under computer control. As such, it will be possible to reprogram the FPGA logic of all boards remotely even after they are installed, if necessary.

3.5.2 Data acquisition and slow control

MINERνA's data acquisition (DAQ) requirements during datat taking are relatively modest, as the average data rate expected in the NuMI beam is only a few 100 kByte/second and a two-second window for readout is available after each $\sim 10\ \mu$s spill. The most demanding requirements from the DAQ arise from calibration (module mapper) and testing (PMTs). The predictable timing of the beam obviates the need for a complicated trigger - instead, a gate is opened just prior to arrival of the beam, and all charge and timing information from the entire detector is simply read-out after the

[5] For testing and commissioning the board's core digitization functionality, an alternative parallel-port interface was used during initial R&D studies.

spill is complete. The slow-control system is also relatively simple, with each PMT powered by its own local Cockroft-Walton HV supply and uses the same hardware as the DAQ.

The DAQ and slow-control system is therefore essentially a communication network for distributing information (synchronization, high-voltage commands, and exceptionally, updated firmware) to the front-end boards and funnelling event data collected from them to the main data acquisition computer. The system consists of the following components:

- The main DAQ computer (Dell Power Edge), including a VME interface board (CAEN V2718+A2818 Kit),
- A VME crate (CAEN VME8010) containing a total of 12 custom-built Chain Read-Out Controller (CROC) modules, with each CROC controlling four LVDS chains, The are no CPU processors in the VME crate.
- 40 LVDS chains (CAT-5e network cable), with each chain linking 12 front-end boards, and
- A third VME crate, containing timing, diagnostic and logic modules.

Due to the distributed nature of the front-end digitizer/high-voltage boards, the central DAQ and slow-control system itself can be easily accommodated in a single electronics rack.

LVDS token-ring chains As explained in Section 3.5.1, the front-end digitizer boards are daisy-chained into 40 LVDS token rings of 12 boards each. Both ends of a chain terminate in a custom built VME chain read out controller (CROC) module described below. The number of digitizers on a chain is limited by the allowable jitter in the high-precision timing information transmitted to each digitizer board over LVDS. As LVDS is a one-way protocol, each digitizer board must receive the period global synchronization signal from the previous member of the chain on one connection, and re-transmit it to the next member on a second connection. From tests using our prototype boards we estimate that each board in a chain will introduce approximately 100 ps of jitter; thus a chain consisting of 12 boards would translate into roughly 1.25 ns timing jitter (worst case). This represents a factor of two saftey margin over the 2.5 ns least-count timing resolution of the front-end TDC's. In the unlikely event the jitter introduced by a chain of 12 front-end boards proves unacceptable, even with this large safety factor, the number CROC modules (and hence chains) could be increased, allowing each chain to have fewer members.

LVDS signals will be transmitted around a ring on standard, commercially-available fire-resistant and halogen-free CAT-5e network cable approved by Fermilab safety division for underground use. The LVDS chains will also be used to transmit configuration and slow-control messages to the cards.

Chain read-out controller (CROC) modules Each CROC module, shown in Figure 97will control four LVDS chains, requiring a total of 12 CROCs (plus spares) for the entire detector. These modules will reside in a VME crates alongside a crate controller and a MINOS timing distribution module. The CROCs also pass timing and synchronization signals from the NuMI/MINOS module to the FEBs without computer intervention.

The readout controller modules have the following functions:

Figure 97: Photo of Prototype CROC 6U VME module.

1. Prior to the arrival of a NuMI spill, as signaled by the VME-resident MINOS timing module, to reset the timing counters of each front-end board and open a 10μsec gate to collect data from the spill.

2. Upon completion of a NuMI spill, to initiate readout of front-end digitizer data over the four associated LVDS rings, into internal RAM.

3. Upon completion of the parallel readout of all four chains, to raise an interrupt with the main DAQ computer, indicating that event data is available. The PVIC/VME interface/crate controller allows VME interrupts to be received directly by the main computer.

4. The internal RAM of each CROC is memory-mapped to the host computer's PCI bus, allowing block transfer of event data via the PVIC/VME interface/crate controller. The relatively long NuMI duty cycle ($\sim$2 seconds) and low data rate (under 1MB per spill for the entire detector) ensures that no deadtime will be associated with the readout itself.

5. Once per second, to globally synchronize the detector's TDCs over LVDS using a high-precision refresh signal from the MINOS timing module. The need for this synchronization drives the choice of LVDS for the readout chains, as opposed a less performant alternative such as Ethernet.

6. Upon command of the main data acquisition computer, to control and monitor the Cockroft-Walton high-voltage power-supplies and to configure the firmware of these boards at run-startup.

VME backbone Communication between the main data acquisition computer will be via commercially avaialble PVIC/VME link, allowing block data transfers to and from VME and interrupts to be received by the computer in response to the NuMI spill gate.

Ancilliary electronics A trigger scaler and TDC to monitor the NuMI timing signals, and a programmable pulse generator to simulate them during beam-off periods, along with other any additional logic needed for monitoring and calibration, will reside in the third VME crate. All VME components will be installed underground, within about 20 meters of the detector.

Data acquisition computer The main DAQ and slow-control computer will be located near the VME electronics, in the NuMI hall, with two high-speed TCP/IP links (one for data, one for monitoring and control messages) to the Fermilab network. A relatively modest, dual-CPU server model will be more than adequate for our purposes. One CPU will be dedicated to real-time data acquisition, and the other will handle control messages and monitoring. An on-board, RAID-5 disk cluster with sufficient capacity to store several weeks of data will serve as a buffer for the data, pending transfer to offline processing nodes and permanent storage.

DAQ Software The MINERνA DAQ software will make significant use of existing packages. The default choice for the client(control room)/server(Near Detector Hall) infrastructure is the GAUCHO package and related software developed by LHCb and the LHC Joint Controls Project. The LHCb package is integrated with GAUDI, PVSS (process visualization and control system(German acronym)), and DIM (Distributed Information Management). This enables data exchange between GAUDI-based (offline software system) jobs running on different processors. LHCb uses this system to control and monitor their high-level trigger processor farm, with PVSS-based user-interface components subscribing to and displaying counters and time-trend data, and controlling and monitoring individual jobs.

While MINERνA's requirements are far simpler (we have only a data provider, the DAQ computer, instead of a farm of hundreds), it appears to meet our needs and is attractive as it allows online monitoring software to be developed and tested seamlessly within the offline framework, and also because it will spare MINERvA the need to develop such a system itself.

Event building and buffer management will utilize the MBM(Memory Buffer Management) package from LHCb which includes the GAUDI offline interface. The producer task reads raw data from the detector and registers RawBank data into the buffer. GAUCHO-based consumer tasks then read data from the buffer allowing control of monitoring jobs and display of accumulated counters, histograms, etc over the network. The DIM package allows each task to be controlled as a finite state machine and expose this information to control room client diplays (see figure 98) .

MINERνA specific software includes CROC and FEB device control libraries. This will involve a high-level interface for LVDS message building and to hide the VME interface from clients. In addition device management to synchronize hardware access, manage device dependencies, and maintain configuration database will be required. Specific producer/consumer jobs using the MBM package templates will need to be developed. The manpower needed to produce this software will come from UC Irvine, Northwestern, PUCP Lima, and UNI Lima.

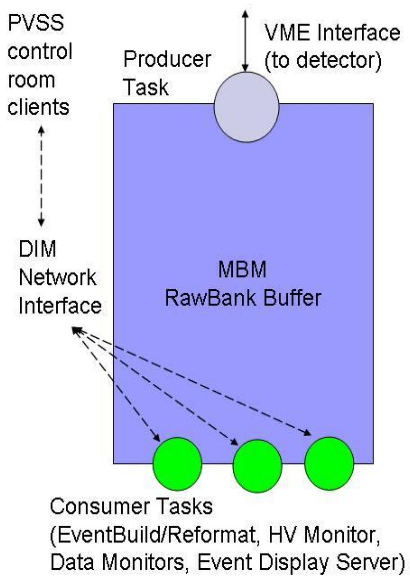

Figure 98: Simplfied Flow Diagram of Event Building and Buffering.

Component	Number	Comments
Channels	30272	WLS Fibers
Front-end boards	473	One per PMT, plus 15% spare
Readout Token Rings	40	12 PMTs/ring
VME Readout Cards	12	4 rings/card, plus two spares
VME Crates	3	Plus one spare
VME PVIC Interface	3	One per crate, plus one spare
PVIC/PCI Interface	1	Plus one spare
DAQ Computer with RAID system	1	Data rate is 120 kByte/spill

Table 15: Parts count for MINERνA electronics design

3.5.3 Control Room Monitors and Displays

In addition to the DAQ computer, which handles the controls and data flow for the DAQ system itself, independent systems which allow physicist operators to monitor and diagnose errors in the apparatus are also required.

Subsystems include:

ACNET Beam Parameter Monitor This subsystem gathers information from the accelerator and associates it with spill data to ensure that the beam flux can be monitored. The MINOS experiment already has such a system in place. MINERνA will either duplicate this system or receive data from the existing MINOS server.

Data Processor This processor will read in data as it is taken and run it through simple versions of the offline algorithms. Quantities such as plane occupancies, pedestals, signals for straight through muons, timing would be accumulated, as well as physics quantities from full reconstruction of interactions. Due to the low data rate, each spill can be read from disk as it is logged. No network event server will be needed. This data processor will be a simple instance of the offline MINERνA data processing code.

Histogram Evaluator and Viewer A separate process will provide a user interface to the updating histograms from the **Data Processor**. Many HEP experiments already have such systems, which can display and compare online histograms with reference sets, flag discrepancies and alert the operator. We propose to reuse one of the existing systems.

Event Display One or more instances of the MINERνA event display need to be available to monitor data as they arrive. The offline event display will run on either the raw data or reconstructed data written out by the **Data Processor**.

Alarm and Message System This system will gather error message from the other online systems, including the slow controls and rack monitors and alert the operator in the event of a serious error. MINOS has an existing system, Distributed Control System, which performs this function. Another alternative would be a SCADA system such as PVSS.

Logbook An online logbook will be available to the operator, the run control and alarm systems should be able to write to this log book to automatically flag begin and end run and serious alarms.

Database The online system will need access to the experiment conditions database, both to obtain hardware information and to store information about running conditions. This can either be the same as the offline database or a separate instance if required by computer security.

We anticipate that during the prototype and testing phases, where data rates are lower and failures will not result in irrevocable loss of data, these functions may be performed by one or two machines. However, the system for beam operations will probably require one machine per monitoring function, as is currently the case for the MINOS experiment.

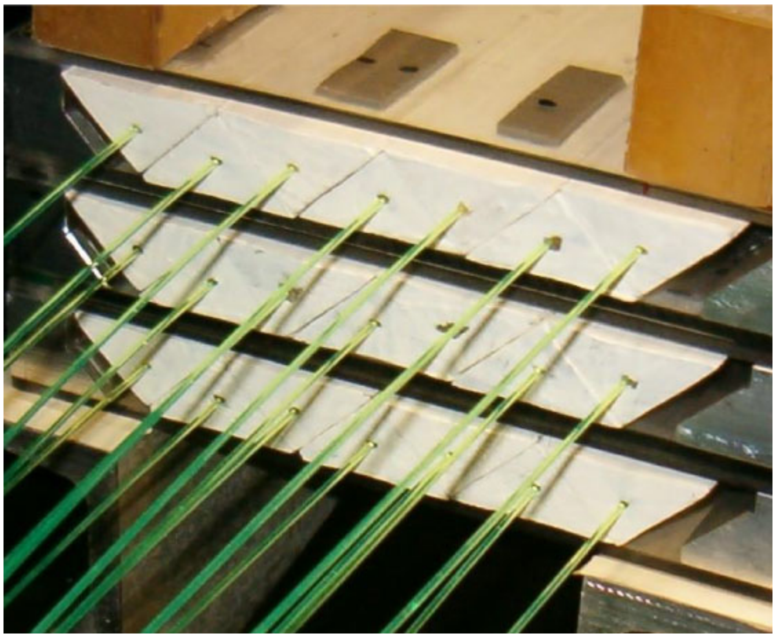

Figure 99: Picture of the VST showing the 3 layers. Scintillator paddles above and below the array serve as the DAQ trigger.

3.6 Vertical Slice Test, VST

We have done a complete test of the MINERνA system. The Vertical Slice Test (VST) approximates the MINERvA detector by including every stage of the eventual detector, except for the clear fiber cables and their connections. Figure 99 shows the optical components of the VST. The VST consists of 3 layers of scintillator bars 0.5 m long . Each layer consists of 7 scintillator bars. The scintillator bars are readout by mirrored WLS fiber (Y11 from Kuraray, 3.5 m long, 1.2 mm diameter), identical to the WLS fiber used in MINERνA . The WLS fibers are glued into the scintillator bars using the production MINERνA glue, Epon 815C epoxy with TETA hardener (Epi-Cure 3234). The WLS fibers are glued into optical connectors used by MINOS which are connected to a MINOS CALDET PMT box. The box contains a 64-channel multi-anode PMT. (The CALDET PMT box was used by MINOS for their CERN testbeam.) Coincidence counters are put above and below the array and cover the array to ensure that only cosmic ray muons that pass through the array trigger an event. In addition, a counter some distance from the array insures the muons are perpendicular to the array.

The VST electronics is serving as the first prototype for the MINERνA electronics, see Figure 100. The VST prototype boards were designed to be compatible with the MINOS CALDET PMT box and to serve as proof of principle for the proposed daisy-chain LVDS readout system. The VST electronics is composed of four identical boards, each of which plugs into the four 16-channel connectors at the back of the MINOS CALDET PMT box. Since these prototypes were produced before TriP-t chips were available, the TriP chip is used - but this is a nearly identical chip and the additional timing feature, which distinguishes the TriP from the TriP-t is not used by MINERνA .

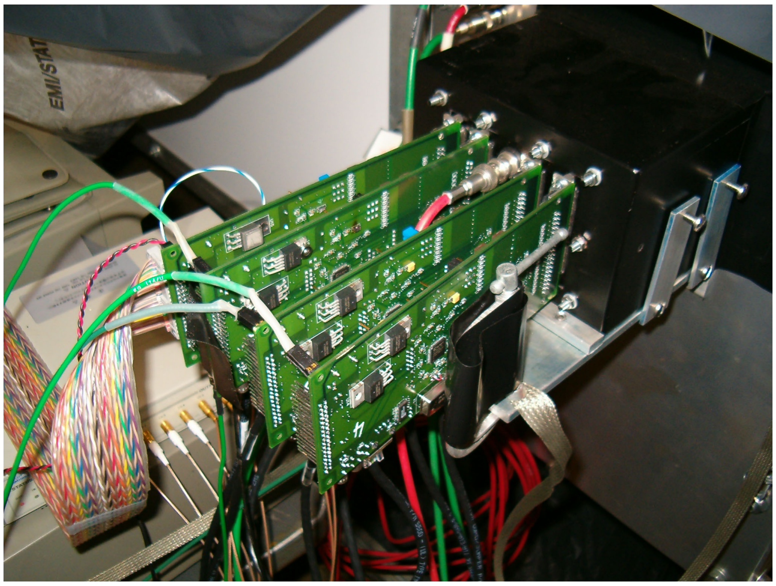

Figure 100: Picture of the MINOS CALDET Box and the prototype MINERνA electronics which was designed to be used with the MINOS box.

The key features required by the final electronics are present on this first prototype. The VST boards are interconnected by an LVDS link using the same protocol as that proposed for the final MINERνA electronics. Each TriP chip is split with 16 channels used for high gain, and 16 channels used for low gain. The discriminator outputs are routed to an FPGA and the TDC function is implemented in the same way as proposed for the final design. One key feature of the final design that has not been tested with the VST boards is the integration of the CW HV generator with the electronics, because this is precluded by using a MINOS CALDET PMT box, which already has an integrated resistive divider base. However, this has been tested using a separate CW generator prototype.

Figure 101 shows the pulse height distribution for cosmic ray muons. In order to determine the single photoelectron (PE) peak, each WLS fiber was pulsed with a LED at a very low light level. Each layer was found to yield roughly 6.2 pe/MeV or an average of 20.7 PE/MIP for a cluster of hits asociated with a muon..

We can use the light measured from the VST to estimate the light for the MINERνA detector by correcting for the losses in the clear fiber cable, the expected phototube quantum efficiencies and the fiber length. From this we derive a worst-case estimate of 18 PE/MIP for the inner detector light yield. If we assume the quantum efficiencies (QE) of the MINERνA PMTs similar to the QE of the MINOS PMTs we get an additional 9% of light. According to the MINOS documentation the QE of VST tube is 9% below the mean of the MINOS PMTs. The light loss from a 1.4 m cable is 0.66. We determined this by measuring the light loss from a 1 m cable, as described earlier, and using the measured clear attenuation length of 6.8 m. We measured that optical grease increases the light by 16% for each connection. The WLS length for the VST is 3.5 m while the longest length in the detector is 3.2 m. This increases the expected light by 6%. Putting all these factors together gives

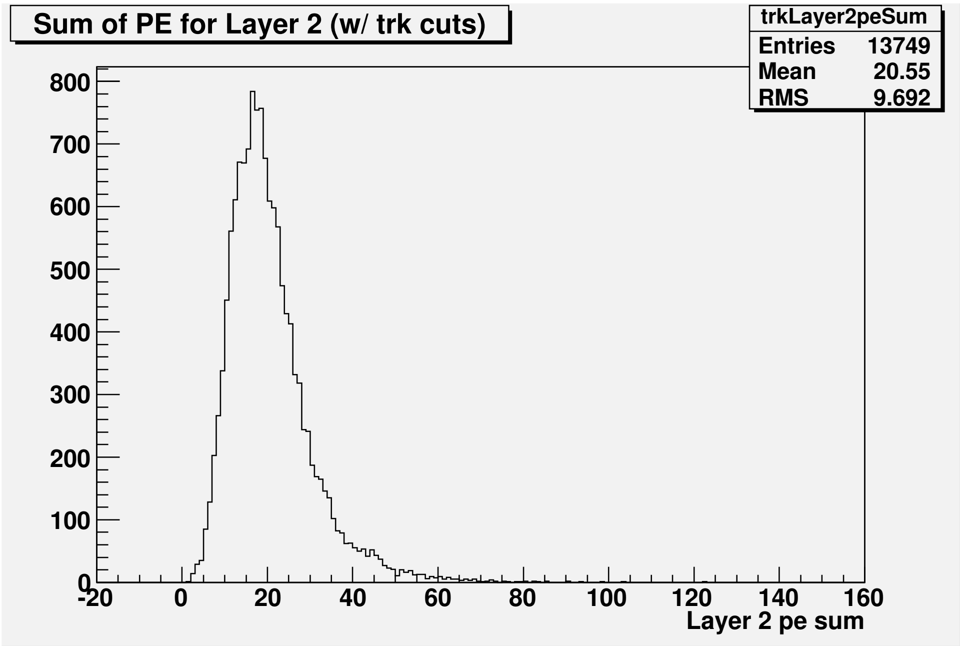

Figure 101: Plot of the pulse height distribution for muons for Layer 2. The average of all 3 layers gives 20.7 pe/layer.

Filter	Effective Transmission	# PEs	Resolution(mm)
0.5	0.43	8.9	3.7
0.63	0.59	12.2	3.2
0.80	0.75	15.5	2.8
1.00	1.00	20.7	2.5

Table 16: Measurement of the position resolution vs light level. A Wratten neutral density filter is inserted in the optical chain and the position resolution is measured.

21.3 pe/layer.

Approximately 1/8 of the detector is readout using 3.1m clear cables, instead of the 1.1 m or 1.4 m clear cable. For this portion, the longest WLS fiber in this section is 2.9 m instead of 3.2 m, compensating for some for the light loss from the longer clear cable. For the configuration of 3.1 m clear cable and 2.9 m WLS fiber, there is an approximately 15% reduction in the light. This gives 18.0 pe/layer. We note that this 18.0 pe/layer is calculated at the geometric point in the detector which gives the lowest amount of light.

We determine the position of the resolution using the VST. The positions are found by weighting strips by photoelectron deposit within a layer. Resolution is found by first averaging layer one and three positions to get a projected position. Next, layer two position is subtracted from that projected position to give a residual. The RMS of the residual for all events divided by $\sqrt{3/2}$, which comes from statistics, gives the actual resolution. Figure 102 shows a resolution of 2.5 mm.

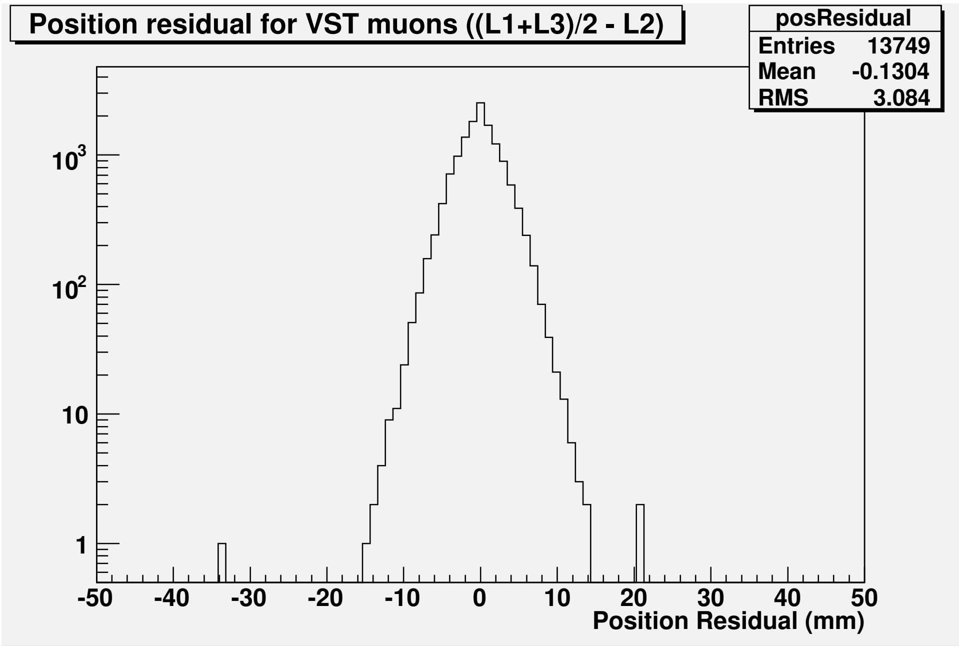

Figure 102: Plots of the $((L1 + L3)/2 - L2)$ where the "L#"s are the position determined in that layer. The tracking resolution is 2.5mm which comes the width of $((L1 + L3)/2 - L2)/\sqrt{3/2}$.

We studied the position resolution vs. light level. To change the light in the array we inserted Kodak Wratten neutral density fibers between the optical connector on the WLS pigtail and the optical connectors on the MINOS PMT box. The Wratten filters are 4 mil thick so the optical connectors cannot quite be mated flush. This causes a little more light loss besides the optical attenuation of the filter. Next the resolution is measured with the Wratten filters in place. Table 16 gives the resolution vs light level. We see that the resolution is still quite good for our requirement of 13.2 pe/layer.

Finally, we have used the VST to determine timing resolution. We specifically used hits on different front-end boards to verify the synchronization of timing across the LVDS chain. For cosmic ray muons, we determine a timing resolution of 2.6 ns. A plot of the residual between two seed strips in the cosmic ray track is shown in Figure 103.

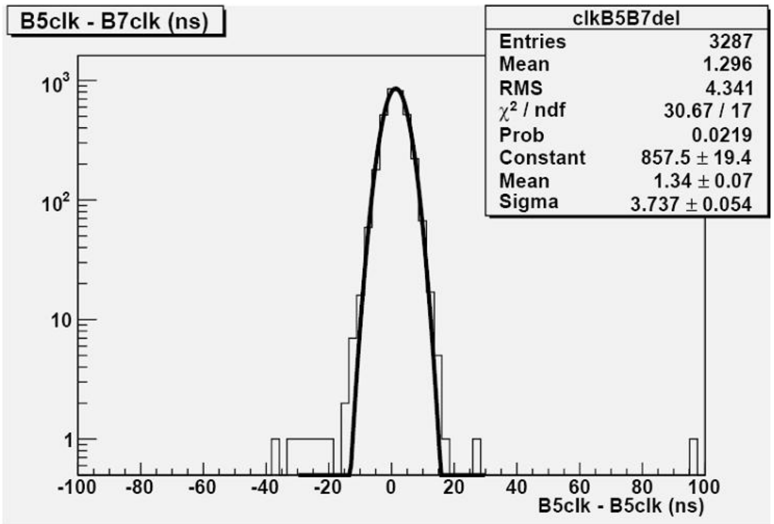

Figure 103: Plots of the time difference between two hits on different layers in the same muon track. The timing resolution is determined to be better than 3ns.

4 Assembly and Installation

Once the detector components, discussed in the preceding chapter, have been constructed, then these components must be assembled to create the MINERνA detector.

The basic functional unit of the detector is called a "module". A module consists of a hexagonal steel frame which, depending on the type of module, contains various scintillator packages or absorber material. Overall, the detector will consist of 108 modules.

The assembly of the MINERνA modules is handled in three steps. First, the scintillator is shipped from the extrusion facility at Fermilab to Virginia where it is packaged into units that can be easily installed into the detector modules. To do this, the raw extrusions must first be cut to length and glued together into a structurally-robust and light tight package. The mirrored wavelength-shifting fibers must be inserted and glued into each extrusion. The final package must be light-tightened and tested. All of this work will take place at two factories located at the College of William and Mary (W&M) and at Hampton University (HU). This task has been named WBS 3 and is being managed by Jeff Nelson of William and Mary.

The second step of assembly involves fabrication of the steel frames, which are the main structural unit of each module. These frames are assembled from six steel segments (or "wedges") which are individually cut from 1.25" thick steel plates. These segments must be welded together to form the frame. This work will be done at Fermilab in the Wideband Hall. The task has been named WBS 8 and is being managed by Jim Kilmer of Fermilab.

In addition to fabricating the steel frames and absorber material for the detector, WBS 8 will also prepare a number fixtures required for the detector assembly and installation. This includes the detector stands, strongbacks and a number of related items.

Finally, once the steel frames and scintillator units have been prepared, the modules themselves will actually be assembled. The scintillator units will be shipped back to Fermilab from Virginia. Scintillator units and nuclear absorber material will be installed into the OD frames. The final units must be scanned with a radioactive source to determine the local performance of the scintillator. This step, known as "mapping," will also be the main quality control step before the detector installation.

The module assembly task has been been named WBS 9 and is managed by Robert Bradford of the University of Rochester (UofR). While module assembly will take place in Wideband Hall at Fermilab, most of the preparatory work is being done at the University of Rochester. In addition to the module assembly and mapping, WBS 9 also is responsible for the veto wall, commissioning the tracking prototype, and fabrication of the PMT racks.

Once assembled, the modules will be stored in Wideband Hall until the detector is installed in the NuMI experimental hall. While it would be ideal for the modules to be installed as they are completed, the feasibility of this, however, is not well understood. The main concern here is that the installation procedure could interfere with the operation of the MINOS near detector. Currently, the collaboration has planned an installation procedure that is minimally invasive for MINOS (during a shutdown), but we are still investigating the feasibility of a prompt installation. Because installation may take place during an accelerator shutdown, it has not been included as part of the Project. Nonetheless, installation related activities are being managed by Jim Kilmer, and this task has been named WBS 11.

This chapter, then will be divided into four sections, one four each of the major tasks addressed in this chapter. Section 4.1 will detail construction of the scintillator modules while Section 4.2 will discuss the OD steel frame construction and physical facilities. Final module assembly will be covered in Section 4.3. Not being technically part of the Project, installation will not be discussed in as much detail as the other three tasks. However, an overview of the detector installation will be presented in Section 4.4. Each section will include a more detailed introduction to the scope of the task, a discussion of required resources, and a breakdown of the main tasks within each WBS structure.

4.1 Scintillator Assembly

WBS 3 designs and constructs all scintillator units for the detector. Of these, there are two kinds: The large hexagonal planes of scintillator for the inner detector, and the smaller "towers" of scintillator for the OD HCAL. This section will begin by defining the scope of WBS 3, including an overview of both scintillator assemblies, and a discussion of the construction process. We will then discuss facilities and resources required for the construction, interfaces with other WBS tasks and outside vendors, major tasks included in the WBS 3 schedule and end with a short section on the R&D effort.

4.1.1 Task Objectives and Overview

The specific tasks for which WBS 3 is responsible include:

1. Design the components of the scintillator assemblies.
2. Purchase the construction supplies, component materials and fabricate the components of the scintillator assemblies.
3. Assemble all MINERνA scintillator units. These include assemblies for the MINERνA detector, the tracking prototype, and the full module prototype. The final MINERνA detector will require 196 ID planes and 648 outer detector assemblies. Once production waste, spares, and prototyping efforts are included, we plan to construct 253 ID and 820 OD assemblies.
4. Test the assemblies for dead readout fibers and light leaks.
5. Package and ship the assemblies to the module assembly site at Fermilab.

4.1.2 Design of the scintillator assemblies

WBS 3 will design and construct two types of scintillator modules - the ID planes, and the OD towers.

Details of the ID planes are shown in Figure 104. The main body of the plane is largely composed of 128 triangular scintillator extrusions, each containing a green WLS fiber. The scintillator extrusions will range in length from 123 to 246 cm and will be glued edge-to-edge using 3M Scotchweld DP190 adhesive to form a large solid hexagonal plane of scintillator. The outer edges of the planes will be treated with a rigid PVC foam, shown as white, yellow, and pink bars in the figure. The yellow bars run parallel to the length of the extrusions and provide structural reinforcement for the plane. At the top of the plane (white bars in the figure), the PVC pieces contain precisely machined grooves which will be used to route the WLS fibers out of the plane for readout purposes. To form a light-tight package, the entire assembly will be wrapped in an outer skin of 0.010” thick Lexan film. A sheet of Lexan, called the “web,” will also be woven through the scintillator plane to provide a convenient gluing surface. A drawing depicting a cut-away side view of a plane is shown in Figure 105.

The plane design builds on the success of the MINOS detector scintillator module assembly [166]. The two assemblies are conceptually very similar - large planar structures composed of extruded scintillator. However, a few modifications are required to meet the needs of MINERνA. Most significantly, the aluminum skins from the MINOS modules were replaced with Lexan; the aluminum skins would have presented too much high-Z material for the MINERνA target region. In addition, the MINERνA triangular strip design uses an axial hole to house the WLS fiber, rather than a groove for better dimensional tolerances.

The readout end of the WLS fibers extends beyond the edge of the planes. In the final assembled module, these fibers must be routed across the face of the OD steel frame. The fiber routing scheme has been carefully planned so that there is appropriate clearance around assembly hardware and other module structure that could damage the fibers. Figure 104 shows the fiber routing for a plane. At their extreme ends, these fibers will be arranged into groups of eight and terminated in a DDK connectors. These connectors will provide an optical connection between the WLS fiber and the clear fiber cables that will carry light signals to the readout PMT’s. The fiber bundles will be encased between two layers of an opaque fire-retardant polyester-reinforced extruded LDPE plastic sheet sold under the band name of “Tuff-Scrim.” The DDK connectors will be installed onto the WLS fibers, polished, and mounted onto a steel strip.

Each assembled detector module will require six OD towers. The OD towers are a scintillator package that will be installed into channels in the steel OD frame and will form the active component of the OD HCAL. Each OD tower consists of eight scintillator extrusions, with a rectangular cross section. The scintillator will be packaged into four individual bundles of two bars, and each bundle will have its own light-tight outer Lexan skin (0.010” thick). Four bundles will be mounted to steel cross pieces that will form an assembly that mount easily into the channels in the OD frame. The WLS readout fibers will be light-tightened with Tuff-Scrim sheeting and will terminate with a DDK connector. An engineer’s drawing of an OD tower assembly is shown in Figure 106.

4.1.3 The ID Plane Assembly Process

The assembly of a MINERνA plane is a multi-step process. The following is a brief overview of the assembly procedure. Many of the figures in this section are photographs we took during assembly of the first MINERνA inner detector plane prototype completed in July, 2006. This prototype was built at William and Mary by members of the Hampton and William and Mary groups.

Receive and Unpack Scintillator The scintillator extrusions will be manufactured at the Fermilab-NIU extrusion facility. The extrusions will be crated and shipped to the scintillator assembly factories in Virginia. As neither the William and Mary nor the Hampton University physics

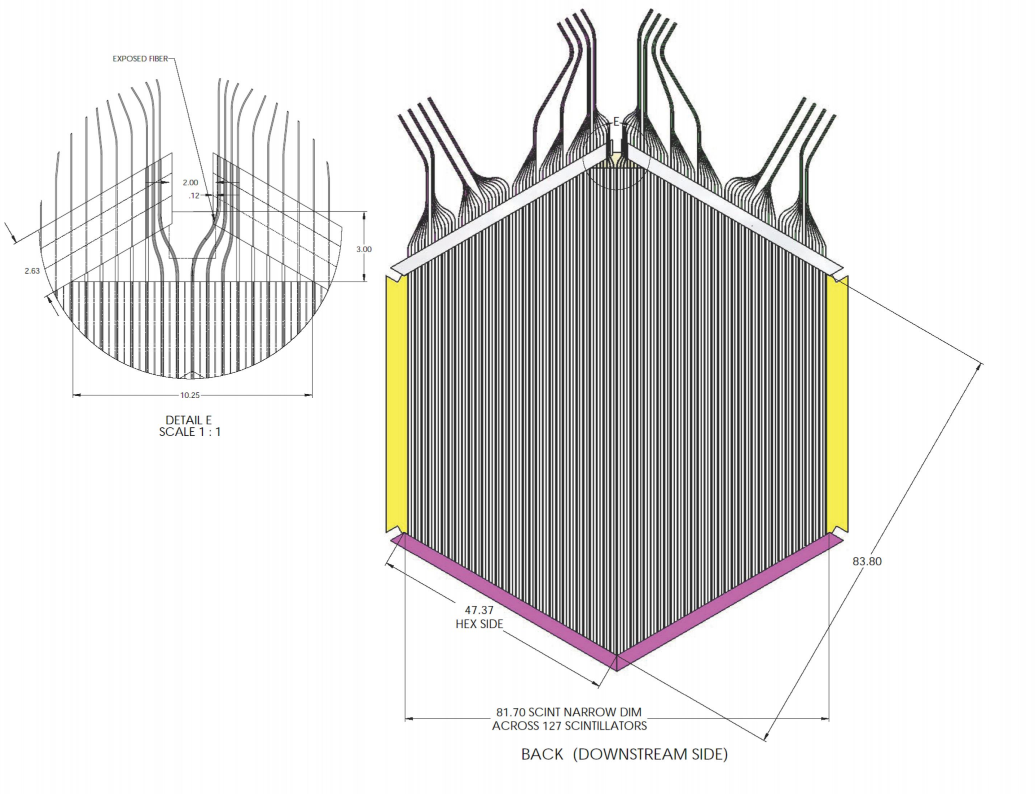

Figure 104: Engineer's drawing of an ID scintillator plane. The WLS readout fibers, shown in a typical routing patter, are drawn at the top of the plane. The white, yellow, and pink bands at the edge of the plane represent rigid PVC pieces which will be added to reinforce the plane's structure and aid in the fiber routing. Image courtesy of Robert Flight.

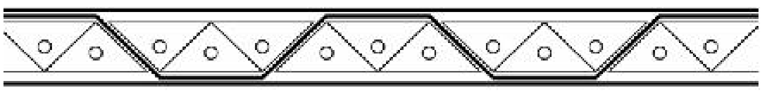

Figure 105: Schematic cross-section of an ID scintillator plane assembly. The scintillator is shown as a plane constructed of triangles. The Lexan web piece is shown as the heavy black line moving through the triangles, and the Lexan outer skins are the thin black lines above and below the plane of scintillator.

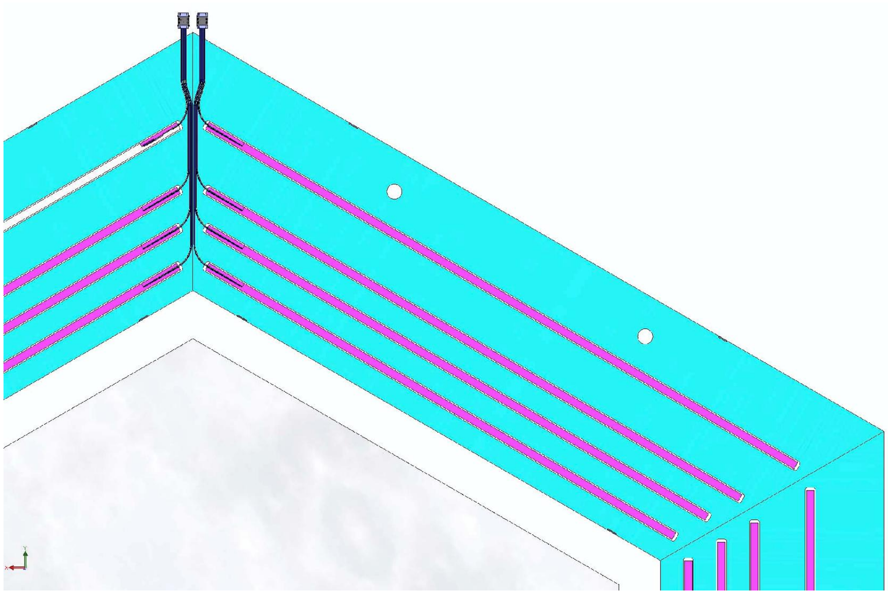

Figure 106: Engineer's drawing showing OD towers (in purple) inserted into the OD steel frame (in blue). The WLS fibers and DDK connectors are shown near the peak in the OD frame toward the left of the picture.

builds have sufficient room to store a truckload of scintillator, a central warehouse will be used for receiving and storage. This warehouse will be climate-controlled. As need dictates, crates will be and transferred to the assembly factories.

Cut Scintillator to Length As manufactured, the extrusions will all be roughly 4 meters in length. Construction of the hexagonal plane, on the other hand, will require scintillator bars of ranging from 123 cm to 256 cm in length. The first step, then, in the manufacturing process will be to cut the extrusions to the proper length. Each of the 4 meter bars will be cut to yield two bars.

A cutting table has been developed to aid in the cutting. The table incorporates a system of rails with stops used to properly position a cutting fence. The scintillator will be cut by a saw equipped with a carbide-tipped blade used for cutting plastics. As plastics are best cut with a slow blade speed, the saw blade will be slowed down using a Variac controller. One quarter of the scintillator required for each plane will be cut in a single pass. A photograph of the prototype cutting table is shown in Figure 107.

During the cutting process, a modest fraction of the waste scintillator removed by the saw blade, called flashing, can melt, adhere to the extrusions, and obstruct the fiber holes. After cutting, the ends of the scintillator are cleared of flashing and painted with reflective paint to improve the light collection uniformity along the ends of the strips. The holes used to hold the WLS fibers will also be inspected and cleared using dental tools as needed.

Assemble Lower Half of Plane The lower Lexan skin will then laid out on a large work surface. A

Figure 107: A photo of the ID scintillator cutting table.

layer of glue will be applied to the skin, and the lower scintillator bars (those lying below the Lexan web) will positioned on top of the skin. More glue will be applied to the scintillator, and the Lexan web piece which runs through the plane will be positioned on top of the scintillator. At this point, the PVC edge pieces will also be positioned on top of the lower skin. Figure 108 shows a photograph of the lower half plane assembly. A vacuum seal will be applied, and the assembly will be left to cure overnight. Figure 109 shows an plane (with lower extrusions having been positioned to provide a smooth surface) while it vacuum cures.

Assemble Upper Half of Plane The next day, more epoxy will be applied to the top of the web, and the upper scintillator bars and top skin will be added. The plane will then be left to vacuum cure for another day.

Insert and Route Fibers After the structure has been assembled, the mirrored WLS fibers will be inserted into the scintillator bars. The readout end of the WLS fibers must follow an appropriate path across the outer OD steel frame in order to avoid damaging the fibers. A sheet of opaque Tuff-Scrim will be used as a routing substrate; the fibers will be fixed into position on the Tuff-Scrim with carpet tape.

Install and Polish DDK Connectors The readout ends of the WLS fibers will be mounted in a "ferrule" which will allow the fibers to plug into a DDK connector. The fibers will be glued into the ferrule, and the entire assembly will be polished using a fly-cutter. 16 connectors will be

Figure 108: Photo showing main components of the lower half plane. The PVC edge pieces are visible toward the top of the photograph. The scintillator extrusions are shown lying under the Lexan web.

Figure 109: The first prototype MINERνA scintillator plane while it vacuum cures.

installed for each plane. The connectors themselves will be mounted to a piece of 1/8" thick aluminum stock. During module assembly, this aluminum stock will be installed on connector mounts on the outer edge of each module's steel frame.

Glue Fibers and light seal To increase light yield, an optical epoxy will be injected around the fibers in the scintillator. This process will use a commercial two-part epoxy mixing and dispensing machine to inject optical epoxy into the fiber hole in each extrusion. After gluing, an upper Tuff-Scrim cover will be added. The edges of the two layers will be heat sealed and taped together to form a light-tight seal for the fibers.

QA and Light-Leak Testing The final assembly step will be a QA procedure. Planes will be inspected for light leaks and damaged fibers.

Ship to Fermilab Finished scintillator planes will be placed in plywood shipping crates and stored at the central warehouse facility. Once a shipment is complete, the full crates will be sent to the module assembly factories at Fermilab by flat-bed truck.

There will be three assembly periods. First, we will assemble two planes plus a spare and 6 towers plus a spare for the full module prototype in 2006. A year later, we will assemble 40 planes plus spares and 120 towers for the tracking prototype. Finally, we will construct the production assemblies for the final detector in 2008 and 2009.

Using the MINOS manpower requirements as guidance, the expected production rate one plane every six days from each workstation at each assembly site with 45 hours of labor per plane.

OD Tower Assembly The outer detector assembly is significantly simpler. The process begins by cutting the scintillator extrusions to one of four prescribed lengths. Once cut, grooves must be machined in the end of each extrusion to permit routing of the WLS fiber out of the scintillator. Two extrusions of the same length will be glued together, and fitted with a Lexan skin to form a "doublet." WLS fibers will be inserted into each extrusion in the doublet and glued into place with optical epoxy. Steel straps will be fixed to four bundles to form the basic structure of the OD tower.

The readout end of each fiber will be covered with Tuff-Scrim sheeting, and one DDK connector ferrule will be installed and polished on each OD tower.

Using the MINOS manpower requirements as guidance, the expected production rate is ten OD towers per 35 hours of labor.

4.1.4 Facilities and Resources

The construction of the MINERνA scintillator assemblies will be undertaken at both Hampton and William and Mary. Both programs have extensive experience in detector production. Since the two institutions are located less than 25 miles from each other (and less than 15 miles from Jefferson Lab), they provide a natural team for undertaking a joint detector production program. This team will benefit from a collaborative prototyping program, and the joint set-up costs are minimal for this project. Bulk purchasing responsibilities will be shared by the two institutions, according to the particular strengths and experience of each.

Each university will provide suitable laboratory space to run an assembly factory. The space must be large enough to safely accommodate the construction of the hexagonal ID planes, which are roughly 256 cm in their largest dimension. The fabrication sites must also have appropriate clearance to permit the planes to pass in and out of the building.

Aside from the basic lab space, both assembly sites must be appropriately outfitted for the construction tasks. The required resources will include:

1. Id and OD Scintillator cutting stations.
2. Lexan cutting templates
3. Folding stations necessary to produce the Lexan web pieces and OD doublet covers.
4. Work surfaces to accommodate both ID plane and OD tower assembly. The surfaces must suitably flat and air-tight to facilitate vacuum curing of the epoxy.
5. Vacuum pumps and bags required for vacuum curing.
6. Adhesive mixing and dispensing equipment (required for structural epoxy).
7. Fly cutter (used to polish DDK connectors)
8. Gluing machine (used to dispense optical epoxy for gluing WLS fibers into scintillator).
9. Facilities and rigging to permit overhead lifting. This will be required to load the scintillator assemblies into shipping crates.

10. Appropriate ventilation and safety equipment.

The William and Mary site will be partially outfitted with a fly cutter obtained from the MINOS scintillator assembly factories.

Both sites will be staffed with a mix of full-time technicians and student labor. Graduate students and technicians will be used to supervise teams of undergraduate labor. Each assembly site will require the equivalent of five full-time laborers. Most custom machining will be done at the William and Mary machine shop.

A shared off-campus facility will be used for storage, shipping and receiving. This facility must be climate controlled to prevent damage to the scintillator during storage, and must have necessary materials handling equipment to permit movement of the large crates used to ship the ID planes. This facility will be used to receive shipments of scintillator from Fermilab. The shipping facility will be used to store the raw extrusions before they are dispatched to the assembly factories. As scintillator assemblies are completed, they will be packaged for shipping and loaded into crates at the factories. Loaded crates will then be moved to the shipping facility, where they will be stored until a full truckload is assembled. Then, the completed assemblies will be shipped to Fermilab.

4.1.5 Interfaces with other WBS Tasks

WBS 3 will receive supplies and materials from three other WBS tasks: WBS 1, WBS 2, and WBS 4. WBS 1 will provide the scintillator extrusions. These will be produced at the NIU-Fermilab extrusion facility, and then shipped to Virginia. WBS 2 will provide the WLS fibers. This effort is being lead by a group from the University of Rochester working at Fermilab. WBS 2 will acquire the fiber from the vendor, verify the fiber quality, mirror one end, and then ship the fiber to Virginia. The fibers will be supplied to WBS 3 pre-cut to their appropriate lengths. WBS 4 will supply the optical connectors and fly cutting bits required to polish them. WBS 4 will perform the majority of connector-related R&D, spec the connectors to the vendor (DDK), and handle the procurement.

The final WBS interface is with WBS 9, module assembly and mapping. The completed scintillator assemblies will be shipped to the module assembly factories at Fermilab, where WBS 9 will use the ID planes and OD towers to build the final detector modules.

WBS 3 will also maintain a number of minor interfaces with private vendors who supply material required for the scintillator assemblies. Epoxy, Lexan, opaque plastic, and PVC foam will all be supplied by private vendors.

4.1.6 Major Tasks

This section will give an overview of the tasks that we have scheduled for the next several years. The subsections will each refer to a specific task or group of tasks in the MINERνA Project file.

- WBS 3.1.1 - WBS 3.1.3: These tasks cover initial R&D and design work for the scintillator assemblies during 2005-2006. The scintillator units will be designed and prototype assemblies will be constructed. Issues relating to the integration of the planes and towers into the MINERνA detector modules will be resolved. The majority of the design and integration work was carried out by Robert Flight, a mechanical engineer from the University of Rochester in collaboration with Hampton and William & Mary. Connector polishing techniques will be tested and practiced.

- WBS 3.1.4-5: These tasks cover outfitting of the scintillator assembly factories at both Hampton University and William and Mary. Workstations will be constructed, and tooling will be purchased during the summer FY 2006 and FY 2007.

- WBS 3.1.6-9 - Full Module Prototype Scintillator Assemblies: In the fall of 2006, a prototype detector module will be build at Fermilab. These tasks cover production of three ID planes and seven OD towers for the prototype module.

- WBS 3.2 - Tracking Prototype: The tracking prototype will consist of 20 detector modules that will be built in the fall of 2007. Tasks under WBS 3.2 cover production of the ID planes and OD towers for the tracking prototype. Tasks cover procurement of the materials for the factories, construction of the assemblies, and shipping of the complete assemblies back to Fermilab.

- WBS 3.3.1-4 Detector components and materials: After the tracking prototype is completed, the assembly factories will prepare for the construction of the final (production) detector. WBS 3.3.1-4 cover procurement of materials for the production detector. This work will take place in FY 2008 and early FY 2009.

- WBS 3.3.5-6 Detector assembly: The scintillator assembly factories will open for their third and final time in mid 2008. These tasks are the construction of the ID planes and OD towers for the production detector.

- WBS 3.3.8 - Storage and shipping: The last step in the process will be to package the final assemblies in shipping crates, store them, and then ship them to Fermilab. This work will be completed in early FY 2009.

4.1.7 R&D and value engineering

A significant amount of R&D has already been completed. In the summer of 2005, a W&M undergraduate researched techniques for injecting optical epoxy into the fiber holes of the scintillator extrusions. Optical epoxy improves the optical contact between the WLS fiber and the scintillator, improving the light collection efficiency of the system. Two different glues were tested, 815C and Eljen optical epoxy. 815C was chosen because it produced the highest light yield. Glue mixing and injection techniques were also researched. In the production factory, glue will be injected into the fiber hole with an air driven glue machine. Final techniques were used to glue WLS fiber into the vertical slice test, a small array of scintillator used by WBS 2 to test detector optics and tracking.

In 2006, significant amounts of time were spent interfacing with WBS 8 and 9 to resolve fiber routing issues. In the final detector modules, the WLS fibers will be routed across the OD steel frame. The fiber path across the steel frame is where the WLS fibers will be least protected and most susceptible to damage. Hence, the path must protect the fibers as much as possible, while being consistent with the overall module design.

With assembly of the prototype plane in the summer of 2006, there was significant development of the cutting table and other factory workstations. These early tests have demonstrated that the labor estimates are reasonably valid.

As planes and towers are developed for the full module prototype, factory outfitting and production techniques will be refined in late 2006 and early 2007.

4.2 OD Steel Frame Construction and Physical Facilities

WBS 8 is responsible for fabrication of the detector module OD steel frames and steel fixtures to be used in Wideband Hall during the detector assembly. In addition, WBS 8 procures all nuclear absorber material for the detector calorimeters and assembles the upstream nuclear targets.

This work will be performed largely by Fermilab technicians and a variety of private sector vendors. Many of the WBS 8 tasks strongly resemble work recently performed for the NuMI/MINOS project. WBS 8 will attempt to profit from this experience by using the same staff and technicians to complete work on MINERνA.

This section will present an overview of WBS 8. The scope and task objectives for WBS 8 will be presented first, followed by an overview of the required facilities, interfaces with other WBS tasks, and concluding with an overview of the WBS 8 schedule.

4.2.1 Task Objectives and Overview

WBS 8 is explicitly responsible for the following tasks:

1. Procure steel for OD detector frames: Each frame will be constructed from six "wedges" (See Figure 110.) which will be flame cut from 1.25" thick steel plates. These frames will be the principle structural unit in each detector module, and will also serve as absorber material for the OD hadronic calorimeter. Each wedge will have four channels cut along its length; these channels will house the scintillator bars that are the active component of the OD HCAL.

   This task has two major considerations. First, the steel plate from which the wedges will be fabricated, and second, the actual cutting of these pieces into the wedges.

   The steel plate is specified in [167]. The steel used in MINERνA will be identical to that used by MINOS. While a magnetic coil is not in the baseline design for MINERνA, this steel is suitable for use as a magnet and preserves the possibility of a magnetic field as a future upgrade. The most important parameter of the steel plates is its flatness. In the specification, the upper limit is required to be 1/2 of the ASTM standard limit for flatness in plates; for MINERνA, this translates to a flatness of less than 3/16". For the MINOS project a steel mill was able to routinely provide material that was within the specification. Less than 1% of the over 4000 plates in MINOS were out of spec.

   Cutting the steel is specified in [168]. In this specification are the tolerances for the part dimensions, flatness of the finished pieces, and fabrication methods. The vendor will evaluate the flatness of the finished pieces on a case-by-case basis. Parts will be flattened as required by the specification. Contingency for the steel pieces is sufficient to cover any additional costs associated with flattening.

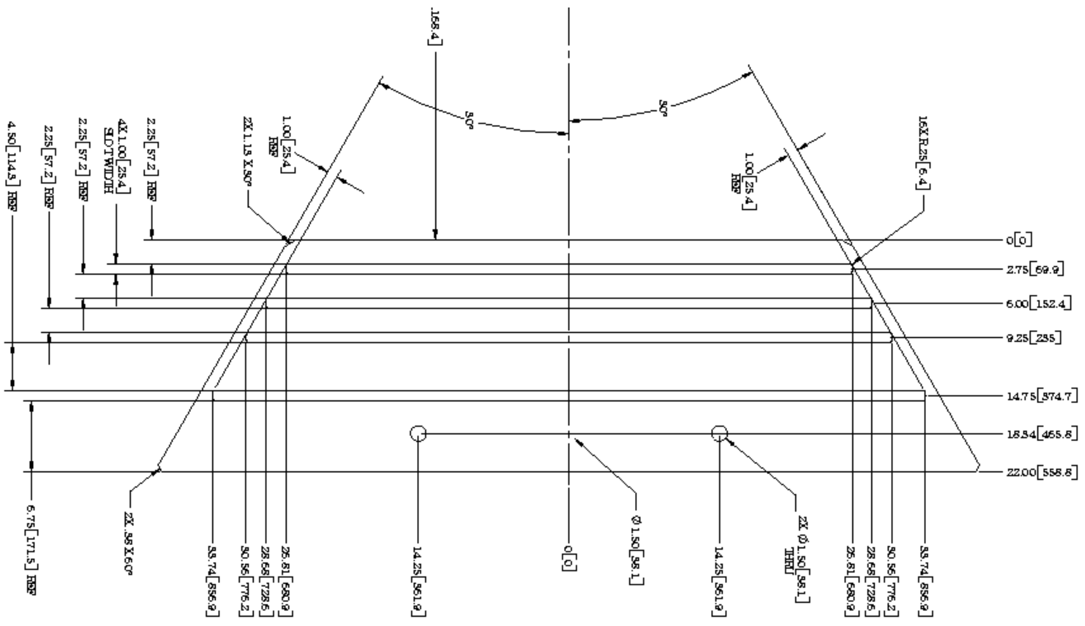

Figure 110: The OD frames are each assembled from six of these steel "wedges".

2. OD Frame Assembly: The steel wedges previously described must be welded to form the OD frames. This work will be done by Fermilab technicians and welders just before each detector module is assembled. Six wedges will be clamped into place on a strongback. The strongback will be held vertically, and the wedges will be welded together to form the frame.

3. Detector Stands, Bookends, and Axial Bolts: WBS 8 supplies all fixtures required to mount the detector. The detector stand will hold MINERνA modules much like a hanging file system in a file drawer. The first module will be anchored to a bookend structural element at the end of the stand. This bookend will keep the modules stable and plumb. Axial bolts will then be used to anchor each succeeding module to the one previously installed. Six axial bolts will be used for each module. Figure 111 shows a drawing of an axial bolt and Figure 112 shows a drawing of the detector stand. MINERνA will require two detector stands in the NuMI experimental hall (one holds the detector in the beam, while a second is used to stage modules during installation) and three smaller detector stands to be used in Wideband Hall during module assembly. Each detector stand must be outfitted with a bookend.

   Fermilab uses the American Institute of Steel Construction, Manual of Steel Construction as the safety code for all structural steel fabrications such as the stand and lifting fixtures.

4. Strongbacks: A strongback is a steel framework that supports modules during assembly and protects them during lifting operations. WBS 8 will procure three strongbacks for use in Wideband Hall during the production frame welding and module assembly periods.

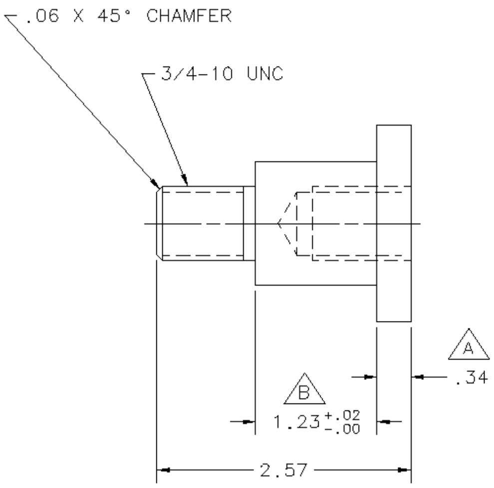

Figure 111: Engineer's drawing of an axial bolt.

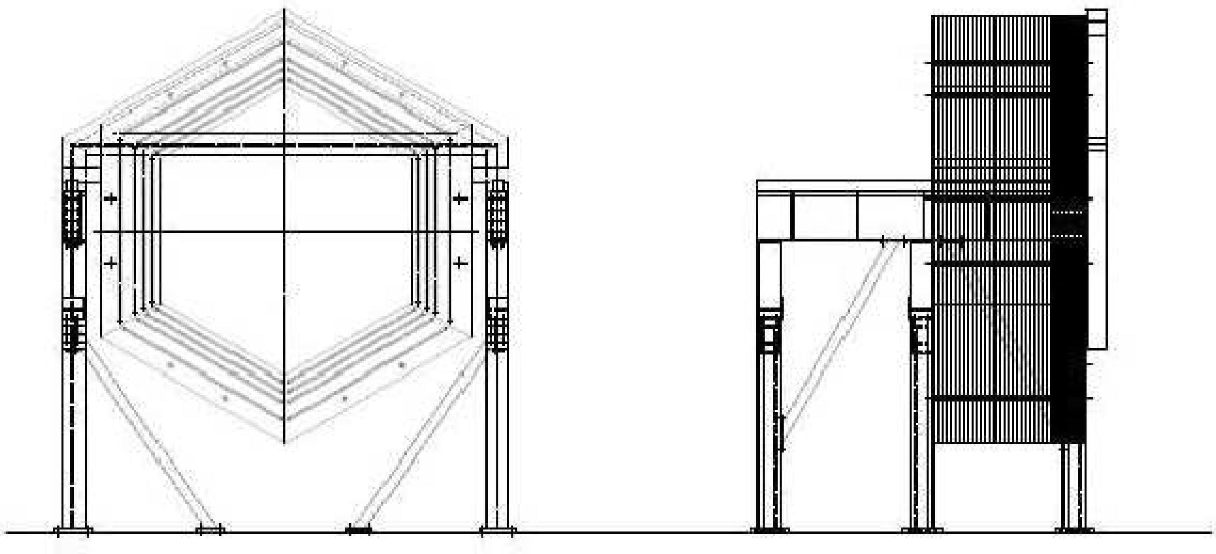

Figure 112: Engineer's drawing showing front and side view of the MINERνA detector stand.

For WBS 8's specific interests, the strongbacks will serve as a welding jig during frame construction. The six wedges of steel will be placed on the strongback in the correct position and clamped down by a series of holding bars. These bars will keep the frame from distorting as it is welded together. After tacking the wedges together the strongback will be moved to a vertical holding fixture that allows the frames to be welded on both sides.

As a lifting fixture the strongback allows the frames to be built on the floor horizontally and then raised to vertical for hanging on the support rails. The pick point on the strongback is chosen so that the frame never hangs in a truly vertical position but always has a slight tilt so the load is stable with the load's center of gravity on top of the strongback.

Finally the strongback is used as the transport fixture for moving the frames from the Wideband hall to the MINOS cavern. Frames are kept on the strongback as they are loaded on the truck for hauling to the surface building.

For lifting fixtures, the "ANSI/ASME B30.20, Below-the-Hook Lifting Devices" safety standard will be used.

5. Procure nuclear absorber material: WBS 8 is to procure lead for the MINERνA OD and DS ECAL and steel for the DS HCAL.

   The OD ECAL is constructed by mounting a lead collar to the outer edges of the scintillator planes which make up the tracking volume of the detector. The collars are constructed from six wedge shaped pieces of lead. In the DS ECAL modules, the entire face of the scintillator planes are to be covered with a hexagonal sheet of lead. In the DS HCAL modules, hexagonal sheets of steel replace one of the scintillator planes.

6. Construct US Nuclear Targets: WBS 8 is to procure lead, steel, and graphite for the US nuclear targets. While these materials will be supplied by outside vendors, the nuclear targets will be assembled by FNAL technicians.

7. PMT Access Platform: The phototube access platform is needed allow a technician to service the the phototubes and the front end electronics, which are mounted above the detector. This will be a rolling platform mounted on rails above MINERνA. The platform will not have drive motors, however a technician should easily be able to push it along the beam axis of the detector to reach any phototube box or fiber cable.

4.2.2 Facilities and Resources

The work required by WBS 8 will be accomplished by a mix of FNAL resources and an array of outside vendors. All of the WBS 8 design work will be accomplished by FNAL engineers and drafters, with some support from Robert Flight of the University of Rochester. The resulting drawings will then be taken to local vendors for fabrication work. Fermilab technicians and welders will also be used during times of OD frame construction. The Fermilab technicians that will be working on the MINERνA project are the same crew that assembled all of the detector planes for the MINOS Near Detector. They have experience with the procedures and the material handling facilities available in the buildings. They also have training for using the cranes, forklifts and working with lead.

The major construction of the MINERνA experiment will occur in the Wideband Experimental Hall. This is where the OD frames and nuclear targets will be assembled. This building has two 15 ton cranes available for assembling the frames and moving materials in the building. Wideband Hall has sufficient electrical utilities for welding and power tools required and will be equipped with an electric forklift for material handling in the building. The north end of the building will be used for storing, preparing and handling the steel parts of the detector and the south end will be used for storing and handling the active scintillator elements. The far south end of the building will have a cage securing access to the frame mapper and its radiation source. Figure 113 shows the proposed configuration of Wideband Hall as it will be used for frame and module assembly activities.

4.2.3 Interfaces

WBS 8 maintains a large number of interfaces, both with other WBS task groups and also with private sector vendors.

WBS 8 relies on vendors largely for supply and fabrication tasks. Because of the MINOS project, WBS 8 has past experience with many of the vendors who will be handling MINERνA tasks. The most important, and involved, vendor interface will be with the suppliers of the OD wedges. The MINERνA steel order is large enough that it will be supplied directly from a steel mill. Once a vendor is selected, MINERνA will be assigned a place in the mill's work schedule, so procurement of the steel will have a large lead time. Since the critical specification of the steel is the flatness of the wedges it will be most important to monitor the quality of the steel parts with a quality assurance plan. Besides regular measurements of the parts as they are received it will be necessary to make some visits to the factory during production startup and periodically thereafter if the parts go out of tolerance.

The second interface is with WBS9. Once finished, OD frames will be delivered to WBS9 who will use the frames to construct detector modules. As frame assembly and module assembly will proceed in tandem, frames will be delivered to WBS9 individually as they are assembled. WBS9 will receive each frame sitting on a strongback in Wideband Hall. WBS 8 will also supply WBS 9 with all of the strongbacks and detector stands required to outfit Wideband Hall for module assembly.

The third interface is with the Installation and Infrastructure task WBS11. WBS 8 supplies WBS11 with a number of fixtures required for the detector installation, including the detector stand, axial bolts, bookends, PMT access platform, strongbacks, and the MINERνA nuclear targets. There is substantial overlap between WBS 8 and WBS11; many of the installation tasks will be handled by the same FNAL crew and technicians that will assemble the OD frames.

4.2.4 Major Tasks

The major tasks required to complete WBS 8 include:

- WBS 8.1.1 and 8.1.2 - Prototype Design Work: These tasks include all of the design and engineering work for items such as the detector stands, axial bolts, strongbacks, and the PMT access platform. While the bulk of the work is to be done by FNAL engineers and drafters (WBS 8.1.2), Robert Flight at the University of Rochester, will give assistance with some tasks (WBS 8.1.1).

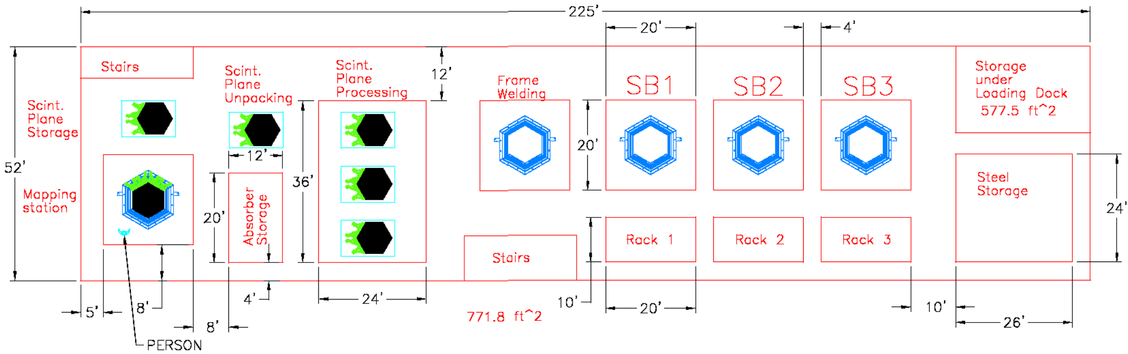

Figure 113: Engineer's drawing showing an initial concept of the Wideband Hall layout. Most frame assembly and module assembly activities take place on the strongbacks, labeled "SB1", "SB2", and "SB3" in the drawing. Areas for scintillator preparation and module mapping are found to the left in the drawing. Drawing courtesy of R. Flight.

- WBS 8.1.3 - Procure Prototype Materials: This task completes procurement of all materials needed for early prototyping efforts, including the full module prototype. For the full module prototype, WBS 8 will deliver a prototype detector stand and bookend, one OD frame, a strongback, and a set of axial bolts.
- WBS 8.1.4 - Assemble Prototype Stand in Wideband Hall: This task covers installation of the prototype detector stand in Wideband Hall, which must be completed before the full module prototype is built.
- WBS 8.1.5 - Outer Detector Frame Prototyping: This task covers assembly, welding, and testing of the OD frame for the full module prototype.
- WBS 8.2.1 - Procure Tracking Prototype Materials: These are all the procurement tasks for the tracking prototype.
- WBS 8.2.3 - Tracking Prototype OD Fabrication: This task is construction of all the OD frames for the tracking prototype.
- WBS 8.3.2 - Procure Production Materials: These are the final procurement tasks required for the production detector assembly. Final OD steel wedges, strongbacks, detector stands and axial bolts will be purchased.
- WBS 8.3.3 - Production OD Fabrication: This task covers construction of the OD frames for the production detector assembly period.

In general, tasks falling under WBS 8.1 will occur during 2006, tasks under WBS 8.2 will happen during 2007, and tasks under WBS 8.3 will occur in 2008-2009.

4.3 Module Assembly and Veto Wall

The main tasks of module assembly are to construct and map all MINERνA detector modules, and build the veto wall. These are the last construction steps before the detector is ready for installation. In addition, we are also responsible for a number of related tasks, such as construction of the PMT racks and the module mapper.

While the final module assembly and mapping for the detector will take place at Fermilab during a period of approximately six months in 2009, the preparations for module assembly require a multi-year effort that is being lead by the University of Rochester, with contributions from Fermilab and collaborators from Peru. The preparatory efforts entail an extensive program of building prototypes, development of assembly protocols, designing custom hardware, procurement, and fabrication. Because module assembly involves the integration of components built by other WBS task groups, our preparations also must emphasize communication with the other L2 managers responsible for these systems.

This section will begin by presenting an overview of WBS 9. This will include an overview of the module assembly and mapping process and some discussion of the less obvious aspects of WBS 9, such as the fabrication of PMT racks. We will then move on to a discussion of how WBS 9 plans to meet these objectives. This will include an overview of resources required both from Fermilab and the university groups, a discussion of the interfaces with other WBS tasks, and an overview of the specific activities that we have scheduled for the next few years.

4.3.1 Task Objectives and Overview

The specific tasks that WBS 9 is responsible for include:

1. Assemble all MINERνA detector modules and map the local response of the scintillator. These include modules for the final detector, the tracking prototype, and the full module prototype.

2. Design and construct the module mapper.

3. Install and commission the tracking prototype.

4. Fabricate mounting racks for the PMT's and develop tools required for PMT maintenance.

5. Develop routing scheme for clear fiber cable routing.

6. Construct the veto wall.

The following subsections will discuss the specifics of each task.

Module Assembly and Mapping Procedure Assembling a MINERνA module is a multi-step process. The following is a brief overview of the module assembly procedure as we currently envision it. Many of the figures in this section are based on photographs we took during mock assembly exercises that were conducted at the University of Rochester using prototype modules constructed from wood. More details about the module assembly procedure are contained in [169].

Receive and prepare materials WBS 9 receives scintillator modules from WBS3. Once these modules arrive at Fermilab from Virginia, we will receive the materials and store them in Wideband Hall.

Once the assembly factory opens, the first step will be to unpack and prepare the scintillator. ID planes and OD towers will be inspected for any obvious shipping damage and broken WLS fibers. If the schedule calls for active target modules or DS ECAL modules to be assembled, then sheets or collars of lead absorber material will be applied to the US face of the scintillator planes. Layout and identification marking will be applied to the modules.

Steel frames will be provided by WBS8. These frames will be inspected and deburred to ensure that rough edges do not damage scintillator or fibers. Markings identifying the type of module to be built will be applied. A traveler providing more specific instructions will also be affixed. After work on the OD frame has finished, the assembly area will be cleaned.

Figure 114 shows a model OD frame mounted on a strongback.

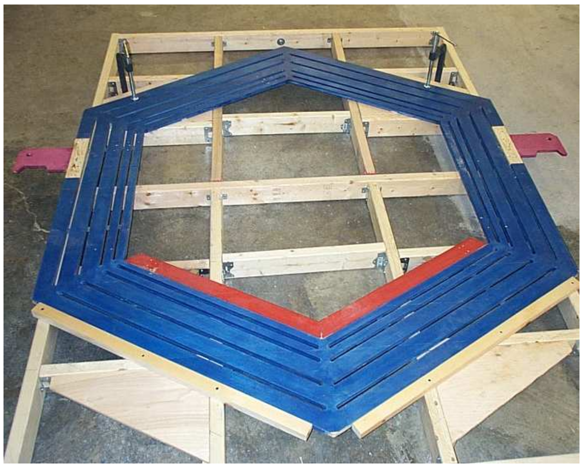

Figure 114: At this point, the steel frame has been welded and is mounted on the steel frame. It is inspected, cleaned, marked, and prepared for assembly.

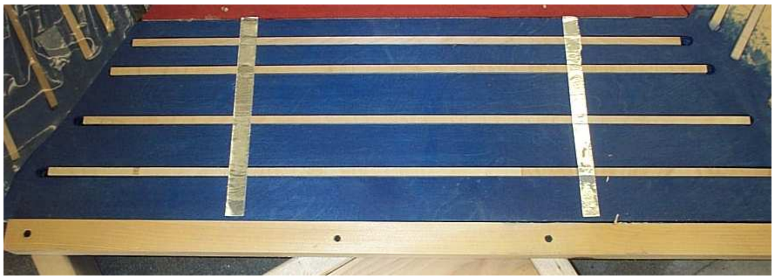

Figure 115: The OD scintillator fits in a series of channels in the OD steel frame. The metal bars, which are perpendicular to the scintillator bars, will be a structural element of the assembly. On an actual module, the scintillator assembly will be held into place with silicone caulk.

OD scintillator installation The scintillator towers will be installed by hand into the slots cut into the OD steel frame. We will use silicone caulk to secure the scintillator towers to the frame. A bead of caulk will be applied to the sidewall of the frame channels that house the scintillator. As the scintillator bars are installed into these channels, the caulk will fill the gap between the scintillator and the steel frame. Installing the caulk before the scintillator minimizes any mess. Figure 115 shows a picture of an installed OD scintillator assembly.

Load-bearing spacer and connector mounting installation The load-bearing spacer will consist of four blocks of material which bolt to the inside surface of the bottom two sectors of the steel frame. This material will bear the weight of the scintillator planes or absorber material that will later be installed into the inner detector. These blocks will be held into position by studs which will have been welded to the OD frame by WBS8.

The connector mounting consists of aluminum angle stock that will mount to the outside sur-

Figure 116: *Left:* Close-up photograph shows the load-bearing spacer (in red) mounted on the OD frame (in blue). *Right:* Angle stock for ID scintillator clear fiber connector mounting attaches to the outer face of the OD steel frame. Note pieces located above and below the module mounting hook.

face of three OD sectors. The clear fiber cable connectors will later mount to this angle stock. Like the load bearing spacer, these pieces will be held by studs which will have been previously welded to the OD frame.

Pictures of the load-bearing spacer and connector mounting on our model are shown in Figure 116.

US plane or absorber material installation The first ID material will then be installed. For most modules, the first scintillator plane will be installed at this point. The scintillator plane will be moved into position with the aid of the Wideband Hall overhead crane and a vacuum lifting fixture. This plane will be installed in a "u" or "v" orientation, depending on the assembly schedule. The WLS fibers from this first scintillator plane will be routed across two sectors of the OD steel frame and the clear fiber connectors will be attached to the mounting stock.

Downstream HCAL modules do not have an US scintillator plane. In these modules, the US scintillator plane is replaced with a large steel plate. These plates will be installed during frame assembly by WBS8.

DS plane installation All module types incorporate a DS scintillator plane. In most modules, this plane will always be installed in an "x" orientation. However, the DS plane in the DS HCAL modules may have an "x," "u," or "v" orientation. Once the plane has been moved into position, the fiber packages will again be routed across the OD steel frame and the connectors will be installed.

H-clip installation The scintillator planes will be fixed into position by a hardware piece we have called an "h-clip." A picture of an h-clip is shown in Figure 117.

Module mapping At this point, the module will be mapped. Mapping will be discussed in greater detail in Section 4.3.1. If the mapping procedure reveals that a module will perform unacceptably, then we will troubleshoot and remap the module at this point.

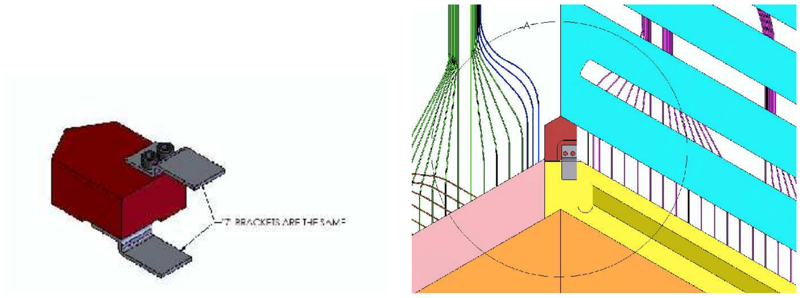

Figure 117: *Left:* Engineering drawing showing proposed h-clip. *Right:* Drawing showing an h-clip installed in a MINERνA module. The triangular end of the h-clip will be welded to the OD frame by WBS8 during frame assembly. The smaller metal pieces will clamp the scintillator planes into position. Images courtesy of R. Flight.

Alignment surveys Before being stored on the detector stands, the modules will be surveyed by the FNAL alignment group. The modules are mapped while lying horizontally on the strongback, but they will be moved into a vertical position for storage and installation. This initial survey will measure the effect of hanging the modules vertically, noting any changes in the position of the scintillator planes in relation to the OD frame.

Package module for storage The module will then be packaged to minimize the risk of damage during storage and installation. Lengths of 2”X4” lumber will be fixed to the OD frame through the axial bolt holes. These wooden “bumpers” will minimize the risk of crushing fibers.

Store module The module is then moved to the storage rack in Wideband Hall, where it will await installation into the NuMI Experimental Hall. A picture of a completed module is shown in Figure 118.

After a factory startup period, we are planning to assemble modules at a rate of one per day. There will be three assembly periods. First, we will assemble one module for the full module prototype that will be built in Fall of 2006. A year later, we will assemble twenty modules for the tracking prototype. Finally, we will construct the production detector modules in early 2009.

Design and Construct Module Mapper Every detector module will be mapped after it has been assembled. The purpose of mapping is to study the local response of the scintillator. The mapper will scan the scintillator of all detector modules at pre-determined points with a radioactive source. The response of the scintillator as a function of position will then be recorded by computer. Mapping allows us to identify any irregularities in the scintillator that will affect the detector performance so that we can account for this while analyzing data. Mapping is also one of our main quality assurance measures for each assembled module.

In consideration of radiation safety, we have decided that the mapper will remain within a fenced area at one end of Wideband Hall at all times. Modules will be transported to the mapping area by

Figure 118: The completed module has been moved to a storage rack. The DS face of the module here is shown so that the WLS fibers can be viewed.

use of the Wideband Hall overhead crane. The module and strongback will be positioned on the floor in the mapping area, and then the mapper will be moved into position above the module.

While we have not yet completed our mapper design, an initial engineer's drawing is shown in Figure 119. As shown in the Figure, the mapper will consist of a large, heavy steel frame and a scanning carriage that incorporates two scanning heads. The frame must be large enough to span an assembled module and rigid enough to withstand the stress of repeated lifting. Each scanning head will incorporate a 5-10 milli-Curie Cs-137 radioactive source shielded in a lead cone. The scanning heads will travel on rails and the motion will be provided by lead screws driven by electric motors. The motors will be controlled by a nearby computer.

As a module is mapped, the scintillator response will read out using M64 PMT's and a prototype electronics system controlled by a computer.

The design goal of the mapper is to safety scan one module within a period of 10-12 hours.

Assemble and Commission the Tracking Prototype WBS 9 has been asked to assemble and commission the tracking prototype. As the modules are assembled, our technicians will "install" the detector on a detector stand in Wideband Hall. This installation exercise, unlike the final detector installation, is part of the Project and has been assigned to WBS 9. As modules are secured on the stand, PMT's and readout cabling will also be installed.

Commissioning will be a busy time, and will involve input from more than just WBS 9. As the detector is turned on, there will be representatives from all levels of the collaboration interested in verifying the performance of specific systems. We will have expertise in the detector modules, but we will largely be reliant on experts from other tasks to handle problems with other systems, such as electronics and software. During this initial period, we will coordinate activities in the Wideband Hall and provide support to the various groups. We will ensure that groups have the tooling and

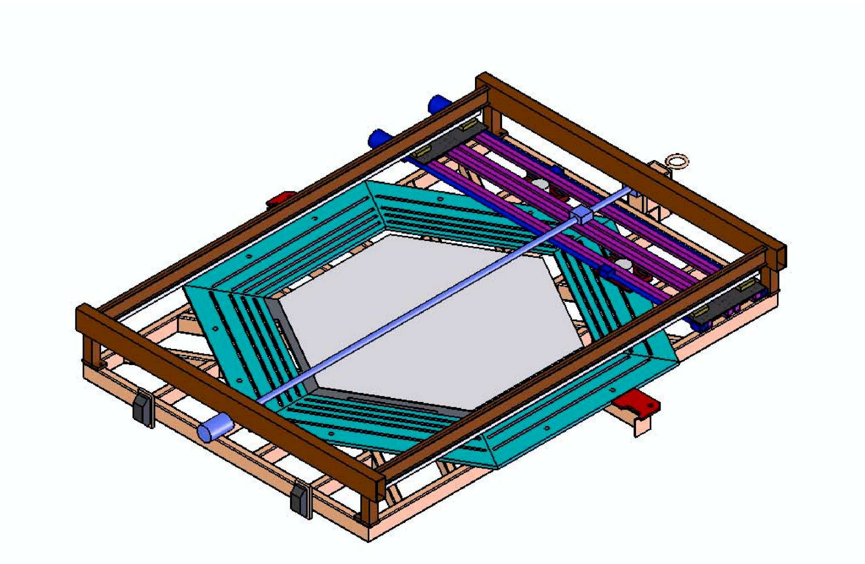

Figure 119: The module mapper incorporates a heavy steel frame and scanning carriage that will carry two Cs-137 radioactive sources. The mapper will be mated to the strongback so that the scanning heads are suspended above the module. Image source: [171].

resources they need to perform their work safely.

As the detector stabilizes and most of the immediate problems are solved, one of the major commissioning activities will be the collection of cosmic ray data over a period of 4-6 weeks. WBS 9 will ensure that the counting house is staffed with a shift crew. We will also verify that the shift crew has been properly trained, that necessary documentation has been provided, and ensure that the daily plan for shift workers is properly implemented.

PMT Racks and Clear Fiber Cable Routing WBS 9 will address certain issues related to the installation and handling of the PMT's and clear fiber cables. This responsibility was assigned to WBS 9 because our lab at the University of Rochester has the capacity to fabricate wooden models of detector components. We fabricated a full-sized model PMT rack based on early engineering designs and used this to study routing of the clear fiber cables and PMT box handling and maintenance issues.

The racks will be designed by a mechanical engineer at the University of Rochester. The final design will be based heavily on our experience with the wooden prototype rack. Racks will be fabricated in Rochester by an off-campus machine shop. Because the PMT's are to be mounted on top of the detector, they must be accessed from an overhead platform that will be provided by WBS8. WBS 9 will also design and provide a lifting jig that can be used during PMT maintenance. Lifting a PMT must be done carefully in order to minimize the possibility of damaging the fiber optic cables used to convey light from the detector to the PMT's.

Finally, we will develop the connector-to-PMT mapping for the clear fiber cables. Because we have the prototype PMT rack, we have been able to experiment with various arrangements of the the clear fiber routing. We have also been able to spec the length of the clear fiber cables based on

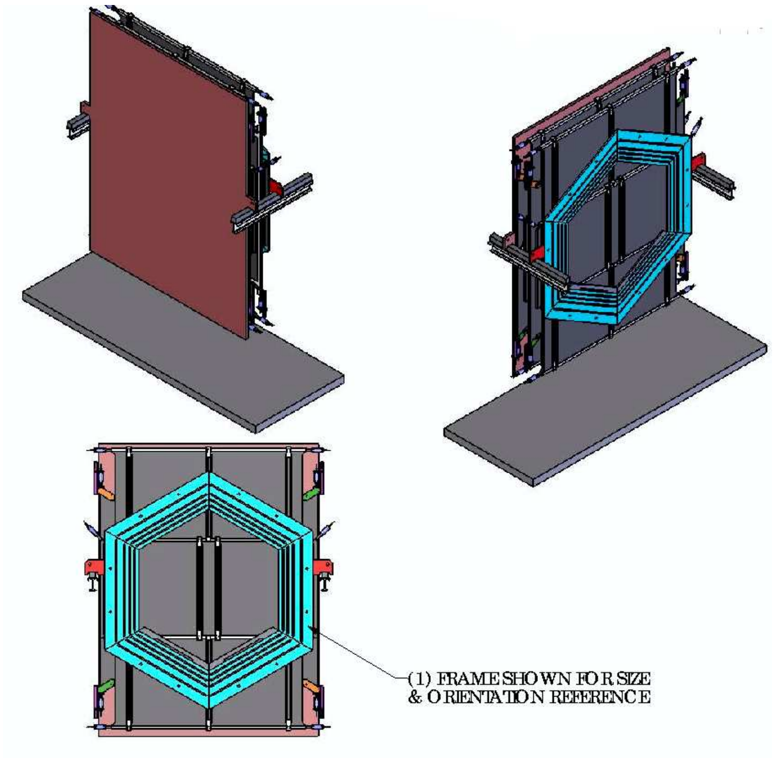

Figure 120: Initial engineer's drawing of the veto wall assembly. The veto wall consists of a a large steel plate (shown in purple) followed by two tiled arrays of scintillator counters (in gray). The steel wall and scintillator arrays cover the front end of the detector. Image source: [170].

our experience with a scale model. While the cable lengths and routing scheme have not yet been finalized, details of the current scheme are available in [169].

Construct Veto Wall The veto wall will be constructed largely from recycled components. The large steel sheet on the US end of the veto wall will be scrap steel from Fermilab surplus. Just downstream of the steel plate will be two walls of scintillator. These walls will be tiled arrays of scintillation counters. The veto wall counters will be constructed with refurbished scintillator taken from the NuTeV experiment. Each panel will have its own WLS light guides and readout PMT's. An initial engineer's drawing of the veto wall is shown in Figure 120.

The scintillator panels will be refurbished as part of a summer research program for high school teachers at the University of Rochester. The teachers will re-wrap and test the NuTeV scintillator during the summers of 2006 and 2007. WBS 9 will coordinate with and provide some support to the summer research program, and take delivery of the refurbished panels. If any of the scintillator or light guides is found to be unusable, then WBS 9 will be responsible for procuring additional panels or light guides.

WBS 9 will design the support structure for the steel wall and scintillator arrays. We will have these parts fabricated and transport all veto wall materials to Fermilab.

4.3.2 Facilities and Resources

WBS 9 requires facilities from both the University of Rochester and Fermilab.

The R&D effort of WBS 9 is centered at the University of Rochester, where we have the core personnel and facilities required to efficiently complete the research effort. This R&D program covers such tasks as development of the initial assembly protocols, testing of materials and tools for use in the module assembly process, refurbishment of the veto wall scintillator, and all design, fabrication, and purchasing tasks. Much of these early tasks are being led by Robert Bradford (the L2 manager for WBS 9), Robert Flight (mechanical engineer employed by the UofR Physics Department), Kevin McFarland (MINERνA spokesman), and Dan Ruggiero (UofR technician) with significant contributions provided by both graduate and undergraduate students. Our research group has been provided with laboratory space dedicated to MINERνA.

While the R&D tasks will be well performed in Rochester, the heavier assembly tasks will require the use of Wideband Hall at Fermilab. Wideband Hall provides ample floor space required to safely assemble and map the detector modules, good overhead crane coverage, and a door large enough to permit the passage of modules out of the building for installation. Wideband Hall will be the location for:

1. Construction of the module mapper.
2. Receipt and storage of detector components provided by university groups.
3. The module assembly and mapping factory. All full-sized prototype modules (including the full module prototype and tracking prototype) and final detector modules will be assembled in Wideband Hall.
4. Installation and commissioning and testing of the tracking prototype.
5. Welding of the OD steel frames (done by WBS8).

Within the Hall, we will required several assembly stations, storage space for detector components, storage racks for completed modules and a mapping station. Because the module mapper will contain radioactive sources, the mapping station must be a fenced enclosure posted with appropriate signage. Figure 113 shows the proposed layout of Wideband Hall. This layout has been negotiated with WBS8 and reviewed by appropriate safety interests from Fermilab.

Most labor for these heavier tasks will be provided by the University of Rochester. The University employs several experienced technicians who will construct the module mapper, coordinate delivery and receipt of detector components, and assemble and map the modules. The technicians will be supervised by Robert Bradford and other UofR personnel. Bradford will relocate temporarily to Fermilab during times of major activity.

During module assembly and mapping, the FNAL Alignment Group will conduct surveys of several modules.

Finally, software for the module mapper will be developed by a number of parties. While the mapper DAQ and motion control software will be provided by Fermilab engineers through WBS7, there will also be input from two institutions located in Lima, Peru, the Pontificia Universidad Catolica del Peru and Universidad Nacional de Ingenieria. Graduate students from these institutions will develop simulations that will guide the design of the mapper, will help integrate the mapper data into the broader MINERνAsoftware environment.

4.3.3 Interfaces with other WBS Tasks

WBS 9 interfaces most closely with WBS3, 8, and 11. WBS3 provides all scintillator assemblies, both the ID planes and the OD towers. These modules will be constructed at two institutions in Virginia, and then shipped to Fermilab. WBS 9 will take delivery of the scintillator units and store them in Wideband Hall. WBS8 will provide steel OD frames for module assembly. The frames will be built in Wideband Hall at the same time that the detector modules are being assembled. Each OD frame will be constructed on one of the three strongbacks in the Wideband Hall assembly area. Having three strongbacks (see Figure 113.) will allow frame welding, module assembly, and module mapping to occur in tandem. Frames will be delivered by WBS8 one-at-a-time as they are constructed. After a frame has been constructed, it will remain on the strongback and WBS 9 will begin using that frame to construct a detector module. After each production module has been assembled and mapped, it will be moved to a detector stand in Wideband Hall. These modules will be stored here until the detector is installed in the NuMIexperimental hall by WBS11. We will also provide WBS11 with the cable routing layouts for the clear fiber cables and PMT racks.

WBS 9 has more minor interfaces with several of the other task groups. These interfaces include:

1. WBS4 - Clear Fiber Cables: WBS 9 used early prototype models to spec the clear fiber cable lengths for WBS4 and develop the connector-to-PMT mapping scheme. WBS4, in turn, will provide WBS 9 will clear fiber cables required for the module mapper and the tracking prototype.

2. WBS5 - PMT boxes: WBS5 will provide WBS 9 with six Hamamatsu M-64 PMT's for use with the module mapper and an additional 110 PMT's for the tracking prototype. These PMT's will have been acquired and tested by WBS6; electronic components of the PMT boxes will be supplied by WBS7.

3. WBS7 - Electronics: A prototype data acquisition system will be supplied by WBS7 for use with the module mapper. This will be used to read out the scintillator response as the scintillator planes are scanned by the mapper. WBS7 will also be providing the DAQ and motion control software for the mapper.

4.3.4 Major Tasks

This section will give an overview of the tasks that we have scheduled for the next several years. The subsections will each refer to a specific task or group of tasks in the MINERνA Project file.

- WBS 9.1.1 - Rochester Prototypes: During the summer of 2005, we constructed wooden models of various detector components. In particular, we built two half-scale detector modules and a full-scale PMT rack. The wooden modules were then used in a series of mock module assembly exercises during which we outlined the assembly protocol, tested materials, and conducted basic time-motion studies. The model PMT rack was used to design the routing scheme of the clear fiber cables.

- WBS 9.1.2 - Full Module Prototype Assembly Fixtures: After studies with the wooden prototypes, then we will prepare for construction of the full-scale module prototype to be built at Fermilab in the Fall of 2006. These preparations include design and fabrication of hardware to be used for the prototype assembly, selection of tools, and acquisition of materials and hardware.

- WBS 9.1.3 - Veto Wall Counters and Veto Wall Design: In the spring and summer of 2006, work will begin on the veto wall. An inventory of the scintillator counters at the University of Rochester will be taken to verify of sizes and quantities of the available counters. Work will then commence on refurbishment and testing of the counters; this will be done by high school teachers and their students as part of a summer outreach activity lead by Kevin McFarland. The counters will be tested during two summers, 2006 and 2007. At this time, initial engineering drawings will be made on the veto wall to verify that the available counters will be sufficient for the detector's needs.

- WBS 9.1.4 - Design and Construct Mapper: The module mapper will be designed and constructed during the summer and fall of 2006. The design work will be done by a mechanical engineer at the University of Rochester. The same engineer will spec the required parts and begin the procurement. The mapper will require a large number of custom parts. We will have these fabricated by local machine shops so that the engineer will be able to readily interact with the machinists.

  The mapper will be constructed at Fermilab using space in Wideband Hall. Once the parts have been acquired at Rochester, then they will be delivered to Fermilab by truck. The University of Rochester employs several technicians that are resident at Fermilab who will be responsible for the physical assembly of the mapper.

  At this time, work will also begin on the readout and motion control software for the mapper.

- WBS 9.1.5 - Full Module Prototype Assembly: At the end of 2006, the collaboration will construct one prototype detector module. The module will be full-sized and should be fully functional, but it will be constructed from prototype components. WBS 9 will assemble this module. This will provide us with the opportunity to train the technicians using actual components and facilities, further refine our assembly procedures, and test the module mapper.

- WBS 9.1.6 - Module Assembly and Mapping Preparations: 2007 will be spent preparing for assembly of the tracking prototype. This will begin with a redesign of any hardware and facilities based on our experience with the full module prototype. Much of the procurement work for the tracking prototype and final detector will be done this year. We will build the

PMT racks, further optimize the module mapper, and fabricate a lifting jig that will be used for PMT installation and maintenance.

- WBS 9.2.1 - Assemble, Map, and Install Tracking Prototype Modules: WBS 9 will assemble and map all 20 modules for the tracking prototype, and install all modules into a detector stand in Wideband Hall.

- WBS 9.2.2 - Install Modules at Wideband: Once the modules have been assembled, WBS 9 will complete the assembly and installation of the tracking prototype in Wideband Hall. These activities will include installation of PMT racks, PMT's, and all cables. Electronics will be installed by WBS7.

- WBS 9.2.3 - Test and Evaluate Tracking Prototype: We will then commission the tracking prototype. We will have it surveyed to verify that the detector dimensions are within spec and collect cosmic ray data to test tracking. WBS 9 will set up a shift schedule and ensure that the counting room is staffed. We will also ensure that all shift takers have been adequately trained.

- WBS 9.3.1 - Veto Wall Assembly: After the tracking prototype has been assembled, then we will complete work on the veto wall. By late 2007, all veto wall counters will have been tested. Based on this information, we will then select the best counters to use in the veto wall. At this point, the design of the veto wall will then be revisited to verify that the support structure will accommodate the actual dimensions of the selected counters. Fabrication of the support structure will be completed and all materials will be shipped to Fermilab. The steel wall will be constructed at Fermilab. All items will be stored until the detector is installed in the NuMIhall.

- WBS 9.3.3 - Assemble and Map Production Modules: In early 2009, we will begin to assemble and map the modules for the MINERνA detector.

4.3.5 Future Work and Engineering

As we are still in the R&D phase of the MINERνA schedule, much of our engineering and optimization work is underway.

While we have practiced and rehearsed our initial assembly procedures, we are attempting to verify that these procedure will be compatible with the actual detector components. The assembly protocols were developed and rehearsed with our half-scale wooden prototype modules. These procedures have been written up in a document which is available in the MINERνA Docdb [169]. We are currently trying to verify our understanding of the OD frames with WBS8 and the scintillator modules with WBS3. These components are crucial for module assembly, so even small changes in the frames or scintillator assemblies could greatly impact WBS 9. We are working to finalize a set of engineering drawings of the OD frame with WBS8. Since our initial prototyping efforts, more details of the scintillator assemblies have become available. We have acquired samples of the materials to be used by WBS3, and we are currently testing to verify that our assembly procedures will work well with the scintillator assemblies. These efforts include such tests as verifying that our adhesives will adhere well to the materials that WBS3 has selected. We are also awaiting delivery of a prototype scintillator plane from WBS3 which we will use to verify dimensional tolerances and use to further test compatibility of our procedures. The full module prototype will give us our first chance to test our assembly procedures on actual full-size and full-weight detector components. We anticipate that this exercise will reveal weaknesses in our procedures or materials, so we have scheduled adequate time after the prototype module assembly to revise our assembly procedures and design.

We are also attempting to optimize work flow in light of the module mapper. Currently, the module assembly schedule in the MINERνA Project file is based on a assembly and mapping rate of one module per day. This rate is largely dominated by time required to map a module, which is predicted to be around 20 hours if we scale from the MINOS mapping rate. Based on initial mapper designs, we feel that we may be able to significantly increase the mapping rate by using two scanning heads in the MINERνA module mapper (MINOS mappers each had one scanning head.). The final mapping rate is yet to be determined, but we feel it may be 10-12 hours. Mapping at this rate would lead to a savings in the assembly costs and would remove much of the schedule contingency associated with the module assembly and mapping. This 10-12 hours spec will be the design goal of the mapper. Much remains to be done before we will know if this rate is feasible. Final design of the mapper will take place during the summer of 2006 and the mapper will be first tested on the full module prototype early in the winter of 2006-2007. Based on the outcomes of this test, we have scheduled time to debug and optimize the mapper in early 2007.

4.4 Detector Installation

WBS 11 is responsible for the installation of the detector, as well as a series of physical improvements required to make the NuMINear Hall suitable for MINERνA. This work is most closely related to WBS8, and much the work required for WBS 11 will be completed by the same individuals.

WBS 11 is not an official part of the MINERνA project. There are two major reasons for this. First, all of the infrastructure improvements in this WBS element are tasks that need to be done for the installation of any experiment and are not unique to MINERνA. These include extension of the hall's drip ceiling, moving the MINOS magnet power supply to make additional room, and installing the quiet power to service any experiment.

Second, the installation of the experiment is off project because with MINOS running the MINERνA project has no control over the timing of the detector installation. The MINERνA project has made various tests with the help of the MINOS experiment to determine how various installation tasks might affect data taking in MINOS. We have taken some test data with the MINOS detector while doing welding and also while using the overhead crane, either of which could generate electronic noise that would interfere with MINOS data taking. While tests so far show minimal effects on MINOS data, the testing has not been comprehensive. Therefore it is entirely possible that MINERνA may have to wait for a shutdown to carry out the installation of the detector. In order to define a clear set of CD4 deliverables, then, the detector installation has not officially been included in the MINERνA project.

This section, then, will give an overview of WBS 11. Emphasis will be placed on the scope of WBS 11, which will be covered first. This will be followed by a discussion of required resources and interfaces with other WBS tasks. An overview of the WBS structure and schedule will not be included.

4.4.1 Task Objectives and Overview

WBS 11 has two main objectives. These include, first, preparation of the NuMINear Hall to house MINERνA, and second, the actual installation of the detector. These two objectives will be discussed in more detail in the following two subsection.

Improvements to the Numi Near Hall The WBS 11 element provides for installing a drip ceiling over the detector. As the hall is located underground, leakage of groundwater (from above) is a major concern. With MINOS, this situation was remedied by the installation of a drip ceiling above the detector. The drip ceiling is attached to the ceiling of the experimental hall and channels ground water away from the detector. The current drip ceiling is sufficient for MINOS, but would not adequately cover the proposed location of MINERνA.

While it would suffice to simply extend the current drip ceiling to cover the MINERνA detector, we will also solicit quotes for extending the drip ceiling to cover the remainder of Numi near hall. The initial design has been for a simple extension of the same roof system that exists over the MINOS detector, but other kinds of roof systems are also being explored.

Quiet power services in the hall will be expanded with the addition of one more 75 KVA transformer and distribution panel. This addition would allow servicing of one experiments power system without having to shut down both experiments. In the recent shutdown the MINOS power supply and its water skid were moved upstream to the end of the hall. This move will provide extra room for experiments directly upstream of the MINOS detector where space is most valuable. With MINERνA in place the power supply would not have been serviceable in the old location if, for example, a transformer needed replacing.

Prior to installation, WBS 11 must install the required detector stands into the NuMIHall. The detector stand consists of a large rail system that supports the MINERνA detector. The detector modules will hang on the rails like a hanging file folder system. Figure 112 shows the side view of the detector on the stand. During the installation of the stand the Alignment Group will provide services to make sure the rails are at the proper elevation and that the rails are on the beamline axis. They will also measure the bookend to make sure that all of the frames are hanging plumb on the stand. The stand columns also supply the support for an additional set of rails that hold the phototube access platform over the top of the detector. This access platform allows servicing of the phototube and front end electronics of the detector. The access platform is not shown in Figure 112.

4.4.2 Detector Installation

The design of MINERνA is similar to MINOS because it is a series of frames that are assembled in a certain order to make up the detector. This allows us to use similar installation techniques that have already been worked out for the assembly of the MINOS detector. Pictures taken during the MINOS Near detector assembly can illustrate the procedure. Frames are brought over from the Wideband Lab to the MINOS Service building by tractor trailer truck one at a time in the order in which they are installed (from downstream to upstream). The strongbacks will be used as the transport fixture for this. They will maintain the frames flat during transport and will also be the lifting fixture during the

Figure 121: MINOS detector module being lowered into the cavern at the shaft.

lowering and raising crane operations. Figure 121 shows a MINOS detector module being lowered into the NuMINear Hall.

The MINOS surface building has two overhead cranes. The first will be used to load the detector modules off of the flatbed truck and stage them in the surface building. The second crane will then lift the modules and lower them down the access shaft into the NUMI Near Hall.

As modules are lowered into the NuMIhall, they will be secured to a cart. The MINOS cart, shown in Figures 121 and 122, will be re-used for the MINERνA installation after some minor modifications. The strongback and frame will be landed on the cart and secured by bolts. Then an electric forklift will be used to push the cart roughly 100 m to the experimental hall.

After the frame is re-secured to the cavern crane it can be unbolted from the cart, moved into position on the detector stand and set in place. The frame will be secured to the detector by axial bolts that keep a uniform distance between frames. A bookend on the downstream end of the stand provides a framework that ensures that the assembly of the detector starts from a straight reference plane. During assembly of the following frames frequent measurements will be taken and adjustments made to maintain the detector straight and plumb. Figure 123 illustrates the mounting of a MINOS detector module.

As each module is installed, some quality assurance and testing will be done. Modules will be

Figure 122: Cart in the Numi Near Hall holding a MINOS detector module.

Figure 123: Mounting a MINOS module on the detector stand.

visually inspected for damage during transport and handling. The light-tightness of each module will also be verified.

As every four modules are installed, a PMT rack will be installed on top. This rack will hold all of the PMT's required to read out the four modules. The PMT's and electronics will be installed, and each module will be tested further.

After the detector is assembled a phototube access platform will be installed on its own rails. This platform will allow for routine maintenance of the phototubes without the need of special equipment.

4.4.3 Facilities and Resources

Most of heavy work associated with detector installation will be handled by Fermilab technicians. WBS 11 will employ the crew used by WBS8 for the OD frame assembly and welding; this is also the same crew who handled the installation of the MINOS near detector. This crew will install the detector stand, handle installation of the detector modules, and install the PMT access platform.

At the time of installation, some physicist involvement will be required. In particular, a group from the University of Rochester will help install the PMT's and clear fiber cables, and test the modules. This group is associated with WBS9. Having been heavily involved in module assembly, they will be familiar with module QA procedures. WBS9 is responsible for commissioning the tracking prototype, so Rochester technicians and physicists will help test and commission each module as they are installed. Representatives from other task groups will handle installation and testing of the electronics and data acquisition system.

As discussed in the previous section, WBS 11 will make use of Wideband Hall, the MINOS surface building and the NuMIhall. Before installation, the assembled modules will be stored in Wideband Hall. All three locations are equipped with adequate overhead cranes to handle any lifting operations required. A flatbed truck will be required to transport modules from Wideband Hall to the MINOS surface building, and an electronic fork lift will be used in the NuMIexperimental hall to push the cart which moves modules from the bottom of the access shaft to the staging area for the overhead crane.

4.4.4 Interfaces with other WBS Tasks

WBS 11 will interface most closely with WBS9. WBS9 will deliver the assembled modules to WBS 11. These modules will be hanging on a storage rack in Wideband Hall. In addition, WBS9 will provide the PMT racks and the veto wall.

PMTs in boxes will be provided by WBS6, and electronics will be provided by WBS7.

5 Software

5.1 Overview

Software and computing resources are an integral part of the MINERνA project. These resources will be used to accommodate two primary tasks for MINERνA:

1. Data storage after acquisition under experimental running conditions
2. Data analysis and numerical modeling.

Detailed numerical modeling is necessary for the experimenters on MINERνA to gain the most complete understanding of the detector as possible. Data event selection and reconstruction goes together with the detailed detector model to both improve understanding of the detector response and analyze physics production data. Physical computing resources, including:

1. Raw and processed data storage
2. Detector model output and analysis storage
3. Raw and modeling data processing computer processor usage

are needed to complete analysis of MINERνA physics data. The MINERνA project has developed a technical design for obtaining these software and computing resources.

Data processing needs for the MINERνA experiment are divided into two main categories:

1. Generation and analysis of detector modeling events.
2. Event selection and reconstruction of real physics data from the physical MINERνA detector.

Certainly, it can be argued that these are not exclusive needs. For example the reconstruction packages used in the reconstruction of real physics events are, or at least may be, the same as those used for certain analysis of real physics data. Software which must be developed or implemented for this experiment includes but is not limited to:

1. The generation of neutrino events, including models of nuclear effects on neutrino-nucleon interactions.
2. Accurate descriptions of the MINERνA detector during design and after construction (as-built).
3. Codes to perform offline calibration and alignment of the detector in a timely fashion
4. A method of relaying accurate commissioning and calibration information to both simulation software and reconstruction software for real physics data.
5. Reconstruction and event selection routines suitable for use with both simulated and real physics data.

6. Analysis and visualization software for interpreting and displaying the results.

These needs can be met using a combination of pre-existing software and new software development or implementation.

The use of pre-existing software packages, particularly those which have been designed with physics analysis as their primary function, will help reduce the amount of time required to meet the software development needs of the MINERνAproject. For example, many packages already exist which can be used for data analysis and visualization. These packages are readily available at little or no cost to the experiment, or individual collaborator's institutions. The software development plan for simulation, reconstruction, and analysis requires the best-use of object-oriented programming techniques. The use of object-oriented programming techniques will allow MINERνA experimenters to use modern, well-supported, software tools to their best advantage, as well as making the use of varying analysis and reconstruction routines reasonably seamless. As of the writing of this document the following software packages were under review (but need not be limited to):

- GAUDI, a framework package, and its support packages.
- Geant4, a simulation package.
- ROOT, a data visualization and analysis package.
- A database, MySQL or Oracle are the current candidates.

Studies of the consistency between Geant3 and Geant4 based models are underway. Collaborators have also been developing specific classes for use with the MINERνA detector.

Meeting these software and physical computing needs is a collaborative effort. The members of the MINERνA collaboration are providing individuals to organize, develop, and train the full collaboration in the proper use of the software under construction. Physical computing resources will need to be provided from various sources, not the least of which is the Fermi Lab Computing Division. From the Laboratory, the MINERνA project will require mass-storage of raw, reconstructed, and simulated data. Centralized access to developed software and data will also be a necessity. These, among other needs from the Fermi Lab Computing Division are addressed in a formal Memorandum of Understanding between the project and the Computing Division. Clearly, meeting the computing needs of the MINERνA project is a collaborative effort.

5.2 Beam Simulation and Neutrino Event Generation

In order to produce a useful numerical model of the MINERνA detector two inputs are required:

1. A high quality model for the neutrino beam energy spectrum.
2. A generator of neutrino-interaction events.

At this time, the members of the MINERνA collaboration plan to neither manufacture nor maintain the external software which provides these necessary components of detector simulation. This decision was made pursuant to the availability of readily available software providing both beam energy spectra for the NuMI beam and not less than two reliable neutrino-event generators.

The neutrino beam energy spectra are provided to the MINERνA project from the NuMI working group of the Fermilab Neutrino Department. Neutrino energy spectra are produced using a numerical modeling package called GNuMI. This model was expressly developed for the NuMI beam line at Fermi Lab, and can provide profiles for various arrangements of the tuning horns along the beam line. These spectra are delivered, and used by the MINERνAcollaboration as text vectors.

Neutrino-interaction events are, in general, generated using one of two readily available neutrino event generators, NEUGEN and NUANCE. Both of these event generators can be used to simulate the four classifications of interactions of interest to the MINERνA project:

1. Quasi-elastic neutrino scattering.

2. Resonance production from neutrino scattering.

3. Deeply-Inelastic neutrino scattering.

4. Coherent production from neutrino scattering.

These event generators have been designed to incorporate nuclear effects in neutrino-interactions by incorporating the best available theoretical models and data. Appropriate accommodation will be made for use output of these event generators as input to numerical simulation of the detector. The MINERνAcollaboration has members who are instrumental in the design and maintenance of these generators through the respective collaborations designing them. Further information containing the methods used in NUANCE and NEUGEN can be found in references [173] and [138].

5.3 Code Management

Maintaining the quality and accessibility of computer code is imperative for the MINERνA collaboration. Proper code management requires two primary objectives:

1. Proper version maintenance and propagation.

2. Enforcement of best-practices in program design and documentation as determined by the members of the MINERνA collaboration.

Laboratory infrastructure and MINERνA collaboration effort are necessary to assist in attaining these objectives.

A Concurrent Versions System (CVS) server has been established at Fermi Lab for use by the MINERνA collaboration for storing and propagating necessary tools and other information. This server, setup by the Computing Division and maintained by the Collaboration, was negotiated as part of the MINERνAMemorandum of Understanding with the Fermi Lab Computing Division. Through CVS multiple versions of the same software can be made available as corrections are made and features are added without loss of the previous versions. This server is availability only to members of the MINERνA collaboration and is not publicly accessible.

The enforcement of best-practices in conforming to the object-oriented nature of the simulation and analysis software development plan is the job of a software librarian. This individual is identified internally by the MINERνA collaboration. The software librarian is responsible for assisting those working on software projects in understanding the best-practices established by the collaboration, ensuring that tests for quality assurance and consistency are performed by developers before releasing new or corrected software for collaboration use, and insisting upon the proper documentation of software projects is produced such that all collaboration members can make use of simulation and analysis software.

5.4 Data Processing (Handling), CPU, and Storage

Data processing, CPU, and data storage requirements are detailed in the Memorandum of Understanding (MOU) between the Computing Division at Fermi Lab and the “project”. These requirements are likely to change as the simulation and reconstruction software is better understood. The current understanding of computing needs for, Monte Carlo generation, is summarized in Table 17

Year	MC Data Store (GB)	MC CPU-year
2009	675	2.25
2010	1350	4.50
2011	4000	13.33
2012	4000	13.33
Total	10025	33.41

Table 17: Current understanding of Monte Carlo computing needs.

During the upcoming prototyping phase of MINERνA, an improved understanding of our offline computing needs will emerge. The prototyping itself, of course, requires some computing resources. At this time 30 GB of mass storage space has been requested from the Computing Division at FNAL as stipulated in the MOU.

5.5 On-line Software

Software support is needed for data acquisition (DAQ). The explicit requirements are under investigation as of the writing of this document and are discussed in section 3 under DAQ and Control and Monitoring.

The prototyping phase of the project will help determine and refine the on-line software needs for MINERνA.

6 Monte Carlo Studies of Detector Performance

This chapter describes the Monte Carlo studies that were carried out to optimize the detector design and quantify the important performance characteristics of the detector, including vertex and tracking resolution, particle identification, and energy resolutions.

6.1 Detector Simulation

Simulation of neutrino interactions in MINERνA is carried out by a GEANT3-based Monte Carlo program. This program combines a flexible description of the detector geometry, the NuMI neutrino beam flux from the beam simulation, neutrino interaction physics from either of the two generators and simulation of the scintillator response with the standard tracking and particle interaction routines available in GEANT.

6.1.1 GNuMI flux interface

The output of the GNuMI simulation of the beamline is a set of files recording the neutrino flux in 0.5 GeV bins for a nominal number of protons on target. The flux files are in a standard format and hence can be interchanged with no additional modifications to the code. In this way different beam configurations can be easily studied. An option exists to generate interactions with a flat energy spectrum. In this case, beam weights are stored in an output ntuple. This is particularly useful if one wishes to study the effect of different beam configurations without furthur Monte Carlo running.

6.1.2 Event generator interface

The Monte Carlo simulation program can be configured to accept neutrino interactions from either NEUGEN3 or NUANCE. The results of a neutrino interaction can be passed to the simulation in a number of ways. By default, the event generation routines in NEUGEN3 are usually called from within the simulation itself. In this mode, the code chooses a neutrino energy from the flux files, samples the density of material along the neutrino path; chooses a vertex and nucleus type, calls the kinematics generator and inserts the list of particles thus obtained into the GEANT data structures. This is not the only mode of generation. As a stand-alone generator, NUANCE provides events in either a text or ntuple format and so a provision is made to read in events from a standard external format. NEUGEN3 has been modified to write out events in the same format, so that the results of both generators may be compared in a consistent manner.

6.1.3 Geometry

Flexibility drives the design of the detector geometry code. The size, segmentation, material and shape of all components of the detector can be set and altered almost entirely from input datacards. The detector is logically divided into longitudinal sections. Each section can have different dimensions, strip sizes and absorber widths. In addition the absorbers in each section can be be constructed from segments of differing material and widths. The geometry description is sufficiently abstract that minor changes in detector design may be accommodated merely by changing the datacard, allowing for fast detector reconfiguration and easy bookkeeping.

6.1.4 Hits and digitizations

Particles are tracked through the GEANT geometry in the standard manner. When a particle traverses a sensitive detector volume the particle type, volume identifier, entrance and exit points and energy deposition (including Landau and other fluctuations) are recorded as a hit. When GEANT has finished tracking the event, the hits are considered and converted to digitizations. There are as many digitizations as there are strips hit. Multiple hits on a single strip are condensed into one digitization, although information on which tracks contributed to the digitization is stored. These digitizations are then passed to the event reconstruction program.

6.1.5 Detector response and calibration simulation

The GEANT detector simulation assumes "ideal" light collection, and records the raw energy deposited in each channel. During event reconstruction, the energy deposited is converted to a number of detected photo-electrons. The scale factor between energy deposited and expected photo-electrons detected is determined by a standalone optical simulation validated for MINOS (see Section 6.2): the expected number of photo-electrons is smeared by Poisson statistics, and a 10% channel-to-channel Gaussian smearing reflecting a conservative estimate of remaining systematics after calibration and attenuation corrections.

6.2 Light Yield Simulation

In addition to the GEANT-3 based detector Monte Carlo, a standalone photon transport Monte Carlo was used to estimate the light yield of the proposed design. The photon transport Monte Carlo (LITEYLDX) was originally written by Keith Ruddick [175] and was modified to simulate the triangular extrusions of MINERνA. It was tuned to reproduce the known characteristics of the MINOS scintillator, namely that the average light yield from a MINOS module is 4.25 photo-electrons/MIP at a distance of 4 meters, and attenuation in the fiber is well described in terms of a double exponential: [176]:

$$\mathrm{N(x) = A(\exp(-x/90cm) + \exp(-x/700cm))}. \quad (13)$$

Particle identification studies described in Section 6.3.5 indicate that for a triangular extrusion, average light levels above 3.9 photo-electrons/MeV are required from a MIP in the inner detector. Coordinate resolution, vertex finding, and track pointing are affected by light levels to a lesser extent. Measurements in the vertical slice test indicate that actual light level in the inner tracker, including transmission and connector losses, will be 4.7 PE/MeV.

The photon transport Monte Carlo was used to calculate, for a given 'configuration' (strip geometry, fiber diameter, and fiber placement), the number of photons trapped in the fiber for a MIP entering at a particular position. This information is then used to determine a relative light collection efficiency for a particular configuration compared to MINOS strips. With the overall normalization

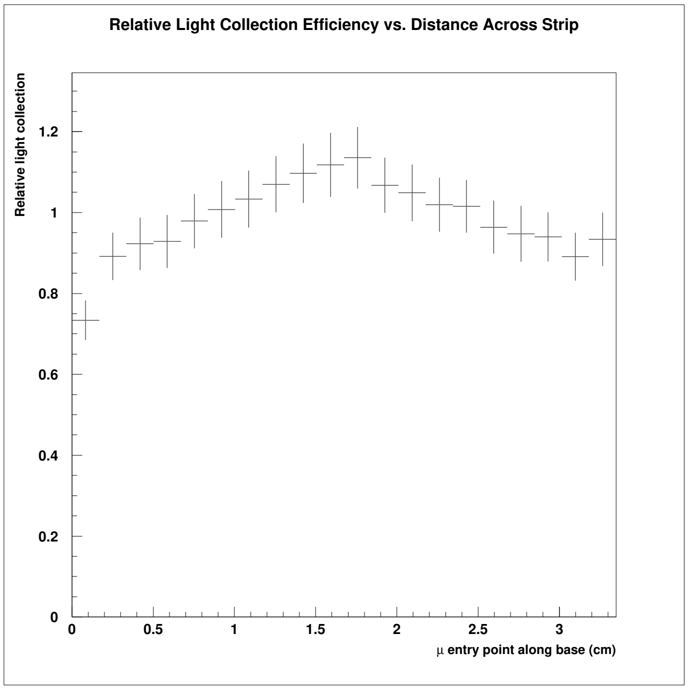

Figure 124: Relative light collection efficiency for a MIP crossing at normal incidence along the base of the scintillator extrusion.

and attenuation curve from MINOS one can then calculate the amount of light for any particular configuration. Figure 124 shows the relative light collection efficiency for a triangular extrusion where the entry point of the minimum ionizing particle is varied across the strip width, and indicates that the collection efficiency varies by $\pm 10\%$ over the strip width.

The overall light levels from 3 lengths of strips are shown in Figure 125. Here we have assumed a 90% reflectivity from the mirror end of the strip, and in all cases a 1 meter WLS 'pigtail' from the end of the near end of the strip to the PMT face. Clear fiber lengths and connectors are not included. Shown are the light levels predicted for 3 strip lengths. In each plot, the lowest curve corresponds to light collected from reflections off the mirrored end, the middle line corresponds to light travelling directly from the MIP to the readout end, and the upper line is the sum. As the figure shows, the light level in the inner tracking detector, with a maximum length of 2.2 m, meets the design requirement of 7.8 PE/MIP over the entire length.

6.3 Event Reconstruction

The output of the detector simulation is a list of digitizations for each strip. We have developed a basic reconstruction program which takes this list and reconstructs the tracks and vertices in an event.

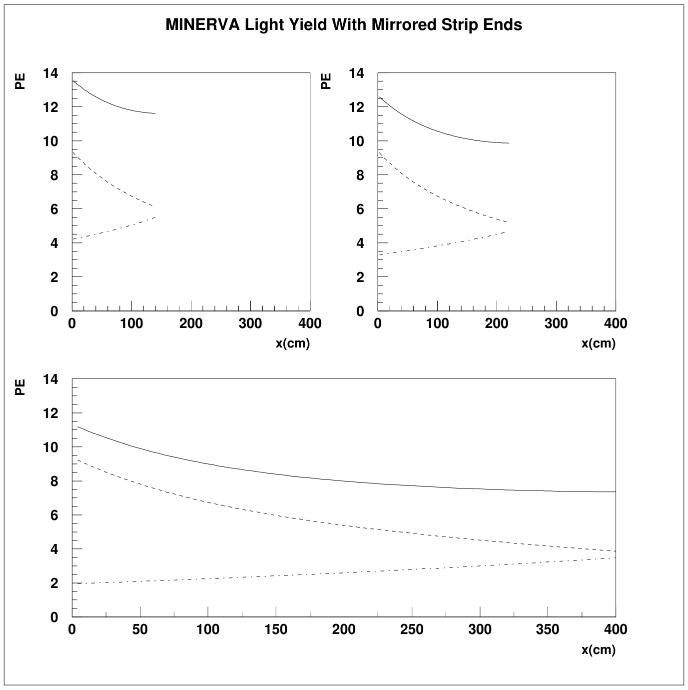

Figure 125: Light yield vs. distance along strip for MINERνA scintillator strips with one-ended readout with a mirrored end. Dot-dashed line is light collected from reflections off the mirrored end, dashed line is light travelling directly to the readout end; solid line is the sum.

6.3.1 Pattern recognition

For our design studies, we have adopted "omniscient" pattern recognition based on Monte Carlo truth information. All hits generated by a given track (ignoring channels with overlap) are used to reconstruct the track. Development of a fully-realistic pattern-recognition algorithm to associate hits to track candidates has not been undertaken as yet due to manpower and time constraints. We are confident that the three-dimensional XUXV modular design of the detector, and its relatively modest occupancy, will allow highly-efficient pattern recognition and track identification. Visual inspection of events through the graphical interface of the detector simulation program reinforces this conclusion.

6.3.2 Coordinate reconstruction

Tracks generating hits in at least six scintillator planes of the inner detector, including three planes of the X view, can be reconstructed. Coordinates are estimated from the raw, smeared digitizations, using only planes which have one or two strips hit. Tracks at high angles to the detector axis may pass through more than two strips in a single plane, and it should be possible to recover these higher-multiplicity hits with a more sophisticated algorithm. For single hits, the coordinate is taken as the center of the strip. For dual hits, the position is interpolated using the charge-sharing between between strips, with a small geometrical correction based on the estimated crossing angle.

The coordinate resolution for a large test sample of single and double hits can be measured directly using the residuals obtained when each coordinate is excluded, in turn, from the track's fit. This coordinate resolution is parameterized as a function of the track's crossing angle, and used to assign errors to coordinates in the fitter.

6.3.3 Track finding

Reconstructed coordinates are used to fit each track using a Kalman filter algorithm[178]. For this proposal, tracking performance has only been studied in the non-magnetic region of the detector; the track model is perforce a strictly linear one. Neglect of the magnetic field is justified because mission-critical resolutions are determined by performance of the fully-active (non-magnetized) volume, and since coordinate resolution for the strips should not depend on the presence of a magnetic field. The momentum resolution for charged tracks in a magnetic field can be reliably estimated from the coordinate resolution, momentum and field strength. As long tracks may pass through many radiation lengths of scintillator and absorbing material, the Kalman filter's ability to correctly account for multiple Coulomb scattering ("process noise") is essential. The algorithm can optionally be used to exclude outliers from the fit.

Figure 126 shows the expected hit residuals, impact parameter and angular resolution for muons from a sample of quasi-elastic interactions, assuming triangular strips of 3 cm width and 1.5 cm thickness (close to the final design values). Hit resolutions of $\sim 3\,\text{mm}$ and angular resolutions of $< 0.5^\circ$ are expected. These are consistent with the measurements made in the Vertical Slice Test which indicated a coordinate resolution of 3.2 mm. The coordinate resolution is degraded to approximately 1.5 cm if rectangular strips are employed instead of triangular ones, since interpolation based on charge is no longer possible.

6.3.4 Vertex finding

In this study, reconstructed tracks are associated to vertices using Monte Carlo truth information. The vertex positions are then fit using a Kalman filter algorithm. Track directions at the vertex are updated taking account of the constraint. This is equivalent to a least squares fit, but mathematically more tractable since it does not involve inversion of large matrices and can be easily extended to a helical track model. The primary vertex resolution for a sample of simulated quasi-elastic interactions with two visible tracks is shown in Figure 127. The transverse (longitudinal) vertex postion can be measured to a precision of better than (slightly more than) a centimeter.

6.3.5 Particle identification

Particle identification in MINERνA will rely on measuring specific energy loss (dE/dx) as well as topology (hadron and electromagnetic showers, decay signatures).

Electromagnetic showers Electromagnetic showers are easily identifiable by their diffuse track and characteristic dE/dx profile in the fully-active central detector and energy deposition in the electromagnetic calorimeters. In addition, the fine granularity of MINERνA allows us to distinguish

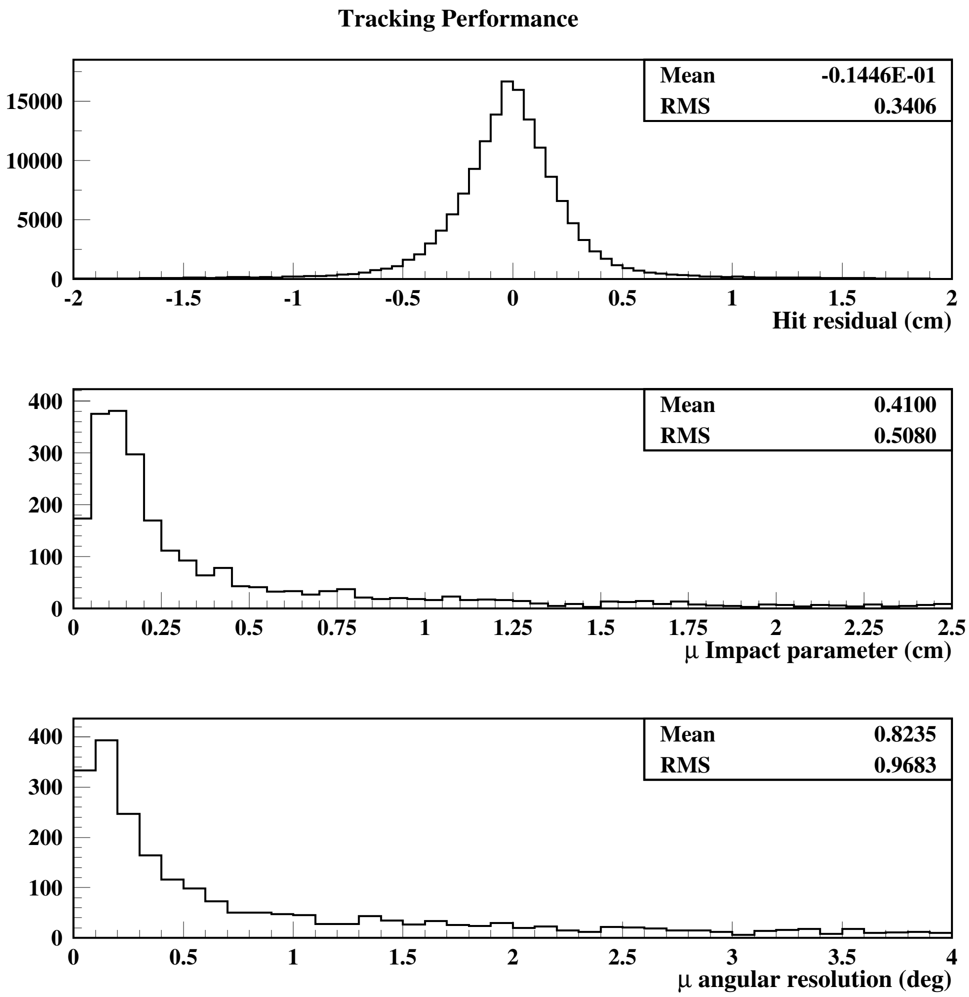

Figure 126: Performance of the tracking algorithm on muons from from a sample of simulated charged-current quasi-elastic interactions. Shown are (top) the hit residuals, (middle) the impact parameter of the muon with the vertex and (bottom) the muon angular resolution.

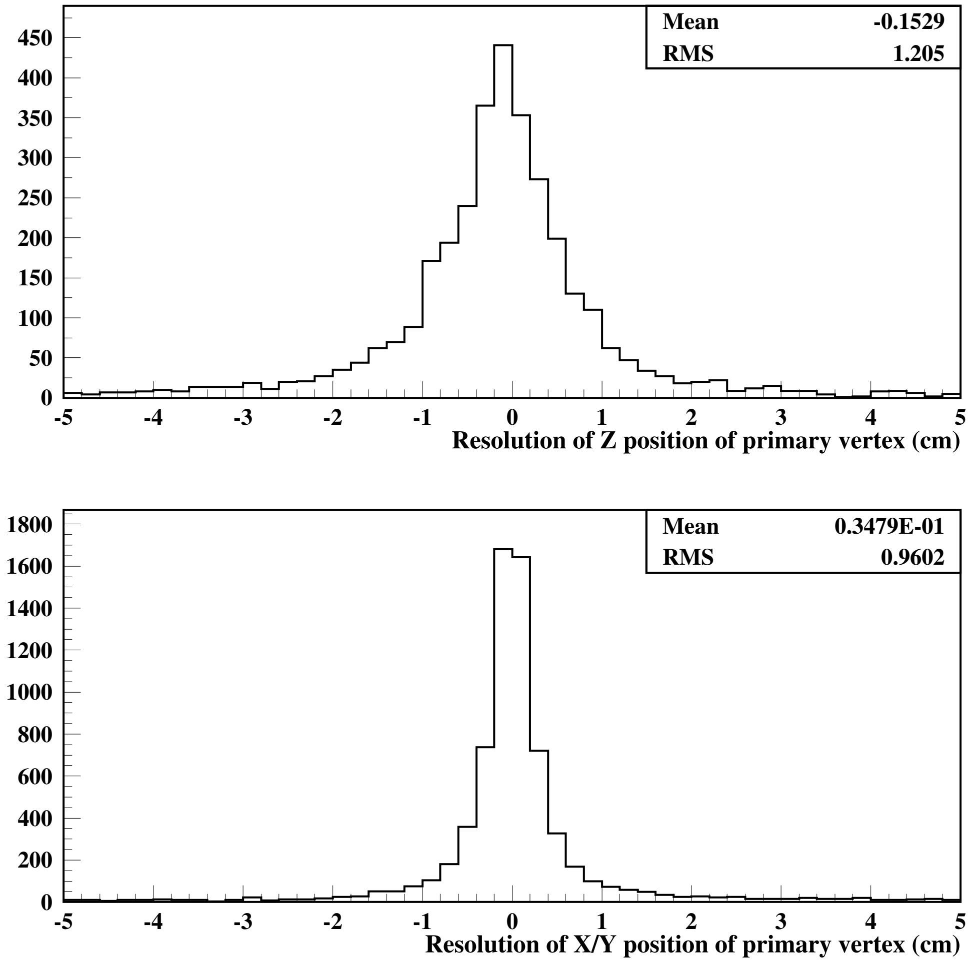

Figure 127: Reconstructed vertex resolution for two track charged current quasielastic events. Shown are (top) the resolution in the longitudinal position of the vertex (Z) and (bottom) the resolution of the transverse position of the vertex (X and Y).

electrons and photons, when the primary vertex is known, using distance to shower onset and shower length. Figure 128 shows the distance between the electromagnetic shower origin and the true primary vertex for charged-current ν_e interactions and π^0 production. The figure also shows the length of the showers, measured in MINERνA scintillator planes, or 1.75 cm of polystyrene. For neutral pions the length is from the beginning of the first showering photon to the end of the second one.

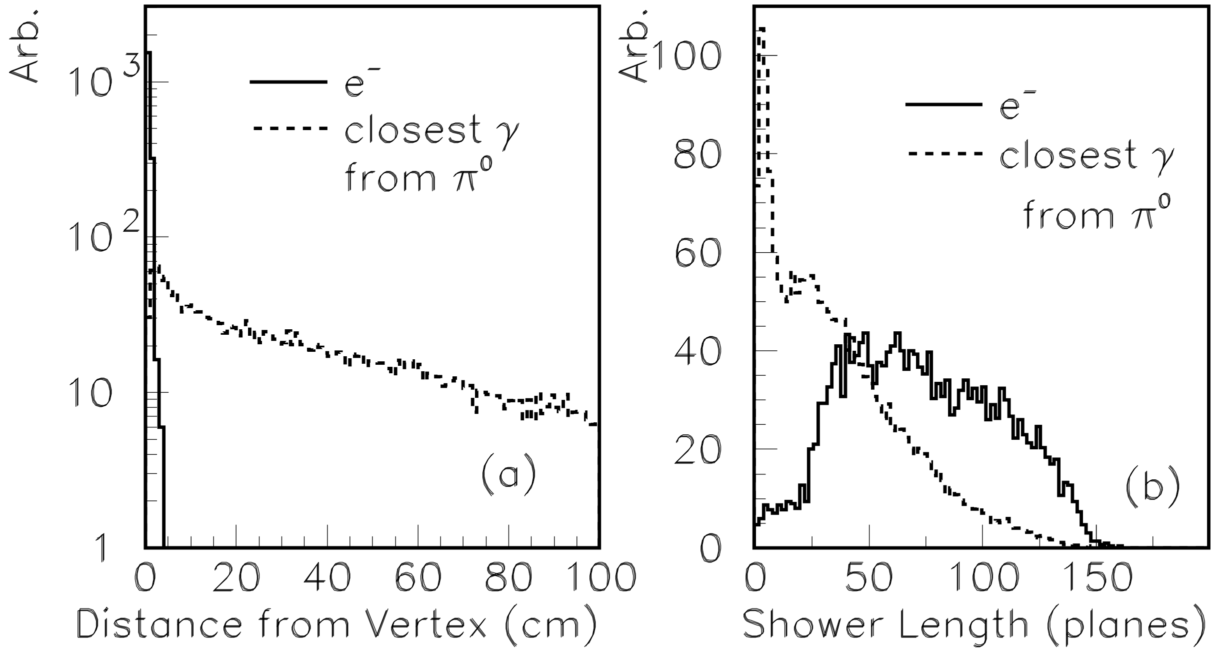

Figure 128: (a) The distance in centimeters between the neutrino vertex, which can be determined from a proton track, and the start of the most upstream electromagnetic shower, for both electrons and photons from neutral pions. (b) The shower length in units of scintillator planes, for electrons and neutral pions.

Electromagnetic energy resolution The energy resolution of the detector has been determined with Monte Carlo simulations using single electrons. The dependence of the resolution on the electron energy, angle, and track length in the inner detector have been determined. For forwardgoing electrons at the front of the inner detector the energy dependence is shown in Figure 129. The energy resolution for this situation can be parametrized as

$$\sigma/E = 1.0\%/\sqrt{E} + 2.7\%. \tag{14}$$

The calorimetric capabilities of the detector for low energy showers are quite strong, for example the energy resolution for these 1 GeV electrons is = 3.7%. Figure 130 shows the energy resolution for 1 GeV electrons as a function of the electron angle. Electrons at less than 20° to the beam direction strike the downstream ECAL while those with $\theta > 20°$ hit the barrel ECAL.

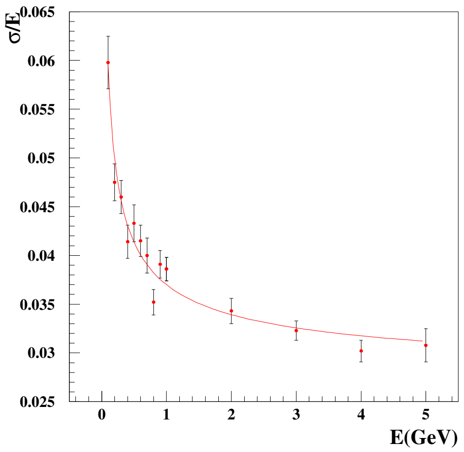

Figure 129: Energy resolution (σ/E) of forward going electrons which start at the front of the inner detector.

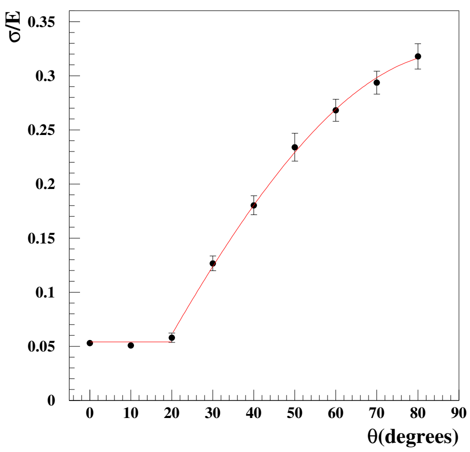

Figure 130: Energy resolution (σ/E) of 1 GeV electrons as a function of the angle the electron makes with respect to the detector axis.

π^0 reconstruction With the surrounding ECALs for containment, MINERνA's π^0 reconstruction capabilities are excellent. This is essential, since π^0 are a major source of background for ν_e appearance oscillation experiments. MINERνA's low density and high granularity make it an excellent photon tracker, able to accurately reconstruct the vertex and kinematics even for coherently-produced π^0's with no accompanying charged tracks.

Muons Energetic muons can be identified by their penetration of material in the calorimeters and/or MINOS near detector. Muons with a momentum measurement in the magnetic field, or which stop inside the detector can be distinguished from protons and kaons by dE/dx. In addition, the delayed $\mu \to e$ decay signature can be detected.

Charged hadrons Hadrons can be identified as such by their interactions in the inner detector and/or hadron calorimeters. Hadrons which stop without interacting or have their momentum measured by the magnetic field can also be distinguished as π, K or p with good efficiency using dE/dx. For studies of single pion and resonance production the ability to reconstruct pion and proton energies and directions is particularly important for full kinematic reconstruction. As discussed in Section 2.2, the resolution in invariant mass in the region around the $\Delta(1232)$ is around 100 MeV and the Q^2 resolution is slightly better than 0.2 (GeV/c)^2.

dE/dx analysis Specific energy loss (dE/dx) will be an important tool for particle identification in MINERνA. For tracks which stop in the inner detector, the charge deposited near the end of the track (corrected for sample length) can be compared with expected curves for, *e.g.,* the $\pi^\pm$, $K^\pm$ and proton hypotheses. This technique does not require an independent momentum measurement, since the range (x_{stop}, in g/cm^2) from the stopping point to a given sampling point is closely correlated with the momentum at the sampling point. The algorithm is calibrated by fitting the expected dE/dx vs. x_{stop}, and the standard deviation of this quantity, $\sigma_{dE/dx}$, as a function of x_{stop} for the three different particle types (see Figure 131). The measured dE/dx for a track is compared to the expected value at each sample, to form χ^2 estimators reflecting the goodness of fit to each of the three particle identification hypotheses:

$$\chi^2(\alpha) = \sum_{i=1}^{N_{sample}} \left[\frac{\left(\frac{dE}{dx}\right)_i^{obs} - \left(\frac{dE_\alpha}{dx}\right)_i^{exp}}{\sigma_i^\alpha} \right]^2,$$

where the sum runs over all measured samples, and $\alpha = \{\pi, K, p\}$. The hypothesis α with the minimum χ^2 is assigned to the track. The frequency of misidentification can be visualized most easily by plotting the difference $\Delta\chi^2$ between the correct χ^2 (for the particle's true type) and the smallest of the two (incorrect) others (Figure 132). With this naïve dE/dx analysis, MINERνA correctly identifies 85% of stopping kaons, 90% of stopping pions, and $> 95\%$ of stopping protons. A similar analysis can be applied to tracks with momenta measured in the magnetic regions of the detector.

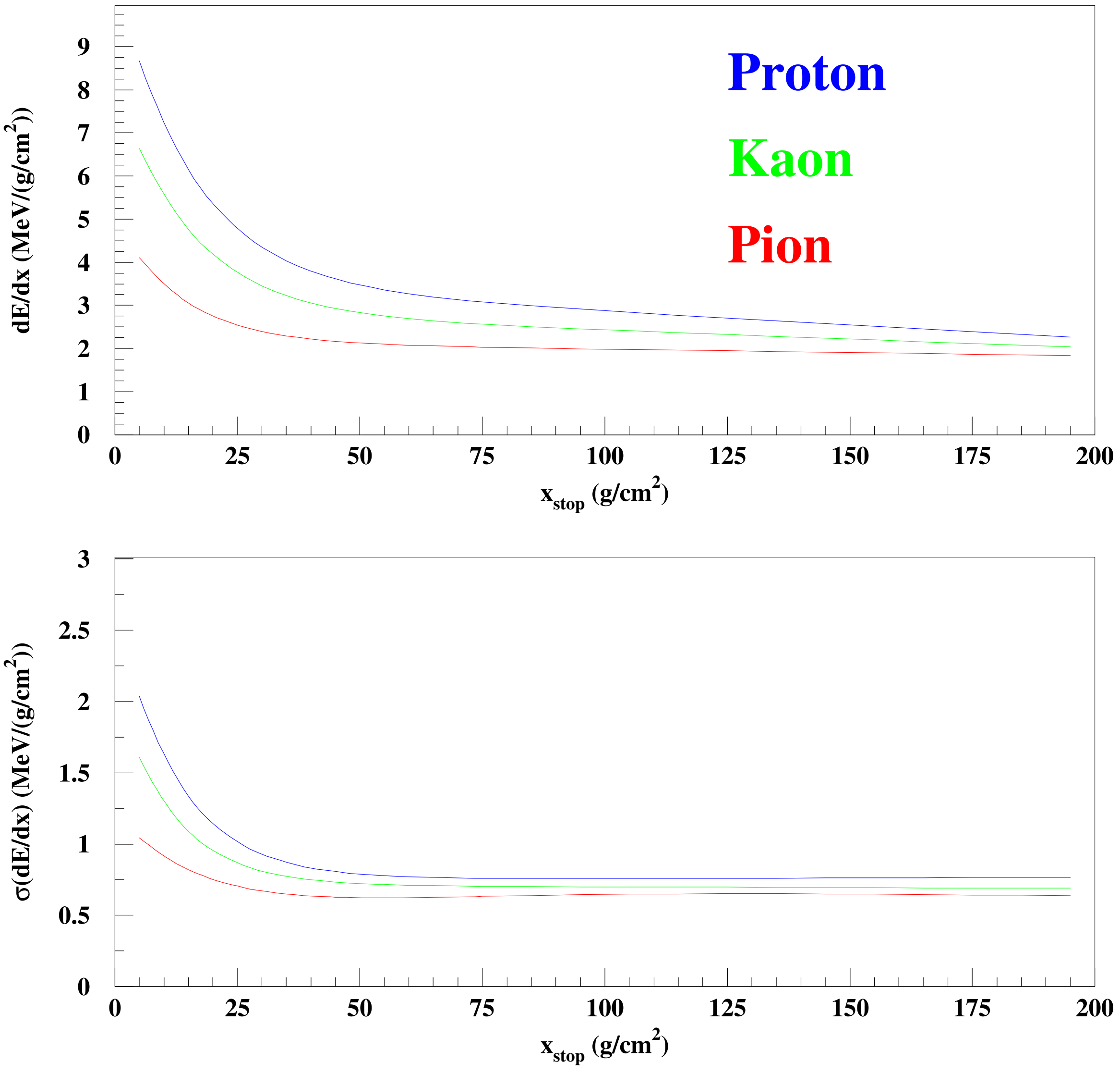

Figure 131: The top figure shows the average specific energy loss dE/dx for stopping $\pi^{\pm}$, kaons and protons, vs. range from the stopping point (in g/cm^2), for the simulated MINERνA inner detector. The bottom figure shows the estimated standard deviation of the energy loss, which is used to form a χ^2 estimator for particle identification.

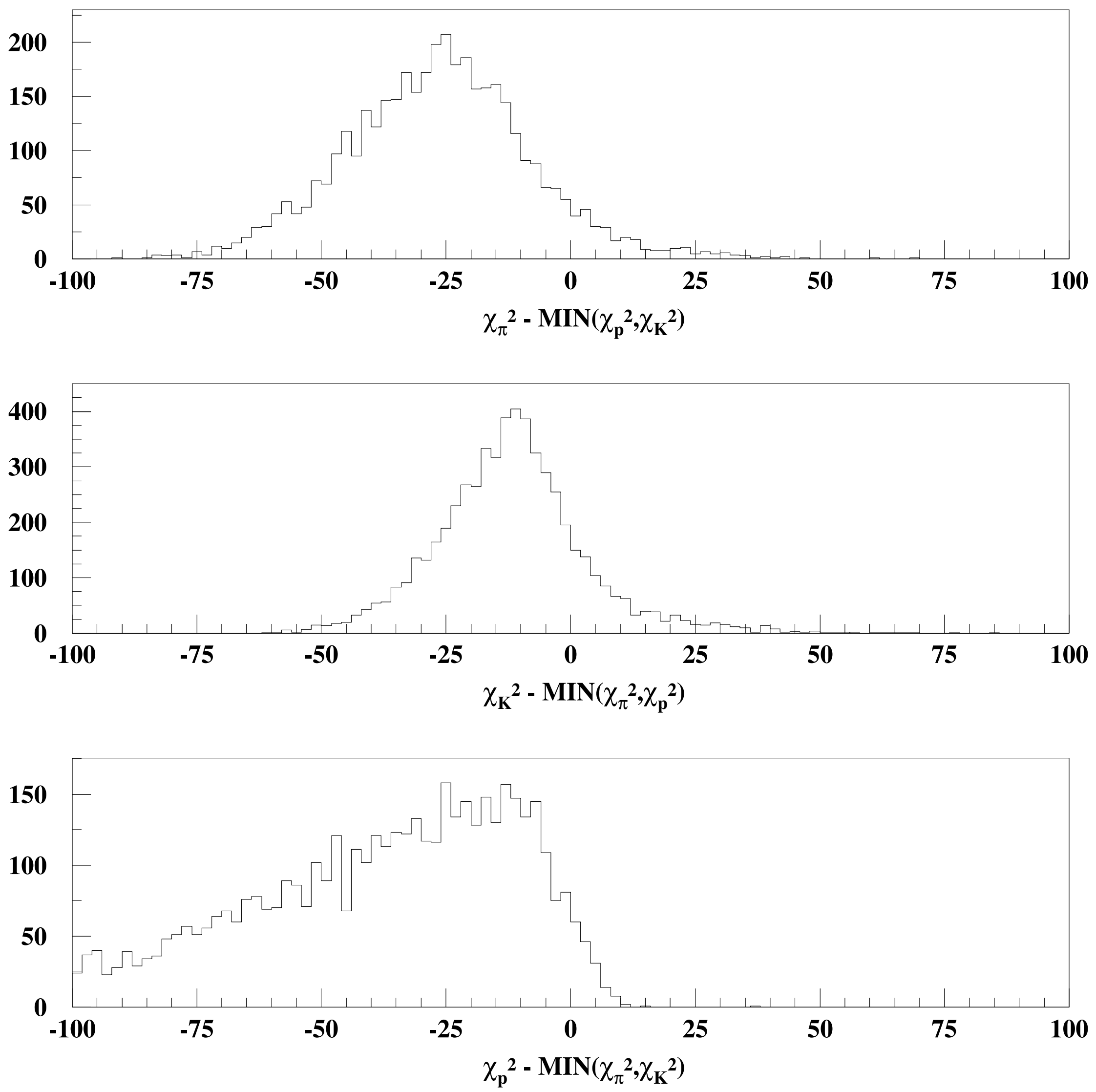

Figure 132: The three plots show the $\Delta\chi^2$ dE/dx estimator for simulated and reconstructed charged pions(top), kaons(middle) and protons(bottom) stopping in the inner detector. Tracks with $\Delta\chi^2 < 0$ are correctly identified.

6.3.6 Energy reconstruction and containment

Muons The energy of muons from charged-current interactions will be measured using range and/or curvature in the magnetized regions of MINERνA and the MINOS spectrometer. For muons stopping in the detector, the momentum resolution will be $\frac{\Delta p}{p} \sim 5\%$. If the MINOS detector is used, the momentum resolution will be 13%[1].

Hadronic calorimetry Containment of hadronic energy is a significant design consideration, as it assists in meeting many of the experiment's physics goals. Studies show that the visible hadronic component of quasi-elastic and resonant events in the fully-active central region of the detector are completely contained, apart from secondary neutrinos and low-energy neutrons. Figure 92 shows the fraction of escaping visible hadronic energy for deep-inelastic reactions in several hadronic energy ranges, and figure 93 shows the probability that a deep-inelastic event will leak visible energy as a function of the true hadronic energy. Only for hadronic energies greater than 8 GeV is there any significant probability of leakage and only above 15 GeV is the average fraction of escaping energy greater than 10%. The fraction of deep-inelastic interactions with hadronic energies over 15 GeV in the low-energy, semi-medium or semi-high energy beams is $< 1\%$, and so visible energy leakage should be insignificant. These estimates ignore downstream components beyond the forward hadron calorimeter, such as the MINOS detector, and are therefore conservative.

To study MINERνA's calorimetric E_h resolution, the detector response to a neutrino sample generated throughout the inner detector by NUANCE, on carbon and hydrogen targets, was simulated. From this simulated sample, events where all hadronic fragments were contained within MINERνA were used. Hits from lepton tracks in charged-current interactions are excluded from the following analysis.

In a fully-active scintillator calorimeter, the total light yield should be essentially proportional to E_h. (The proportionality is not unity due to escaping neutrinos, rest masses of charged pions, nuclear binding energy in the initial and secondary reactions and other nuclear effects such as pion absorption.) While the central inner detector volume is fully active, there are also regions with passive iron or lead absorber sandwiched between scintillators. In these sampling calorimeter regions, not all energy deposited results in scintillation light, so the light yield is corrected accordingly.

Figure 133 shows reconstructed E_h vs. true E_h computed from the kinematics of the incoming and outgoing leptons. The relative deviation of the reconstructed energy from the true E_h, $\Delta E_h/E_h$, multiplied by $\sqrt{E_h}$ is shown in figure 133, giving a average resolution for reconstruction of E_h of $\frac{\Delta E_h}{E_h} = \frac{23\%}{\sqrt{E_h(\mathrm{GeV})}}$. This $1/\sqrt{E_h}$ resolution has some energy dependence and is best represented by

$$\frac{\Delta E_h}{E_h} = 4\% + \frac{18\%}{\sqrt{E_h(\mathrm{GeV})}}.$$

6.4 Event classification

Particle identification and event classification will play a central role in the analysis of data from MINERνA. One possible method of event classification is use of artificial neural network (ANN) techniques.

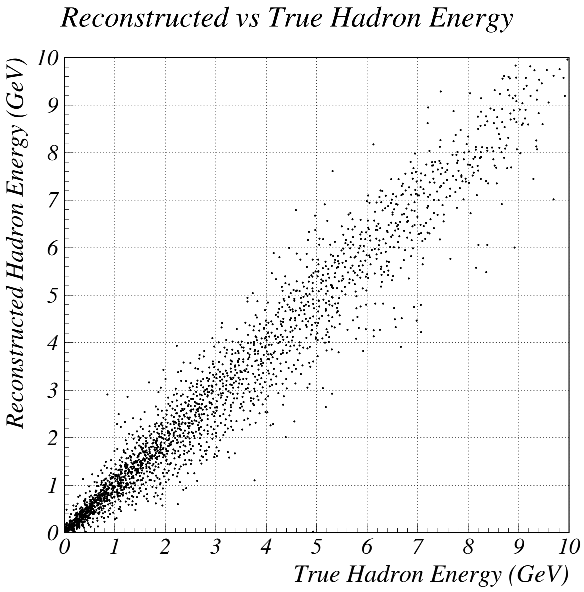

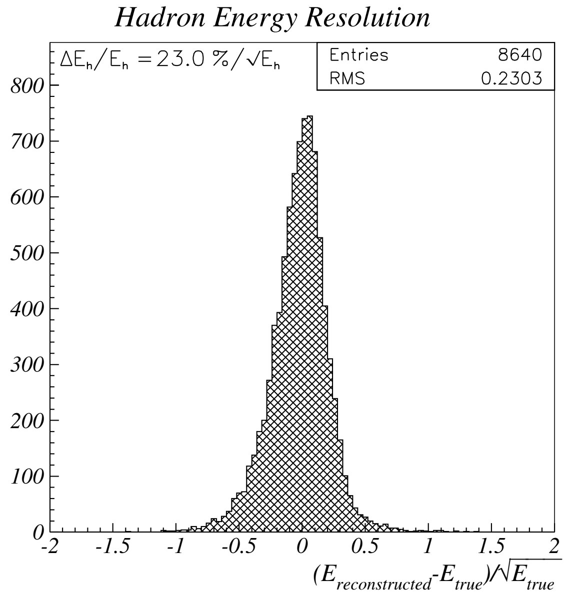

Figure 133: The left graph shows on the vertical axis the the hadronic energy E_h reconstructed from scintillator output in MINERνA vs. the true $E_h = E_\nu - E_\mu$. Right figure shows the relative deviation of the fit, $(\Delta E_h/E_h)\sqrt{E_h}$.

Event classification will be based on topological characteristics as well as on particle ID. Separation of CC from NC interactions will be based on muon identification. Detection of muon decays for low energy muons stopping in the carbon gives the potential for accurate CC identification even at high y$_{Bj}$. In each such class further event identification will be based on other particle ID, energy/momentum measurements and kinematics. Neural networks are designed for such categorization and have been frequently used in the analysis of data from high energy physics experiments (see, for example, the DONUT[9] experiment).

7 Integrated Safety Management

The MINERνA Project will implement the principles of Integrated Safety Management (ISM), in accordance with terms of Fermilab's contract with the Department of Energy. Briefly, there are five basic principles of ISM:

- Define the scope of the work;
- Identify hazards associated with the work;
- Develop and implement ES&H controls;
- Perform work safely;
- Assess the performance for continuous improvement.

These principles are very general and can be applied to a wide range of tasks. At the project level, this Technical Design Report represents the implementation of the first principle, as it defines the scope of the MINERνA detector. The MINERνA Hazard Analysis [180] specifies the anticipated hazards associated with the project. The development and implementation of ES&H controls is facilitated through the MINERνA ES&H Review Committee, which is appointed by the Particle Physics Division Head. The final two principles will be implemented as the project proceeds.

7.1 Fermilab ES&H Requirements

Fermilab's ES&H policies and requirements are set forth in the Fermilab Environment, Safety and Health Manual (FESHM). All work performed at Fermilab is done in accordance with the specifications of the FESHM. Pursuant to Chapter 2010 of the FESHM, the MINERνA Project will prepare a Safety Assessment Document and undergo safety reviews at several levels. These include internal reviews organized by the Project Manager, subsystem design reviews by the MINERνA ES&H Review Committee, project reviews by the Department of Energy, and a final operational readiness review before operations may commence.

Chapter 2060 of the FESHM describes the hazard assessment process and includes a matrix of hazards that may be encountered in activities at Fermilab. These hazards and their impact on the design and construction of the MINERνA are considered individually in the following sections.

7.2 Safety Off-site

Some of the work on the MINERνA detector subsystems will be performed at university laboratories and workshops. This work includes the fabrication, assembly and/or testing of several elements or subsystems of the detector. These activities are subject to the safety regulations of the respective institution. One of the goals of the internal reviews is to verify that these are equivalent to the safety standards of the FESHM. In the event that any special ES&H guidelines are needed, these are explicitly stated in a Memorandum of Understanding between Fermilab and the university.

7.3 Fire Safety

The plastic scintillator core of the MINERνA detector is the primary concern for fire safety. The scintillator constitutes a large fuel load, approximately 17 metric tons of polystyrene plastic. Its location underground in the MINOS Hall implies that, in the event of a fire, the smoke would present a hazard to any personnel in the hall. This hazard is addressed by occupancy limits in the hall and by the emergency exit corridor, which is physically separated from the detector hall and has a separate ventilation system.

Significant material damage to both the MINERνA and MINOS detectors could result from a fire. Smoke deposition on electronics can be an especially expensive form of damage, due to the corrosive effects of halogens in the smoke. The airflow in the hall at the MINERνA location is toward the MINOS detector. Electronics racks will be equipped with smoke detectors as described below. The MINOS racks are also equipped with smoke detectors.

Fire safety is integrated into the design of the detector in two ways: Potential sources of ignition are isolated and the fuel load is minimized or mitigated. Materials in the detector are chosen to optimize fire safety and are reviewed by the Fermilab ES&H Section. The ES&H section tests samples of the material in accordance with industry standards. Examples of fuel load minimization and mitigation include:

- Electronics are contained in fireproof PMT boxes.
- Welding operations are carried out away from the fuel load.
- The scintillator module covering is fire retardant.
- Cable jackets and connectors are made of low-smoke, low-flammability materials. To minimize the potential for smoke damage in the event of a fire, non-halogenated materials are selected for cable jacketing where other technical requirements allow.

7.4 Electronics Safety

The MINERνA ES&H Review Committee reviews all custom-built electronics that are installed in the MINERνA detector.

7.4.1 Rack Protection System

External electronics racks will be equipped with a Rack Protection System (RPS) similar to those designed for the MINOS experiment. The RPS triggers an alarm and shuts off power to the rack in the event of an abnormal situation, the specifics of which can vary from one rack to another but which may include a smoke alarm, cooling fan failure, or voltages or currents out of tolerance.

7.5 Radiation Safety

The MINERνA detector will not contain any radioactive materials, nor will it be located in an experimental area where radioactivation of its components would be a concern. Hence, the radiation safety issues in the detector design are minimal.

7.5.1 Non-Ionizing Radiation

The light injection system will employ ultraviolet LEDs, which will send calibration pulses of UV light to the optical fibers. Safety measures include enclosing the LEDs in a pulser box and placarding in accordance with the FESHM.

The detector will not contain any lasers. During the detector installation, the module locations will be surveyed. This process may involve the use of some Class 1 lasers by trained surveyors.

7.5.2 Ionizing Radiation

The response of each scintillator module will be mapped with a scanner using radioactive sources. From studies for similar mapping devices on the MINOS experiment [182], the radioisotope $^{137}Cs_{55}$ has been identified as having good radiation safety characteristics for this device. The sources are of approximately 5 mCi activity and when in use they may produce dose equivalent rates of more than 5 mrem/hr. The area in which the dose equivalent rate exceeds 5 mrem/hr is classified as a Radiation Area. Work in the Radiation Area will be conducted in accordance with the requirements of the Fermilab Radiological Control Manual (FRCM), which is part of the FESHM. Personnel working in the Radiation Area will have the appropriate training and dosimetry. The mapper operation procedures will be detailed in a separate document. When not in use, the radioactive sources will be secured in accordance with Fermilab policy.

7.6 Chemical Safety

The MINERνA detector construction will involve the use of some hazardous or toxic materials. The project will maintain a set of Material Safety Data Sheets (MSDS) for such materials. The following subsections describe the ES&H considerations for each.

7.6.1 Epoxies and Adhesives

The scintillator planes are assembled with epoxies and adhesives. Some of these may present hazards of inhalation, eye irritation, or skin damage while they are being applied. While working with such materials, the plane assembly teams will use personal protective equipment such as face masks, safety glasses, and gloves as necessary.

7.6.2 Solvents

Small amounts of solvents, such as ethanol or isopropyl alcohol, may be used to clean the optical elements of the detector and test stands. Such solvents will be handled in accordance with FESHM guidelines and stored in a flammable materials cabinet when not in use.

7.6.3 Electrostatic Painting

The PMT boxes will be painted electrostatically. Electrostatic painting has safety and health advantages over brush painting in that fumes from the process are greatly reduced. Furthermore, it eliminates the need to use solvents for touchup and cleanup. Training will be provided for the personnel doing the painting.

7.6.4 Lead Safety

The MINERνA detector will contain approximately 3.5 metric tons of lead. The lead will be painted or otherwise encapsulated and hermetically enclosed in the detector. Technicians installing the lead will be trained as lead workers in accordance with Fermilab standards.

The module mapper will contain a relatively small amount of lead for shielding the radioactive sources. The shielding will consist of lead collimators and ”garages” made of lead blocks, in which the sources will be parked when not in use. The lead will be painted or otherwise encapsulated by Fermilab ES&H personnel before it is installed.

7.7 Steel Handling

Safety in the fabrication of the steel parts of the detector at assembly is primarily ensured by allowing only trained staff to operate the cranes and forklift. All steel pieces will be deburred by flame cutting. The steel support structures and other steel devices are built to industry standards [183]. All lifting fixtures are required to be designed and constructed according to the American National Standard [184]. Any lifting fixture must have an engineering note reviewed by another mechanical engineer and then load tested in front of witnesses at 125% of rated load. All of the documents for any mechanical equipment for the experiment will be reviewed by the experiment’s Particle Physics Division Safety Review Panel. All procedures and engineering notes are approved by this panel before first use is allowed.

7.7.1 Detector Support Stand

The detector modules will be stored on custom-built steel racks while awaiting installation in the MINOS Hall. The actual detector support stand will be of similar construction. The detector support stand, the underground storage racks, the bookends that keep the detector planes aligned, and all lifting fixtures will be designed by Fermilab engineers. The structures will be reviewed and will undergo appropriate load tests, which will be documented in Engineering notes.

7.8 Installation Issues

The MINERνA detector will be installed in the Near Detector Hall at the downstream end of the NuMI beamline at Fermilab, approximately 100 m underground. The hall is outfitted with utilities, cranes and fire protection systems installed for the MINOS detector. MINERνA may require relatively minor upgrades to these. Once the detector and power distribution designs are finalized, the fire protection systems in the Near Detector Hall will be evaluated to see if additional protection is required.

There are a number of hazards associated with the installation and operation of the MINERνA underground. This environment compounds the normal hazards associated with moving equipment weighing several tons, operation of electrical devices, and possible fringe magnetic fields from the MINOS detector. The following safeguards have been adopted to address these hazards.

Access to the Near Detector is restricted; it is accessible only through the surface building, in which the access to the elevator is locked. Only personnel with underground safety training are permitted to check out a key. Detector components are lowered down the shaft by crane, mounted on a cart, and taken to the detector site underground. The procedures for installing the detector modules, racks and other components will be similar to those employed safely and successfully for the installation of MINOS.

7.8.1 Magnetic Fields

The MINERνA detector design does not include a magnet coil. The nearby MINOS detector is magnetized during operation. Therefore, the installation of the MINERνA detector stand will have to take place at a time when the MINOS detector is turned off. It is still to be determined whether the installation of the MINERνA detector elements can take place while the MINOS magnetic coil is energized. The residual field in the MINOS steel plates does not pose a significant hazard. Any access to the MINERνA area while the MINOS magnet is operating will be made in accordance with the procedures posted in the MINOS Hall.

7.8.2 Life Safety & Egress

Safe passageways for access to detectors and egress from the area are important factors for underground safety. Placement of the MINERνA detector is determined by an acceptable safety factor. Since the MINOS Near Detector may provide useful data on muons produced in neutrino interactions in the MINERνA detector, the muon acceptance in MINOS is a consideration in the placement of MINERνA. Ideally, the detectors should be as close to each other as possible to maximize the acceptance. A passageway between the detectors wide enough to allow safe access is the lower limitation on the detector separation. This limit is taken to be a 56-cm (22-inch) gap between the downstream face of MINERνA and the upstream face of MINOS.

7.8.3 Near Hall Occupancy

The MINERνA detector will be installed in the MINOS Near Detector Hall, approximately 100 meters underground. The considerations of fire protection and life safety for the installation of MINERνA are very similar to those for the NuMI Project, during which the underground hall was built and the MINOS Near Detector installed [185]. There are two specified occupancy limits for the near hall: one for installation conditions and a more restrictive one for operational conditions. In the event that MINOS is operating during the MINERνA installation, an appropriate review by Fermilab ES&H will determine which limit is applicable to the MINERνA installation. Once this decision is reached, the MINERνA installation will abide by the underground occupancy limits, coordinating with the MINOS collaboration and any other groups working in the underground hall. All personnel working in the underground hall are required to take NuMI/MINOS underground safety training.

7.9 Cryogenic Safety

The baseline design of the MINERνA detector does not include any cryogenic systems. However, the possibility exists that a helium target may be considered as an added feature at a later time. In such a case, standard Fermilab procedures for cryogenic safety will apply [186] to the design, fabrication, installation and operation of the liquid helium target. These include design and safety reviews, as well as the preparation of a target safety review book.

7.10 Environmental Considerations

The construction, installation, operation and eventual decommissioning of the MINERνA detector are not anticipated to have any significant impact on the environment. The MINERνA Project submitted an Environmental Evaluation Notification Form to the Department of Energy in accordance with the National Environmental Policy Act (NEPA). The project was subsequently granted a Categorical Exclusion under NEPA on December 2, 2005 [187].

8 Project Management

This chapter describes the mission, scope, participation, and personnel of the MINERvA Project Office, which appears as a level 2 project in the MINERvA Work Breakdown Structure (WBS). At Level 2, the MINERvA Project has nine major technical subprojects:

- Scintillator Extrusions: WBS 1.0
- Wavelength Shifting Fibers: WBS 2.0
- Scintillator Plane Assembly: WBS 3.0
- Clear Fiber Cables: WBS 4.0
- Photomultiplier Boxes WBS 5.0
- Photomultiplier Procurement and Testing: WBS 6.0
- Electronics and DAQ WBS 7.0
- Frames, Absorbers, and Detector Stand WBS 8.0
- Module and Veto Wall Assembly WBS 9.0

The project office is WBS 10.0 and provides management and oversight for the other subprojects. This chapter defines the WBS of the detector through level two and describes some of the key procedures and practices that will be followed throughout the course of the project.

8.1 MINERvA Management Task

The basic functions of the Project Office fall into four general categories:

- oversight/reporting
- technical assistance, problem resolution;
- management/leadership; and
- administrative support.

Oversight/reporting includes, but is not limited to:

1. developing and maintaining the Work Breakdown Structure and baseline resource loaded cost and schedule
2. tracking the status of the project relative to the baseline using formal project management tools such as Earned Value and Schedule Variance;

3. providing regular (periodic) and ad hoc reports on the status of the project to Fermilab management and the funding agencies;
4. reporting on the status of the project to the MINERvA experimental collaboration;
5. developing and maintaining a Project Management Plan and working with the DOE MINERνA Program Director to develop and maintain the Project Execution Plan, Acquisition Execution plan, and other formal plans;
6. developing and maintaining a Quality Assurance Program;
7. preparing annual budget requests and establishing work plans;
8. negotiating Memoranda of Understanding (MOU's) and Statements of Work (SOW's) with participating institutions;
9. reporting schedule and cost variances and developing mitigation plans;
10. developing, maintaining and updating the Risk Analysis/Mitigation plan; and
11. managing the change control process .

Technical Assistance and Management/Leadership includes, but is not limited to:

1. developing, selecting, or organizing the development of standards and procedures, captured in documents, for the use in the MINERvA project and enforcing adherence to them;
2. ensuring that all work done by the subprojects meets the technical requirements, conforms to safety requirements, and satisfies the quality assurance criteria of DOE, Fermilab, and MINERvA. This includes visiting production sites at universities, vendors, and other labs;
3. approving, after evaluation and review, all major procurements and contracts;
4. identifying possible conflicts between projects and resolving them;
5. evaluating or arranging to have evaluations made of proposed changes to the technical baseline, cost or schedule, and providing the technical input to the change control process;
6. identifying resource shortfalls and reallocating human resources or funds in a manner required to maintain the schedule and budget;
7. appointing the level 2 subproject leaders and ensuring that the leadership of the subprojects is functioning at an acceptable level;
8. organizing "internal" reviews and responding to their findings; and
9. participating in and responding to the findings of external reviews

Administrative Functions of the Project Office include but are not limited to:

1. preparing and distributing reports;
2. arranging and accounting for travel;
3. maintaining key schedules and scheduling key meetings;
4. providing support for meetings;
5. maintaining general office supplies and equipment
6. procuring computers, PC software, and general software;
7. evaluating, selecting, acquiring and supporting special project management and report preparation software;
8. supporting guests and visitors, including helping them with travel, housing, support, and workspace;
9. organizing training; and
10. providing administrative support for internal and external reviews.

The MINERvA Project Office will reside in the Particle Physics Division (PPD). The relationship between the PPD and the MINERvA project is described in the PMP. Other Fermilab divisions and sections, including Computing Division, Accelerator Division, Technical Division, Facility Engineering Systems Section (FESS) and Business Systems Section (BSS) are involved in MINERvA. The interactions of those divisions with the project is described in the PMP.

8.2 Key Roles in the Project Managmenet/Project Office

The key management roles are described here. It should be noted that a single person may hold more than one of the roles described below, or for example there may be more than one person selected to fill a specific role. For example, several of the level two subtasks are co-managed by two people.

- Project Manager

  The Project Manager is appointed by the Fermilab Director, and is responsible for the execution of the MINERvA Project. Therefore, the MINERvA PM must develop and maintain the Project Management Plan; negotiate and update the Memoranda of Understanding (MOU) between Fermilab and the collaborating institutions; and direct the activities of subsystem managers. These MOUs determine the resources which are available to the project from the collaborating institutions. Implicit in these responsibilities is the requirement that the PM administer both human and financial resources available to the project through these MOUs.

  The MINERvA PM works with representatives of the divisions and sections at Fermilab to obtain Laboratory resources for the project as approved by the Fermilab Directorate. This may include the development of additional MOU between the Project and specific Fermilab divisions or sections.

The PM assigns responsibilities and resources to the Subsystem Managers. The progress of these assignments is monitored through monthly status reports generated by the Subsystem Managers, by means of regular Subsystem Managers meetings, and through daily communications. The MINERvA PM is responsible for developing, maintaining, and tracking the schedule for the project, which will include a complete list of milestones to facilitate monitoring the progress of the project. The MINERvA PM provides monthly reports summarizing the progress of the Project to the Fermilab Director and the Federal Project Director.

The PM may delegate responsibilities to the Deputy Project Manager to optimize the efficiency of the project.

- Deputy Project Manager

  The Deputy Project Manager assists the MINERvA PM in all matters relating to the MINERvA Project, including the planning, procurement, disposition and accounting of resources, progress reports on project activities, ES& H issues, and Risk Management. In the absence of the Project Manager, the DPM assumes the project management responsibilities.

- University Project Manager Representative

  The University Project Manager Representative (PMR) assists the MINERvA PM in all matters relating to activities and resources at collaborating universities, including the planning, procurement, disposition and accounting for resources allocated to the universities, progress reports on activities carried out off-site, off-site ES&H issues, liaison with university Institutional Representatives, fabrication of detector components off-site, and their timely delivery at Fermilab. The PMR coordinates activities between universities which work on closely-related WBS elements occurs.

- Project Mechanical Engineer

  The MINERvA Project Mechanical Engineer is responsible for coordination of mechanical aspects of the design and fabrication phases of the project. The Project Mechanical Engineer is directly responsible to the MINERvA Project Manager and receives input from the DPM, PMR and Level 2 Subsystem Managers. In cooperation with them the Project Engineer works with the MINERvA ES&H Coordinator to implement Fermilab's policy of Integrated Safety Management (ISM) in the project and resolve any ES&H issues that may arise.

- Project Electrical Engineer

  The MINERvA Project Electrical Engineer is responsible for coordination of electrical aspects of the design and fabrication phases of the project. The Project Electrical Engineer is directly responsible to the MINERvA Project Manager and receives input from the DPM, PMR and Level 2 Subsystem Managers. In cooperation with them the Project Engineer works with the MINERvA ES& H Coordinator to implement Fermilab's policy of Integrated Safety Management (ISM) in the project and resolve any ES& H issues that may arise.

- Document Coordinator

The MINERvA Documentation Coordinator supports the Project Manager in the preparation and revision of the PMP and other project documentation. The Documentation Coordinator also assists in the preparation of MOU and SOW with the collaborating institutions and with the organization of materials for internal and external reviews of the project. The Documentation Coordinator supports the ES& H Coordinator in the compilation of relevant safety documentation for the project.

MINERvA documentation is maintained within a document database, the DocDB document management system. The Documentation Coordinator is the administrator for the database.

The MINERvA Documentation Coordinator also coordinates Quality Assurance issues and maintains the MINERvA Quality Assurance Plan, as discussed in Section 7.1. The Documentation Coordinator also maintains and tracks documentation of internal QA reviews, reviews Memoranda of Understanding and other documentation, and advises the Project Manager on QA issues.

- Safety Officer

  The ES& H Coordinator addresses the administrative aspects of all ES& H work associated with the MINERvA Project and reports to the MINERvA Project Manager. The ES& H Coordinator compiles and maintains the MINERvA Hazard Assessment Document, Preliminary Safety Assessment Document (PSAD), and the MINERvA Safety Assessment Document (SAD). The ES& H Coordinator plans and coordinates ES& H reviews of the project and assembles the associated documentation.

- Scheduler

  The MINERvA Scheduler maintains and updates the MINERvA Project cost and schedule plan and prepares the schedule information for monthly reports and scheduled reviews, submitting them to the MINERvA PM for approval and transmission. The Scheduler also works with PM in identifying schedule issues in a proactive manner in order to track and report deviations from baseline schedules and costs.

- Budget Officer

  The Budget Officer has the responsibility for preparing cost information for the monthly reports, submitting them to the PM for approval and transmission. The Budget Officer monitors expenditures of US and non-US funds, tracks and reports deviations from baseline schedules and costs as specified in Section 5, and prepares the Project Accounting Task Structure. The Budget Officer verifies costs in MOUs/SOWs, using COBRA for tracking earned value on a monthly basis and as needed for reports/reviews. The Budget Officer tracks requisitions as needed and tracking monthly costs and obligations versus Cost & Schedule Plan (CSP).

  The Budget Officer also assists collaborating researchers in preparing initial budget estimates and collaborates with the Fermilab Office of Project Management Oversight to develop project controls.

  The Financial Management System (FMS) in use by Fermilab allows individual cost codes to be established, where necessary. The Budget Officer has the responsibility for establishing the proper cost codes. The FMS is also used to track and monitor such expenses as charge-backs from other Divisions/Sections, and other Fermilab related costs. At the successful completion of each project phase or WBS task, the Project Manager or designated representative is required to verify that work was performed and completed in accordance with acceptable standards before final payment is authorized by the Business Services Section.

8.3 MINERvA Detector Work Breakdown Structure

The MINERvA Work Breakdown Structure is defined in table 8.3 to Level 2.

8.4 MINERvA Management Procedures

- Internal Reviews

  Each Level 2 subsystem will undergo technical reviews to help optimize the design and cost of the subsystem, as well as to coordinate its schedule with those of the other subsystems. A committee appointed by the Project Manager, comprising members of the MINERvA Collaboration and experts from Fermilab and other institutions, review each subsystem at least once, with additional reviews at the discretion of the Project Manager. The review committee submits a written report to the Project Manager, who acts upon the committee's findings as necessary.

  Each Level 2 Subsystem will also undergo a review to ensure compliance with applicable Fermilab ES& H requirements. Additional ES& H reviews may be scheduled at the Project Manager's discretion. The MINERvA ES& H Review Committee is discussed in detail in Section 6.1.1. The Committee will submit a written report of its findings to the Project Manager and the Particle Physics Division Head. The Project Manager will address any findings of noncompliance with ES& H requirements and inform the Division Head in writing of the resolution of those findings.

- External Reviews

  The Fermilab Director will appoint a committee to conduct periodic reviews of the MINERvA Project to monitor its progress. Director's Reviews are held at the Director's discretion, typically on an annual basis.

  In addition to external reviews organized by MINERvA, there will be reviews organized by and reporting to external funding agencies and Fermilab. The MINERνA Project Manager or the MINERvA spokespersons, as appropriate to the particular review, will organize MINERvA presentations at these reviews. It will be the role of the MINERvA Project Manager to provide the required support for the preparation for the review through the Project Office, to participate as required in the review, and help resolve any issues emerging from the review.

Table 18: Work Breakdown Structure for the MINERvA Detector Project.

WBS	Title	Description
0	MINERvA	Design and construct the MINER A Detector
1	Scintillator Extrusion	Prototype and fabricate the triangular (inner detector) and rectangular (outer detector) plastic scintillating strips which comprise the sensitive elements of the detector
2	WLS Fibers	Fabricate and test wavelength-shifting fibers for insertion in scintillator bars.
3	Scintillator Plane Assembly	Assemble scintillator bars and WLS fibers into detector planes.
4	Clear Fiber Cables	Fabricate and test clear fiber bundles, connectors and Optical Detector Units to carry light from the WLS fibers to the MAPMTS.
5	Photomultiplier Tube Boxes	Fabricate housings, install internal optical cables, mount MAPMTS and test output. Develop, test and integrate light-injection calibration system into PMT boxes.
6	Photomultiplier Tubes	Procure and test MAPMTs
7	Electronics and DAQ	Fabricate and test front-end digitizer/HV boards, VME chain controllers, computer readout system and associated power and monitoring infrastructure.
8	Frames, Absorbers and Stand	Fabricate graphite, iron and lead absorbers and nuclear target planes, steel outer frames for detector modules and detector support stand.
9	Module and Veto Wall Assembly	Assemble scintillator planes, frames, absorbers, and target planes into detector modules; scan response; fabricate associated power, cooling and monitoring systems. Refurbish and test the upstream veto planes. Fabricate PMT box support framework.
10	Project Management	Manage the construction process

8.5 Reporting

The MINERvA Project Manager will provide the MINERvA spokespersons with contributions for reports which they require or which are required by them for Fermilab or funding agencies. The MINERvA Project Manager will develop, in conjunction with her or his team, a reporting procedure for the whole project as well as for the Project Office subproject. Such reporting should guarantee good information flow within the project but should require no more effort than is needed to meet this objective.

8.6 Assignment of Responsibility for Work

At some point a subgroup or collaborating institution may want (or be required) to formalize its activity and assume responsibility for work on a MINERνA subsystem. The work may be an individual subtask or subtask component. Assumption of responsibility for an activity will be done by submitting a proposal to the relevant Level 2 Manager. The Manager will work with the proponents to develop the final proposal and after the Level 2 manager approves it, she or he will submit it to the MINERvA Project Manager, and the Spokespersons for concurrence.

After a positive decision, the task manager will negotiate an "assignment of responsibility" for the project or subtask. This agreement with the group will be written and will specify all requirements (performance, interfacing, etc.) all deliverables, schedule, costs, and manpower requirements. Deliverables will normally include technical components (with interconnections, power, etc) quality assurance data (results of acceptance tests) test and debugging procedures, supporting computer programs (simulations, readout, diagnostic, monitoring) complete documentation (schematics, troubleshooting), safety information and procedures, and a maintenance and repair plan. The agreement will also specify commitments to debug, integrate, and maintain all devices.

The MINERvA Project Manager and spokespersons will approve the agreement, and if required, the agreement will then be submitted to Fermilab and the funding agencies for approval. The agreement must be reflected in the group's formal MOU and funding and manpower plan. The group will then undertake the subtask. Reports and cost and schedule data will be provided for the regular reports and upon special request. Reviews will be conducted as needed.

The level 2 manager must ensure that all work assigned under the task is being carried out on schedule, within budget, is technically sound and meets the requirements of the project for quality and ES& H. If work is not being done or is not meeting the requirements, action must be taken to correct the situation. If the corrective action requires changes in MOU's or SOW's, the problem must be brought to the MINERvA Project Manager for resolution.

8.7 Value Management

The MINERvA Project has implemented a design review system, in which each major subsystem is closely examined to obtain optimal value for the system, given the technical requirements and schedule constraints imposed on it. These reviews are documented in the project's document database, which uses the DocDB document management system. Documentation and updates are thus available to the project management staff, subsystem managers and other project personnel.

Specific project notes on design modifications are maintained in an assigned Value Engineering category in the document database. The database allows for easy access, review and updating by participants in the MINERvA Project.

8.8 Risk Management

The MINERvA Project has adopted a standard risk management process . The MINERvA Project employs several tools to implement the risk management process. These include, but are not limited to, project reviews, monthly reports and the Level 2 Managers meeting. This meeting is held weekly and provides a forum for identification of risks and discussion of risk handling strategies. Risk management documentation is maintained in the MINERvA document database, from which it is available to all of the affected project members and stakeholders.

Part IV
Bibliography

References

[1] MINOS Collaboration, "MINOS Technical Design Report", NuMI-NOTE-GEN-0337 (1998).

[2] N. V. Mokhov, "The MARS Monte Carlo", FERMILAB FN-628 (1995); N. V. Mokhov and O. E. Krivosheev, "MARS Code Status", FERMILAB-Conf-00/181 (20 00); http://www-ap.fnal.gov/MARS/.

[3] N. Mokhov and A. Van Ginneken, J. Nucl. Sci. Tech. **S1**, 172 (2000).

[4] M. Messier (private communication)

[5] Y. Hayato, To be published in *Proceedings of the Second Workshop on Neutrino-Nucleus Interactions in the Few-GeV Region (NUINT02),* Irvine, California (2002).

[6] G. Ambrosini *et al.* [NA56/SPY Collaboration], Eur. Phys. J. C **10**, 605 (1999).

[7] P-907: Proposal to Measure Particle Production in the Meson Area Using Main Injector Primary and Secondary Beams, May 2000

(http://ppd.fnal.gov/experiments/e907/Proposal/E907_Propsal.html)

[8] NuMI Technical Design Handbook

(http://www-numi.fnal.gov/numiwork/tdh/tdh_index.html)

[9] K. Kodama *et al.*, Nucl. Phys. Proc. Suppl **98**, 43-47 (2001)

[10] M. Hasegawa *et al.* [K2K Collaboration], Phys. Rev. Lett. **95**, 252301 (2005) [arXiv:hep-ex/0506008].

[11] S. Kopp, Z. Pavlovic, and D. Indurthy, "Systematic Uncertainties in the NuMI Beam Flux" MINOS-doc-1283, (2006)

[12] C.H. Llewellyn Smith, Phys. Rep. 3C (1972).

[13] J. Arrington, nucl-ex[0305009].

[14] M. K. Jones *et al.*, Phys. Rev. Lett, 84, (2000) 1398 ; O. Gayou *et al.*, Phys. Rev. Lett, 88 (2002) 092301.

[15] J.J. Kelly, Phys. Rev. C70 (2004) 068202.

[16] R. Bradford, et al., hep[ex0602017].

[17] H. Budd, A. Bodek and J. Arrington, hep-ex[0308005].

[18] R. F. Wagenbrunn *et al.*, hep-ph[0212190].

[19] R. C. Merenyi *et al.*, Phys. Rev. D 45, 743 (1992)

[20] V. Bernard, L. Elouadrhiri, U.G. Meissner, J.Phys.G28 (2002), hep-ph[0107088].

[21] G. Zeller, private communication.

[22] K. Tsushima, Hungchong Kim, K. Saito, hep-ph[0307013].

[23] T. Kitagaki *et al.*, Phys. Rev. D26 (1983) 436.

[24] T. Kitagaki *et al.*, Phys. Rev. D42 (1990) 1331.

[25] S.J. Barish *et al.*, Phys. Rev. D16 (1977) 3103.
BNL D2

[26] N.J. Baker *et al.*, Phys. Rev. D23 (1981) 2499.

[27] W.A. Mann *et al.*, Phys. Rev. Lett. 31 (1973) 844.

[28] J. Brunner *et al.*, Z. Phys. C45 (1990) 551.

[29] M. Pohl *et al.*, Lett. Nuovo Cimento 26 (1979) 332.

[30] D. Allasia *et al.* Nucl. Phys. B **343** (1990) 285

[31] S.V. Belikov *et al.*, Z. Phys. A320 (1985) 625.

[32] S. Bonetti *et al.*, Nuovo Cimento 38 (1977) 260.

[33] K.L. Miller *et al.*, Phys. Rev. D26 (1982) 537.

[34] Glen Cowan, Statistical Data Analysis, Oxford Clarendon Press (1 998)

[35] H. Budd, A. Bodek and J. Arrington, hep-ex[0410055].

[36] D. Casper, Nucl. Phys. Proc. Suppl. 112 (2002) 161.

[37] R.A. Smith and E.J. Moniz, Nucl. Phys. B43 (1972) 605.

[38] Ghent Theory group in Belgium, Jan Ryckebusch (jan@inwpent5.UGent.be).

[39] D. Rein and L. M. Sehgal, Annals Phys. **133**, 79 (1981).

[40] M.H. Ahn, et al. (K2K), Submitted to PRD, hep-ex/0606032.

[41] T. Sato, D. Uno, and T.-S.H. Lee, Phys. Rev. C**67** 065201 (2003).

[42] E. Paschos, M. Sakuda, J.-Y. Yu, Phys. Rev. D**69** 014013 (2004).

[43] E. Paschos, et al., Proc. NuInt04 (L'Aquila), hep-ph/0408185.

[44] O. Lalakulich and E. Paschos, Phys. Rev. D**71** 074003 (2005).

[45] O. Lalakulich, E. Paschos, G. Piranishvili, Phys. Rev. D**74** 014009 (2006).

[46] T. Sato, et al., Proc. NuInt05 (Okayama),nucl-th/0601069.

[47] T. Kitagaki, et al., Phys. Rev. D**34** 2554 (1986).

[48] T. Kitagaki, et al., Phys. Rev. D**42** 1331 (1990).

[49] M. Hasegawa, et al. (K2K), Phys. Rev. Lett. **95** 252301 (2005).

[50] M. Wascko (MiniBoone), Proc. NuInt05 (Okayama), hep-ex/060 2050.

[51] D. Rein and L. M. Sehgal, Nucl. Phys. **B223**, 29 (1983).

[52] E. A. Paschos and A. V. Kartavtsev, (2003), hep-ph/0309148.

[53] Super-Kamiokande and K2K, C. Mauger, Nucl. Phys. Proc. Suppl. **112**, 146 (2002).

[54] BooNE, J. L. Raaf, Nucl. Phys. Proc. Suppl. **139**, 47 (2005), hep-ex/0408015.

[55] B. Z. Kopeliovich, Nucl. Phys. Proc. Suppl. **139**, 219 (2005), hep-ph/0409079.

[56] E. A. Paschos, A. Kartavtsev, and G. J. Gounaris, (2005), hep-ph/0512139.

[57] D. Rein and L. M. Sehgal, (2006), hep-ph/0606185.

[58] S. K. Singh, M. Sajjad Athar, and S. Ahmad, (2006), nucl-th/0601045.

[59] MiniBooNE, J. Monroe, Nucl. Phys. Proc. Suppl. **139**, 59 (2005), hep-ex/0408019.

[60] K2K, T. Ishida, Prepared for 1st Workshop on Neutrino - Nucleus Interactions in the Few GeV Region (NuInt01), Tsukuba, Japan, 13-16 Dec 2001.

[61] N.J. Baker *et al.*, Phys. Rev. D **24**, 2779 (1981).

[62] A. Alavi-Harati *et al.*, Phys. Rev. **87** 132001 (2001).

[63] P.G. Ratcliffe, Phys. Rev. **D59**, 014038 (1999).

[64] N. Cabibbo *et al.*, Semileptonic Hyperon Decay and CKM Unitarity, [arXiv:hep-ph/0307214] (July 2003).

[65] T. Alexopoulos *et al.* (KTeV Collaboration), Phys. Rev. Lett. **93**, 181802 (2004).

[66] T. Nakano *et al.*, [arXiv:hep-ex/0301020]; V.V. Barmin
em et al., [arXiv:hep-ex0304040]; S. Stepanyan [arXiv:hep-ex/0307018].

[67] R. Jaffe and F. Wilczek, Di-quarks and Exotic Spectroscopy, [arXiv:hep-ph/0307341] (July 2003).

[68] S. Kuhlmann *et al.*, Phys. Lett. B **476**, 291 (2000).

[69] H. Deden and et al., [Gargamelle Neutrino Collaboration], "Experimental Study Of Structure Functions And Sum Rules In Charge Changing Interactions Of Neutrinos And Anti-Neutrinos On Nucleons," Nucl. Phys. **B85**, 269 (1975).

[70] K. Varvell *et al.* [BEBC WA59 Collaboration], Z. Phys. C **36**, 1 (1987)

[71] M. Shifman, Handbook of QCD, Volume 3, 1451, World Scientific (2001)

[72] F. E. Close and N. Isgur, Phys. Lett. B **509**, 81 (2001)

[73] W. Melnitchouk, R. Ent and C. Keppel, Phys. Rept. **406**, 127 (2005) [arXiv:hep-ph/0501217].

[74] I. Niculescu *et al.*, Phys. Rev. Lett. **85**, 1186 (2000)

[75] C. E. Keppel, *Prepared for Exclusive Processes at High Momentum Transfer, Newport News, Virginia, 15-18 May 2002*

[76] J. Arrington, R. Ent, C. E. Keppel, J. Mammei and I. Niculescu, arXiv:nucl-ex/0307012 (submitted to Phys. Rev. Lett.)

[77] A. Fantoni [HERMES Collaboration], Eur. Phys. J. A **17**, 385 (2003).

[78] I. Niculescu *et al.*, Phys. Rev. Lett. **85**, 1182 (2000).

[79] A. Bodek and U. K. Yang, arXiv:hep-ex/0203009.

[80] D. Dolgov *et al.* [LHPC collaboration], Phys. Rev. D **66**, 034506 (2002) [arXiv:hep-lat/0201021].

[81] I. Niculescu, J. Arrington, R. Ent and C. E. Keppel, Phys. Rev. C **73**, 045206 (2006) [arXiv:hep-ph/0509241].

[82] X. Ji, Phys. Rev. Lett. **78**, 610 (1997).

[83] X. Ji, Phys. Rev. **D55**, 7114 (1997).

[84] A. V. Radyushkin, Phys. Lett. **B380**, 417 (1996).

[85] A. V. Radyushkin, Phys. Lett. **B385**, 333 (1996).

[86] J.C. Collins, L. Frankfurt, and M. Strikman, Phys. Rev. **D56**, 2982 (1997).

[87] A. V. Radyushkin, Nucl. Phys. **A711**, 99 (2002).

[88] M. Vanderhaeghen, Nucl. Phys. **A711**, 109 (2002).

[89] M. Diehl, hep-ph/0307382 (2003).

[90] C. Munoz Camacho, et al. nucl-ex/0607029 (2006).

[91] A. Psaker, W. Melnitchouk and A. Radyushkin, in preparation.

[92] D. Drakoulakos *et al.* [Minerva Collaboration], fine-grained detector in the NuMI beam," arXiv:hep-ex/0405002. Pgs. 99 - 108, 192 - 200.

[93] B.Z. Kopeliovich, hep-ph/0409079.

[94] M.K. Jones *et al.*, Phys. Rev. **C48**, 2800 (1993); R.D. Ransome *et al.*, Phys. Rev. **C46**, 273 (1992); R.D. Ransome *et al.*, Phys. Rev. **C45**, R509 (1992).

[95] D. Rowntree *et al.*, Phys. Rev. **C60**, 054610 (1999); B. Kotlinksi *et al.*, Eur. Phys. J. **A9**, 537 (2000).

[96] E. A. Paschos, M. Sakuda, I. Schienbein and J. Y. Yu, arXiv:hep-ph/0408185.

[97] M. Arneodo, Phys. Rept. **240**, 301 (1994).

[98] G. Piller and W. Weise, Phys. Rept. **330**, 1 (2000).

[99] B. L. Ioffe, V. A. Khoze, and L. N. Lipatov, *Hard processes: Phenomenology, Quark-Parton Model* (Elsevier Science Publishers, North Holland, 1984).

[100] G.B. West, Ann. Phys. **74** (1972) 464.

[101] S. V. Akulinichev, S. A. Kulagin, and G. M. Vagradov, Phys. Lett. B **158**, 485 (1985); S. V. Akulinichev, S. Shlomo, S. A. Kulagin, and G. M. Vagradov, Phys. Rev. Lett. **55**, 2239 (1985).

[102] S. A. Kulagin, Nucl. Phys. A **500**, 653 (1989).

[103] C. Ciofi degli Atti and S. Liuti, Phys. Rev. C **41**, 1100 (1990).

[104] F. Gross and S. Liuti, Phys. Rev. C **45**, 1374 (1992).

[105] S. A. Kulagin, G. Piller and W. Weise, Phys. Rev. C **50**, 1154 (1994).

[106] S. A. Kulagin, W. Melnitchouk, G. Piller, and W. Weise, Phys. Rev. C **52**, 932 (1995).

[107] S. A. Kulagin, Nucl. Phys. A **A 640**, 435 (1998).

[108] W. Melnitchouk, A. W. Schreiber and A. W. Thomas, Phys. Rev. D **49**, 1183 (1994).

[109] J. Gomez, *et al.,* Phys. Rev. D **49**, 4348 (1994).

[110] S. I. Alekhin, S. A. Kulagin and S. Liuti, Phys Rev. D **69**, 114009 (2004).

[111] S. A. Kulagin and R. Petti, paper in preparation.

[112] T. H. Bauer, R. D. Spital, D. R. Yennie and F. M. Pipkin, Rev. Mod. Phys. **50**, 261 (1978) [Erratum-ibid. **51**, 407 (1979)].

[113] C. A. Pickety, and L. Stodolsky, Nucl. Phys. B **15**, 571 (1970).

[114] S. L. Adler, Phys. Rev. **135**, B963 (1964).

[115] R. J. Glauber, Phys. Rev. **100**, 242 (1955).

[116] V. N. Gribov, Sov. Phys. JETP **29**, 483 (1970) [Zh. Eksp. Teor. Fiz. **56**, 892 (1969)] ; Sov. Phys. JETP **30**, 709 (1970) [Zh. Eksp. Teor. Fiz. **57**, 1306 (1969)].

[117] B. Z. Kopeliovich, and P. Marage, Int. J. Mod. Phys. A **8**, 1513 (1993).

[118] S. A. Kulagin, arXiv:hep-ph/9812532.

[119] E. A. Paschos and L. Wolfenstein, Phys. Rev. D **7**, 91 (1973).

[120] G. P. Zeller *et al.* [NuTeV Collaboration], Phys. Rev. Lett. **88**, 091802 (2002) [Erratum-ibid. **90**, 239902 (2003)] [arXiv:hep-ex/0110059].

[121] S. A. Kulagin, Phys. Rev. D **67**, 091301 (2003) [arXiv:hep-ph/0301045].

[122] S. A. Kulagin, arXiv:hep-ph/0406220.

[123] S. A. Kulagin, arXiv:hep-ph/0409057.

[124] D. H. Lu, A.W. Thomas, and K. Tsushima, arXiv:nucl- th/0112001, K. Tsushima, H. Kim, and K. Saito, Phys. Rev. C **70**, 038501 (2004)

[125] J.J. Aubert et al., Phys. Lett. **123B**, 275 (1983); D.F. Geesaman, K. Saito, and A.W. Thomas, Annu. Rev. Nucl. Part. Sci. **45**, 337 (1995).

[126] B. Buck and S.M. Perez, Phys. Rev. Lett. **50**, 1975 (1983).

[127] S. Dieterich, et al., Phys. Lett. B **500**, 47 (2001), S. Strauch et al., Phys. Rev. Lett. **91**, 052301 (2003).

[128] JLab experiment E3-104, co-spokespersons R. Ent, R. Ransome, S. Struach, P. Ulmer. `http://www.jlab.org/exp_prog/proposals/03/PR03-104.ps`

[129] C.H.Q. Ingram, Nucl. Phys. A **684**, 122 (2001).

[130] M. K. Jones *et al.*, Phys. Rev. C **48**, 2800 (1993).

[131] M. Nakahata *et al*, Nucl. Instrum. Meth. **A421**, 113 (1 999); E. Blaufuss *et al*, Nucl. Instrum. Meth. **A458** 638 (2001).

[132] M. Diwan and J. Nelson, NuMI-NOTE-STEEL-0639 (2000)

[133] PhD Thesis of C. Smith, University College London, London, 2002 *Calibration of the MINOS Detectors and Extraction of Neutrino Oscillation Parameters*; PhD Thesis of R. Nichol, University College London, London, 2003 *Calibration of the MINOS Detectors*

[134] PhD thesis of M. A. Kordosky, University of Texas at Austin, August 2004 *Hadronic Interactions in the MINOS Detectors*

[135] PhD thesis of P. L. Vahle, University of Texas at Austin, August 2004 *Electromagnetic Interactions in the MINOS Detectors*

[136] E. A. Paschos, L. Pasquali and J. Y. Yu, Nucl. Phys. B **588**, 263 (2000) and E. A. Paschos, J. Y. Yu and M. Sakuda [arXiv:hep-ph/0308130].

[137] D. Ashery *et al.*, Phys. Rev. **C23**, 2173 (1981).

[138] H. Gallagher, Nucl. Phys. Proc. Suppl. **112**, 188 (2002)

[139] NuMI Fluxes courtesy of Mark Messier

[140] The simulation assumed the active material was resistive plate chambers and the absorber was particle board (hydrocarbons).

[141] G.P.Zeller, submitted to proceedings of 2nd International Workshop on Neutrino - Nucleus Interactions in the Few GeV Region (NUINT 02), Irvine, California, 12-15 Dec 2002 [hep-ex/0312061]

[142] Kamiokande Collaboration, S. Hatakeyama *et al.*, Phys. Rev. Lett. **81** (1998) 2016; Soudan-2 Collaboration, W. W. Allison *et al*, Phys. Lett. **B 449** (1999) 137; MACRO Collaboration, Ambrosio *et al*, Phys. Lett. **B434**, 451 (1998)

[143] Y. Fukuda et al., *Phys. Rev. Lett.* **81** (1998) 1158; Erratum **81** (1998) 4279, B.T. Cleveland et al., *Astrophys. J.* **496** (1998) 505. W. Hampel et al. (GALLEX Collaboration), *Phys.Lett.* **B 447** (1999) 127., J.N. Abdurashitov et al. (SAGE Collaboration), *Phys. Rev.* **C 60** (1999) 055801 [astro-ph/9907113]

[144] Q.R. Ahmad *et al.* Phys.Rev.Lett.**89** (2002) 011302 nucl-ex/0204009

[145] Y. Fukuda *et al.*, Phys.Rev.Lett.**81** (1998) 1562 [hep-ex/9807003]; M. Sanchez et al., Phys. Rev. **D 68**, 113004 (2003)

[146] KamLAND Collaboration (K. Eguchi et al.), Phys. Rev. Lett.**90** (2003) 021802 [hep-ex/0212021]

[147] K2K Collaboration (M.H. Ahn et al.), Phys.Rev.Lett.**90** (2003) 41801 [hep-ex/0212007]

[148] B. Pontecorvo and J. Exptl, Theoret. Phys. **34** 247 (1958); Z. Maki, M. Nakagawa and S. Sakata, Prog. Theor. Phys. **28**, 870 (1962).

[149] M. Maltoni *et al*, submitted to New J. Phys, [hep-ph/0405172]

[150] By CHOOZ Collaboration (M. Apollonio et al.), Phys.Lett.**B466** (1999) 415 [hep-ex/9907037]

[151] W. Grimus and L. Lavoura, Phys. Lett. **B572**, 189 (2003); A. Aranda, C.D. Carone, R.F. Lebed, Phys. Rev. **D62**, 016009 (2000).

[152] "A Long Baseline Neutrino Oscillation Experiment at Fermilab", E.Ables *et al*, FERMILAB-PROPOSAL-0875, Feb. 1995, 241pp.

[153] "NOVA: Proposal to build an Off-Axis Detector to Study $\nu_\mu \rightarrow \nu_e$ oscillations in the NuMI Beamline", I. Ambats *et al.*, FERMILAB-PROPOSAL-0929, Mar 2004.

[154] Y. Itow *et al*, "The JHF-Kamioka Neutrino Project", KEK report 2001-4, June 2001. [hep-ex/0106019]

[155] J. Nelson, "MINOS Oscillation Results", Neutrino 2006, Santa Fe, NM, June, 2006.
bibitemingram C.H.Q. Ingram, Nucl. Phys. A **684**, 122 (2001).

[156] B. Choudhary, Y. Huang, D. Michael, H. Kim, NuMI-NOTE-L-414, Dec 1998.

[157] E. Gallas & J. Li., "Polishing Optical Fibers for the D0 ICD in Run II", FNAL-TM-2062, 1998.

[158] The MINERνA Collaboration,
Proposal to perform a high-statistics neutrino scattering experiment using a fine-grained detector in the NuMI beam, Fermilab Proposal P-938, e-print hep-ex/0405002; see Sect. 16.5.2.

[159] M. Bonkowski, *Magnetic Field Measurement Results*,
MINERνA note MINERvA-doc-88-v1, (measurements of December 2004).

[160] D. Cherdack and W.A. Mann, *Magnetic Shielding Capabilities of the MINERvA PMT Box*, MINERνA note MINERvA-doc-164-v1.

[161] P. Adamson, et al., Nucl. Inst. Meth. A**492**,
325 (2002).

[162] P. Shanahan, priv. comm. (Nov., 2005).

[163] A. Cabrera, et al., NuMI-934 internal report.

[164] P. Harris (Sussex Univ.) provided excellent
guidance and some pieces necessary for prototyping.

[165] "MCM II and the Trip Chip", J. Estrada, C. Garcia, B. Hoeneisen and P. Rubinov, August 2002, FERMILAB-TM-2226.

[166] MINOS Technical Design Report, Chapter 5: Scintillator detector fabrication, Fermilab Public

[167] Specification 9216.000-ES-435360. Available through the Fermilab Particle Physics Division.

[168] Specification 9216.000-ES-435361. Available through the Fermilab Particle Physics Division.

[169] R. Bradford, *Assembly Roadmap from Prototype Studies*, posted to FNAL MINERνA Docdb as document number 561.

[170] R. Flight, *Detector Assembly Drawings, as of 11/15/05*, available in MINERνA Docdb as document number 226.

[171] R. Flight, *Mapper Drawings*, available in MINERνA Docdb as document number 897.

[172] R. Flight, *Fiber Routing Update*, available in MINERνA Docdb as document number 741.

[173] D. Casper, "The `nuance` Neutrino Physics Simulation, and the Future", *http://nuint.ps.uci.edu/nuance/files/nuance_nuint01.pdf*

[174] O. Benhar, [arXiv:nucl-th/0307061].

[175] K. Ruddick (private communication).

[176] L. Mualem (private communication).

[177] MINOS Collaboration, P. Adamson *et al.*, IEEE Trans. Nucl. Sci. **49**, 861 (2002).

[178] R. Fruhwirth, Nucl. Inst. Meth. **A262**, 444 (1987).

[179] "Studies of Extruded Plastic Scintillator for MINOS", Karol Lang and Todd Soesby, NuMI-NOTE-L-250, Feb 1997.

[180] M. Andrews, MINERνA Hazard Assessment, MINERνA Document 310 (2006)

[181] MINERνA Project Management Plan, MINERνA Document 59 (2006)

[182] L. Mualem, *The case for using Cesium-137 on the module mapper instead of Co-60*, NuMI-L-0653 (2000)

[183] American Institute of Steel Construction, Inc., *Manual of Steel Construction, Allowable Stress Design*, Ninth Edition

[184] American National Standard ANSI/ASME B30.20, *Below-the-hook lifting devices*

[185] Gage-Babcock & Associates, Inc. *Fire Protection/Life Safety Recommendations for the Fermilab NuMI Project* (1998)

[186] Fermilab ES&H Manual, Chapter 5032.2, Guidelines for the Design, Review and Approval of Liquid Cryogenic Targets (1995)

[187] J. Livengood, Letter to G. Brown, *National Environmental Policy Act (NEPA) Determination at Fermi National Accelerator Laboratory - "Main Injector Neutrino ExpeRiment ν–A(MINERνA)"* MINERνA Document 311 (December 2, 2005)